Finite-Element Modeling of Early-Age Concrete Behavior

by

Yalin Liu

A dissertation submitted to the Graduate Faculty of
Auburn University
in partial fulfillment of the
requirements for the Degree of
Doctor of Philosophy

Auburn, Alabama
August 4, 2018

Keywords: Thermal stress, Temperature Effects, Creep, Modified B3 Model,
Concrete Culvert, Nonlinear

Approved by

Anton K. Schindler, Chair, Professor and Director of the Highway Research Center
James S. Davidson, Professor of Civil Engineering
Robert W. Barnes, Associate Professor of Civil Engineering
Andrzej Nowak, Professor and Department Chair of Civil Engineering
Ben Farrow, Associate Professor of McWhorter School of Building Science

ABSTRACT

Early-age cracking of concrete may influence the long-term durability of a structure. Cracking occurs when the tensile stress in concrete exceeds its tensile strength. Early-age stress development in concrete is influenced by temperature changes, modulus of elasticity, creep or stress relaxation, shrinkage, coefficient of thermal expansion, and the degree of restraint. In this dissertation, three-dimensional, finite-element analysis was used to model the early-age stress development of concrete.

Four creep compliance models including the B3 Model, Modified B3 Model, B3 Model with R_T, and B4 Model were incorporated in the finite-element model. Experimental results from restraint to volume change tests with rigid cracking frame were used to assess the accuracy of the finite-element analysis. The results show that the Modified B3 Model provides the most accurate prediction of the measured early-age concrete stresses.

Extensive cracking was found in several cast-in-place concrete culverts in Alabama. A parametric study was performed by finite-element analysis of culverts and results revealed that the following measures will reduce the risk of early-age cracking in cast-in-place concrete culverts: lower coefficient of thermal expansion concrete, contraction joints, sand-lightweight concrete or all-lightweight concrete, scheduling the casting of the culvert wall to minimize the difference in its placement time relative to its previously cast base, and scheduling construction to avoid concrete placement during hot weather conditions.

The high-stress nonlinearity coupled with creep was considered in this study by correcting the model with a reduced effective modulus when the tensile stress is above 70% of its tensile strength. The experimental results of concrete mixtures were used to verify the accuracy of the proposed finite-element model from initial setting to the age of cracking. The coefficient of determination for all stress data points above a concrete tensile strength of 70% increased from 0.39 to 0.81 when using the predictions from the proposed model compared to the original linear-elastic model. The proposed model that accounts for creep and high-stress nonlinearity has a coefficient of determination of 0.97 for all the data points from 22 concretes tested, and provides an accurate prediction of early-age concrete stresses from setting to cracking.

ACKNOWLEDGEMENT

Great gratitude to my parents, brother and big sister for their sincere love and support in my life. They are my motivations to finish this project.

TABLE OF CONTENTS

LIST OF FIGURES

xvii

LIST OF TABLES

CHAPTER 1 OVERALL INTRODUCTION

1.1   BACKGROUND

Stress assessment and cracking risk of early-age concrete have attracted considerable interest (ACI 231 2010) because early-age cracking can increase the rate and amount of chloride penetration, which may accelerate the reinforcing steel corrosion rate, influence aesthetics, cause leakage, and decrease long-term durability of structures (Darwin and Browning 2008). Reliable material models and structural analysis methods are needed to estimate the risk of cracking and to evaluate potential options to mitigate early-age cracking in concrete.

Early-age stress development in concrete is influenced by temperature changes, thermal coefficient of expansion, shrinkage, degree of restraint, modulus of elasticity, and creep or stress relaxation. The schematic diagram of stress development during the concrete hardening phase is shown in Figure 1-1. Cracks occur when tensile stress in the concrete exceeds its tensile strength. Quantification of many of the influencing factors above is complicated, and many of these variables have complex interactions that affect early-age concrete stress development.
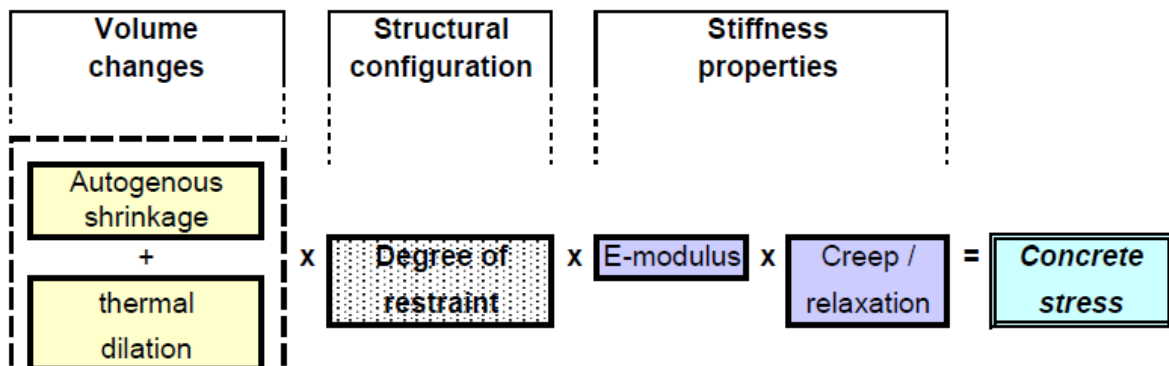
Figure 1-1 Stress development during the concrete hardening phase-schematic diagram

(Bjøntegaard 2011)

In some structures, such as bridge decks, pavements, culverts, and retaining walls, high tensile stress might develop due to high axial restraint. It is estimated that more than 100,000 bridges in the United States developed early-age transverse cracks (Krauss and Rogalla, 1996). Early-age cracking in retaining wall and culvert wall is shown in Figure 1-2 and Figure 1-3, respectively.

Figure 1-2 Thermal cracking in walls due to external restraint provided by footing

(Bjontegard 2013)
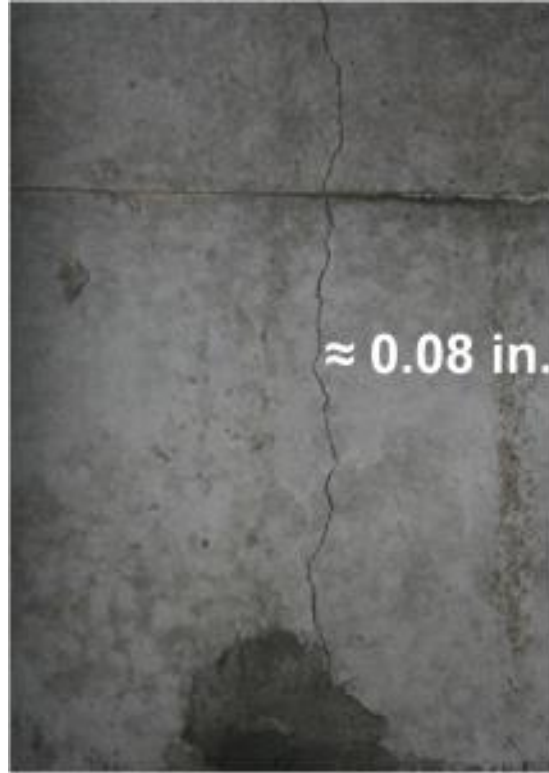
Figure 1-3 Cracking in Culvert Wall (Minton 2012)

Modeling of early-age stresses in such structures requires the validation of a creep model with realistic restraint conditions. Many models are reported in literature to predict the creep and shrinkage behavior of hardened concrete which include the B4 Model (Bažant, Hubler et al. 2014), the B3 Model (Bažant and Baweja 2000), ACI 209R-92(ACI 209 1992), CEB MC90 (CEB 1999), and the GL2000 (Gardner and Lockman 2001). These models are designed for mature concrete that were calibrated for 1 day or later. Early-age concrete have different behavior than mature concrete, because it has changing temperature due to hydration heat and changing mechanical properties. There is the Modified B3 Model (Byard and Schindler 2013), which could be used as it captures the early-age behavior of concrete from setting through later ages.

1.2   FINITE-ELEMENT METHOD

The finite-element method (FEM) is a numerical analysis technique for obtaining approximate solutions to a wide variety of engineering problems. The FEM can be used in conventional structural analysis for modeling both elastic-linear and nonlinear behavior. The advantages of using FEM are that complicated geometries and boundary conditions can be studied and representative 3-dimensional models can be developed to evaluate the behavior of full-scale structures.

The FEM program used for early-age concrete stress analysis needs to be able to corporate thermal properties, boundary conditions and restraint, and constitutive models of mechanical properties. However, in commercial FEM programs, there are no available models to accurately modify the behavior of early-age concrete. Several commercial FEM programs can be used to model early-age concrete stress development; having the need calibration to ensure their accurate models are obtained. For example, Witasse and Hendriks (2002) did finite-element modeling of early-age concrete behavior using DIANA, Truman et al. (1991) reported using ABAQUS code for early-age concrete stress anlysis, and Wu et al. (2011) estimated cracking risk of concrete at-early-age based on thermal stress analysis by using ANSYS program.

1.3   RESEARCH APPROACH

A three-dimensional finite-element model (FEM) that can accurately simulate the early-age stress development of concrete was developed. This FEM considers the changing mechanical properties, thermal effects, creep or relaxation, and drying shrinkage. A commercial software called ABAQUS was used for the finite-element analysis. The creep and drying shrinkage effects were handled by coding in the user-defined subroutines UMAT and UEXPAN of the software. A rate-type creep analysis was used herein to implement the creep models in the FEM.

4

Experimental results from restraint to volume change tests with rigid cracking frame (RCF) were used to verify the accuracy of the finite-element analysis. The RCF consists of dog-bone shaped formwork with dimensions of 6×6×50 in., two mild steel crossheads, and two Invar sidebars. The test setup can capture the early-age concrete stress development from setting to cracking. A total of 72 experimental concrete mixtures from three projects at Auburn University were used for the analysis herein. Four creep models were evaluated to determine their accuracy: the B3 Model, the Modified B3 Model, the B3 Model with R_T, and the B4 Model.

Finite-element analysis was also used to model the early-age stress development in concrete culverts by accounting for the following factors: construction sequencing, support restraint, concrete constituents, temperature effects, and the time-dependent development of mechanical properties, creep/relaxation, and drying shrinkage. A parametric study was performed to quantify the effect of changing joint spacing, joint type, construction sequence, concrete coefficient of thermal expansion, placement season, and concrete type on the early-age cracking risk. The finite-element model results revealed the measures to reduce the risk of early-age cracking in cast-in-place concrete culverts.

Since high-stress nonlinearity coupled with creep is of paramount importance when determining the cracking risk of concrete, the high-stress nonlinearity was considered in this study by correcting the model with a reduced effective modulus when the tensile stress is above 70% of its tensile strength. A total of 22 experimental concrete mixtures tested in the RFC are used to verify the proposed model to simulate early-age concrete stress development from initial set to the age of cracking.

5

1.4   RESEARCH OBJECTIVES

The primary objective of the research is to provide finite-element modeling (FEM) approach to estimate the cracking risk of concrete structures in both design and construction stages. A secondary objective is to develop a representaive finite-element model (FEM) that can accurately simulate the early-age stress development of concrete considering the changing mechanical properties, thermal effect, creep or relaxation, and drying shrinkage. By using the FEM to change variables of the concrete structure, such as different concrete materials, properties, construction sequences and so on, methods of reducing early-age cracking can be determined. Thus an accurate FEM accurately considers the effect of temperature change, creep or relaxation, shrinkage, and the degree of restraint is needed. In order to achive this objective, experimental results from restraint to volume change tests with rigid cracking frames were used to verify the accuracy of the FEM. The research presented in this dissertation is divided into three parts, and each part focused on different aspects of early-age concrete analysis.

Part I focuses on finite-element modeling of early-age concrete stress development with different creep models. The research described in Part I has the following objectives:

- Develop FEM method to simulate the early-age stress development of concrete based on structural and material modeling.

- Use the developed FEM to model the stress development of the 72 experimental concretes.

- Compare the stress results from the FEM to the measured stress results from experiments to verify the accuracy of the finite-element model.

- Using four creep models in the FEM for all the 72 concretes to determine the accuracy of the B3 Model, the Modified B3 Model, the B3 Model with R_T, and the B4 Model.

6

The focus of Part II was to perform three-dimensional finite-element modeling of cast-in-place concrete culverts and provide recommendations to mitigate early-age cracking of the culverts. The research described in Part II is focused on the following objectives:

- Model the early-age stress development of Culvert J from a project which were surveyed to show a lot of cracking.

- Perform cracking risk analysis of the modeled culvert to explain the reasons for the cracking found in the culverts.

- Perform a parametric study to evaluate the effects of changing joint spacing, joint type, construction sequence, concrete coefficient of thermal expansion, placement season, and concrete type on the early-age cracking risk.

- Provide methods to mitigate early-age cracking in cast-in-place concrete culverts for engineering practice.

Part III focuses on finite-element modeling of early-age concrete behavior under high level of tensile stresses. The research described in Part III has the following objectives:

- Use the most accurate creep model obtained from Part I to model early-age concrete stress development from initial setting to cracking.

- Correct the model with a reduced effective modulus and a damage factor to account for high-stress nonlinearity when the tensile stress is above 70% of its tensile strength.

- Compare the stress results from the FEM to the measured stress results from experiments to verify the accuracy of the proposed model that accounts for creep and high-stress nonlinearity.

7

1.5 DISSERTATION OUTLINE

This dissertation is divided into three parts. Part I focuses on finite-element modeling of early-age concrete stress development with different creep models. Part II focuses on the finite-element modeling and analysis of the early-age cracking risk of cast-in-place concrete culverts. Part III focuses on finite-element modeling of early-age concrete stress behavior under high-level of tensile stress. Each part is focused on different aspects of early-age concrete behavior; thus, each part was written to be a stand-alone document.

In Part I, the finite-element model was developed to simulate the early-age concrete stress development. A literature review of the factors that influence the early-age stress including temperature histories, changing mechanical properties, creep effects, and degree of restraint are presented in Chapter 3. The mathematical modeling of early-age concrete behavior, and four creep models including the B3 Model, Modified B3 Model, B3 Model with R_T, and B4 Model that were incorporated in the finite-element model, were discussed in Chapter 4. The details of the experimental work to verify the FEM is presented in Chapter 5. The development of the finite-element model, and the algorithm of incorporating the creep model in the FEM are presented in Chapter 6. Results and discussions of this part of work are presented in Chapter 7. The conclusions of Part I is presented in Chapter 8.

In Part II, measures to mitigate early-age cracking in culverts by evaluating the cracking risk were analyzed. This part of dissertation comprises of five chapters. A literature review containing culvert information, concrete culvert cracking background, and causes and influencing factors of cracking in culvert are summarized in Chapter 10. The process of modeling concrete culvert using finite-element method (FEM), which includes incorporating culvert geometry, material properties, creep model, and drying shrinkage model are presented in Chapter 11. The results of the

parametric study conducted with the FEM to evaluate the effect of changing joint spacing, joint type, construction sequence, concrete coefficient of thermal expansion, placement season, and concrete type are summarized in Chapter 12. Conclusions for this part are presented in Chapter 13.

In Part III, nonlinear behavior at high tensile stresses is considered in the finite-element model. This part of dissertation comprises of five chapters. A literature review containing concrete nonlinear tensile stress-strain behavior with and without creep effects, rate-type creep law, and experimental work to verify the model are summarized in Chapter 15. The process of modeling early-age concrete behavior using finite-element method (FEM), which includes incorporating material properties, creep model, and nonlinear behavior at high-stress level are presented in Chapter 16. The modeling results of early-age concrete stress development from setting to the age of cracking and comparisons with experimental work are summarized in Chapter 17. Conclusions for this part are presented in Chapter 18.

PART I:
FINITE-ELEMENT MODELING OF EARLY-AGE CONCRETE STRESS DEVELOPMENT WITH FOUR CREEP MODELS

CHAPTER 2 PART I: INTRODUCTION

2.1   BACKGROUND

Cracking in concrete structures at early ages is a result of tensile stresses induced by restraint of volume change effects. Stress assessment and cracking risk of early-age concrete have attracted considerable interest (ACI 231 2010) because early-age cracking can decrease the long-term durability of structures (Darwin and Browning 2008). Early-age stress development in concrete is influenced by temperature changes, modulus of elasticity, creep or stress relaxation, shrinkage, thermal coefficient of expansion, and the restraint conditions.

In some structures, such as bridge decks, pavements, culverts, and retaining walls, high tensile stress might develop due to high axial restraint. When the tensile stress exceeds its tensile strength, cracking may occur in these concrete structures. It is estimated that more than 100,000 bridges in the United States developed early-age transverse cracks (Krauss and Rogalla 1996). Modeling of early-age stresses in such structures requires the validation of a creep model with realistic restraint conditions. For this purpose, the stress-strain development in an axially restrained concrete specimen starting after placement using Rigid Cracking Frame (RCF) was used to evaluate the accuracy of existing creep models. A three-dimensional, finite-element model (FEM) is then developed to model the development of early-age stresses, which can then be used to assess the cracking risk of as-built structures.

The early-age behavior of concrete is much different than mature concrete, because it is changing temperature due to the effects of hydration and includes rapidly changing mechanical properties. Four creep models were used and compared in this study to determine their accuracy to predict the early-age stress development of concrete. Three-dimensional, finite-element analysis was

11

employed to simulate the early-age stress development of concrete. Therefore, a model to determine the early-age stresses in concrete structures are provided. By modifying concrete properties, concrete constituents, or construction procedures, the risk of cracking can be reduced.

2.2 OBJECTIVES

The primary research objective of this part is to develop a finite-element model with accurate creep models to simulate the early-age stress development of concrete and verify the model by experimental results. The objectives of the research described in this part are as follows:

- Develop FEM method to simulate the early-age stress development of concrete based on structural and material modeling.

- Use the developed FEM to model the stress development of the 72 experimental concretes.

- Compare the stress results from the FEM to the measured stress results from experiments to verify the accuracy of the finite-element model.

- Using four creep models in the FEM for all the 72 concretes to determine the accuracy of the B3 Model, the Modified B3 Model, the B3 Model with R_T, and the B4 Model.

2.3 RESEARCH APPROACH

Three-dimensional, finite-element analysis was used to model the early-age stress development of concrete and a rate-type creep analysis was used herein. Four creep compliance models including the B3 Model, Modified B3 Model, B3 Model with R_T, and B4 Model were incorporated in the finite-element model. Experimental results from restraint to volume change tests with rigid cracking frame were used to assess the accuracy of the finite-element analysis. The experimental tests include 72 concrete mixtures which contain varying cementitious materials, mixture proportions, temperature histories, aggregate types, water-to-cementitious materials ratios, and

chemical admixtures. The commercial finite-element program ABAQUS was used for the FEM and its material subroutine UMAT was used to code the creep models.

2.4   OUTLINE

In this part, the finite-element model was developed to simulate the early-age concrete stress development. A literature review of the factors that influence the early-age stress including temperature histories, changing mechanical properties, creep effects, and degree of restraint are presented in Chapter 3. The mathematical modeling of early-age concrete behavior, and four creep models including the B3 Model, Modified B3 Model, B3 Model with R_T, and B4 Model that were incorporated in the finite-element model, were discussed in Chapter 4. The details of the experimental work to verify the FEM is presented in Chapter 5. The development of the finite-element model, and the algorithm of incorporating the creep model in the FEM are presented in Chapter 6. Results and discussions of this part of work are presented in Chapter 7. The conclusions of Part I is presented in Chapter 8.

CHAPTER 3 PART I: LITERATURE REVIEW

The relevant research literature are summarized and presented in this chapter. The review include factors affect the early-age stress development and cracking, which are temperature change, shrinkage, creep, mechanical properties of concrete, and degree of restraint.

3.1   TEMPERATURE AND THERMAL STRESS DEVELOPMENT

The thermal stress of early-age concrete is influenced by its temperature, coefficient of thermal expansion, the modulus of elasticity, creep or relaxation, and the degree of restraint. The development of thermal stress can be determined with Equation 3-1 (Schindler and McCullough 2002).

$$\sigma = K_r \times CTE \times \Delta T \times E_c \qquad \textbf{(Equation 3-1)}$$

Where,

σ = the thermal stress (psi),

Ec = the creep-adjusted modulus of elasticity of the concrete (psi),

Kr = the internal/external restraint factor,

CTE = the coefficient of thermal expansion of concrete (in./in./˚F),

ΔT = the difference in temperature = $T_{zero\text{-}stress}$ - T_{min} (˚F),

$T_{zero\text{-}stress}$ = the temperature at zero stress in the concrete (˚F), and

T_{min} = the minimum temperature recorded by the concrete member (˚F).
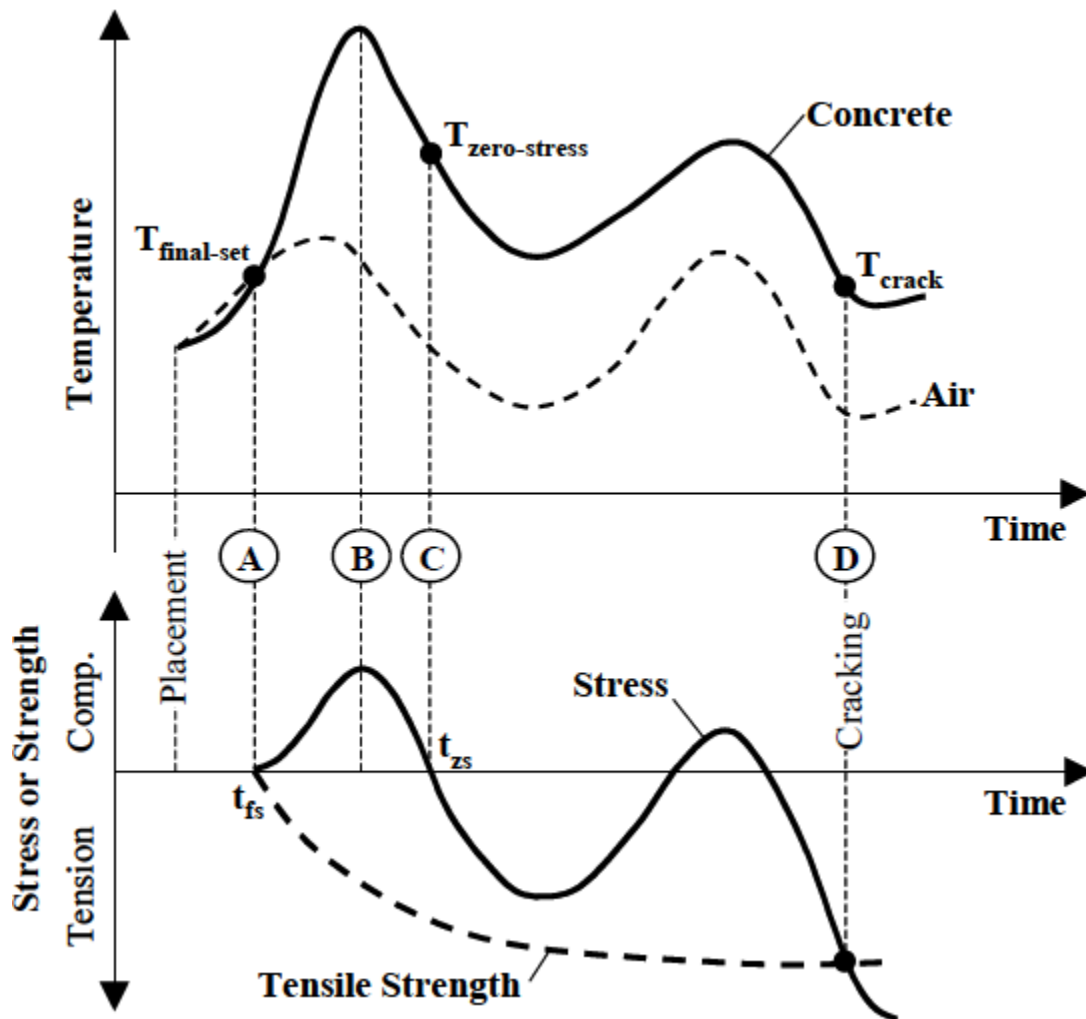
Figure 3-1 Evolution of early-age thermal stresses (Schindler and McCullough 2002)

A fully restrained concrete element considering only uniaxial stress is used to illustrate the development of early-age thermal stresses and how it is effected by changing temperature and mechanical properties is shown in Figure 3-1. After the placement of the fresh concrete and before final set, the concrete is in plastic state and no stresses are generated. After final set (t_{fs}), compressive stress begins to develop, because the increasing temperature due to hydration heat.

The mechanical properties of concrete such as the tensile strength and stiffness starts to develop at final set, and develop rapidly with concrete aging. After the temperature goes to a maximum point T_{max} (line B), the temperature is decreasing, the concrete starts to contract and thus the compressive stress starts to decrease and gradually reaches a zero value at time t_{zs}. The temperature at zero stress is defined as T_{zs}. Thereafter, tensile stress begin to develop in concrete and will vary under the temperature changing cycle, and finally goes to a high value that exceed the tensile stress of the concrete (line D). Then cracks occur in concrete, and the cracking time is denoted as t_c (Springenschmidt et al. 1994). In this process, the creep or relaxation effect on concrete stress need to be considered.

3.2   THERMAL DILATION

3.2.1   Coefficient of Thermal Expansion

The coefficient of thermal expansion of concrete mainly depends on the composition of the concrete mixture and its hygral state at the time of the temperature change. The coefficient of thermal expansion of concrete is influenced by two main components: the hydrated cement paste and aggregates. The linear coefficient of thermal expansion of hydrated cement paste varies between about 6×10^{-6} and 11×10^{-6} per °F, and is higher than the coefficient of aggregate (Neville 2011). As aggregate makes up 65-70% by volume of concrete mixture, the influence of the coefficient of aggregate is to influence the coefficient of thermal expansion of the concrete containing the given aggregate. Generally, the higher the coefficient of thermal expansion of the aggregate, the higher the coefficient of thermal expansion of the concrete, but the latter also depends on aggregate content and mixture proportions. Table 3-1 presents the values of the coefficient of thermal expansion of concretes made with different aggregates.

Table 3-1 Coefficient of thermal expansion of concretes made with different aggregates

(Neville 2011)

Type of Aggregate	Linear Coefficient of Thermal Expansion		
	Air-Cured Concrete	Water-Cured Concrete	Air-Cured and Wetted Concrete
	$10^{-6}/°F$	$10^{-6}/°F$	$10^{-6}/°F$
Gravel	7.3	6.8	6.5
Granite	5.3	4.8	4.3
Quartzite	7.1	6.8	6..5
Dolerite	5.3	4.7	4.4
Sandstone	6.5	5.6	4.8
Limestone	4.1	3.4	3.3
Portland stone	4.1	3.4	3.6
Blastfurnace slag	5.9	5.1	4.9
Expanded slag	6.7	5.1	4.7

3.2.2   Autogenous Shrinkage

Chemical shrinkage in concrete is the phenomena where the absolute volume of cement plus water decreases progressively with hydration (Tazawa 1998). Before setting, the concrete is still in plastic condition; therefore, this volume change due to chemical shrinkage does not generate stresses (Holt 2001). After setting of low water-to-cement ratio systems (w/c<0.42), hydration products formed a rigid skeletal formwork in the paste matrix, and with continued hydration when no moisture movement to or from the cement paste is permitted, shrinkage occurs. This shrinkage is the result of withdrawal of water from the capillary pores by the hydration of the hitherto unhydrated cement, a process known as self-desiccation (Neville 2011). The change in volume due to the chemical process of hydration of cement, exclusive of effects of applied load and change

17

in either thermal condition or moisture content is called autogenous shrinkage (ACI CT 2016).

Figure 3-2 shows an illustration of the relationship between chemical and autogenous shrinkage (horizontal direction), where C is the cement volume, W is the volume of water, Hy is the volume of hydration products, and V is the volume of voids.

Autogenous shrinkage is relatively small, except in extremely low water-to-cementitious ratios. For higher *w/cm*, generally above 0.42, autogenous shrinkage and associated stresses are not a major concern and can be neglected (Holt 2001).
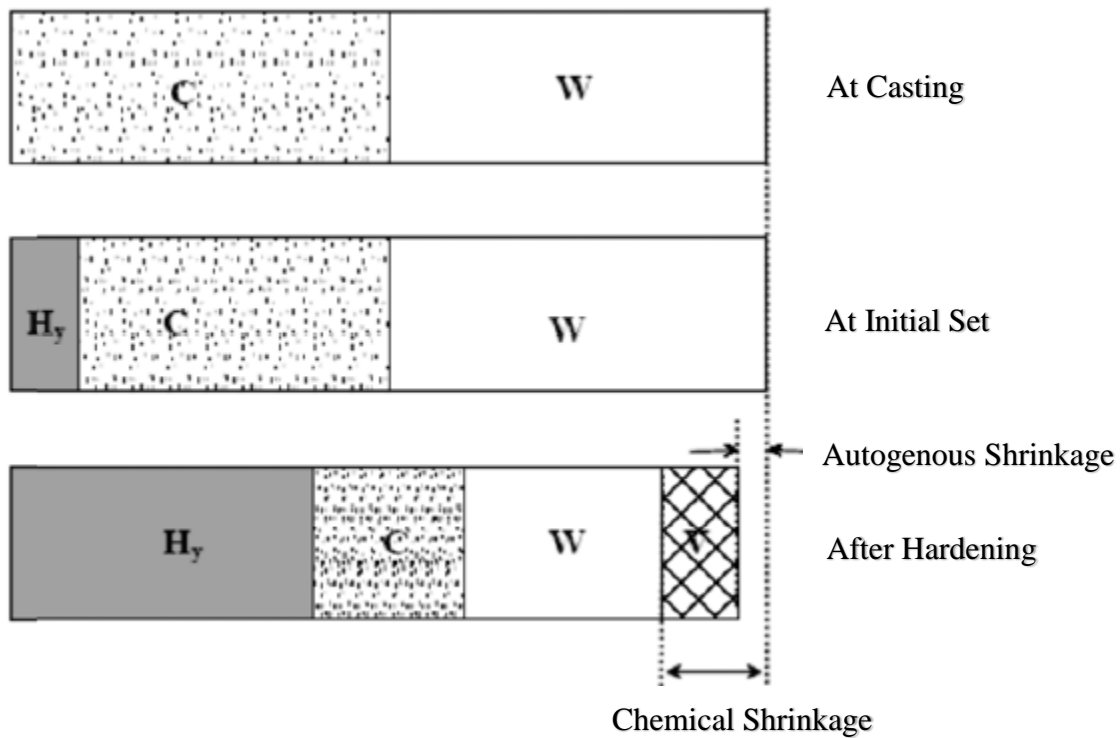
Figure 3-2 Volume reduction due to autogenous shrinkage (Holt 2001)

3.2.3 Drying Shrinkage

Removal of water from concrete that is stored in unsaturated air causes drying shrinkage (Neville 2011). When concrete is exposed to ambient humidity below 100%, loss of physically absorbed water from the hydrated cement paste results in drying shrinkage strain (Mehta and Monteiro 2013). The differential relative humidity between concrete and the environment is the driving force for drying shrinkage, and the concrete mixture proportions, the aggregate type, the time and humidity, and the geometry of concrete all affect the drying shrinkage (Mehta and Monteiro 2014).

Restraint of drying shrinkage of concrete can lead to internals tensile stress development, and when the tensile stress exceeds its tensile strength, the concrete cracks. Another consequence of drying shrinkage is curling or warping of concrete slabs, and if an effort is made to reduce drying shrinkage, curling will also be reduced (ACI 360R 2006). There are several models in literature to describe the development of drying shrinkage. ACI 209 (2008) provides details of four different models for the prediction of shrinkage of hardened concrete.

3.3 CREEP AND RELAXATION

When concrete is loaded, there is an instant elastic response, and if the load remains applied there will be additional time-dependent response. Creep and stress relaxation are viscoelastic phenomena that describe the time-dependent behavior of concrete. Creep is the time dependent increase in strain under a sustained stress (ACI 209 1992). Relaxation represents the time-dependent decrease in the uniaxial stress at age t caused by a unit constant strain imposed at t' (Bažant and Wittmann 1982). Compliance characterizes both the elastic deformation and time-dependent part, and is defined as the total load induced strain (elastic plus creep strain) at age t per unit stress caused by a unit uniaxial sustained load applied at loading age t' (ACI 209 1992). Figure

3-3 illustrates the creep and relaxation effects. Stress relaxation is beneficial in delaying the cracking time of early-age cracking in concrete (Mehta and Monteiro 2014).
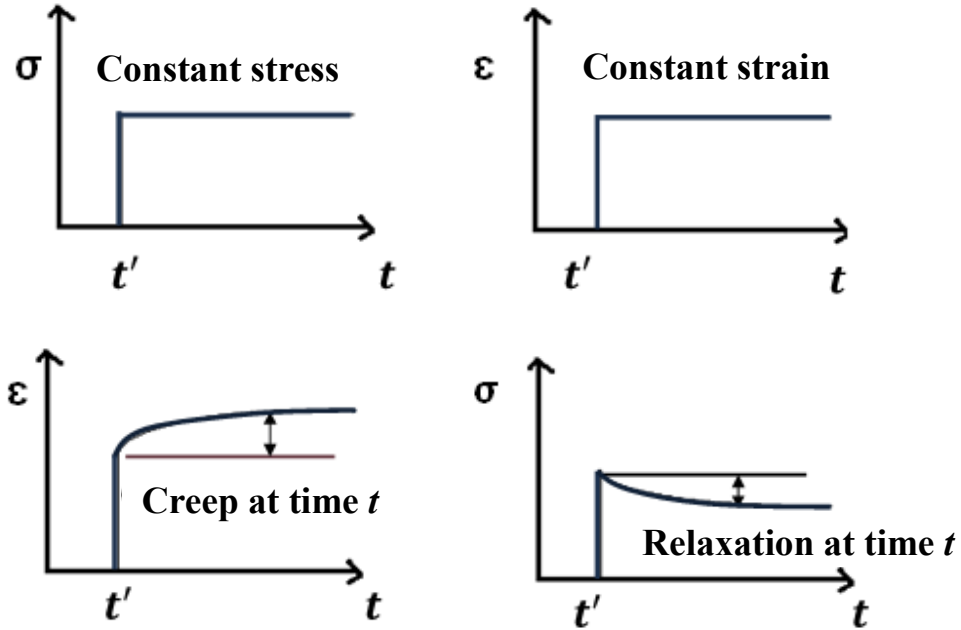
Figure 3-3 Illustration of creep and relaxation effects (adapted from Neville and Brooks 1991)

The stress and strain relations due to creep and relaxation are shown in Equation 3-2 and Equation 3-3, respectively. The compliance function $J(t, t')$ and relaxation function $R(t, t')$ are alternative descriptions of the same intrinsic phenomenon, and by definition, the two functions are integral equation kernels inverse to each other (Bažant and Wittmann 1982).

$$\varepsilon(t) = J(t, t')\sigma(t') \qquad \textbf{(Equation 3-2)}$$

$$\sigma(t) = R(t, t')\varepsilon(t') \qquad \textbf{(Equation 3-3)}$$

Where,

t' = age at loading (days),

t = concrete age (days),

$\varepsilon(t)$ = strain at time t (in./in.),

$\sigma(t)$= stress at time t (psi),

$J(t, t')$ = compliance function (1/psi), and

$R(t, t')$ = relaxation function (psi).

3.4   MECHANICAL PROPERTIES OF CONCRETE

The accuracy of early-age thermal stress analysis is affected by how the thermal properties and mechanical properties are described. Therefore, the changing mechanical properties of early-age concrete need to be considered in order to obtain accurate crack predictions. The strength and modulus of elasticity growth in young concrete have been extensively studied and modeled in literature. The compressive strength, splitting tensile strength, and modulus of elasticity development can be measured by cylinders match cured to the structure concrete mixture.

A regression analysis can be performed on the discrete data points from tests with the hyperbolic function (see Equation 3-4) recommended by ASTM C1074 (2016). From the regression analysis, the best-fit values for S_u, t_0, and K can be determined.

$$S = S_u \frac{K(t - t_0)}{1 + K(t - t_0)} \qquad \textbf{(Equation 3-4)}$$

Where,

S = average cube strength at age t (psi),

t = test age (days),

S_u = limiting strength (psi),

t_0 = age when strength development is assumed to begin (days), and

K = the rate constant.

3.4.1 Compressive Strength

The compressive strength of concrete is influenced by many factors, mainly including the water-to-cementitious materials-ratio (*w/cm*), air content, cement type, aggregate type, aggregate size, temperature history, curing conditions, and rate of loading (Mehta and Monteiro 2014).

Several functions exist in literature to model the compressive strength of concrete, and ACI 209-71 proposed Equation 3-5 for predicting compressive strength at any day based on the 28-day strength of the concrete.

$$f_c(t) = f_{c28} \left(\frac{t}{\alpha + \beta \cdot t} \right)$$
                                                           (Equation 3-5)

Where,

f_c = compressive strength of samples moist-cured at 73° F,

t = concrete age (days),

α =4.0 and β =0.85 (for Type I cement),

α =2.3 and β =0.92 (for Type III cement).

3.4.2 Tensile Strength

Tensile strength is a more important parameter to assess the risk of cracking of early-age concrete. Splitting test and flexural test are normally used to determine the tensile strength of concrete, as the direct uniaxial tensile tests are difficult to carry out.

ACI 207.2 R (2007) provided the Equation 3-6 to estimate the splitting tensile strength of concrete by a given compressive strength.

$$f_{st} = 3.7 \times \sqrt{f_c} \qquad \text{(Equation 3-6)}$$

Where,

f_{st} = splitting tensile strength (psi), and

f_c = concrete compressive strength (psi).

For concrete containing lightweight aggregate, Greene and Graybeal (2013) developed an expression shown in Equation 3-7, to estimate the splitting tensile strength from known compressive strength values. A lightweight modification factor (λ) is determined from the concrete density, as shown in Equation 3-8.

$$f_{st} = 0.212\lambda f_c^{0.5} \qquad \text{(Equation 3-7)}$$

$$0.5 \leq \lambda = 7.5w_c \leq 1.00 \qquad \text{(Equation 3-8)}$$

Where,

w_c= density of normalweight concrete or equilibrium density of lightweight concrete (kcf),

f_{st} = splitting tensile strength (ksi),

f_c = concrete compressive strength (ksi), and

λ = lightweight modification factor (unitless).

3.4.3 Modulus of Elasticity

ACI 318（2014）provided Equation 3-9 to estimate the modulus of elasticity for a concrete from a known density and compressive strength.

$$E_C = 33w_c^{1.5}\sqrt{f_c}$$ **(Equation 3-9)**

Where,

E_C = modulus of elasticity (psi),

w_c = density of concrete (lb/ft^3), and

f_c = concrete compressive strength (psi).

AASHTO provided a new function for determining the modulus of elasticity of concrete that deals with lightweight and normalweight concrete, which is shown in Equation 3-10.

$$E_C = 120,000K_1w_c^2f_c^{0.33}$$ **(Equation 3-10)**

Where,

E_C = modulus of elasticity (psi),

K_1 = aggregate correction factor (unitless),

w_c = density of normalweight concrete or equilibrium density of lightweight concrete (kcf),

f_c = concrete compressive strength (psi).

3.5   DEGREE OF RESTRAINT

If the length or volume changes caused by temperature change and shrinkage with a concrete element could take place freely, there would be no stress development. However, nearly all structural members are restrained to a certain degree. The degree of restraint is defined as the ratio of actual stress resulting from volume change to the stress that would result if completely restrained; and the degree of restraint is primarily influenced by the relative dimensions, strength, and modulus of elasticity of the concrete member and the restraining material (ACI 207.2 R 2007). The restraint conditions are of greatest concern are those the restraint conditions that induce tensile stresses in concrete that can lead to cracking.

There are traditionally two restraint conditions, namely external restraint and internal restraint. External restraint could occur at the end and at the inner supports of frames, slabs, beams and so on, where the deformations are impeded by the adjacent members. Another kind of continuous external restraint is within a slab or foundation cast on subsoil or a wall on foundations. Internal restraint occurs in concrete elements with nonuniform volume change on a cross section such is the situation when the interior temperatures are greater than surface temperatures for mass concrete slabs or walls. For example, when the formwork is removed from a hot concrete structural element, the rapid cooling of the surface would lead to surface contraction that is restrained by the core, which may result in surface cracking (Bjøntegaard 2011).

The estimation of restraint actions is influenced by many challenging aspects (Rostásy et al. 1998): 1) the time-dependent changing viscoelastic and viscoplastic behavior and strength of early-age

25

concrete; 2) the realistic measurement or prediction of the field of temperature, thermal strain, and degree of hydration; 3) the realistic modeling of the interaction of the restraining effects.

3.6   EQUIVALENT AGE AT DIFFERENT TEMPERATURES

The maturity method is used to account for the effect of time and temperature on concrete strength gain (Pinto and Hover 1999). The effects of temperature on creep, shrinkage and aging rates can be captured by equivalent age. The equivalent age is used to replace the real age of concrete. Several functions can be used to calculate the maturity of concrete. The Arrhenius equation is more representative and selected in this study (Carino 2004).

$$t_e = \sum e^{\frac{-E}{R}} \left[\frac{1}{273 + T_C} - \frac{1}{273 + T_r} \right] \cdot \Delta t \qquad \textbf{(Equation 3-11)}$$

Where,

t_e = equivalent age at the reference curing temperature (hour),

T_C = average temperature of concrete during time interval Δt (°C),

T_r = reference temperature (°C),

E = activation energy (J/mol), and

R = universal gas constant, 8.3144 J/(mol K).

Therefore, based on Equation 3-11, assume the exponential term varies linearly with the time interval Δt, the incremental equivalent age can be expressed as:

$$\Delta t_{e,i} = e^{\frac{-E}{R}} \left[\frac{1}{273 + T_C} - \frac{1}{273 + (T_i + T_{i-1})/2} \right] \cdot \Delta t_i \qquad \textbf{(Equation 3-12)}$$

The temperature at the time step used the average value of the current temperature and the previous temperature. Then the equivalent age can be obtained by:

$$t_{e,i+1} = t_{e,i} + \Delta t_{e,i} \qquad \textbf{(Equation 3-13)}$$

The time t_i and Δt_i that were used to calculate the creep in the subroutine are all replaced by the equivalent age $t_{e,i}$ and $\Delta t_{e,i}$.

The activation energy of all the concrete here is calculated based on the method provided by Schindler (2004):

$$E = 22,100 \cdot P_{C_3A}{}^{0.3} \cdot P_{C_4AF}{}^{0.25} \cdot Blaine^{0.35} \qquad \textbf{(Equation 3-14)}$$

Where,

P_{C_3A} = weight ratio of C$_3$A in terms of total cement content,

P_{C_4AF} = weight ratio of C$_4$AF in terms of total cement content, and

$Blaine$ = Blaine value, specific surface area of cement (m^2/kg).

CHAPTER 4 PART I: MATHEMATICAL MODELING OF EARLY-AGE CONCRETE BEHAVIOR

4.1   VISCOELASTIC BEHAVIOR

When concrete is subjected to loading, there are three possible fundamental deformations, which are elastic, plastic, and viscous deformation (Emborg 1998). Combinations of these deformations would occur as visco-elastic and elasto-plastic deformations. For thermal stress analysis of early-age concrete, the viscoelastic behavior is a very important parameter (Emborg 1998). The validity and reliability of early-age concrete stress analysis depends on the goodness of the viscoelastic model to describe the viscoelastic behavior of concrete. For the modeling of viscoelastic responses of concrete, several methods have been suggested in literature and will be discussed in the following sections.

4.1.1   Rheological Model
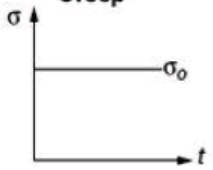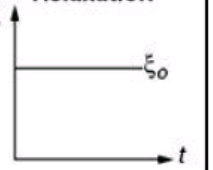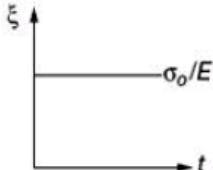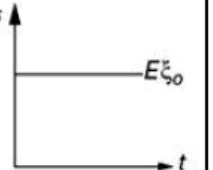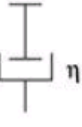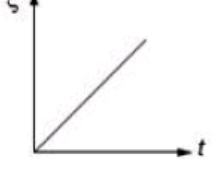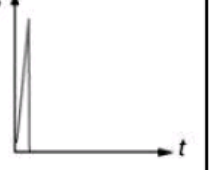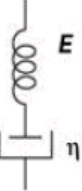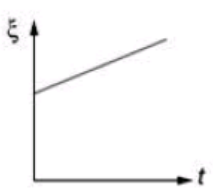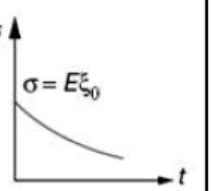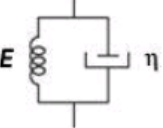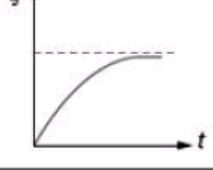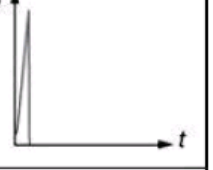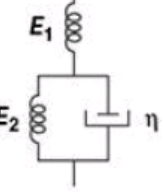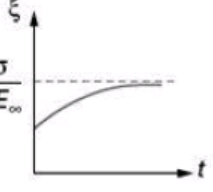
Concrete exhibits elastic and viscous behavior, so a viscoelastic model is effective to simulate concrete behavior. A viscoelastic material have both elastic and viscous behavior-a bit like a solid and a bit like fluid. A linear-viscoelastic model exhibits combinations of the linear-elastic spring and the linear-viscous dash-pot, which is called rheological model or mechanical model (Kelly 2018). A linear spring with stiffness E has the constitutive relation as shown in Equation 4-1. A dash-pot with viscosity η behaves with a strain-rate proportional to stress as shown in Equation 4-2. Table 4-1 shows some simple rheological models and their creep and relaxation responses.

$$\varepsilon = \frac{1}{E}\sigma \qquad \textbf{(Equation 4-1)}$$

$$\dot{\varepsilon}=\frac{1}{\eta}\sigma \qquad\qquad \text{(Equation 4-2)}$$

Table 4-1 Simple rheological models and their creep and relaxation responses (Mehta and Monteiro 2014)

Name	Representation	Creep	Relaxation
		σ_o	ξ_o
(a) Spring	E	σ_o/E	$E\xi_o$
(b) Dashpoot	η		
(c) Maxwell	E η		$\sigma = E\xi_0$
(d) Kelvin	E η		
(e) Standard Solid	E_1 E_2 η	$\dfrac{\sigma}{E_\infty}$	

4.1.2 Kelvin Chain Model

A Kelvin model consists of a spring and a dash-pot in parallel (Figure 4-1). The spring and the dash-pot experience the same strain and the total stress of the model is the sum of stress in the spring and the dash-pot (see Equation 4-3 to Equation 4-5) (Kelly 2018). The Kelvin Chain is rheological model composed of a series coupling of many Kelvin units, and each unit consists of a parallel coupling of a spring and a dashpot.

$$\varepsilon = \frac{1}{E}\sigma_1 \qquad \textbf{(Equation 4-3)}$$

$$\dot{\varepsilon} = \frac{1}{\eta}\sigma_2 \qquad \textbf{(Equation 4-4)}$$

$$\sigma = \sigma_1 + \sigma_2 \qquad \textbf{(Equation 4-5)}$$
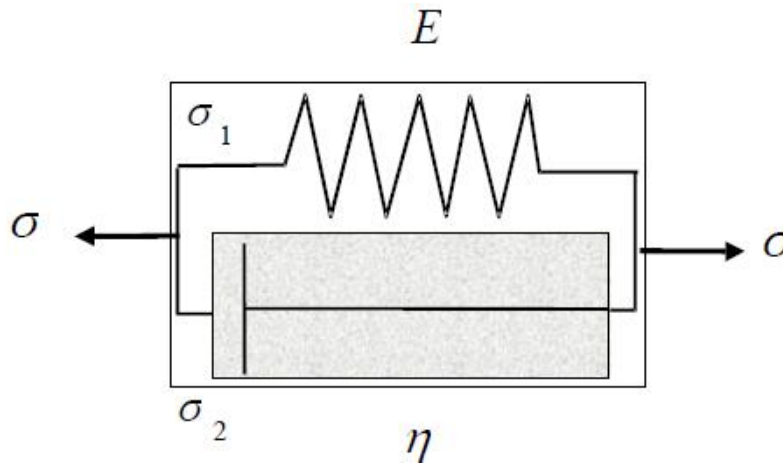
Figure 4-1 The Kelvin model (Kelly 2018)

If a constant load σ_0 is applied to the Kelvin model, the spring cannot stretch immediately because of the hold of the dashpot. The stress is initially taken by the dash-pot, gradually decreasing and

finally taken over all by the spring. The creep curve has an initial slope of $\frac{\sigma_0}{\eta}$, and maximum strain

of $\frac{\sigma_0}{E}$. The strain change with time for the Kelvin model is obtained by solving the first order

differential Equation 4-3 to Equation 4-5 with $\varepsilon(0) = 0$ (Kelly 2018):

$$\varepsilon(0) = \frac{\sigma_0}{E}(1 - e^{-\left(\frac{E}{\eta}\right)t})$$

(Equation 4-6)

Then the creep compliance function is (Kelly 2018):

$$J(t) = \frac{1}{E}\left(1 - e^{-\frac{t}{t_R}}\right)$$

(Equation 4-7)

$$t_R = \frac{E}{\eta}$$

(Equation 4-8)

The parameter t_R is called the retardation time of the material and represent how rapid the creep

strain develops.

4.2   SOLIDIFICATION THEORY

Bažant and Prasannan (1989 a,b) presented a constitutive law for creep based on solidification

theory, in which the micromechanical analysis of the solidification process is used to represent the

aging. Aging is modeled as a growth of the volume fraction of load-bearing hydrated cement,

which itself is treated as non-aging and thus is described as non-aging viscoelastic material. In the

solidification theory, the total strain ε of concrete can be decomposed as (Bažant and Prasannan

1989a):

$$\varepsilon = \frac{\sigma}{E_0} + \varepsilon^c + \varepsilon^0, \qquad \varepsilon^c = \varepsilon^v + \varepsilon^f$$

(Equation 4-9)

Where, σ = stress, E_0 = elastic modulus, $\frac{\sigma}{E_0}$ = elastic strain, ε^c = creep strain, ε^v = viscoelastic strain, ε^f = viscous strain (flow), and ε^0 = sum of the hygrothermal strain such as drying shrinkage, thermal dilatation, chemical strain such as autogeneous shrinkage, and the cracking strain at high stresses. All the strains in Equation 4-9 are depicted in Figure 4-2 (Bažant and Prasannan 1989a).
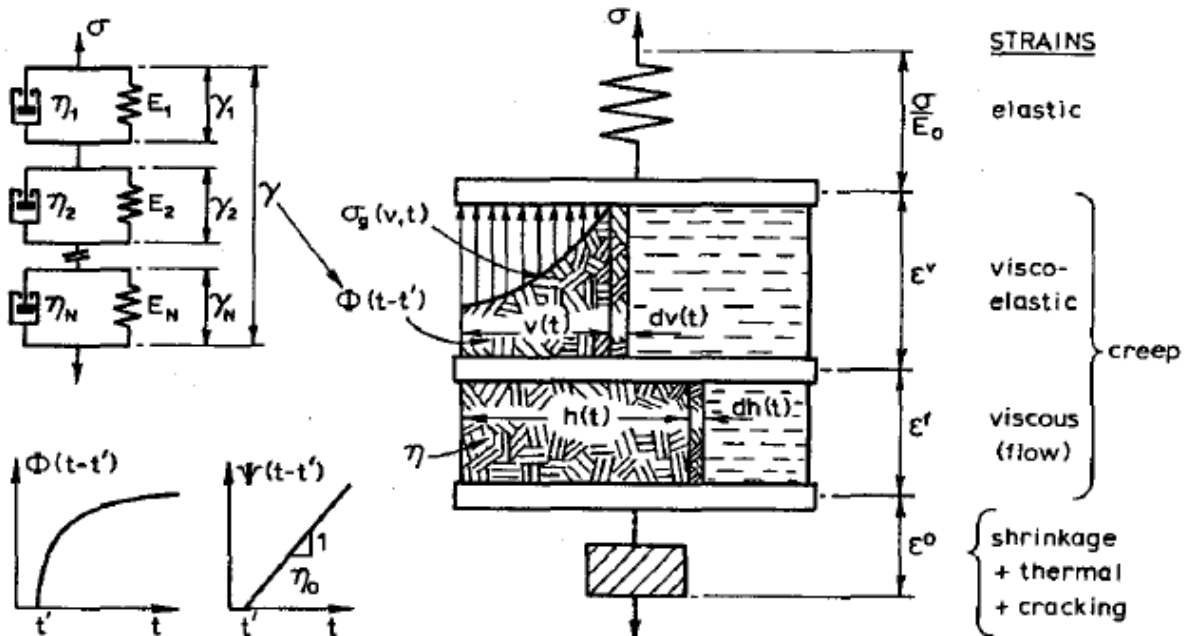
Figure 4-2 Model for role of solidification in creep (Bažant and Prasannan 1989a)

The main feature of the solidification theory is that the aging aspect of basic creep of concrete is considered to be due to the growth of the volume fraction $v(t)$ (Figure 4-2) of the effective load-bearing portion of solidified matter (i.e. hydrated cement), which represents both the increase of the volume fraction of hydrated cement and the increase of load-bearing solid fraction caused by formation of further bonds (or polymerization of calcium silicate hydrates) (Bažant and Xi 1995).

The volume growth $v(t)$ and $h(t)$ can be mathematically formulated. The elementary volume $dv(t)$ that solidifies at time t is assumed to be represented by a layer deposited on the surface of the material that previously solidified from a fluid. $\sigma_g(v, t)$ is the microstress in the solidified matter at time t and is at the location where the solidification occurred when the volume of all the solidified matter is v. $\Phi(t - t')$ is the microscopic creep compliance function of the solidified matter for the visco-elastic strain, and $\Psi(t - t')$ is the corresponding microscopic compliance function of the solidified matter for the viscous strain, which is nonaging (Bažant and Prasannan 1989a).

In the formulation of the solidification theory, the creep of the nonaging constituent is described by a Kelvin chain with a number N of Kelvin units (Bažant and Prasannan 1989b). Each Kelvin unit has a parallel of a spring with an elastic moduli E_μ and a dashpot with a viscosity of η_μ. γ_μ is the strain of the μth unit and μ ranges from 1 to N. The differential equation for a nonaging Kelvin chain is shown in Equation 4-10, and the total strain of all the Kelvin units is γ for a constant stress, σ.

$$E_\mu \gamma_\mu + \eta_\mu \dot{\gamma}_\mu = \sigma, \qquad \gamma = \sum_{\mu=1}^{N} \gamma_\mu \qquad \textbf{(Equation 4-10)}$$

4.3 CONSTITUTIVE EQUATIONS BASED ON THE PRINCIPLE OF SUPERPOSITION

When the stresses in concrete vary, such as the early-age stresses caused by temperatures change due to heat of hydration, the previous explanation of material behavior under constant stress must be extended to formulate a constitutive equation valid for variable stresses and often the principle of superposition is used for this case. "The principle of superposition, which is equivalent to the

hypothesis of linearity, states that a response to a sum of two stress (or strain) histories is the sum of the responses to each of them taken separately" (Bažant and Wittmann 1982). The principle is sufficiently good prediction if the stresses and their changes are sufficiently small, and the time history is sufficiently short (Bažant 1972). The principle of superposition yields good approximation when concrete is within the service stress range (Bažant and Wittmann 1982). It is generally agreed that the use of the principle of superposition is valid below stress-to-strength ratios of 40%~60%, but the ratio can be as high as 85% (Neville et al. 1983).

According to this principle, for a variable stress history, the final strain $\varepsilon(t)$ caused by stress history $\sigma(t)$ is the sum of individual strain caused by the decomposed small increments $d\sigma(t')$ applied at t. Figure 4-3 illustrate the principle of superposition. Equation 4-11and Equation 4-12 describe this principle, and the integral in this equation is applicable for both continuous and discontinuous stress histories (Bažant and Wittmann 1982):

$$\varepsilon(t) = \int_0^t J(t, t') d\sigma(t') + \varepsilon^0(t)$$
(Equation 4-11)

$$\varepsilon^0(t) = \varepsilon_{sh,total}(t, t_0) + \alpha_T \Delta T$$
(Equation 4-12)

Where,

$J(t, t')$ = compliance function at time t for a loading at time t',

$d\sigma(t')$ = stress increment at time t', and

$\varepsilon^0(t)$ = the strain due to thermal dilation and drying shrinkage which is stress independent

strains.
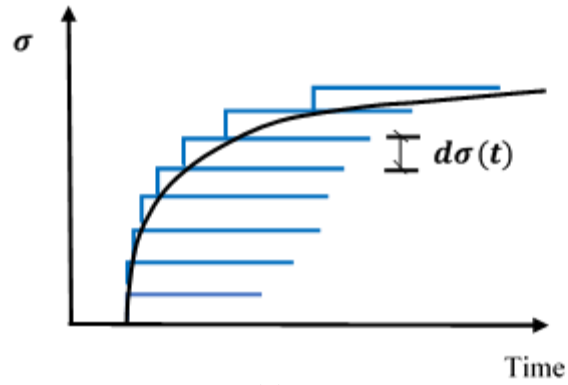
(a)
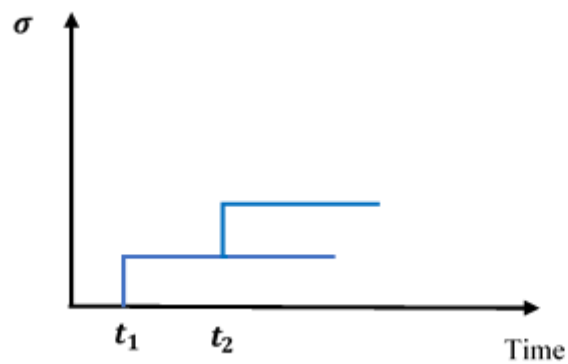
(b)
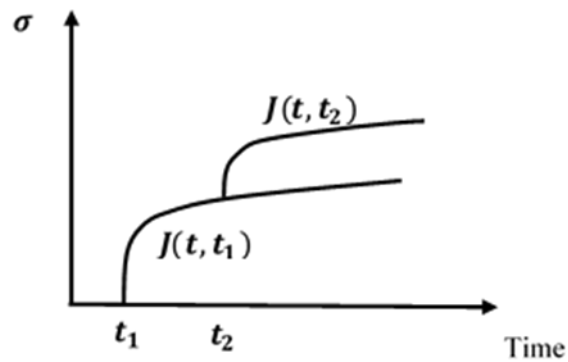
(c)

Figure 4-3 Use of principle of superposition to model viscoelastic response: (a) an arbitary stress history as a sum of inifinitesimal stress increments, (b) two stress increment occur at different times, (c) strain response by superposition of the two stress increments [adapted from Emborg 1988b]

The variation of stress at prescribed strain history can be written in a similar way by a relaxation function shown as Equation 4-13 (Bažant and Wittmann 1982),

$$\sigma(t) = \int_0^t R(t,t')[d\varepsilon(t') - d\varepsilon^0(t)] \qquad \textbf{(Equation 4-13)}$$

Where,

$R(t,t')$ is the relaxation function of time for a deformation at time t', and

$d\varepsilon(t')$ is the strain increment introduced at time t'.

4.4   RATE-TYPE FORMULATION OF CREEP

The integral equation (Equation (Equation 4-11) to calculate variable stresses by the principle of superposition is computationally inefficient for large concrete structures (Yu et al. 2012). Therefore, a rate-type creep law with internal variables whose current values account for the previous history of strains are provided for the analysis (Yu et al. 2012). The benefits of the rate-type approach includes that there is no need to store and track the strain history and there is no need to sum the history over all the previous time steps. Moreover, it makes the creep computations more efficient and make it possible to take into account the evolution of various inelastic and nonlinear phenomena. The rate-type creep law is visualized by the Kelvin chain model, and this model consists of a series of Kelvin units, which involves a spring and a dashpot in parallel (Bažant and Prasannan 1989a,b). The spring and the dashpot experience the same strain (ε), and the total stress (σ) of the model is the sum of stress in the spring and the dashpot as shown in Equation 4-14 (Bažant and Prasannan 1989a,b):

$$\sigma = E\varepsilon + \eta\dot{\varepsilon} \qquad\qquad \textbf{(Equation 4-14)}$$

Where,

E is the spring stiffness (psi), and

η is the viscosity of the dashpot (psi·s).

Yu et al. (2012) summaries the details of the rate-type creep law and the implementation of different creep models with this approach using finite-element analysis. Wei and Hanson (2012) and Byard and Schindler (2015) both used the integral type method with the principle of superposition to model early-age concrete stress. In this dissertation, three-dimensional, FEM will be used with the rate-type creep law. This approach will allow the modeling of in-place stresses of various concrete structures that have three-dimensional stress states and varying degree of restraints.

4.5   MATHEMATICAL MODELS FOR CREEP IN ACI 209.2R

There are numerous models for calculating shrinkage and creep of concrete in literature. ACI 209.2R (2008) provides details of ACI 209R-92 model, CEB MC90-99 Model, GL2000 Model, and B3 Model. These models are intended for the prediction of shrinkage and creep in compression in hardened concrete and it may be assumed that predictions apply to concrete under tension. These models presented here are valid for hardened concrete moist cured for at least 1 day and loaded after curing or later (ACI 209.2R 2008).

4.6 CREEP MODELS USED IN THIS STUDY

4.6.1 B3 Model

The B3 Model for concrete creep is based on solidification theory and the Kelvin chain model. The solidification theory for concrete creep describes the cement hydration as a growth of the volume fraction of load-bearing solidified matter (hydrated cement), and the solidified material is treated as non-aging viscoelastic material (Bažant and Prasannan 1989a,b).

The B3 Model compliance function is expressed in Equation 4-15 to Equation 4-20 (Bažant and Baweja 2000), and the compliance $J(t, t')$ (1/psi) can be decomposed in to three terms, q_1 the instantaneous strain due to unit stress (1/psi), $C_0(t, t')$ compliance function for basic creep (no moisture loss) (1/psi), and $C_d(t, t', t_0)$ additional compliance due to drying (1/psi). The basic creep function is described in Equation 4-16 (Bažant and Baweja 2000).

$$J(t, t') = q_1 + C_0(t, t') + C_d(t, t', t_0) \qquad \textbf{(Equation 4-15)}$$

$$C_0(t, t') = q_2 Q(t, t') + q_3 \ln[1 + (t - t')^n] + q_4(\frac{t}{t'}) \qquad \textbf{(Equation 4-16)}$$

Where, t, t', t_0 are age of concrete, age at loading, and age when drying begins, respectively (days). The creep strain is treated as a sum of aging $(q_2 Q(t, t'))$, non-aging $(q_3 \ln[1 + (t - t')^n])$ viscoelastic strains, and aging viscous or flow strain $(q_4(\frac{t}{t'}))$. Based on this, the B3 Model can be modified to account for the early-age behavior of concrete.

The terms q_1 to q_4 are empirical material constitutive parameters based on concrete composition and strength, and are determined with Equation 4-17 to Equation 4-20 (Bažant and Baweja 2000).

$$q_1 = 0.6 \times \frac{10^6}{E_{c,28}} \qquad \text{(Equation 4-17)}$$

$$q_2 = 451.1 c^{0.5} \overline{f_c}^{-0.9} \qquad \text{(Equation 4-18)}$$

$$q_3 = 0.29 \left(\frac{w}{c}\right)^4 q_2 \qquad \text{(Equation 4-19)}$$

$$q_4 = 0.14 \left(\frac{a}{c}\right)^{-0.7} \qquad \text{(Equation 4-20)}$$

Where,

$n = 0.1$,

$m = 0.5$,

a/c = aggregate-to-cement ratio by mass,

w/c = water-to-cement ratio by mass,

a = the total aggregate content (lb/ft^3), and

c = the cement content (lb/ft^3),

4.6.2 Modified B3 Model

The B3 Model is not intended or calibrated for concretes younger than 1 day. In particular, as the early-age shrinkage in concrete is governed by exothermal chemical reactions and the transition between liquid and solid phase, the model is not intended for predicting the early-age shrinkage and creep effects (Bažant et al. 2014). Early-age stress development in concrete is different from stress in hardened concrete because of hydration process, rapid temperature change, and high

viscoelastic behavior. A model to calculate early-age stress can be obtained by modifying a later-age compliance model to consider early-age properties (Byard and Schindler 2015).

For early-age concrete stress development, the stress developed from setting should be accounted for in order to achieve accurate later-age cracking prediction. Early-age concrete shows both rapidly changing elastic properties and high viscoelastic properties. Østergaard et al. (2001) provides a modification to q_2 of the B3 Model to capture the early-age high viscoelastic behavior as shown in Equation 4-21. In this expression, q_5 is the concrete structural setting time in days and should be less than the age at loading, t'. This modification provides a higher early-age viscoelastic behavior while leaving the viscoelastic behavior of the original B3 Model unchanged at later ages.

$$q'_2 = q_2 \left(\frac{t'}{t' - q_5} \right) \hspace{2cm} \textbf{(Equation 4-21)}$$

Since the B3 Model uses a constant asymptotic modulus of elasticity, Byard and Schindler (2015) found that the B3 Model overestimates the early-age compressive stress due to thermal effects. Overestimating the initial compressive stresses leads to an underestimation of early-age tensile stresses that occur after the time of zero stress. The modulus of elasticity of early-age concrete is changing rapidly, therefore the use of a constant modulus of elasticity is not suitable for early-age concrete. Byard and Schindler (2015) therefore introduced an elastic property modifier similar in format to the modification for viscoelastic behavior as provided in Equation 4-22. In this expression, q_6 is the concrete structural setting time in days, which must be less than the age at loading, t'. This modification also only has an effect for 2 days or less, which leaves the later-age elastic compliance of the original B3 Model unchanged.

$$q'_1 = q_1 \left(\frac{t'}{t' - q_6} \right)$$ **(Equation 4-22)**

The final Modified B3 Model with the two modifications can be expressed as shown in Equation

(Equation 4-23. The definitions of all the variables in Equation 4-23 can be found from Equation

4-15 to Equation 4-20. As a practical simplification when RCF testing cannot be performed, Byard

and Schindler (2015) recommended the use of equivalent age at initial set as the values for q_5 and

q_6.

$$J(t, t') = q_1 \left(\frac{t'}{t' - q_6} \right) + q_2 \left(\frac{t'}{t' - q_5} \right) Q(t, t') + q_3 \ln[1 + (t - t')^n] + q_4 (\frac{t}{t'})$$ **(Equation 4-23)**

4.6.3 B3 Model with R_T

Temperature affects creep in two ways: 1) it directly influences creep by increasing the creep rate

and 2) it indirectly influences the aging rate of the concrete (Bažant et al. 2014). The maturity

method with equivalent age (Carino 2004) is used to allow the models to capture the temperature

effects on concrete aging rate. Some researchers provide coefficients multiplied to the compliance

function to account for the effect of temperature on the creep rate (Emborg 1998; Umehara et al.

1995). Many researchers only consider equivalent age for temperature effect on aging of concrete,

and ignore the effect of temperature on the creep rate. Bažant and Baweja (2000) provide two

components to consider the effect of temperature on creep: 1) use of equivalent age to account for

temperature effects on time and 2) use of a vertical scaling factor, R_T, applied to the basic creep,

which is also used in the B4 Model (Bažant et al. 2014). The formula to calculate R_T is expressed

in Equation 4-24 and the final B3 Model with R_T is shown Equation 4-25.

$$R_T = \exp\left[\frac{U'_C}{R}\left(\frac{1}{T_0} - \frac{1}{T}\right)\right]$$ **(Equation 4-24)**

$$J(t,t') = q_1 + R_T C_0(t,t') + C_d(t,t',t_0)$$ **(Equation 4-25)**

$$U'_C/R = 0.18(3418w^{-0.27}\,\overline{f_c}^{\,0.54})$$ **(Equation 4-26)**

Where,

$T_0 = 293°K$,

w = water content of concrete (lb/ft^3),

$\overline{f_c}$ = cylinder compressive strength of concrete (psi),

R = gas constant (8.314 J/mol·K), and

U'_C = activation energy of creep describing magnification of creep due to temperature increase (J/mol).

4.6.4   B4 Model

The B4 Model (Bažant et al. 2014) is a new prediction model for creep and shrinkage which is intended to be an improvement over the B3 Model. The main changes in the B4 Model include enhanced multi-decade prediction, separation of drying shrinkage and autogenous shrinkage, consideration of the effects of various admixtures and aggregate types (Bažant et al. 2014).

The B4 Model provides scaling factors to parameters q_1 through q_4 to consider the effects of concrete ingredients such as retarder, silica fume, fly ash, high-range water-reducing admixture, silica fume, and air-entraining agent. In the B3 Model, the parameters in formulas are based on

concrete strength, mixture composition, cement type, aggregate types, and curing procedure. These parameters have been completely revised and refined based on extensive statistical optimization of a new enlarged database of laboratory tests used to calibrate the Model B4 (Bažant et al. 2014). Note that other than the autogenous shrinkage term, the B3 Model and B4 Model retain the same mathematical form.

Bažant et al. (2014) reported that the B4 Model is more sophisticated than the B3 Model and it is only necessary for special types of structures that have a high level of sensitivity to creep and shrinkage effects, such as long-span box girders, large offshore structures, and super-tall buildings. The B4 Model is as defined in Equation 4-27 through Equation 4-30 (Bažant et al. 2014).

$$q_1 = \frac{1}{E_0} = \frac{p_1}{E_{28}} \qquad \textbf{(Equation 4-27)}$$

$$q_2 = \frac{p_2}{1\text{GPa}}(\frac{w/c}{0.38})^{p_{2w}} \qquad \textbf{(Equation 4-28)}$$

$$q_3 = p_3 q_2 (\frac{a/c}{6})^{p_{3a}}(\frac{w/c}{0.38})^{p_{3w}} \qquad \textbf{(Equation 4-29)}$$

$$q_4 = \frac{p_4}{1\text{GPa}}(\frac{a/c}{6})^{p_{4a}}(\frac{w/c}{0.38})^{p_{4w}} \qquad \textbf{(Equation 4-30)}$$

Where $p_1, p_2, p_{2w}, p_3, p_{3a}, p_{3w}, p_4, p_{4a}, p_{4w}$ are creep parameters for the B4 Model that depend on the cement type and their values can be found in Bažant et al. (2014). In the case of multiple admixtures, the effects of specific admixtures and their interactions have been ranked empirically. Only the first applicable modifier listed in the table should be selected (Bažant et al. 2014).

Table 4-2 Admixture dependent parameter scaling factors for creep for B4 Model (Bažant et al. 2014)

Admixture class (% of c)	$\times p_2$	$\times p_3$	$\times p_4$	$\times p_5$
Re(≤ 0.5), Fly(≤ 15)	0.31	7.14	1.35	0.48
Re(> 0.5), Fly(≤ 15)	1.43	0.58	0.90	0.46
Fly(≥ 15)	0.37	2.33	0.63	1.60
Super(≥ 0)	0.72	2.19	1.72	0.48
Silica(≥ 0)	1.12	3.11	0.51	0.61
AEA(≥ 0)	0.90	3.17	1.00	0.10
WR(≤ 2)	1.00	2.10	1.68	0.45
WR($> 2, \leq 3$)	1.41	0.72	1.76	0.60
WR(> 3)	1.28	2.58	0.73	1.10

Re retarder, *Fly* fly ash, *Super* superplasticizer, *Silica* silica fume, *AEA* air entraining agent, *WR* water reducer

4.7   RELAXATION FUNCTION

If creep is assumed to be linear in terms of stress and follows the principle of superposition, the creep properties are fully defined either by creep function or by the relaxation function, and one follows from the other (Bažant and Kim 1979). Their relationship is given by a linear Volterra's integral equation (Bažant 1975), which can be numerically solved by computer programs. A general algebraic formula for inverting the creep function to the relaxation function is needed for convenience in structural calculations for designers.

Bažant and Kim (1979) developed an approximate formula for $R(t,t')$, that can be computed from the compliance function $J(t,t')$. The relaxation function can be written in Equation 4-31 to Equation 4-35.

$$R(t, t') = A - B \qquad \textbf{(Equation 4-31)}$$

$$A = \frac{1 - \Delta_0}{J(t, t')} \qquad \textbf{(Equation 4-32)}$$

$$B = \frac{c_1 \alpha(t, t')}{J(t, t - \eta)} \qquad \textbf{(Equation 4-33)}$$

$$\alpha(t, t') = \frac{J(t' + \xi, t')}{J(t, t - \xi)} - 1 \qquad \textbf{(Equation 4-34)}$$

$$\xi = \frac{t - t'}{2} \qquad \textbf{(Equation 4-35)}$$

Where,

$\eta = 1$ day,

$\Delta_0 = 0.008$, and

$c_1 = 0.115$.

If the material is nonaging such as polymers, then the compliance function $J(t, t')$ depends only on the time lag t-t', and thus $\alpha(t, t')$ and B would be 0. Then $R(t, t') \approx 1/J(t, t')$. This expression coincides with the effective modulus approximation for concrete (McMillan 1916), and an elastic analysis with the effective modulus (Equation 4-36) can replace the structural creep analysis. In B3 Model, $E(t')$ is calculated as $J(t' + 0.01, t')$, which agrees well with the conventional elastic modulus E_{28}.

$$E_{eff} = \frac{1}{J(t, t')} = \frac{E(t')}{1 + \varphi(t, t')} \qquad \text{(Equation 4-36)}$$

$$\varphi(t, t') = \frac{J(t, t') - 1/E(t')}{1/E(t')} \qquad \text{(Equation 4-37)}$$

$$E(t') = \frac{1}{J(t', t')} \qquad \text{(Equation 4-38)}$$

Where,

$\varphi(t, t')$ is creep coefficient which is the ratio of creep strain to the elastic strain, and

$E(t')$ is elastic or instantaneous modulus at age t'.

Later an improved formula for $R(t, t')$ was developed by Bažant et.al (2013) that is significantly more accurate for long-time relaxation of concrete loaded at a young age. The new relaxation function is described in Equation 4-39 to Equation 4-42.

$$R(t, t') = \frac{1}{J(t, t')} \left[1 + \frac{c_1 \alpha(t, t') J(t, t')}{qJ(t, t - \eta)} \right]^{-q} \qquad \text{(Equation 4-39)}$$

$$\alpha(t, t') = \frac{J(t' + \xi, t')}{J(t, t - \xi)} - 1 \qquad \text{(Equation 4-40)}$$

$$\xi = \frac{t - t'}{2} \qquad \text{(Equation 4-41)}$$

$$c_1 = 0.0119 \, \text{LN} \, t' + 0.08 \qquad \text{(Equation 4-42)}$$

Where,

$\eta = 1$ day, and

$q = 10$.

CHAPTER 5 PART I: EXPERIMENTAL PLAN

5.1   RESTRAINED STRESS MEASUREMENT

A schematic of the test equipment and procedure is shown in Figure 5-1. Figure 5-1 shows the match-cured temperature conditions used to test all concretes, rigid cracking frame equipment, and match-cured concrete cylinders. Restrained to volume change tests with rigid cracking frame (RCF) were used to measure the early-age stress development in various concretes. The rigid cracking frame shown in Figure 5-2 and Figure 5-3 consists of dog-bone shaped formwork with dimensions of $6\times6\times49$ in., two mild steel crossheads, and two Invar sidebars. The formwork is lined with plastic and then sealed after concrete placement; therefore, no drying shrinkage occurs. The concrete curing temperature in the setup is controlled to simulate typical concrete elements such as bridge decks, mass concrete, concrete culverts, etc. More details of the RCF test can be found in Byard (2011).

After the concrete starts to hydrate and volume change starts to occur due to temperature and autogenous shrinkage effects, the concrete deformation is restrained by the RCF which causes stress to develop. The concrete stress developed in the RCF is influenced by the temperature change, coefficient of thermal expansion, modulus of elasticity, creep (relaxation), and autogenous shrinkage. For the rigid cracking frame, the deformation of concrete is restrained by the Invar bars; however, the stiffness of the Invar bars is such that some deformation is allowed to occur. So the degree of restraint the RCF provides for the concrete needs to be considered for the calculation of concrete stress. When the concrete is fresh, the rigid cracking frame has 100% restraint and when the concrete is mature, the frame provides approximately 80% restraint to the concrete specimen (Mangold 1998). This changing restraint can be captured by the FEM.

48
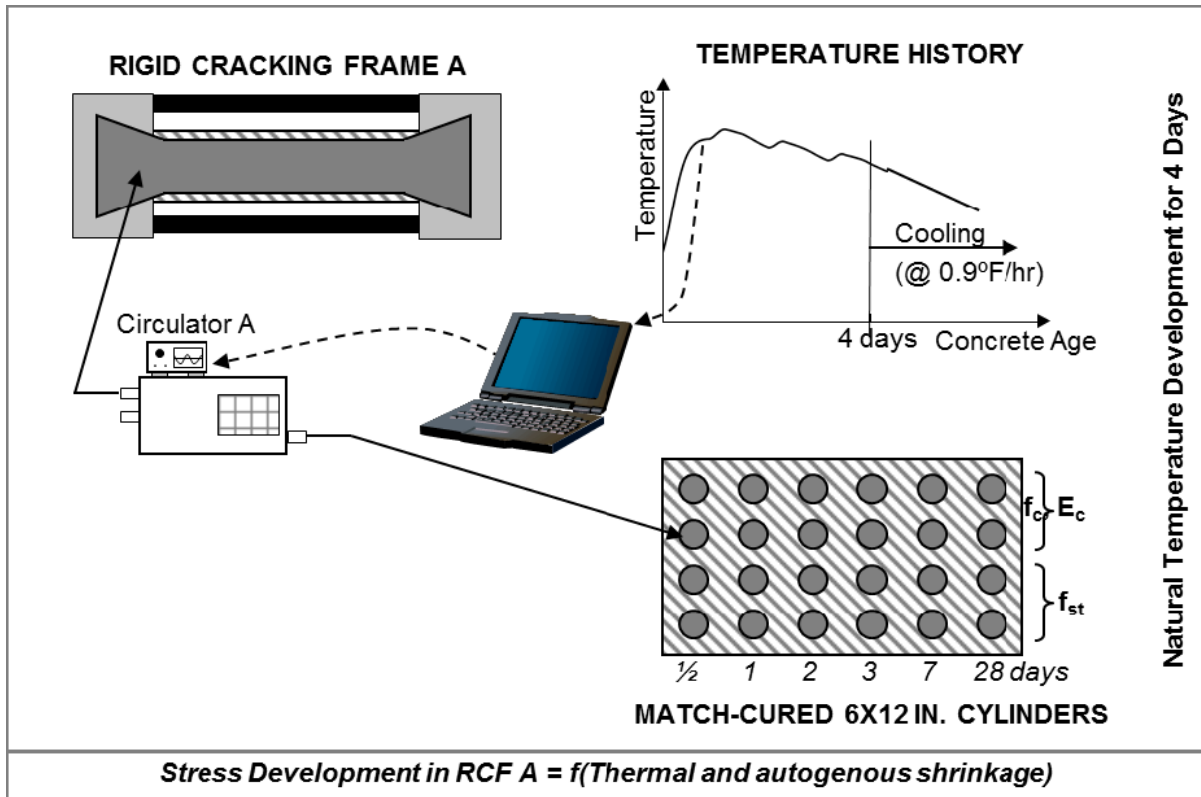
Figure 5-1 Experimental test setup (Tankasala 2017)
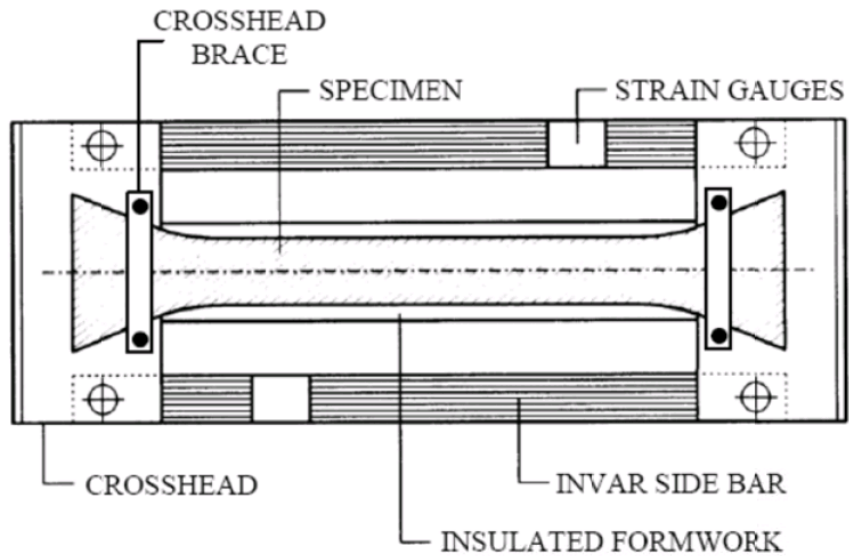
Figure 5-2 Schematic diagram of rigid cracking frame (Mangold 1998)

Figure 5-3 Actual rigid cracking frame equipment (Meadows 2007)

5.1.1 Degree of Restraint of RCF

For the rigid cracking frame, the deformation of concrete is restrained by the Invar bars, and at the same time there is always some small deformation in the steel bars (See Figure 5-4). Therefore, the degree of restraint the RCF provides the concrete need to be considered for the calculation of concrete stress.

Below shows the mechanism of calculating the restraint ratio in the cracking frame (Equation 5-1 to Equation 5-6).
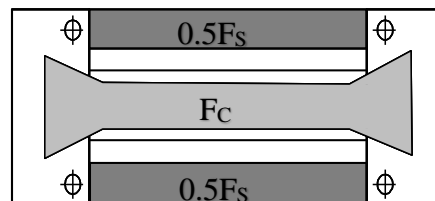
Figure 5-4 Schematic diagram of Rigid Cracking Frame

$$F_S = F_C \qquad \text{(Equation 5-1)}$$

$$\varepsilon_c E_c A_c = \varepsilon_s E_s A_s \qquad \text{(Equation 5-2)}$$

$$\frac{\varepsilon_s}{\varepsilon_c} = (E_c A_c)/(E_s A_s) \qquad \text{(Equation 5-3)}$$

The restraint strain is determined as the difference between the free strain of the concrete specimen (ε_{Free}) and the allowed strain in the test configuration (strain in steel bars $\varepsilon_{Restrained}$) (Rostásy, et al. 1998).

$$\varepsilon_{Free} = \varepsilon_c + \varepsilon_s \qquad \text{(Equation 5-4)}$$

$$\varepsilon_{Restrained} = \varepsilon_s \qquad \text{(Equation 5-5)}$$

$$R = \frac{\varepsilon_{Free} - \varepsilon_{Restrained}}{\varepsilon_{Free}} = \frac{\varepsilon_c}{\varepsilon_c + \varepsilon_s} = \frac{1}{1 + \varepsilon_s/\varepsilon_c} \qquad \text{(Equation 5-6)}$$

$$= \frac{1}{1 + (E_c A_c)/(E_s A_s)}$$

The cross sections of concrete and Invar bars are constant. The elastic modulus of the Invar bar is also constant and so only the elastic modulus of the concrete is changing with time. Therefore, when the concrete is fresh, the rigid cracking frame provides 100% restraint and when the concrete is hardened, the frame could provide approximately 80% restraint (Mangold 1998). In the finite-element model, it is assumed that one side of the concrete specimen is fully restrained, and the other side provides a restraint changing with time which is calculated based on the concrete elastic modulus $E_c(t)$.

5.2 MISCELLANEOUS PROPERTIES

5.2.1 Concrete Mechanical Properties

For each concrete mixture, twenty-four 6×12 in. cylinders were cast to test the development of compressive strength, splitting tensile strength, and modulus of elasticity. The cylinders were placed in a temperature-controlled box and cured using the same temperature history as the RCF. The mechanical properties of cylinders were tested at the ages of 0.5, 1, 2, 3, 7, and 28 days.

5.2.2 CTE Test

Since it is difficult to test the coefficient of thermal expansion (CTE) of concrete at early ages, the CTE of hardened concrete was tested after 28 days using a modified approach based on AASHTO T 336 (2009). Details of the setup and test procedure can be found in Byard (2011).

5.2.3 Setting Test

The setting test used a mortar sample obtained by wet sieving the concrete through a #4 sieve. The mortar is match cured to the temperature profile of the concrete in the RCF. Penetration resistance testing according to ASTM C403 (2016) is performed to obtain the initial set and final set. When the concrete achieves a penetration resistance of 500 psi and 4000 psi, initial set and final set times are obtained, respectively. The initial setting times can be used to calculate the parameters q_5 and q_6 for the Modified B3 Model (Byard and Schindler 2015).

5.3 EARLY-AGE CONCRETE STRESS DEVELOPMENT DATABASE

Seventy-two concrete mixtures prepared for three projects were used for the analysis reported herein. Table 5-1 shows a general summary of the concrete mixture proportions. Table 5-2 shows the mixture proportions of six example concretes from the three projects. The stress development and predicted stress for these four concretes will be shown as examples in this part of dissertation.

Table 5-1 Summary of concrete mixture proportions

Variable	Min.	Average	Max.
Cement and SCMs (lb/yd^3)	470	609	738
Cement Content (lb/yd^3)	282	539	738
Water Content (lb/yd^3)	211	248	276
w/cm	0.30	0.41	0.53
Class C Fly Ash （%）	0	5.2	30
Class F Fly Ash （%）	0	0.63	25
Silica Fume （%）	0	0.17	6
GGBF Slag （%）	0	6.0	50
Density (lb/ft^3)	87	135	151

Table 5-2 Sample mixture properties

Item	Project A		Project B		Project C	
	23D	**30A**	**0.42 Shale SLW (Sum)**	**0.42 LS (Sum)**	**SLWC 0.38**	**ICC 0.38**
Water Content (lb/yd^3)	237	232	276	260	243	243
Type 1 Cement Content (lb/yd^3)	395	611	658	620	435	435
SCMs Content (lb/yd^3)	169 (GGBF Slag)	0	0	0	195 (Class F Fly Ash)	195 (Class F Fly Ash)
Coarse Aggregate (lb/yd^3)	1927 (SSD River Gravel)	1910 (SSD River Gravel)	933 (SD Lightweight Shale)	1760 (SSD Limestone)	910 (SD Lightweight Shale)	1740 (SSD River Gravel)
Fine Aggregate (lb/yd^3)	1270 (SSD River Sand)	1266 (SSD River Sand)	1354 (SSD River Sand)	1211 (SSD River Sand)	1190 (SSD River Sand)	1000 (SSD Sand) plus 140 (SD Lightweight Shale)
Total Air Content (%)	2.0	2.0.	5.5	5.5	5.0	5.0
Water-to Cementitious Materials Ratio (*w/cm*)	0.42	0.38	0.42	0.42	0.38	0.38

Note: SCMs = Supplementary Cementing Materials; SD = pre-wetted surface dry; SSD = saturated surface dry.

A mixture identification system is used to refer to a specific type of concrete mixture. For each series of experiment the mixture identification system follows the convention used by the original author who performed the experiments.

5.3.1 Lightweight Aggregate

Lightweight aggregate (LWA) can be manufactured into coarse aggregate or fine aggregate for use in concrete. The density of lightweight concrete is reduced compared to normalweight concrete. Manufactured LWA includes expanded shale, clay, and slate.

The aggregates in concrete significantly influence the coefficient of thermal expansion (CTE) and the modulus of elasticity of the concrete (Mindess et al. 2002). The coefficient of thermal expansion of LWAs are reported to be reduced when compared to river gravel, and thus concrete with LWA has a smaller CTE than concrete with river gravel (Mehta and Monteiro 2014). The modulus of elasticity of lightweight concrete is lower than that of normalweight concrete (Mindess et al. 2002). Numerous studies have shown that concrete using LWA leads to an increased availability of moisture in the concrete leading to minimal or zero autogenous shrinkage, and thus relieving a component of early-age stresses for the concrete (Jensen et al. 2007; Bentz and Weiss 2011; Byard et al. 2012).

5.3.2 Internal Curing

ESCSI Guide Specifications (2012) for Internally Cured Concrete provides the following definition of internal curing: "Pre-wetted expanded shale, clay or slate lightweight is incorporated into a conventional concrete mixture to provide reservoirs of water with the concrete that slowly release the water after the concrete sets to provides internal curing to the mixture."

LWA has a high water-absorption capacity when pre-wetted and introduced in the concrete, and it can desorb water into the cement paste and relieve the concrete from autogenous shrinkage stresses (Bentz et al. 2005; Byard et al. 2012). As cement paste hydrates and self-desiccates, water from capillary pores are consumed and then the pressure in the capillary pores decrease. This creates suction that pulls water out of the saturated LWA into the cement paste. Smaller pores remove available water more easily than large pores. Castro et al. (2011) found that various commercially available LWAs desorb between 85 to 98% of the absorbed water at 93% relative humidity. The desorption properties of LWA depend on the aggregate pore size distribution, the porous nature of the paste, and the internal relative humidity (Jensen et al. 2007).

Concrete with LWA addition are classified into different types, and the commonly used ones are sand-lightweight (SLW) concrete, all-lightweight (ALW) concrete, and internally-cured (IC) concrete. SLW concrete has coarse LWA and fine normalweight aggregate. ALW concrete's coarse and fine aggregates are both LWA. IC concrete has coarse normalweight aggregate and involves replacing a portion of fine normalweight aggregate with fine LWA. The name IC concrete is commonly used in literature (Jensen et al. 2007), but for all concrete containing pre-wetted lightweight aggregate, internal curing takes place. Herein, in order to distinguish from concrete having LWA, normalweight (NW) concrete is used for concrete without any LWA.

5.3.3 Project A

Meadows (2007) performed 34 RCF tests at Auburn University with different concrete mixture proportions and curing conditions. Type I cement, Type III cement, Class C fly ash, Class F fly ash, slag cement, and silica fume were used in the mixtures. Different water-to-cementitious materials ratios (*w/cm*) ranging from 0.32 to 0.53 were used. The fresh concrete placement temperature and ambient temperature were simulated with different combinations of 50 °F, 73 °C,

and 95 °C. The concrete mixtures also used air-entraining admixtures (AEA), low-range water-reducing (LRWR), mid-range water-reducing (MRWR), and high-range water-reducing (HRWR) admixtures. All concretes used river gravel (RG) as coarse aggregate. The coefficient of thermal expansion (CTE) of these concretes were tested to be 5.94×10^{-6} in/in/°F.

The mixture identification system is originally following that of Meadows (2007) with modifications. The mixture with ID "23A (30%Slag 73ºF)" means that the mix ID is 23 defined by Meadow (2007), the A defines the batch ID which denotes a different concrete temperature, and the text in parentheses defines the specialty of this mixture, which is that the concrete has 30% of slag cement replacement for this mixture. All the mixtures that do not include the cement type or *w/cm* in parenthesis, used Type I cement and *w/cm* of 0.42. Some summary mechanical properties and temperature information of all concretes from project A are shown in Table 5-3 and Table 5-4.

Table 5-3 Properties of concrete from Project A (Meadows 2007) [Part 1 of 2]

Mixture	Fresh Concrete Temperature (ºF)	Ambient Temperature (ºF)	Activation Energy (J/mol)	28-day Compressive Strength (psi)	28-day Modulus of Elasticity (ksi)	28-day Tensile Strength (psi)
12A (Control 73ºF)	73	73	43140	5680	5750	660
12B (Control 50ºF)	50	50	43140	7040	6250	755
12C (Control 95ºF)	95	95	43140	5160	6050	600
12D (Control 73ºF)	73	95	43140	5890	6350	645
12E (Control 50ºF)	50	95	43140	5460	6000	595
21 (30%Class C)	73	73	38670	5790	6000	560
22 (20%Class C)	73	73	40490	5700	6050	630
23A (30%Slag 73ºF)	73	73	49420	5650	6100	705
23B (30%Slag 50ºF)	50	50	49420	6320	6500	655
23C (30%Slag 95ºF)	95	95	49420	5190	6150	565
23D (30%Slag 73ºF)	73	95	49420	5510	6200	680
23E (30%Slag 50ºF)	50	95	49420	5710	6200	665
24A (50%Slag 73ºF)	73	73	52960	5350	6500	665
24B (50%Slag 50ºF)	50	50	52960	6400	6400	720
24C (50%Slag 95ºF)	95	95	52960	5610	6350	605
24D (50%Slag 73ºF)	73	95	52960	5650	6150	635
24E (50%Slag 50ºF)	50	95	52960	4410	6100	620

Table 5-4 Properties of concrete from Project A (Meadows 2007) [Part 2 of 2]

Mixture	Fresh Concrete Temperature (ºF)	Ambient Temperature (ºF)	Activation Energy (J/mol)	28-day Compressive Strength (psi)	28-day Modulus of Elasticity (ksi)	28-day Tensile Strength (psi)
25 (25%ClassC 6%Slag)	73	73	39580	5870	6150	555
26 (25%ClassF 6%Slag)	73	73	36390	5150	5450	595
27 (20%ClassF 30%Slag)	73	73	43230	6060	6250	635
28 (W/C=0.32)	73	73	44130	7770	6650	770
30A (W/C=0.38 73ºF)	73	73	44130	6120	6000	690
30B (W/C=0.38 50ºF)	50	50	44130	7520	6500	740
30C (W/C=0.38 95ºF)	95	95	44130	5910	6250	565
30D (W/C=0.38 73ºF)	73	95	44130	6240	6100	720
30E (W/C=0.38 50ºF)	50	95	44130	8190	6450	625
31 (W/C=0.48)	73	73	44130	5000	5750	630
32 (W/C=0.53)	73	73	45250	4720	5800	600
33A (Type III 73ºF)	73	73	45250	5900	6500	580
33B (Type III 50ºF)	50	50	45250	7330	6250	720
33C (Type III 95ºF)	95	95	45250	5140	5500	555
33D (Type III 73ºF)	73	95	45250	5620	5950	635
33E (Type III 50ºF)	50	95	45250	6950	6200	675
34 (AEA)	73	73	44130	4260	5250	465

5.3.4 Project B

Byard (2011) performed RCF tests for 28 concretes at Auburn University with different aggregate types, water-to-cement ratios (*w/c*), and curing conditions. Concretes tested contained coarse normalweight aggregate that included river gravel (RG) and limestone (LS). In addition,

lightweight aggregates (LWA) that consisted of expanded clay, shale, and slate were used to produce internal curing (IC), sand-lightweight (SLW), and all-lightweight (ALW) concretes. The SLW concrete contained coarse LWA and fine normalweight aggregate. The ALW concrete's coarse and fine aggregates were both LWA. The IC concrete had coarse normalweight aggregate and involved replacing a small portion of fine normalweight aggregate with fine LWA. Twenty-two concretes with *w/c* of 0.42 were tested under both fall (Fall) and summer (Sum) simulated temperature conditions. Simulation of summer-time placement started with a concrete temperature of 95 °F and fall season started with a concrete temperature of 73 °F. Three concretes with *w/c* of 0.36 and another three concretes with *w/c* of 0.30 were tested only under fall-simulated conditions. All concretes used Type I cement without any supplementary cementing materials. The activation energy value for the concrete was determined to be 41,520 J/mol.

The mixture identification system used here is to refer to water-to-cement ratio, a specific type of LWA, mixture type, and simulated placement season. For example, "0.42 Slate IC (Fall)" represents that the water-to-cement ratio is 0.42, the LWA type is slate, the mixture type is IC, and the placement season is fall. Another example of mixture denoted "0.42 RG (Fall)" represents that the water-to-cement ratio is 0.42, the coarse aggregate type is river gravel, and the placement season is fall. The mechanical properties and coefficient of thermal expansion of concrete from project B are shown in Table 5-5.

Table 5-5 Properties of concrete from Project B (Byard 2011)

Mixture	Coefficient of Thermal Expansion (/°F)	28-day Compressive Strength (psi)	28-day Modulus of Elasticity (ksi)	28-day Tensile Strength (psi)
0.42 Slate IC (Fall)	5.90	5840	4500	465
0.42 Slate IC (Sum)	5.90	5580	4200	430
0.42 Slate SLW (Fall)	5.10	5140	3500	495
0.42 Slate SLW (Sum)	5.10	5130	3550	485
0.42 Slate ALW (Fall)	4.30	4760	2450	385
0.42 Slate ALW (Sum)	4.30	4610	2650	460
0.42 Clay IC (Fall)	5.80	5820	4300	505
0.42 Clay IC (Sum)	5.80	5640	4250	460
0.42 Clay SLW (Fall)	5.10	5020	2800	530
0.42 Clay SLW (Sum)	5.10	5380	2850	510
0.42 Clay ALW (Fall)	4.00	4860	2050	505
0.42 Clay ALW (Sum)	4.00	4490	2000	480
0.42 Shale IC (Fall)	6.00	5610	4350	455
0.42 Shale IC (Sum)	6.00	5640	4250	505
0.42 Shale SLW (Fall)	5.20	5040	3200	500
0.42 Shale SLW (Sum)	5.20	4920	3400	520
0.42 Shale ALW (Fall)	4.00	4780	2350	445
0.42 Shale ALW (Sum)	4.00	4320	2150	485
0.42 RG (Fall)	6.20	5700	4550	465
0.42 RG (Sum)	6.20	5310	4750	410
0.42 LS (Fall)	4.91	6080	5520	450
0.42 LS (Sum)	4.91	5630	4940	500
0.36 RG (Fall)	6.18	6435	5535	485
0.36 ICM (Fall)	6.02	6890	5250	565
0.36 ICH (Fall)	6.02	6960	4865	525
0.30 RG (Fall)	6.62	8115	5700	600
0.30 ICM (Fall)	6.04	8120	5265	665
0.30 ICH (Fall)	6.01	8860	5170	610

5.3.5 Project C

Tankasala (2017) performed RCF tests at Auburn University for 10 concretes with different aggregates and *w/cm*, placed under simulated mass concrete conditions. These concretes included a reference (REF) concrete with river gravel, internally cured (IC) concrete, sand-lightweight (SLW) concrete, all-lightweight (ALW) concrete, and inverse sand-lightweight (ISLW) concrete. ISLWC represent concrete with normalweight coarse aggregate and fine lightweight aggregate. Two *w/cm* ratios of 0.45 and 0.38 were used for each concrete type tested during Project C. Fall-simulated placement condition with an initial temperature of 73 °F was used for all the concretes. All these concretes contained 30% of Class F fly ash replacement, which is representative of mass concrete.

Table 5-6 Properties of concrete from project C (Tankasala 2017)

Mixture	Coefficient of Thermal Expansion (/°F)	28-day Compressive Strength (psi)	28-day Modulus of Elasticity (ksi)	28-day Tensile Strength (psi)
REF 0.38	6.07	5970	4550	510
ICC 0.38	5.95	6180	4500	530
ISLWC 0.38	5.29	5200	2950	340
SLWC 0.38	5.24	5850	4000	480
ALWC 0.38	4.17	4370	2950	380
REF 0.45	5.86	4710	4050	430
ICC 0.45	5.81	4900	3950	470
ISLWC 0.45	5.19	4160	2750	330
SLWC 0.45	5.13	4640	3550	460
ALWC 0.45	4.14	3980	2650	360

All the concrete contains 30% of Class F fly ash replacement. The lightweight aggregate used in this study is expanded shale. The activation energy value for the concrete is 33,835 J/mol. The

mechanical properties and coefficient of thermal expansion for the concretes from project C are

shown in Table 5-6.

CHAPTER 6   PART I: FINITE-ELEMENT MODEL

Eight-node linear hexahedral (brick) elements with three translational degrees of freedom at each node (C3D8) were used for the FEM in ABAQUS. For the element type C3D8, the "C" denotes continuum stress/displacement, "3D" denotes three-dimensional element, and "8" denotes number of nodes. For the rigid cracking frame (RCF), the deformation of the concrete is restrained by the Invar bars, and at the same time there is always some deformation in the Invar bars. These strains were captured by modeling the two Invar bars in the FEM of the RCF. The FEM mesh for the RCF with concrete is shown in Figure 6-1. The Invar side bars were assigned a modulus of elasticity of 21,500 ksi and the crossheads at the two ends were assigned a very high modulus of elasticity to function as a rigid body to restrain both the concrete and Invar bars. Figure 6-2 shows the temperature history of two example concrete mixtures with summer and fall season placement conditions. After concrete placement, the temperature starts to rise because of the heat of hydration. After reaching the peak temperature, the concrete gradually cools down to the ambient temperature.
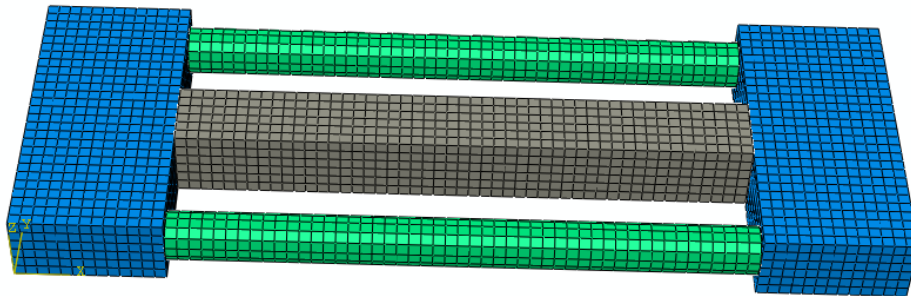
Figure 6-1 Mesh of finite-element model of rigid cracking frame

The concrete temperature profiles and CTE value of each concrete mixture were input into the FEM. Then the thermal strain was calculated based on the CTE, and the small deformation of the

Invar bars was captured by the FEM itself and considered with the thermal strain to get the final strain to calculate the concrete stresses. Then based on the strain increment at each time step and the compliance subroutine, the stress with time was calculated and output from the FEM. The effect of varying concrete temperatures on all concrete properties was considered by using the equivalent age maturity method (Carino 2004). Therefore, all ages mentioned in this study, unless stated to be different, are presented in equivalent age. Since the concrete in the RCF was sealed and there was no moisture loss, drying creep and drying shrinkage were neglected.
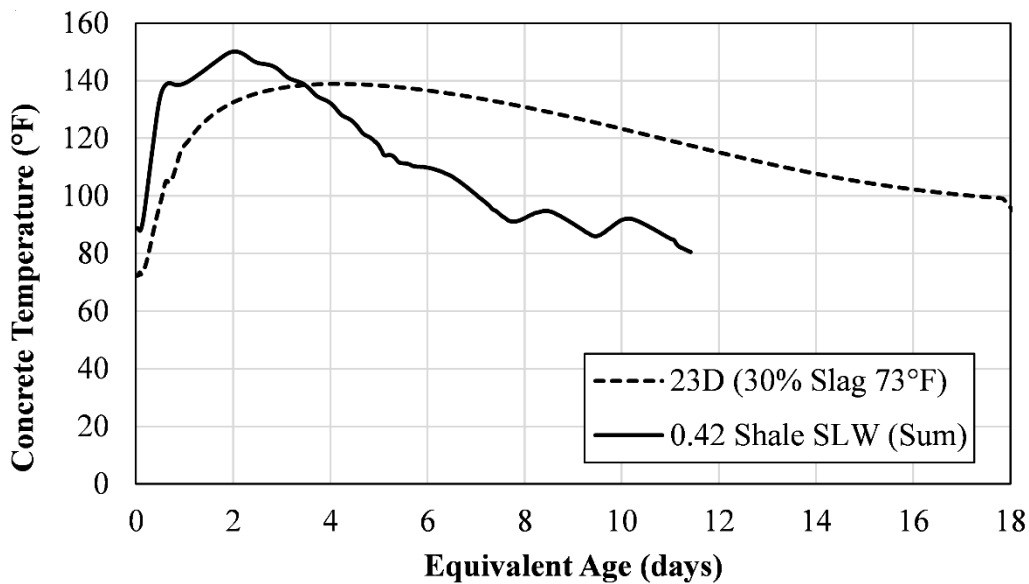
Figure 6-2 Concrete temperature histories of two example concretes

6.1 INCORPORATING CREEP IN THE FEM

6.1.1 UMAT Subroutine

ABAQUS provides the facility for users to program in their own material models. UMAT is the subroutine that allows users to define any constitutive material models, including those not exist in the standard material library of the program (Dassault Systèmes Simulia Corp. 2012b). UMAT

is the user subroutine that can be used to define a material's mechanical behavior in ABAQUS/Standard module. For three-dimensional analysis, the material Jacobian matrix for the constitutive model can be defined in UMAT.

The quantities like stress, strain, strain increment, total and incremental values of time, temperature, element, current step, increment numbers and so on are available in UMAT. The subroutine UMAT is a FORTRAN programming language environment. Coding the UMAT requires that all variables be defined and initialized properly and enough storage space defined in the program for state variables with the *DEPVAR option in the *Material section.

Using the subroutine needs the following specific ABAQUS "Keywords" in the input file as:

*MATERIAL, NAME = \<user named\>

*USER MATERIAL, CONST = \<number of constants\>

 *DEPVAR \<number of solution dependent variables\>

An already developed UMAT code for basic concrete creep behavior based on B3 Model was obtained from Yu et al. (2012). Modifications to the routine for equivalent age, modified B3 Model, B4 Model, and temperature parameter R_T were made by the author. Simple models to verify the subroutine code for creep, relaxation and the variable stresses were built and compared to analytical solutions before using it for the experiment simulation.

In this study, concrete creep is assumed to be aging linear viscoelastic and is modeled by a rate-type law based on a Kelvin chain model. In the B3 Model, the basic creep compliance function

can be converted into a rate-type creep law according to the solidification theory (Bažant and Prasannan 1989a,b).

Concrete creep is modeled by the rate-type law instead of the integral type analysis. This approach in the FEM uses a step-by-step analysis, and in each time step, the integration points of each finite element is considered within the UMAT subroutine. The inelastic creep problem for the structure is reduced to a sequence of elasticity problems by converting the incremental stress-strain relation for each time step, Δt, to a quasi-elastic stress-strain relation as shown in Equation 6-1 (Yu et al. 2012).

$$\Delta\sigma = E''(\Delta\varepsilon - \Delta\varepsilon'') \quad\quad\quad \textbf{(Equation 6-1)}$$

Where, in the three-dimensional FEM, $\Delta\boldsymbol{\sigma}$ is a 6×1 column matrix of stress increments during each time step (psi), $\boldsymbol{E''}$ is a 6×6 matrix of incremental modulus (psi) for an isotropic material using a constant concrete Poisson ratio, $\Delta\boldsymbol{\varepsilon''}$ is a 6×1 column matrix of inelastic strain increments from creep (in./in.), and $\Delta\boldsymbol{\varepsilon}$ is a 6×1 column matrix of strain increments from shrinkage and thermal dilation (in./in.). This quasi-elastic stress-strain relation makes it possible to calculate the strain response for any stress history (creep), as well as the stress response for any given strain history (relaxation) (Bažant and Prasannan 1989a,b).

6.1.2 Algorithm and Numerical Implementation for B3 Model

The coding of the B3 Model into ABAQUS subroutine UMAT is described in this section. As creep is a time-dependent phenomena, a commercial finite element program can be used to do a step-by-step analysis of structural creep problem, and it is simplified to a sequence of elastic finite-element analyses for elastic stress-strain relation with actual inelastic strain for each time step (Bažant et al. 2012).

Concrete creep is assumed to be aging linear viscoelasticity and is modeled by a rate-type law based on Kelvin chain. In B3 Model, it's particularly easy to converse the compliance function of basic creep to a rate-type creep law according to the solidification theory.

For the solidification theory, the aging is modeled as a growth of the volume fraction of the loading-bearing solidified matter (hydrated cement), which itself is viewed as nonaging viscoelastic material (Bažant and Prasannan 1989a,b). Then it is possible to use a non-aging compliance function for the solidifying component and a unique continuous retardation spectrum can be determined by a simple explicit formula like Widders's formula (Bažant et al. 2012).

The Kelvin chain model used for B3 Model in Abaqus UMAT subroutine consists of a series of Kelvin units. μ represents the number of Kelvin units and ranges from 1 to N. Each unit has a spring of stiffness $E_\mu(t)$ and a dash-pot of viscosity $\eta_\mu(t)$. $\tau_\mu = \eta_\mu(t)/E_\mu(t)$ is the chosen retardation time. For step-by-step analysis, if the time step Δt is short enough, the moduli and viscosity of Kelvin units can be regarded as approximately constant in the step (Yu et al. 2012).

A continuous retardation spectrum, $L(\tau)$, which relates to the Kelvin chain and can be identified from the compliance function analytically by Laplace transform inversion (as shown in Equation 6-2) (Bažant and Xi. 1995; Yu et al. 2012).

$$L(\tau_\mu) = -\frac{\lim_{k \to \infty} (-k\tau_\mu)^k C^{(k)}(k\tau_\mu)}{(k-1)!} \qquad \textbf{(Equation 6-2)}$$

Where,

μ = the number of Kelvin units and ranges from 1 to N,

$L(\tau) = $ a continuous retardation spectrum,

$\tau_\mu = $ retardation time, and

$C^{(k)} = $ the k-th derivative on time t of the creep part of the compliance function.

$L(\tau)$ varies in each time step for each integration point of each finite element. For B3 Model, k=3 is used and a simple approximation of the retardation spectrum is presented below (Bažant and Xi. 1995).

$$L(\tau_\mu) = q_2 n(n-1)\frac{(3\tau_\mu)^n}{1 + (3\tau_\mu)^n} \qquad \textbf{(Equation 6-3)}$$

Where,

$L(\tau_\mu) = $ a continuous spectrum,

$q_2 = $ empirical material constitutive parameter in B3 Model (see Equation 4-18),

$\tau_\mu = $ retardation time, and

$n = $ a constant.

Constant A_μ may generally be found by the method of curve-fitting of data, and an approximate formula giving A_μ had been provided in Bažant and Xi (1995) where a form of continuous retardation spectrum for A_μ can be discretized. Then the discrete spectrum, $A(\tau_\mu)$, is a discrete approximation of the continuous retardation spectrum (Yu et al. 2012).

$$A(\tau_\mu) = \frac{1}{E_\mu(t)} = L(\tau_\mu) \ln 10 \Delta(\log \tau_\mu) = L(\tau_\mu) \ln 10 \qquad \textbf{(Equation 6-4)}$$

Where,

$\Delta(\log \tau_\mu) = \log 10 = 1$,

$A(\tau_\mu)$ = a discrete spectrum,

$E_\mu(t)$ = a spring of stiffness for Kelvin unit, and

$L(\tau_\mu)$ = a continuous spectrum.

The discrete spectrum relates to a finite Kelvin units and is needed for numerical calculations. The compliance function $J(t, t')$ can be represented by the Kelvin chain model with sufficient precision. The Kelvin chain model converts the creep law to a system of ordinary first-order linear differential equations for the rate of Kelvin units. The exponential algorithm is devised for the numerical integration of first-order ordinary differential equations. In the exponential algorithm, it is assumed that within each short time step, the stress varies linearly. One calculates the following parameters for each integration point of each finite element in each time step (Bažant and Prasannan 1989a; Yu et al. 2012),

$$\beta_\mu = e^{-\Delta t/\tau_\mu} \qquad \textbf{(Equation 6-5)}$$

$$\lambda_\mu = \tau_\mu(1 - \beta_\mu)/ \Delta t \qquad \textbf{(Equation 6-6)}$$

$$D_\mu = \frac{1}{A(\tau_\mu)(1 - \lambda_\mu)} \qquad \textbf{(Equation 6-7)}$$

$$\frac{1}{E''(t_{n-1/2})} = \frac{1}{E_0} + \sum_{\mu=1}^{N} D_\mu^{-1}$$

(Equation 6-8)

Where,

β_μ, λ_μ = internal variables of Kelvin units,

D_μ = elastic moduli of Kelvin units,

Δt = time increment at each time step,

τ_μ = retardation time,

$A(\tau_\mu)$ = a discrete spectrum,

E_0 = conventional short-time elastic modulus, and

E'' = the incremental modulus.

The inelastic strain increments which also called the eigenstrains are calculated by Equation 6-9, then the stress increment at each time step would be obtained by the following quasi-elastic stress-strain relation as shown in Equation 6-10 (Bažant and Prasannan 1989a; Yu et al. 2012):

$$\Delta\varepsilon'' = \sum_{\mu=1}^{N} (1 - \beta_\mu)\, \gamma_\mu^{(n-1)}$$

(Equation 6-9)

$$\Delta\sigma = E''(\Delta\varepsilon - \Delta\varepsilon'')$$

(Equation 6-10)

Where,

$\Delta\varepsilon'' =$ inelastic strain increments which also called the eigenstrains,

$\Delta\varepsilon =$ the strain due to thermal dilation or shrinkage,

$\Delta\sigma =$ stress increment at each time step,

$E'' =$ the incremental modulus, and

$\beta_\mu, \gamma_\mu =$ internal variables of Kelvin units.

Then the nonlinear structural creep problem is reduced to a sequence of incremental elasticity problems and can be programed in finite element software. The internal variables of Kelvin chain units is updated at each integration point at each time step (Bažant and Prasannan 1989a; Yu et al. 2012):

$$\gamma_\mu^{(n)} = \lambda_\mu \Delta\sigma D_\mu^{-1} + \beta_\mu \gamma_\mu^{(n-1)} \qquad \textbf{(Equation 6-11)}$$

Where,

$\gamma_\mu, \beta_\mu, \lambda_\mu =$ internal variables of Kelvin units,

$\Delta\sigma =$ stress increment at each time step, and

$D_\mu =$ elastic moduli of Kelvin units,

For B3 Model, a simpler exponential algorithm which only needs the compliance rate $\dot{J}(t, t')$ is applied (Yu et al. 2012).

$$A^b(\tau_\mu) = (\sqrt{1/t_{n-1/2}} + q_3/q_2)A(\tau_\mu)$$

(Equation 6-12)

$$\Delta\varepsilon'' = \Delta\varepsilon''_1 + \Delta\varepsilon''_2$$

(Equation 6-13)

$$\Delta\varepsilon''_1 = \sum_{\mu=1}^{N}(\sqrt{1/t_{n-1/2}} + q_3/q_2)(1 - \beta_\mu)\gamma_\mu^{(n-1)}$$

(Equation 6-14)

$$\Delta\varepsilon''_2 = q_4\sigma^{(n-1)}\Delta t/t_{n-1/2}$$

(Equation 6-15)

Where,

$\Delta\varepsilon''_1$ represents the inelastic strain increments of the current volume fraction of solids,

$\Delta\varepsilon''_2$ is the inelastic strain increment of viscous flow,

$A^b(\tau_\mu) =$ a discrete spectrum for B3 Model,

$n =$ number of time steps,

$\sigma^{(n-1)} =$ stress at time step (n-1),

$\gamma_\mu, \beta_\mu, \lambda_\mu =$ internal variables of Kelvin units, and

$q_2, q_3, q_4 =$ empirical material constitutive parameter in B3 Model (see Equation 4-18 to Equation 4-20).

This quasi-elastic stress-strain relation makes it possible to calculate the strain response for any stress history (creep), as well as the stress response for any given strain history (relaxation) (Bažant and Prasannan 1989a,b).

For B3 model the compliance function of basic creep is converted to a rate-type creep law according to the Solidification theory. The theory of the code in UMAT for the B3 Model is summarized by Yu et al. (2012). The derivation of the exponential algorithm for the rate-type form was given for the B3 Model based on solidification theory in Bažant and Prasannan (1989a,b). The calculation of the continuous retardation spectrum and its discretization are presented in Bažant and Xi (1995).

6.1.3 Algorithm Utilizing FEM for B3 Model

The Algorithm utilizing ABAQUS for B3 Model is as follows (also shown in Figure 6-3):

1. Select the retardation times for basic creep of B3 Model. $\tau_\mu = 10^{\mu-7}, \mu = 1, 2, \dots, N$. $N = 22$. Initial the internal variable $\gamma_\mu{}^{(0)} = 0$.

2. Loop over time steps. $t_n = discrete\ times,\ (n = 1, 2, \dots)$. $t_{n-1/2} = t_0 + [(t_n - t_0)(t_{n-1} - t_0)]^{1/2}$ for n>1. When n=1, $t_{1/2} = (t_0 + t_1)/2$.

3. Calculate the strain due to thermal dilation, $\Delta\varepsilon$.

4. Compute current stress $\sigma^{(n-1)}$ in the subroutine UMAT.

5. Calculate $L(\tau_\mu)$, $A(\tau_\mu)$, $A^b(\tau_\mu)$, β_μ, λ_μ, D_μ and the incremental modulus E''.

6. Compute the inelastic strain increment, $\Delta\varepsilon'' = \Delta\varepsilon''_1 + \Delta\varepsilon''_2$

7. By the quasielastic stress-strain relation $\Delta\sigma = E''(\Delta\varepsilon - \Delta\varepsilon'')$ to get the stress increment at this time step. For 3-D analysis in ABAQUS, a constant 6×6 matrix for isotropic material with a Poisson ν is used in the subroutine.

8. Update the internal variable $\gamma_\mu{}^{(n)}$

9. End of loop over finite elements and their integration points

10. Go to step 2 and begin the next time step.

11. End of loop over all time steps.
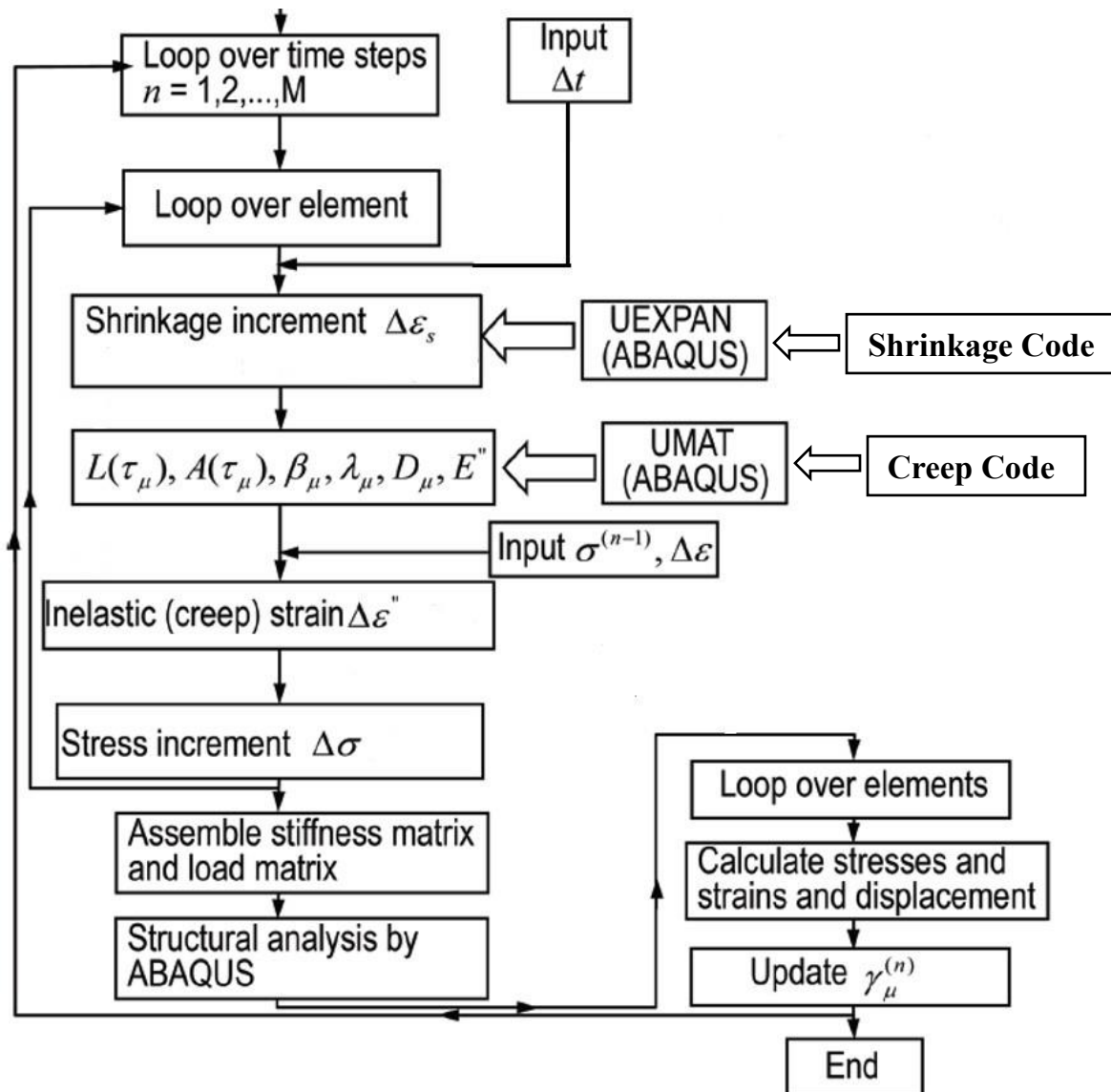
Figure 6-3 Algorithm utilizing ABAQUS (Yu et al. 2012)

6.1.4 Modeling Procedure in FEM

The procedure of building a finite-element model in ABAQUS CAE module for simulating early-age concrete stress is shown below:

1. In *PARTS, create three-dimensional geometry of model creation

2. In *Materials, define material properties for concrete, activate subroutine selections here,

3. For concrete properties, use "Depvar" to define number of solution-dependent state variables; use "Expansion" to give a constant CTE value for the concrete; use "User Material" to define the mechanical constants for the Subroutine.

4. Define *Section and *Assembly for each part of the model

5. In *Steps, define the total time period for analysis and time increment size

6. In *Amplitude, input temperature profile

7. In *BCs, define boundary conditions for the model

8. In *Predefined Fields, define the initial temperature for the concrete

9. Create a job and in "General" find the user subroutine file

10. Run the analysis

11. Output stress and other results

6.2 SIMPLE MODEL VERIFICATION

6.2.1 Creep Response Verification

A short concrete column member was simulated in ABAQUS to check accuracy of the model for creep and relaxation. A concrete column model was built in FEM, with one-end restrained and a constant load applied at the other end (see Figure 6-4). The values of q_1 to q_4, the loading age of 7 days, and a load of 2000 psi pressure were input in the FEM for analysis.
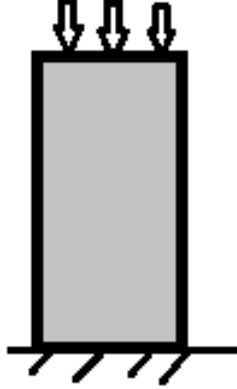
Figure 6-4 Simple concrete column model to check creep response

A given concrete example is used to verify the creep code in the FEM. Part of the concrete properties are from the example in Bažant and Baweja (2000). Calculations are made with four digit accuracy. The properties of this given concrete are: 1) Type I cement concrete; 2) age at loading t' =7 days; 4) cylinder compression strength $\overline{f_c}$ = 4000 psi; 5) cement content c = 13.69 ld/ft³; 6) water content of concrete w =8.23 lb/ft³; 7) water-cement ratio w/c =0.6; 8) aggregate-cement ratio a/c=7.0; 9) applied stress (50% of $\overline{f_c}$); 10) calculate the creep strain of concrete at age 14 days.

$$E_{c,28} = 57000\left(\overline{f_c}\right)^{0.5} = 57000 \times (4000)^{0.5} = 3605,000 \, psi \qquad \textbf{(Equation 6-16)}$$

$$q_1 = 0.6 \times 10^6 / E_{c,28} = 0.1664 \qquad \textbf{(Equation 6-17)}$$

$$q_2 = 451.1 c^{0.5} \overline{f_c}^{-0.9} = 451.1 \times 13.69^{0.5} \times 4000^{-0.9} = 0.9564 \qquad \textbf{(Equation 6-18)}$$

$$q_3 = 0.29 (\frac{w}{c})^4 q_2 = 0.29 \times (0.6)^4 \times 0.9564 = 0.0359 \qquad \textbf{(Equation 6-19)}$$

76

$$q_4 = 0.14(\frac{a}{c})^{-0.7} = 0.14(7)^{-0.7} = 0.0359 \qquad \textbf{(Equation 6-20)}$$

$$C_0(t, t') = q_2 Q(t, t') + q_3 \ln[1 + (t - t')^n] + q_4(\frac{t}{t'}) \qquad \textbf{(Equation 6-21)}$$

$$Q(t, t') = Q_f(t')[1 + (\frac{Q_f(t')}{Z(t, t')})^{r(t')}]^{-1/r(t')} \qquad \textbf{(Equation 6-22)}$$

$$Q_f(t') = [0.086(t')^{2/9} + 1.21(t')^{4/9}]^{-1} = 0.33327 \qquad \textbf{(Equation 6-23)}$$

$$r(t') = 1.7(t')^{0.12} + 8 = 10.1471 \qquad \textbf{(Equation 6-24)}$$

$$Z(t, t') = (t')^{-m} \ln[1 + (t - t')^n] = 0.3005 \qquad \textbf{(Equation 6-25)}$$

$$Q(t, t') = 0.2916 \qquad \textbf{(Equation 6-26)}$$

$$C_0(t, t') = 0.3324 \qquad \textbf{(Equation 6-27)}$$

$$J(t, t') = q_1 + C_0(t, t') = 0.4988 \qquad \textbf{(Equation 6-28)}$$

$$\text{Creep strain} = J(t, t')\sigma = 0.4988 \times 2000 = 998 \times 10^{-6} \qquad \textbf{(Equation 6-29)}$$

$$Strain\ from\ FEM = 984 \times 10^{-6}\ at\ age\ t = 14\ days \qquad \textbf{(Equation 6-30)}$$
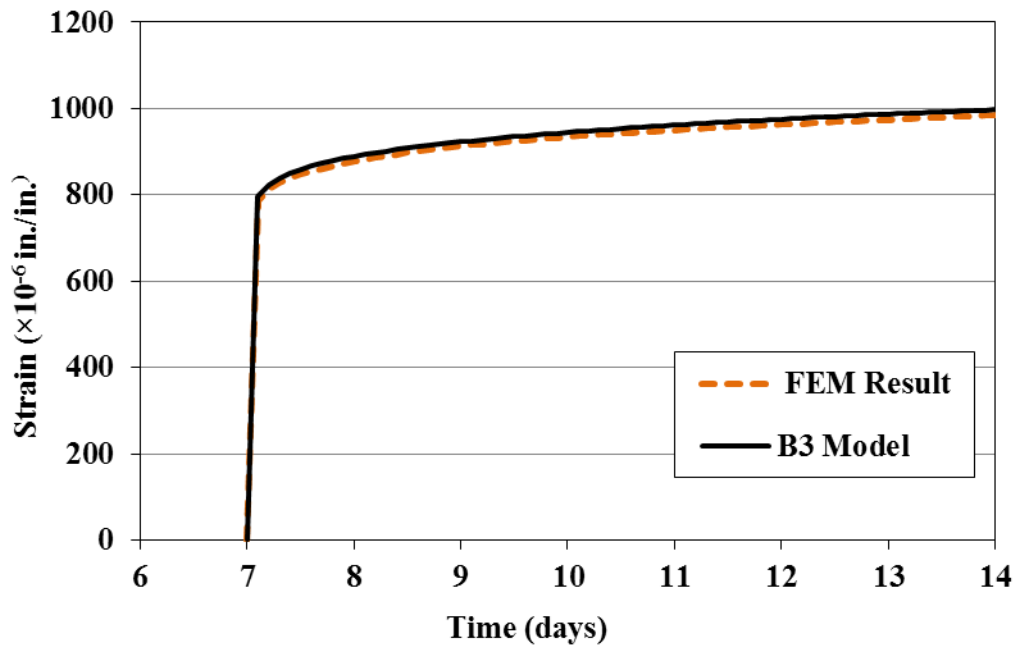
Figure 6-5 Creep response verification result

The creep response verification results are shown in Figure 6-5, and the two curves match very well. The strain at 14 days calculated from B3 Model by analytical method is $998 \times 10^{-6} \, in/in$, the strain from the FEM result is $984 \times 10^{-6} \, in/in$, and the difference is 1.4%, which is acceptable. These results prove that the code for creep model in the FEM is performing the calculations correctly.

6.2.2 Relaxation Response Verification

A concrete short column model was built in ABAQUS, with one-end restrained and a constant constant displacement applied at the other end (see Figure 6-4). Relaxation occurs under constant strain, which is realized by the application of displacement in the ABAQUS model. The values of q_1 to q_4, the loading age of 7 days, and a defined displacement which leads to the target strain value were input in the FEM for relaxation analysis.
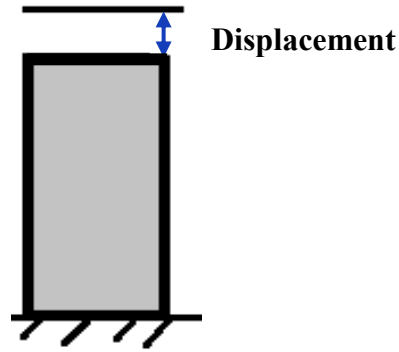
Figure 6-6 Simple concrete column model to check the relaxation response

A constant strain value of 333×10^{-6} $in./in.$ (which comes from $q_1 \times 2000\ psi = 333 \times 10^{-6} in./in.$) was applied to the model. The analytical relaxation result is based on the relaxation function discussed in Section 4.7, and the relaxation function is converted from the B3 Model. Figure 6-7 shows the relaxation response results from the two methods, and the two curves match very well. The stress calculated by analytical formula at age of 14 days is 656 psi (see Equation 6-32). The stress value at 14 days from the FEM result is 636 psi (see Equation 6-32). The results of the two methods differ 3.1%, which is acceptable.

$$R(t, t') = R(14,7) = 1.971 \times 10^6\ psi \qquad \textbf{(Equation 6-31)}$$

$$\sigma = R(t, t') \times \varepsilon = (1.971 \times 10^6)(333 \times 10^{-6}\frac{in}{in}) = 656\ psi \qquad \textbf{(Equation 6-32)}$$
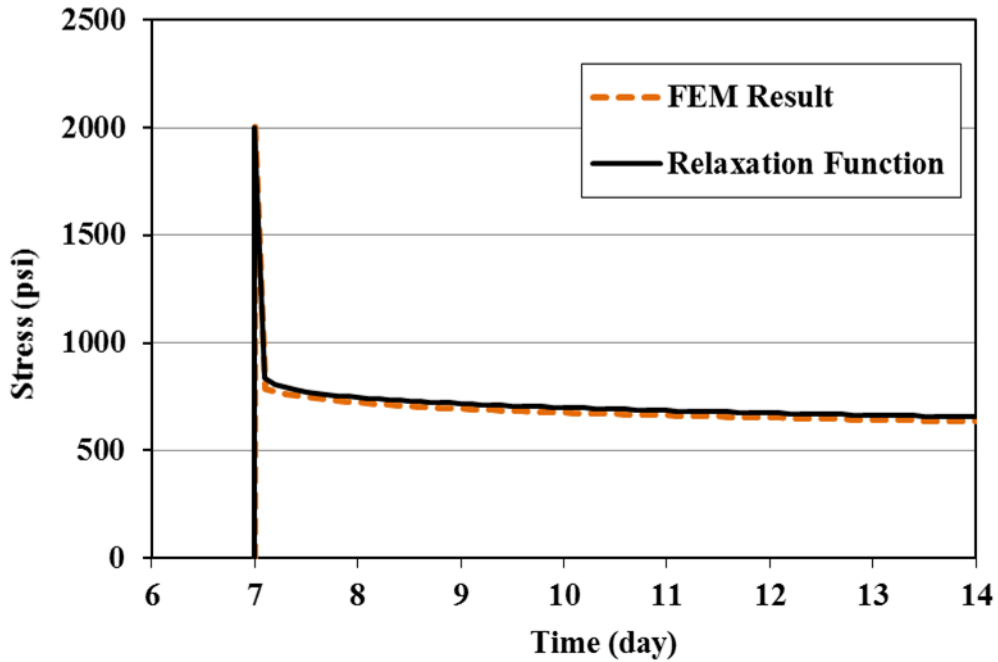
Figure 6-7 Relaxation response verification result

6.2.3 Variable Loads Application

The model with variable load history is checked herein. Three loading steps were applied to the model: 2900 psi at age of 7 days, a total of 3900 psi at age of 14 days, and a total of 4900 psi at age of 35 days (see Figure 6-8). The creep parameters input in the subroutine include: $q_1 = 0.15$, $q_2 = 1.0$, $q_3 = 0.15$, and $q_4 = 0.14$.

The principle of superposition was used with the B3 Model for the variable stress situation by the analytical calculation, which means a linear combination of a compliance function of $J(t, 7)$ with load of 2900 psi applied at 7 days, a compliance function of $J(t, 14)$ with a load of 1000 psi applied at age of 14 days, and a compliance function of $J(t, 35)$ with a load of 1000 psi applied at 35 days. The FEM result is based on rate-type creep law for variable stress.

For example, to calculate the strain ε at time step $t = 50$ days for the model (see Equation 6-33 to Equation 6-37):

$$\varepsilon(t) = \varepsilon_1 + \varepsilon_2 + \varepsilon_3 = J(t, t'_1)\sigma_1 + J(t, t'_2)\sigma_2 + J(t, t'_3)\sigma_3 \qquad \textbf{(Equation 6-33)}$$

$$\sigma_1 = 2900 \; psi, \; t'_1 = 7 \; days, \; J(t, t'_1) = J(50,7) = 0.8739 \; psi^{-1} \qquad \textbf{(Equation 6-34)}$$

$$\sigma_2 = 1000 \; psi, \; t'_2 = 14 \; days, \; J(t, t'_2) = J(50,14) = 0.6871 \; psi^{-1} \qquad \textbf{(Equation 6-35)}$$

$$\sigma_3 = 1000 \; psi, \; t'_3 = 35 \; days, \; J(t, t'_3) = J(50,35) = 0.4648 \; psi^{-1} \qquad \textbf{(Equation 6-36)}$$

$$\varepsilon(t) = 0.8739 \; psi^{-1} \times 2900 \; psi + 0.6871 \; psi^{-1} \times 1000 \; psi \qquad \textbf{(Equation 6-37)}$$
$$+ \; 0.4648 \; psi^{-1} \times 1000 \; psi = 3688 \times 10^{-6} \; in./in.$$

Therefore, the strain value calculated based on the principle of superposition is $3688 \times 10^{-6} \; in./in.$, while the strain result from the FEM at 50 days is $3765 \times 10^{-6} \; in/in$. This difference in strain is about 2.1%, which is acceptable. The creep response under variable load by the two methods are shown in Figure 6-9, and the two curves match very well. It is concluded that the calcualted result by the B3 Model determined with analytical expressions have good agreement with the FEM result. Therefore, the code for creep function in the FEM provide predictions that match the hand calculated values.
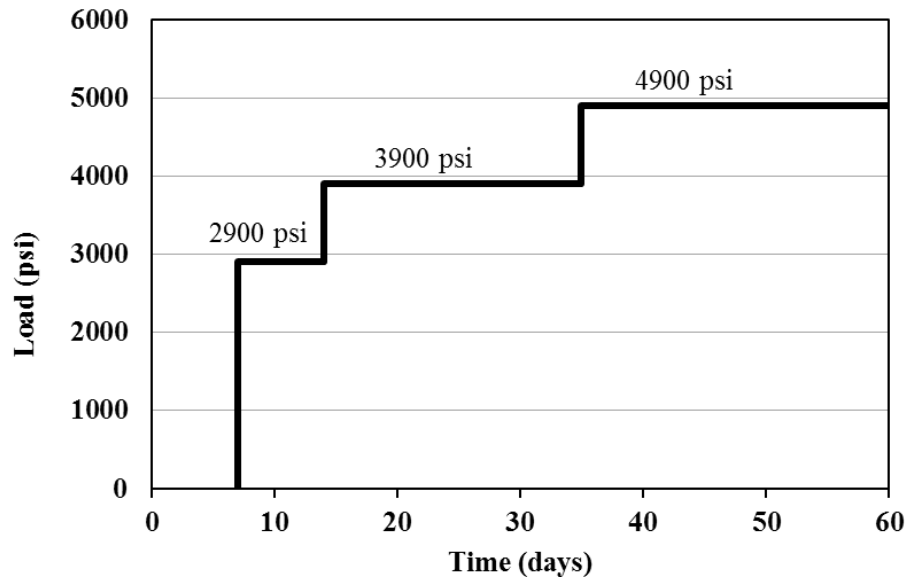
Figure 6-8 Variable load steps applied to the model
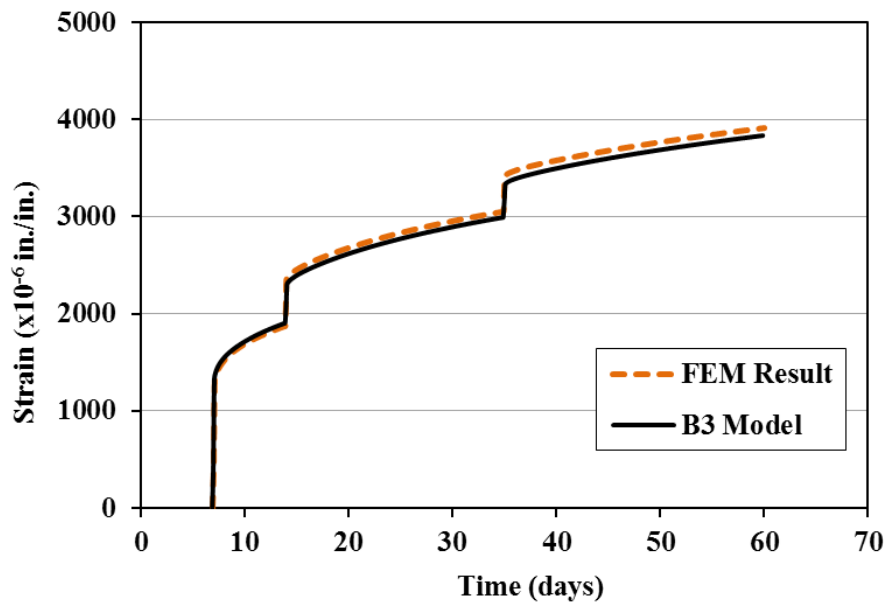
Figure 6-9 Creep response under variable loads

CHAPTER 7 PART I: RESULTS AND DISCUSSIONS

7.1 SAMPLE RESULTS AND STRESS PREDICTIONS

The stress predicted with the B3 Model, Modified B3 Model, B3 Model with R_T, B4 Model, and the measured stress development for 23D (30%Slag 23°C), 30A (W/C=0.38 23°C), 0.42 Shale SLW (Sum), and ICC 0.38 results are presented in Figure 7-1 to Figure 7-4. The complete measured and predicted stress results for all the 72 concrete mixtures can be found in Appendix A to Appendix C. Negative values represent compressive stress and positive values represent tensile stress. In these figures, the measured stress development shown in 1-hour increment is compared to the stress development predicted with the FEM that use each of the four creep models.
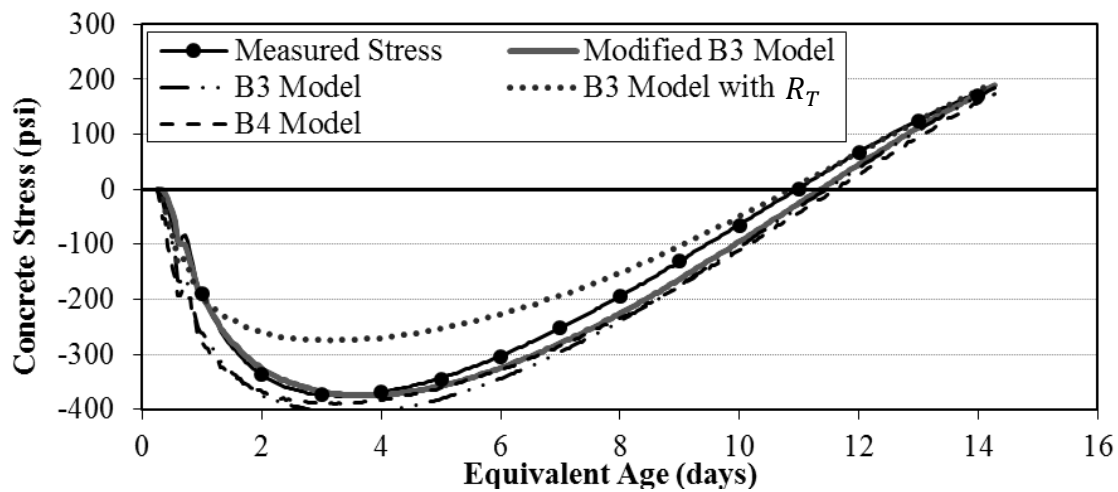
Figure 7-1 Stress development results for 23D (30%Slag 23°C)
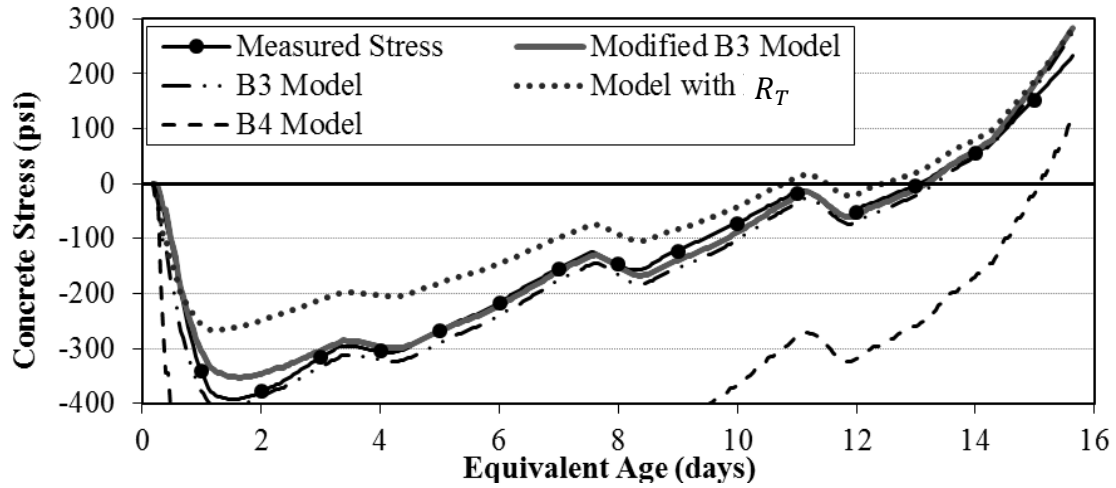
Figure 7-2 Stress development results for ICC 0.38
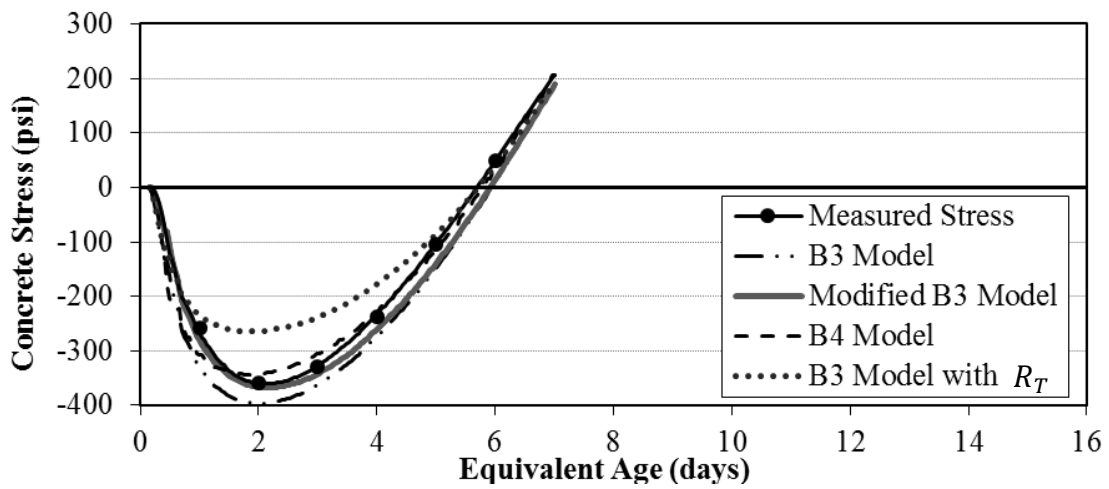
Figure 7-3 Stress development results for 30A (W/C=0.38 23ºC)
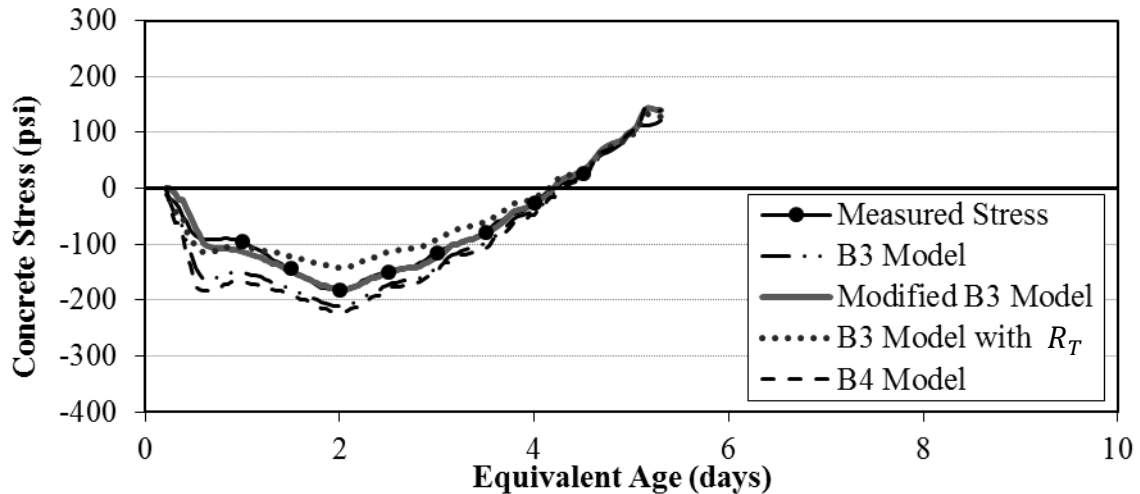
Figure 7-4 Stress development results for 0.42 Shale SLW

Immediately following final set, compressive stress develops due to the rise in concrete temperature and the restraint of concrete expansion. When the concrete begins to cool, tensile stress develops because of the restraint of concrete contraction. From these figures, it can be seen that the B3 Model and B4 Model generally overestimate the early-age compressive stress, while the B3 Model with RT underestimates the compressive stress. The Modified B3 Model is between the two extremes and most closely predicts the measured stress. The B4 Model sometimes predicts stress similar to the other models; however, sometimes it significantly overestimates the compressive stress as shown in Figure 7-2. This is because in the B4 Model, modifiers for concrete constituents such as fly ash, AEA, water reducer, and so on are provided that do not improve the B4 Model's ability to accurately predict the early-age stress of concrete. For the concrete mixtures without modifiers, the B4 Model predictions are closer to that of the other models.

7.2   ASSESSMENT OF THE STRESS PREDICTION ACCURACY

7.2.1   Stress Residual Assessment

The stress residual is determined as the deviation between the measured stress and the predicted stress as shown in Equation 7-1. A positive residual means the predicted stress is greater than the measured value and the stresses are overestimated. Al-Manaseer and Lam (2005) also used the stress residual method to assess the accuracy of various shrinkage and creep prediction models.

$$\sigma_{Residual} = y_i - f_i \qquad \textbf{(Equation 7-1)}$$

Where,

$\sigma_{Residual}$ = stress residual (psi),

y_i = predicted stress (psi), and

f_i = measured stress (psi).

7.2.2   Statistical Assessment

To evaluate how well a model predicts the measured stress, the coefficient of determination (r^2) and unbiased estimate of standard deviation of the absolute error (S_j) were used in this study. Equation 7-2 defines the coefficient of determination and Equation 7-3 defines the unbiased estimate of standard deviation of the absolute error (Montgomery et al. 2015).

$$r^2 = 1 - \frac{SS_{Res}}{SS_T} \qquad \textbf{(Equation 7-2)}$$

$$S_j = \sqrt{\frac{1}{n-1} \sum_{1}^{n} (y_i - f_i)^2}$$

Where,

SS_{Res} = sum of squares of the error $= \sum (y_i - f_i)^2$ (psi²),

SS_T = total sum of square of the error $= \sum (y_i - \bar{y})^2$ (psi²),

y_i = predicted value (psi),

f_i = measured data (psi),

$\bar{y}$ = mean measured data (psi),

S_j = unbiased estimate of the standard deviation of the absolute error (psi), and

n = number of data points (unitless).

The coefficient of determination (r^2) is a measure of how well the predicted data represents the measured dataset. The closer the values of r^2 to 1, the better the model characterizes the measured data. The smaller the value of Sj, the less deviation of the predicted value to the measured data, and therefore the better the model.

7.2.3   Stress-to-Strength Range used to Evaluate Accuracy of Stress Prediction

The stress-strain relationship of concrete becomes nonlinear at higher stress-to-strength ratios, which is caused by microcracking in the interfacial transition zones that begin to increase and the proliferation and propagation of cracks in the bulk concrete matrix (Mehta and Monteiro 2006).

Since the principle of superposition yields good approximation when concrete is within the elastic stress range, some researchers (e.g. Byard and Schindler 2015) have focused on assessing the accuracy of the stress predictions in a stress-to-strength ratio of 70%. Therefore, the data points used herein for the purpose of evaluating the accuracy of the stress predictions were limited to those below a stress-to-strength ratio of 70%.

7.3 SENSITIVITY ANALYSIS OF MESH SIZE AND TIME STEP

The element size and mesh density may influence the finite-element modeling results (Liu and Glass 2013). The time step deviation may also influence the precision of the FEM results (Dassault Systèmes Simulia Corp. 2012a). Based on the reasons outlined below, a time step of 1 hour and an element size of 1 in. were used in this FEM.

The 1-hour time step is representative to characterize the temperature change due to heat hydration as shown in Figure 6-2. Shorter and longer time steps were evaluated to determine the effect of time step duration on the accuracy of the modeled stress. Two datasets from experiments using the Modified B3 Model were selected to check time steps of 0.5, 1.0, 1.5, and 2.0 hours for the FEM. The resulting values for the measured stress and predicted stress with different time steps differed by less than 1 percent. So the 1-hour time step was used in the FEM analysis.

Similarly for the same two datasets, the meshed element sizes of 0.25 in., 0.5 in. 1.0 in., and 2.0 in. were used to check the analysis results. The resulting stresses for these mesh densities also differed by less than 1 percent. However, the analysis time for 1 in. size model was about 5 minutes while the 0.5 in. size mesh required 30 minutes. Therefore, a 1 in. element size provides good accuracy with a reasonable analysis time.

7.4 RESIDUAL ANALYSIS RESULTS

The concrete stress residuals versus equivalent age for all four creep models are shown in Figure 7-5 to Figure 7-8. Also shown in these figures are the present of residuals in the following four ranges:1) 0 to 100 psi, 2) 0 to -100 psi, 3) greater than 100 psi, and 4) less than -100 psi.
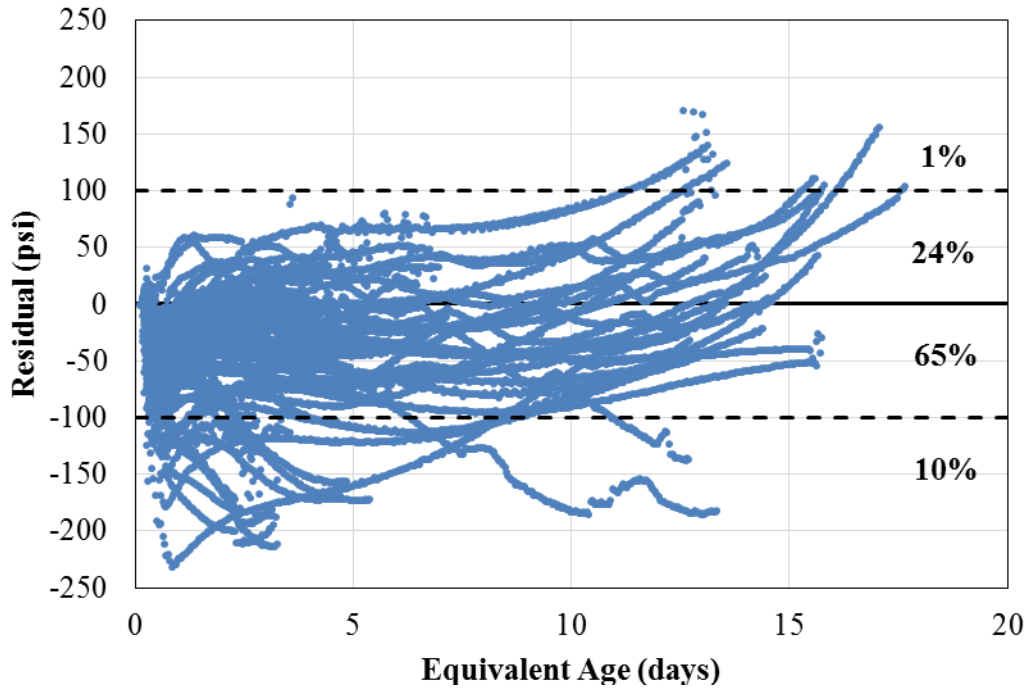
Figure 7-5 Residual stress results for B3 Model
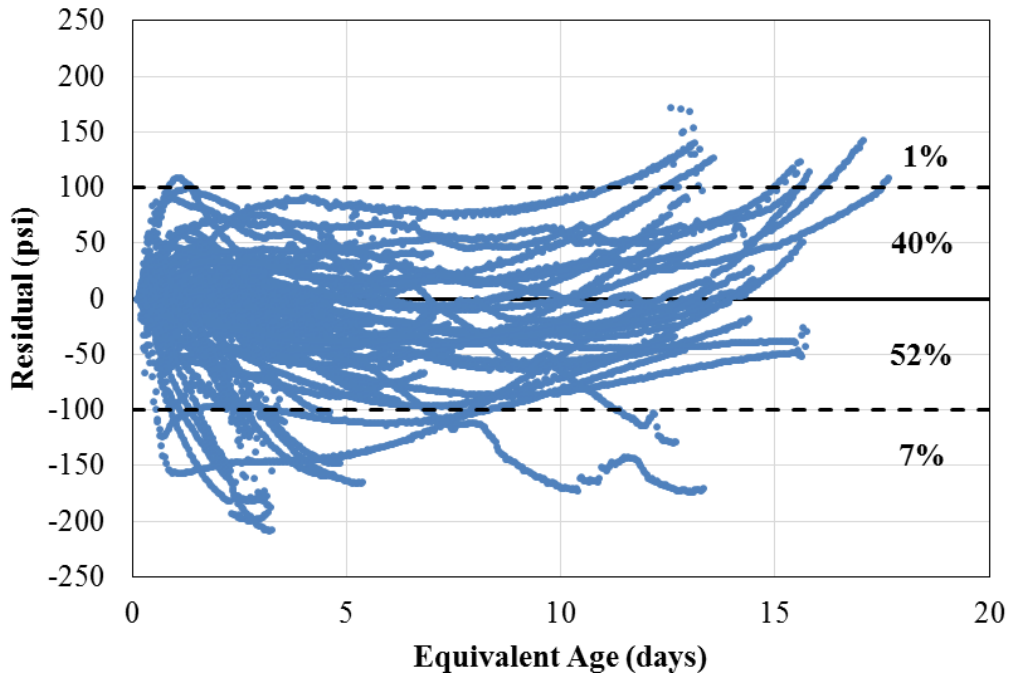
Figure 7-6 Residual stress results for Modified B3 Model
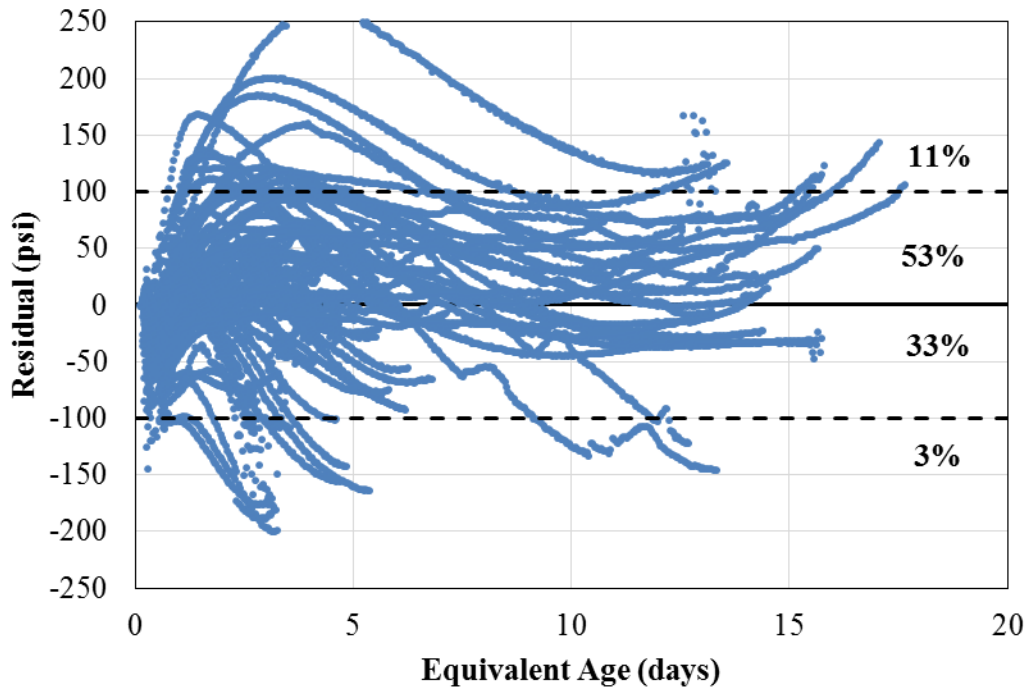
Figure 7-7 Residual stress results for B3 Model with R_T

90
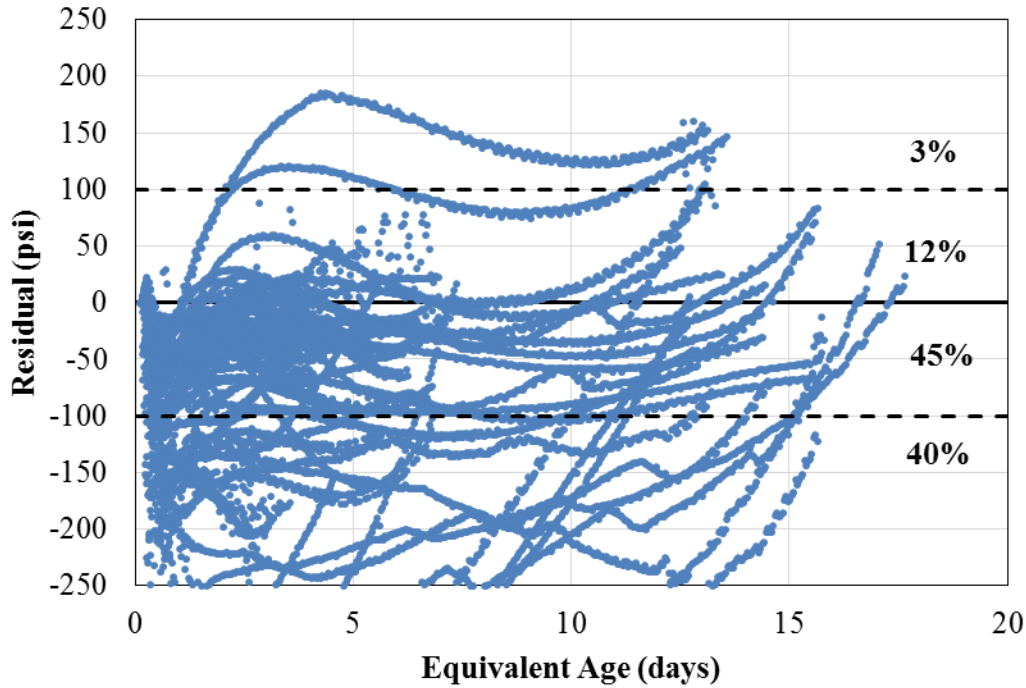
Figure 7-8 Residual stress results for B4 Model

From these four figures, it can be seen that for the B3 Model, Modified B3 Model, B3 Model with R_T, and B4 Model, the residuals data points that fall in ±100 psi range are 89%, 92%, 86%, and 57%, respectively. These results show that the Modified B3 Model has most data points that fall in the +100 psi residual range. It can also be observed from Figure 7-5 that the B3 Model underestimates 65% of the measured stresses in the range from 0 to -100 psi, and overestimates 24% in the range from 0 to 100 psi. The B3 Model with R_T shown in Figure 7-7 overestimates 53% of the measured stresses in the range from 0 to -100 psi, and underestimates 33% of the stresses in the range from 0 to 100 psi. The B4 Model shown in Figure 7-8 underestimates the majority of the measured stresses model with a total of 85% data points below zero. When compared with the other three models, the Modified B3 Model provides equally well-balanced estimates in the positive and negative stress residual ranges, which indicates that there is no bias to either underestimate or overestimate the measured stresses.

7.5   STATISTICAL ANALYSIS RESULTS

The r^2 and S_j values for the stresses predicted by the B3 Model, Modified B3 Model, B3 Model with R_T, and B4 Model versus the measured stress for each concrete are presented in Table 7-1 to Table 7-5. The r^2 and S_j of all the data collected are shown in the last row of Table 7-5 and provide an overall indication of how well the four creep models predict the measured stresses.

The results in these tables show that the Modified B3 Model performs the best compared to the other three models. By analyzing all the data points from the 72 concretes tested, the r^2 of the Modified B3 Model is 0.88, which is the greatest and the S_j equals 56 psi, which is the least among the four models. For the Modified B3 Model, the final r^2 value of 88% for all the data in the database suggests that 88% of the error in the data is explained by the model. Since this is sufficiently high, no modification to the Modified B3 Model is recommended and it can be concluded that the FEM provides accurate predictions of measured early-age concrete stresses.

Table 7-1 Statistical results for four creep models from Project A (Part 1 of 2)

Mixture	r^2				S_j (psi)			
	B3 Model	Modified B3 Model	B3 Model with R_T	B4 Model	B3 Model	Modified B3 Model	B3 Model with R_T	B4 Model
12A (Control 73ºF)	0.97	0.99	0.89	0.97	30	20	58	32
12B (Control 50ºF)	-0.85	-0.27	-0.20	-0.99	160	133	129	166
12C (Control 95ºF)	0.97	0.98	0.74	0.97	33	28	100	32
12D (Control 73ºF)	0.91	0.95	0.88	0.96	67	49	76	46
12E (Control 50ºF)	0.72	0.80	0.96	0.71	109	94	41	111
21 (30%Class C)	-0.15	0.22	0.30	0.30	128	105	100	100
22 (20%Class C)	-0.01	0.41	0.55	-6.57	119	90	79	324
23A (30%Slag 73ºF)	0.68	0.81	0.90	0.53	69	52	39	83
23B (30%Slag 50ºF)	0.35	0.62	0.45	-0.09	74	54	66	92
23C (30%Slag 95ºF)	0.94	0.99	0.86	0.96	37	19	58	31
23D (30%Slag 73ºF)	0.95	0.99	0.90	0.95	38	21	57	39
23E (30%Slag 50ºF)	0.82	0.88	0.96	0.78	82	68	39	91
24A (50%Slag 73ºF)	0.58	0.71	0.75	0.33	61	51	47	77
24B (50%Slag 50ºF)	1.00	0.93	0.99	0.91	4	15	5	17
24C (50%Slag 95ºF)	0.79	0.89	0.96	0.86	58	42	26	48
24D (50%Slag 73ºF)	0.59	0.72	0.75	0.35	61	60	47	77
24E (50%Slag 50ºF)	0.92	0.94	0.95	0.58	37	33	30	85

Table 7-2 Statistical Results for Four Creep Models from Project A (Part 2 of 2)

Mixture	r^2				S_j (psi)			
	B3 Model	Modified B3 Model	B3 Model with R_T	B4 Model	B3 Model	Modified B3 Model	B3 Model with R_T	B4 Model
25 (25%ClassC 6%Slag)	-1.24	-0.28	-0.19	-10.99	141	106	103	325
26 (25%ClassF 6%Slag)	0.62	0.74	0.77	-3.18	72	60	56	241
27 (20%ClassF 30%Slag)	0.97	0.88	0.96	0.02	18	33	20	96
28 (W/C=0.32)	0.83	0.93	0.88	0.20	74	48	61	160
30A (W/C=0.38 73ºF)	0.94	0.98	0.89	0.98	53	30	57	23
30B (W/C=0.38 50ºF)	-0.99	-0.42	-0.21	-0.64	179	151	140	162
30C (W/C=0.38 95ºF)	0.88	0.85	0.29	0.59	75	85	181	137
30D (W/C=0.38 73ºF)	0.96	0.96	0.69	0.84	49	51	136	98
30E (W/C=0.38 50ºF)	0.70	0.80	0.96	0.97	134	108	46	40
31 (W/C=0.48)	0.88	0.93	0.94	0.94	48	37	34	34
32 (W/C=0.53)	0.49	0.62	0.82	0.86	81	70	49	42
33A (Type III 73ºF)	0.97	0.94	0.76	-0.89	31	50	97	270
33B (Type III 50ºF)	-0.17	0.14	0.28	-6.91	158	136	124	412
33C (Type III 95ºF)	0.84	0.93	0.87	-2.18	63	42	58	286
33D (Type III 73ºF)	0.99	0.99	0.75	-0.72	19	22	193	291
33E (Type III 50ºF)	0.82	0.90	0.94	-1.50	95	71	54	356
34 (AEA)	0.71	0.83	0.89	-0.16	66	51	37	119

Table 7-3 Statistical Results for Four Creep Models from Project B (Part 1 of 2)

Mixture	r^2				S_j (psi)			
	B3 Model	Modified B3 Model	B3 Model with R_T	B4 Model	B3 Model	Modified B3 Model	B3 Model with R_T	B4 Model
0.42 Slate IC (Fall)	0.93	0.96	0.95	0.83	29	23	25	45
0.42 Slate IC (Sum)	0.67	0.90	0.91	0.53	51	28	26	61
0.42 Slate SLW (Fall)	0.96	0.90	0.87	0.96	20	31	35	21
0.42 Slate SLW (Sum)	0.80	0.97	0.91	0.64	34	12	23	46
0.42 Slate ALW (Fall)	0.86	0.83	0.83	0.84	30	33	32	31
0.42 Slate ALW (Sum)	0.81	0.78	0.70	0.81	37	39	46	37
0.42 Clay IC (Fall)	0.98	0.94	0.93	0.91	16	27	27	31
0.42 Clay IC (Sum)	0.98	0.93	0.72	0.86	14	27	53	38
0.42 Clay SLW (Fall)	0.94	0.97	0.98	0.74	14	10	9	30
0.42 Clay SLW (Sum)	0.74	0.97	0.98	0.66	44	15	14	50
0.42 Clay ALW (Fall)	0.85	0.81	0.87	0.56	19	21	18	32
0.42 Clay ALW (Sum)	0.71	0.93	0.97	0.34	32	15	10	49
0.42 Shale IC (Fall)	0.99	0.97	0.94	0.95	12	19	25	23
0.42 Shale IC (Sum)	0.89	0.96	0.89	0.82	36	22	34	45

Table 7-4 Statistical Results for Four Creep Models from Project B (Part 2 of 2)

Mixture	r^2				S_j (psi)			
	B3 Model	Modified B3 Model	B3 Model with R_T	B4 Model	B3 Model	Modified B3 Model	B3 Model with R_T	B4 Model
0.42 Shale SLW (Fall)	0.94	0.99	0.98	0.76	19	7	11	38
0.42 Shale SLW (Sum)	0.87	0.99	0.93	0.75	31	10	23	43
0.42 Shale ALW (Fall)	0.88	0.82	0.87	0.76	18	21	18	25
0.42 Shale ALW (Sum)	0.93	0.86	0.81	0.92	21	29	32	22
0.42 RG (Fall)	0.33	0.84	0.80	-0.42	58	28	32	84
0.42 RG (Sum)	-3.54	-1.43	-0.39	-5.03	112	82	62	129
0.42 LS (Fall)	0.90	0.94	0.94	0.81	35	27	27	48
0.42 LS (Sum)	0.82	0.98	0.97	0.88	30	15	21	37
0.36 RG (Fall)	0.63	0.79	0.82	-0.99	75	56	52	317
0.36 ICM (Fall)	0.48	0.77	0.84	-0.88	76	50	42	144
0.36 ICH (Fall)	0.37	0.71	0.81	-1.10	85	58	47	155
0.30 RG (Fall)	0.63	0.75	0.85	-1.15	137	114	87	331
0.30 ICM (Fall)	0.66	0.81	0.86	-1.34	102	78	66	269
0.30 ICH (Fall)	0.17	0.67	0.84	-3.91	115	73	51	280

Table 7-5 Statistical Results for Four Creep Models from Project C and Summary Data for

All Data Points

Mixture	r^2				S_j (psi)			
	B3 Model	Modified B3 Model	B3 Model with R_T	B4 Model	B3 Model	Modified B3 Model	B3 Model with R_T	B4 Model
REF 0.38	0.55	0.63	0.73	-10.71	121	110	94	464
ICC 0.38	0.98	0.99	0.81	-3.02	24	17	68	312
ISLWC 0.38	0.59	0.79	0.86	-10.13	53	39	32	278
SLWC 0.38	0.90	0.89	0.62	-1.60	43	46	86	224
ALWC 0.38	0.86	0.80	0.55	-3.42	38	32	58	179
REF 0.45	0.79	0.75	0.68	-0.67	64	69	78	179
ICC 0.45	0.97	0.89	0.75	-0.18	20	42	62	135
ISLWC 0.45	0.38	0.78	0.95	-6.66	54	32	16	190
SLWC 0.45	0.84	0.71	0.44	0.48	49	69	91	88
ALWC 0.45	0.60	0.41	0.27	0.50	44	54	60	50
All Data Points	**0.83**	**0.88**	**0.82**	**-0.15**	**66**	**56**	**69**	**172**

CHAPTER 8 PART I: CONCLUSION

A three-dimensional, finite-element model (FEM) of concrete subjected to restraint to volume change tests was developed and its results compared to test results. This FEM was used to simulate the early-age concrete stress development considering temperature histories, changing mechanical properties, and creep effects. Four creep models including the B3 Model, Modified B3 Model, B3 Model with R_T, and B4 Model were incorporated in the FEM to determine their level of accuracy by comparing their stress results to the measured experimental data. Early-age stress development from restraint to volume change tests from 72 concretes was used to verify the accuracy of the four creep models. These concretes used varying cementitious materials, aggregate types, *w/cm*, chemical admixtures, and temperature histories. The results presented in this paper support the following conclusions:

1. The finite-element model provides accurate predictions of measured early-age concrete stresses.

2. The residual analysis of the four creep models show that the B3 Model and B4 Model generally overestimate the early-age concrete stress, while the B3 Model with R_T underestimates the stresses. The B4 Model significantly overestimates the early-age compressive stress when its modifiers for concrete constituents are used. The Modified B3 Model provides the best prediction of early-age concrete stresses.

3. The statistical analysis of stress results based on the B3 Model, Modified B3 Model, B3 Model with R_T, and B4 Model resulted in r^2 of 0.83, 0.88, 0.82, -0.15 and S_j of 66 psi, 56 psi, 69 psi and 172 psi, respectively, for all the data in the database. These results show that the Modified B3 Model provides the most accurate predictions of the early-age concrete stress among the models considered.

PART II:
FINITE-ELEMENT MODELING AND ANALYSIS OF EARLY-AGE CONCRETE CRACKING RISK OF CAST-IN-PLACE CONCRETE CULVERTS

CHAPTER 9 PART II: INTRODUCTION

9.1   BACKGROUND

Extensive cracking was found in various cast-in-place (CIP) reinforced concrete box culverts located in the Anniston East Bypass (AEB) in Anniston, Alabama (Minton 2012). An example of a 0.08 in. wide crack in a culvert wall is shown in Figure 9-1. Many cracks in the AEB culverts had widths wider than 0.04 in. and far exceeded 0.012 in. (0.3 mm), which is the tolerable limit for the exposure condition of these culverts in accordance with ACI 224 (2001). Because of the numerous wide cracks encountered, condition surveys were conducted on other CIP reinforced concrete box culverts throughout Alabama. Fourteen culverts were surveyed and similar cracks were found in most of these culverts, with most of the excessively wide cracks being transverse and located either in the base or in the walls of the culverts (Minton 2012). The lengths of these culverts varied from 122 ft to 1005 ft (Minton 2012). For the 14 surveyed culverts, 11 used construction joints and 3 used contraction joints to connect adjacent culvert sections. These construction joints (herein called tied joints) had deformed reinforcement continuing longitudinally through the joint, which restrains longitudinal contraction and expansion of adjacent culvert sections. However, the contraction joints used in three projects allow adjacent concrete sections to contract independently and expand. The spacing of these tied or contraction joints between culvert sections ranged from 30 ft to 53 ft (Minton 2012).

Figure 9-1 Cracking in culvert wall

The primary cause of cracking was attributed to restraint of thermal and drying shrinkage effects. Early-age stress development in concrete is influenced by temperature changes, modulus of elasticity, stress relaxation, shrinkage, thermal coefficient of expansion, and the degree of restraint. Cracks occur when tensile stress in the concrete exceeds its tensile strength.

9.2 RESEARCH OBJECTIVES

The primary objective of this part of the dissertation is to determine means to mitigate early-age cracking in CIP culverts. In order to achieve this objective, a secondary objective is to develop a finite-element model (FEM) that can simulate the early-age stress development of concrete

considering the changing mechanical properties, thermal effect, creep or relaxation, and drying shrinkage. Experimental results from restraint to volume change tests with rigid cracking frames were used to verify the accuracy of the FEM, and this was done in Part I of the dissertation. In order to determine measures to mitigate culvert cracking, a parametric study was performed with the FEM to evaluate the effect of changing joint spacing, joint type, construction sequence, concrete coefficient of thermal expansion, placement season, and concrete type.

9.3   RESEARCH APPROACH

Restraint to volume change tests with rigid cracking frames (RCF) were used to measure the early-age stress development in various concretes, which has been discussed in Part I. Seventy-two concrete mixtures were tested to assess the early-age stress development by using the RCF, and three-dimensional finite-element analysis was used to model these 72 concretes. By comparing FEM results with experimental results, it is concluded that the Modified B3 Model performs the best to predict early-age concrete stress development, and thus was used to evaluate the causes of cracking in CIP concrete box culverts in Part II.

The concrete temperature profile used for the stress calculation in the FEM was obtained from ConcreteWorks, which is an early-age concrete temperature development and thermal stress analysis software. Concrete creep and drying shrinkage were modeled with user-defined subroutines in ABAQUS. The ABAQUS material subroutine UMAT was used to define the creep effects of the concrete. The user-subroutine UEXPAN was used to calculate incremental thermal strains as function of concrete temperature. The drying shrinkage model was also coded into this subroutine considering the concrete properties.

Culvert J, one of culverts that exhibited extensive cracking, was used as baseline for the FEM. Eight-node linear hexahedral (brick) elements with three translational degrees of freedom at each node (C3D8) were used. The FEM was used to perform parametric studies to determine the influence of changing the contraction joint spacing, two concrete CTE values, three placement seasons, two joint types, three construction sequences, and three concrete types on early-age cracking risk.

9.4   RESEARCH OUTLINE

This part of dissertation comprises five chapters. A literature review containing culvert information, concrete culvert cracking background, and causes and influencing factors of cracking in culvert are summarized in Chapter 10. The process of modeling concrete culvert using finite-element method (FEM), which includes incorporating culvert geometry, material properties, creep model, and drying shrinkage model, is presented in Chapter 11. The results of the parametric study conducted with the FEM to evaluate the effect of changing joint spacing, joint type, construction sequence, concrete coefficient of thermal expansion, placement season, and concrete type are summarized in Chapter 12. Conclusions for this part are presented in Chapter 13.

CHAPTER 10 PART II: LITERATURE REVIEW

10.1   OVERVIEW OF BOX CULVERTS

Culverts are structures that allow water to flow inside from one side to the other side of an obstruction. They are generally under a road, railroad, trail, or similar obstruction, and are embedded and surrounded by soil. The culverts can be made from corrugated metal, plastic, reinforced concrete, or other materials.

Culverts are commonly used both as cross-drains for ditch relief and to pass water under a road at natural drainage and stream crossings. Some culverts are bridge-like in that its design allows vehicle or pedestrian traffic to cross over the waterway and also allow adequate water to pass through. The sizes and shapes of culverts are various, which include round, box-like, elliptical, flat-bottomed, and pear-shaped constructions. The selection of the type and shape of a culvert is based on many factors such as requirements for hydraulic performance, limitation on upstream water surface elevation, and roadway embankment height (Turner-Fairbank Highway research Center. 1998).

Box culverts are designed not only to be hydralic structures, but also to support lateral loads from earth pressure and vertical loads from earth and vehicle pressures (WisDOT 2011). Reinforced box culverts can be precast or cast-in-place (CIP) and their selection of them depends on many factors. Precast culvers can be produced at a plant and transported to the field site and the benefits of this type include reduction of issues related to construction time, site constraint, and traffic management. The disadvantages of precast culverts are limitations of certain sizes and skews because of transportation and handling concerns, and the possible high cost of tranportaion to the job site (FDOT 2011). CIP concrete culverts are built with available ready-mixed concrete and

their advantages include that the culverts can be specifically designed to meet the unique needs of the site (ConnDOT 2000).

10.2   CULVERT CRACKING BACKGROUND

10.2.1 Culvert Cracking in Anniston East Bypass (AEB)

Extensive cracking was found in various CIP reinforced concrete box culverts on the Anniston East Bypass (AEB) in Anniston, designed and owned by Alabama Department of Transportation (ALDOT) (Minton 2012). Figure 10-1 shows the entrance of AEB Culvert at 175+70. A crack wider than 0.012 in. is the tolerable limit for the exposure condition of these culverts in accordance with ACI 224 (2001). Many of the observed cracks in the AEB culverts were wider than 0.04 in. Illustration of one crack type found in AEB culvert is shown in Figure 10-2. The majority of the transverse cracks were located in the top slab and walls, and some were observed in the walls only.

Figure 10-1 AEB Culvert at 175+70 Entrance (Minton 2012)

Figure 10-2 Transverse base crack in the AEB project (crack width>0.06 in.) (Minton 2012)

10.2.2 Summary of Surveyed Culverts

Because of the numerous wide cracks encountered, follow-up culvert crack condition surveys were conducted of existing CIP reinforced concrete box culverts throughout Alabama. These surveys include documenting the width and location of all the transverse cracks observed and other signs of distress (Minton 2012). A total of 14 culverts were visited and the geometry, length, fill height, and joint information for all the culverts are shown in Table 10-1. There are two types of joints used in these culverts, one is a construction joint (herein called tied joint) which has deformed reinforcement continuing longitudinally through the joint, which restrains longitudinal contraction and expansion of adjacent culvert sections, another is a contraction joint which allows adjacent concrete sections to independently contract and expand.

From the Table 10-1, it is shown that the lengths of these culverts varied from 122 ft to 1005 ft, 11 used construction joints and 3 used contraction joints to connect adjacent culvert sections, and the spacing of these tied or contraction joints between culvert sections ranged from 30 ft to 53 ft.

Table 10-1 Surveyed Culverts Information (Minton 2012)

Culvert ID	Size (No. Barrels x Width x Height)	Length	Maximum Fill Height	Ceiling Thickness	Interior Wall Thickness	Exterior Wall Thickness	Joint Type	Joint Spacing
AEB 149+60 (C)	1×8'×8'	1,005'	56'	17	--	14	Tied	48
AEB 162+90 (D)	1×6'×6'	355'	36'	13.5	--	11.5	Tied	53
AEB 175+70 (E)	1×8'×6'	508'	52'	16.5	--	10.5	Tied	52
AEB 240+37 (J)	2×8'×8'	892'	59'	18.5	9	15	Tied	50
AEB 257+69 (I)	1×6'×6'	625'	78'	18	--	13	Contraction	49
Centreville 1808+98	3×12'×7'	286'	12'	14	6	10.5	Tied	51
Corridor X 4877+13	3×8'×10'	901'	124'	2'-10''	12	2'-11''	Contraction	38
Corridor X 4959+43	3×8'×10'	945'	110'	2'-8''	12''	2'-10''	Contraction	44
Corridor X Exit 85	3×6'×6'	>900'	N/A	N/A	N/A	N/A	Tied	46
Dadeville 45+31.55	3×10'×10'	305'	32'	16.5''	7''	12''	Tied	44
Dutton 548+23	1×8'×8'	929'	114'-120'	24''	N/A	19.5''	Tied	46
I-85 North	2×10'×7'	122'	N/A	N/A	N/A	N/A	Tied	35
I-85 South	2×12'×7'	287'	N/A	N/A	N/A	N/A	Tied	41
Prattville US-82	N/A	N/A	N/A	N/A	N/A	N/A	Tied	30

10.2.3 Definitions and Terminology of Culvert

The terms that used in this study are defined as follows by the American Concrete Institute (ACI CT 2016):

- **Cast-in-place concrete** - concrete that is deposited and allowed to harden in the place where it is required to be in the completed structure, as opposed to precast concrete.

- **Precast concrete** – concrete cast elsewhere than its final position.

- **Construction joint** – the surface where two successive placements of concrete meet, across which it may be desirable to achieve bond and through which reinforcement may be continuous.

- **Contraction joint** – a formed, sawed, or tooled groove in a concrete structure to create a weakened plane to regulate the location of cracking resulting from dimensional change of different parts of the structure.

- **Transverse crack** – a crack that crosses the longer dimension of the member.

- **Longitudinal crack** – a crack that develops parallel to the length of a member.

10.3 CAUSES OF EARLY-AGE CRACKING

The primary cause of early-age cracking in the concrete culverts was attributed to restraint of thermal and drying shrinkage effects (Minton 2012). Early-age stress development in concrete is influenced by temperature changes, modulus of elasticity, stress relaxation, shrinkage, thermal coefficient of expansion, and the degree of restraint. Cracks occur when tensile stress in the concrete exceeds its tensile strength. The development of thermal stress can be determined with Equation 10-1 (Schindler and McCullough 2002).

$$\sigma = K_r \times CTE \times \Delta T \times E_c \qquad \textbf{(Equation 10-1)}$$

Where,

σ is the thermal stress (psi),

E_c is the creep-adjusted modulus of elasticity of the concrete (psi),

K_r is the internal/external restraint factor,

CTE is the coefficient of thermal expansion of concrete (in./in./˚F),

ΔT is the difference in temperature $= T_{zero\text{-}stress} - T_{min}$ (˚F),

$T_{zero\text{-}stress}$ is the temperature at zero stress in the concrete (˚F), and

T_{min} is the minimum temperature recorded by the concrete member (˚F).

More details of the factors influencing early-age cracking of concrete, which include thermal dilation, creep effect, and concrete mechanical properties, have been discussed in Part I (Chapter 3 of this dissertation). Other causes of early-age cracking involve drying shrinkage and external restraint are discussed in the following sections of this chapter.

10.4 LONG-TERM DURABILITY

Corrosion is harmful damage that occurs in reinforced concrete structures. Corrosion of steel is an electrochemical process that needs an oxidizing agent, moisture, and electron flow with the steel (Mehta and Monteiro 2014). Ordinary reinforcing steel is usually coated with a protective thin iron-oxide film, which is impermeable and adherent in a highly alkaline environment (Mehta and Monteiro 2014). A critical requirement for corrosion is the breakdown of the pacifying iron-oxide film on steel and this can be achieved by two ways. One is the removal of alkalies and calcium hydroxide through leaching or carbonation, and this reduces the pH and corrosion initiates when pH < 11.5 at steel level. Another way is that a critical amount of chlorides is deposited at the steel level and corrosion initiates when a threshold of chloride content is reached, even if pH > 11.5 (Mehta and Monteiro 2014).

The common sources of chlorides are admixtures, deicing salts, seawater, and salt-contaminated aggregates. The first way takes very long and the second way is the main cause and can occur over

a short period. After the breakdown of the pacifying iron-oxide film on steel, the process of corrosion initiates and an electrochemical reaction can occur at the steel surface in the presence of moisture and oxygen. The positively charged iron (Fe^{2+}) in the steel at the node move to the cathode to react with the negatively charged hydroxide ions (OH^-) which comes from water and oxygen, which forms iron oxide or rust and this is accompanied by an increase in volume. (Mehta and Monteiro 2014). This process can be illustrated in Figure 10-3. This volume increase causes high radial bursting stresses around reinforcing bars and would result in concrete expansion and cracking. These cracks can propagate along the bar, leading to the formation of longitudinal cracks (cracks running parallel to the bars), spalling of the concrete or delamination of the concrete surface (ACI 224 2007).
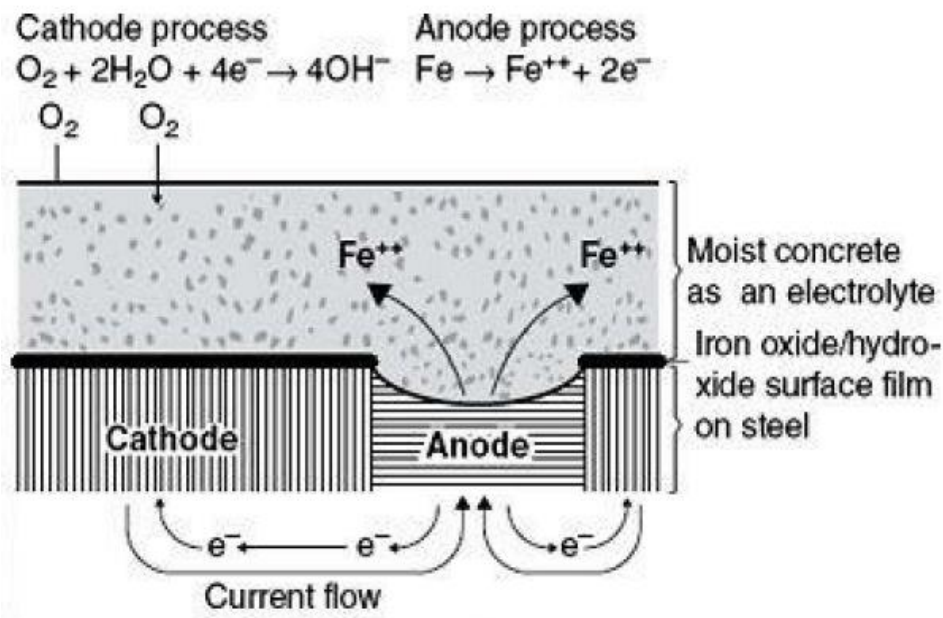

Figure 10-3 Illustration of corrosion process (Mehta and Monteiro 2014)

The cracks can provide easy access for corrosive agents (moisture, oxygen, and chlorides) which provide a condition to accelerate the corrosion and cracks. Common protection against corrosion

include use of concrete with low permeability and adequate cover. For severe exposure conditions, additional protective measures like coated reinforcement, sealers, or overlays on the concrete, corrosion inhibiting admixtures, and cathodic protection (Transportation Research Board 1979) can be used.

10.5 CRACK CONTROL

10.5.1 Reinforcement

The reinforcement ratio and steel bar size in reinforced concrete have an effect on the crack width and spacing. Research by McCullough and Dossey (1999) based on observations from 12 years of monitoring experimental test sections in Houston, Texas showed that as the steel percentage in the continuously reinforced concrete (CRC) pavement increases, the crack spacing, crack width, and steel stress decrease. This is because as the steel percentage is increased, cracks begin to form closer together and the steel restrains cracks from opening when the volume change occurs in the concrete (McCullough and Dossey 1999). The effect of bar size was also studied and results showed that the pavement with a larger bar size would have a larger crack spacing, and this is because the larger bar has a larger bond slip area which leads to crack widths that are larger and a mean crack spacing that is also larger (McCullough and Dossey 1999).

ACI 224R-01 "Control of Cracking of Concrete Structures" states: "The minimum amount and spacing of reinforcement to be used in structural floors, roof slabs, and walls for control of temperature and shrinkage cracking is given in ACI 318 (2014) or ACI 350 (2001)". The minimum-reinforcement percentage, which is between 0.18 and 0.20%, does not normally control cracks to within generally acceptable design limits. To control cracks to a more acceptable level, the percentage requirement needs to exceed about 0.60%". For concrete members that are in

environmental exposure conditions or required to be liquid-tight, the required ratios of shrinkage

and temperature reinforcement are summarized in Table 10-2.

Table 10-2 Minimum shrinkage and temperature reinforcement (ACI 350 2001)

Length between movement joints (ft)	Minimum shrinkage and temperature reinforcement ratio	
	Grade 40	Grade 60
Less than 20	0.0030	0.0030
20 to less than 30	0.0040	0.0030
30 to less than 40	0.0050	0.0040
40 and greater	0.0060*	0.0050

*Maximum shrinkage and temperature reinforcement where movement joints are not provided.

Note: When using this table, the actual joint spacing shall be multiplied by 1.5 if no more than 50% of the reinforcement passes through the joint.

Section 5.10.8 of the *AASHTO LRFD Bridge Design Specifications* (2016) provides two governing

equations for the shrinkage and temperature reinforcement in CIP reinforced concrete box culverts.

$$A_s \geq \frac{1.30bh}{2(b + h)f_y} \qquad \textbf{(Equation 10-2)}$$

Where,

A_s = area of temperature and shrinkage reinforcement per length of culvert component

(in.^{2}/ft),

b = smallest height/width of the culvert component section (in.),

h = smallest thickness of the culvert component section (in.), and

f_y = yield strength of the reinforcement ≤ 75 ksi (ksi).

$$0.11 \text{ in.}^2/\text{ft} \leq A_s \leq 0.60 \text{ in.}^2/\text{ft} \qquad \textbf{(Equation 10-3)}$$

The reinforcement based on these equations should be distributed uniformly around the perimeter of the culvert component. For example, a culvert wall with a height of 8 ft, a thickness of 9 in., and an assumed reinforcement yield strength of 60 ksi, the temperature and shrinkage reinforcement area would be 0.089 in.^{2}/ft. If the same wall was 15 in. thick, the shrinkage and temperature reinforcement area would be 0.141 in.^{2}/ft.

10.5.2 Joints

Joints are an important aspect of crack control and construction (Kosmatka et al. 2002). Joints can serve as intentional cracks and a weakened plane to ensure the cracks occur in places that are of minor importance (ACI 224 1995). Joints also allow for concrete to be cast in sections instead of continuously. Construction joints or contraction joints are used in culvert base slab, wall, and roof sections. A discussion of the purpose of each joint type and its use is provided in the following part.

10.5.2.1 *Construction joints*

For many structures, placing concrete in a continuous or very large operation is impractical; therefore, construction joints are needed to accommodate the construction sequence for casting the concrete (ACI 224 1995). Construction joints separate the sections of concrete that have been placed at different times (Kosmatka et al. 2002). The type and layout of construction joints should be determined before concrete placement, so that these construction joints will coincide with the location of isolation and contraction joints. When construction and contraction joints do not coincide, butt and bonded joints are used as construction joints. Bonded construction joints are

used when there is sufficient time to permit the concrete to harden and tie bars or continuous

reinforcement may be used in bonded joints (ACI 224 1995). Butt joints can be used in thin, lightly

loaded slabs; however, for thicker slabs or slabs with heavy loads, key or dowels joints should be

used (ACI 224 1995).

Figure 10-4 shows a transverse construction joint used in culverts AEB Culvert at 240+37 that

were defined as ¾'' Vee Joints with reinforcement continuously through them (Minton 2012).

Figure 10-5 illustrates two types of butt construction joints.
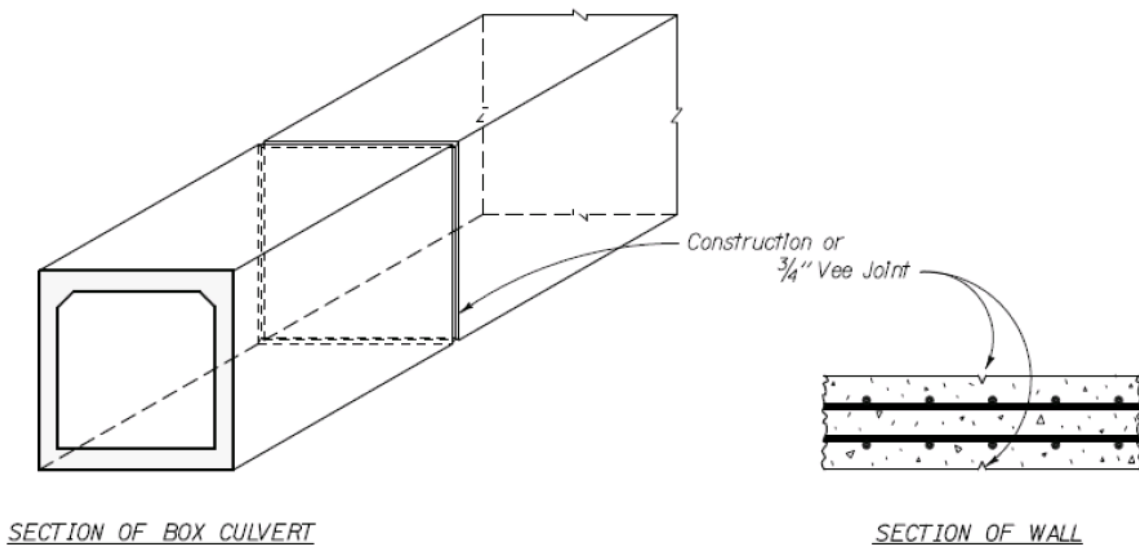
SECTION OF BOX CULVERT   SECTION OF WALL

NOTE

A ¾" Vee Joint is equivalent to and can be used instead of a Construction Joint for box culvert construction. The term Joint shall refer to either and shall be determined by the Project Engineer.

No Joint is required for box culverts up to 60 ft. long. Box culverts 60 ft. to 90 ft. long require one (1) joint, 90 ft. to 135 ft. two (2) joints, and 135 ft. to 170 ft. three (3) joints. For box culverts over 170 ft. long place joints at approximate equal intervals of not less than 40 ft. nor more than 55 ft. The joints shall be normal to the centerline of the box culvert with longitudinal reinforcing extending through the joint. Use no key or expansion material in joints.

Figure 10-4 Vee joint detail (ALDOT 2010)
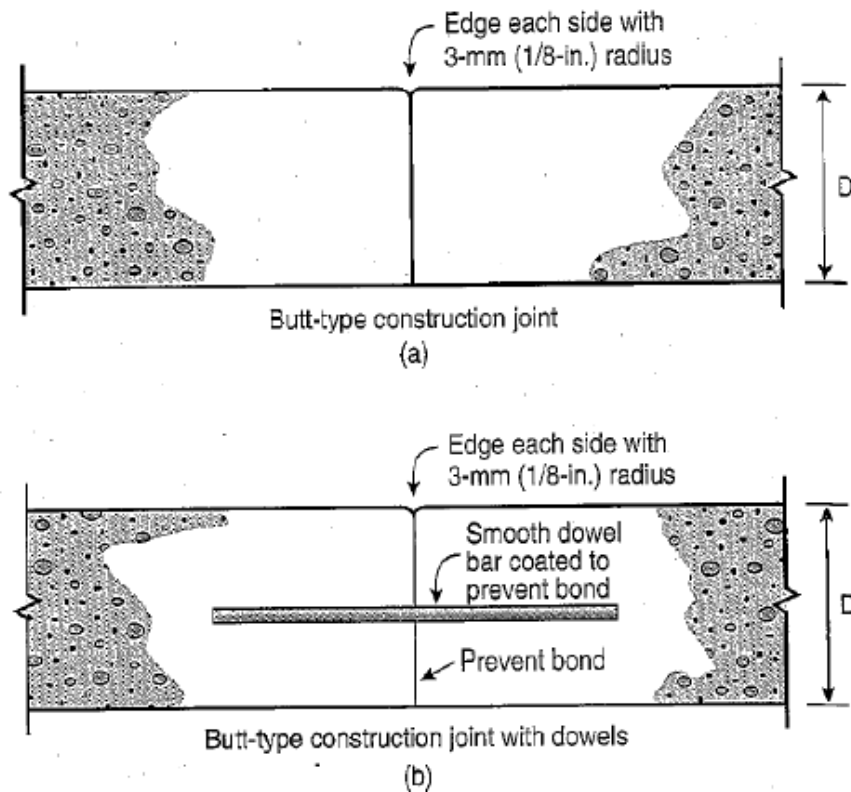
Figure 10-5 Illustration of (a) Butt construction joint and (b) Butt construction joint with dowel bars (Kosmatka et al. 2002)

10.5.2.2   *Contraction joint*

Contraction joints allow the concrete to move and allow for controlled cracking due to shrinkage and thermal stresses to occur (Kosmatka et al. 2002). The purpose of contraction joints is also to relieve the tensile stresses caused by shrinkage and thermal effects (ACI 224 1995). The function of a contraction joint to relieve stress in a long concrete wall is shown in Figure 10-6. The wall is restrained at the bottom by the footing, and this restraint produce stresses in the concrete that exceeds the tensile capacity and cause cracking.

115
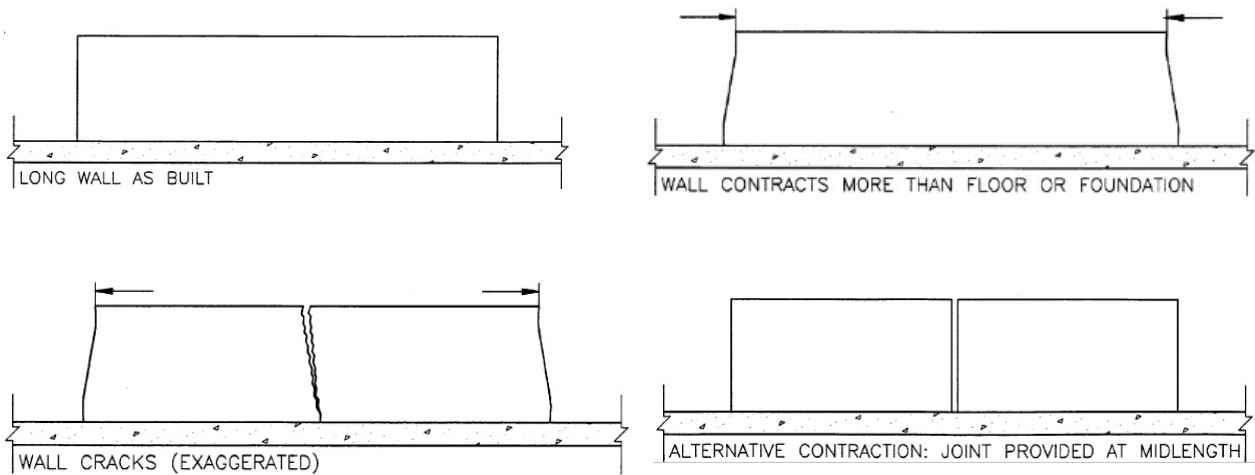
Figure 10-6 Contraction Joint Concept (ACI 224 1995)

The formation of contraction joint includes using saw cutting, or hand tooling, preformed inserts. Saw cutting is to cut a groove into hardened concrete with a saw and this should be done soon after the concrete has hardened (ACI 224 1995). A hand-tooled contraction joint is to create a groove using a hand tool to the required depth. Preformed joints are to create groove by putting wood, rubber, metal or plastic strips into concrete before finishing. For a thick floor slab, a premolded insert can be placed on the bottom of the slab, and the combined depth of the top and bottom inserts should exceed ¼ the slab depth (ACI 224 1995). The contraction joints subdivide the entire slab into smaller parts, and should be capable of transferring vertical loads from one part to the other. This load transfer can be accomplished through aggregate interlock, through a preformed key, or by the use of dowelled joint (ACI 224 1995). Figure 10-7 illustrate a saw-cut contraction joint, a contraction joint formed by a premolded strip, a contraction joint for a thick slab, and a doweled contraction joint. A keyed contraction joint from the AEB project is shown in Figure 10-8.
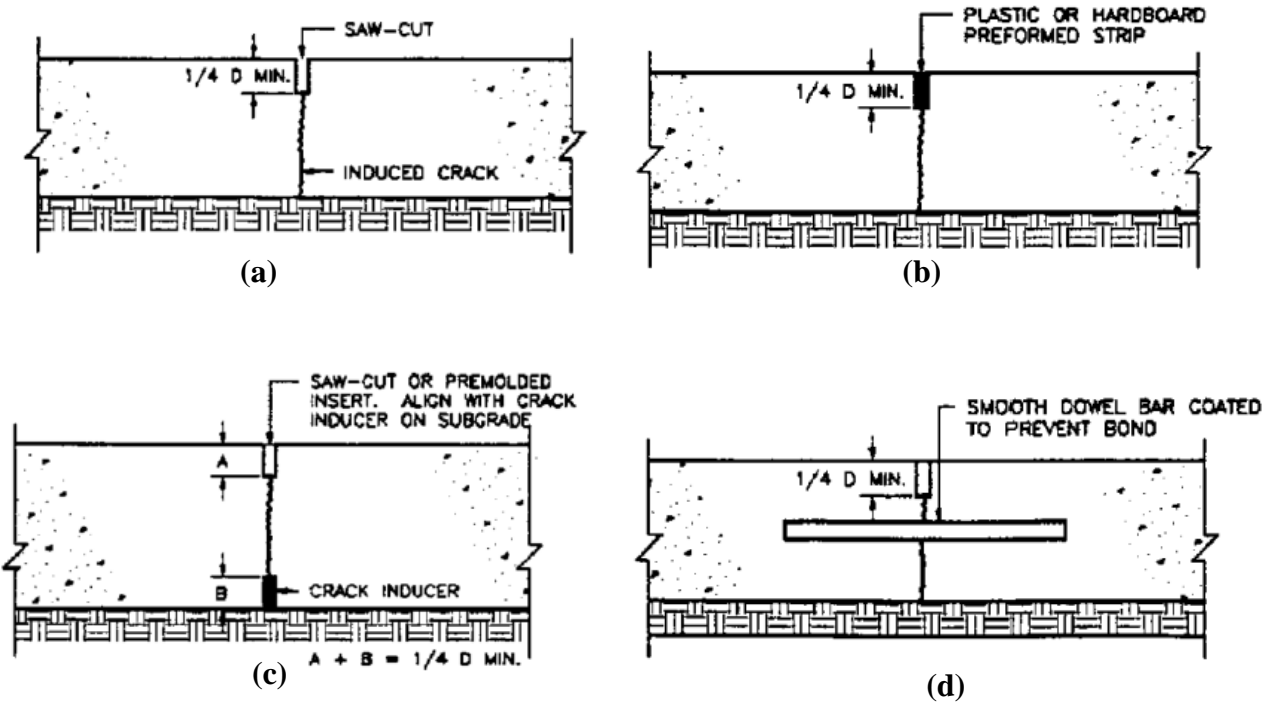
Figure 10-7 Illustration of (a) Saw cut contraction joint, (b) contration joint with a premolded insert, (c) contration joint in a thick slab, and (d) doweled contraction joint (ACI 224 1995)
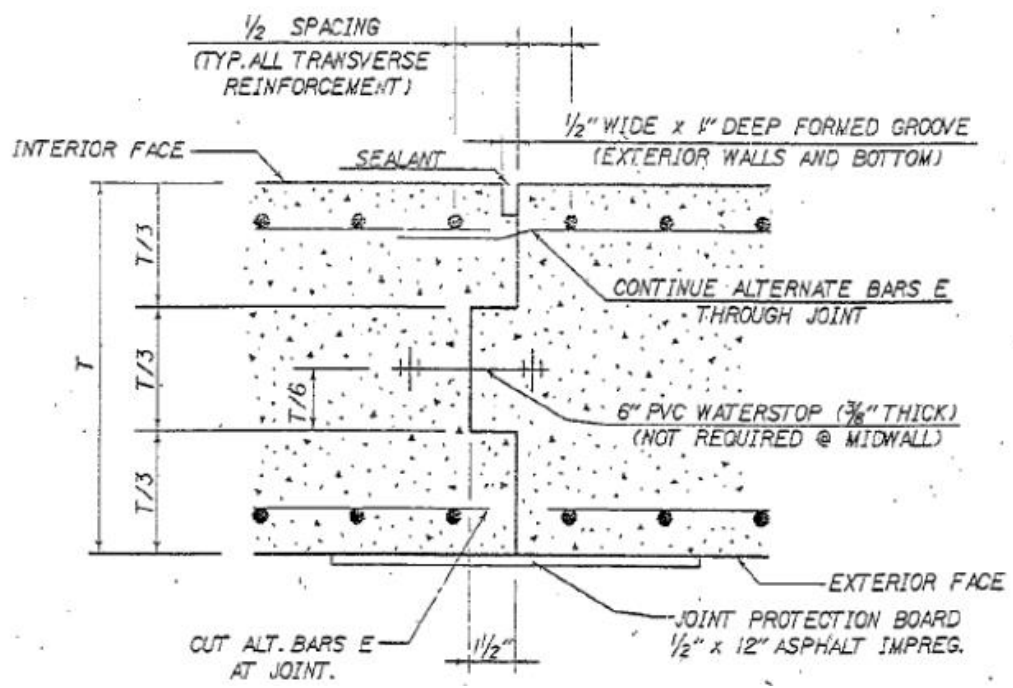

Figure 10-8 Contraction joint from the AEB project (ALDOT 2001)

117

Different contraction joint spacings are recommended in literature. Several recommendations compiled by ACI 224 (1995) for contraction joint spacing are shown in Table 10-3, and AASHTO (2010b) recommends that contraction joint spacings in tunnels be provide every 30 ft.

Table 10-3 Recommended Contraction Joint Spacings (ACI 224 1995)

Author	Spacings
Merrill (1943)	20 ft (6 m) for walls with frequent openings, 25 ft (7.5 m) in solid walls.
Fintel (1974)	15 to 20 ft (4.5 m to 6 m) for walls and slabs on grade. Recommends joint placement at abrupt changes in plan and at changes in building height to account for potential stress concentrations.
Wood (1981)	20 to 30 ft (6 to 9 m) for walls.
PCA (1982)	20 to 25 ft (6 to 7.5 m) for walls depending on number of openings.
ACI 302.1R	15 to 20 ft (4.5 to 6 m) recommended until 302.1R-89, then changed to 24 to 36 times slab thickness.
ACI 350R-83	30 ft (9 m) in sanitary structures.
ACI 350R	Joint spacing varies with amount and grade of shrinkage and temperature reinforcement.
ACI 224R-92	One to three times the height of the wall in solid walls.

10.6 BOX CULVERT CONSTRUCTION PRACTICES OF THE ALABAMA DEPARTMENT OF TRANSPORTATION

10.6.1 General Construction

The contractor shall have the choice to use either precast or cast-in-place concrete culverts if the plans do not show the required culvert type. For culverts constructed with cast-in-place concrete, the sequence of concrete placement for slabs and walls should follow the rule that the bottom slab shall be placed first and allowed to be set before the continuing construction of the walls and top

slabs (ALDOT 2012). Standard specifications for highway construction in ALDOT (2012) stated that "Culvert walls and top slab that have an overall height of 8 ft or less may be constructed with a continuous placement of concrete, while for the walls and top slab have overall height greater than 8 ft shall be constructed by separate concrete placements".

10.6.2 Required Construction Joints

All culverts longer than 60 ft should have construction joints and the spacing of the joints should be set to provide approximately equal length sections along the culvert. For culvert lengths between 60 ft and 90 ft, one construction joint will be required; for culvert lengths greater than 90 ft and less than 135 ft, two construction joints will be required; for culverts from 136 ft to 170 ft in length, three construction joints will be required; for culverts over 170 ft in length, construction joints shall be spaced at approximately equal intervals of not less than 40 ft nor more than 55 ft (ALDOT 2012).

10.7   EXAMPLES OF BOX CULVERT CRACK CONDITION SURVEY

10.7.1 Culvert C

The condition survey of AEB Culvert at 149+60 (Culvert C) performed on July 12, 2010 is reviewed in this section (Minton 2012). This culvert was built with transverse construction joints with continuous longitudinal reinforcement and the average joint spacing was 48 ft. The joint plan of this culvert was shown in Figure 10-4. The entrance of the culvert are shown in Figure 10-9.

The survey results show that the widest crack observed was 1/8 in. in the north wall at stations 308 ft 0 in. (shown in Figure 10-10) and 314 ft 0 in., and the widest joint opening was ¼ in. at station 293 ft 3 in. in the base of the culvert (Minton 2012).

Figure 10-9 Entrance of culvert C (Minton 2012)

Figure 10-10 Transverse crack in AEB culvert at 149+60 in the north wall (Minton 2012)

10.7.2 Culvert J

The survey for AEB Culvert at 240+37 (Culvert J) that performed on November 9, 2010 is reviewed in this section. This culvert was also built with construction joints with continuous

reinforcement, and the joint spacing was 50 ft. The survey results indicate that many of the cracks in this culvert had been repaired when the team visited; however, some of these cracks had begun to reopen. The widest crack was 3/16 in. wide at station 595 ft 0 in., and the widest construction joint opening was 3/16 in. at station 69 ft 0 in. in the ceiling, both walls, and the base (Minton 2012). One example of cracking in the base of Culvert J is shown in Figure 10-11. The Anniston East Bypass (AEB) Culvert at 240+37 is known as Culvert J in this study was used as baseline. The cross-section drawing of this culvert is shown in Figure 10-12.

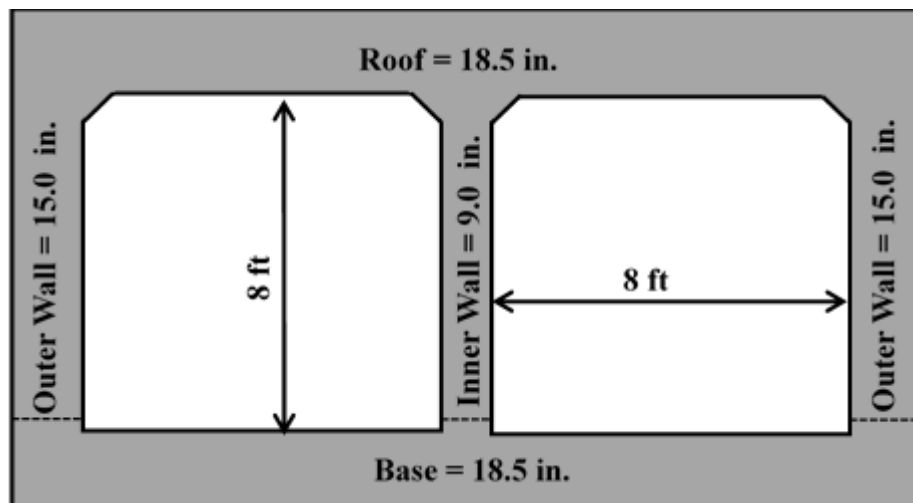**Figure 10-11 Base Crack from AEB Culvert at 240+37 (Minton 2012)**

Figure 10-12 Cross section geometry of Culvert J

10.8 SHRINKAGE EFFECTS

The loss of moisture from the concrete's cement paste phase due to differences in relative humidity causes drying shrinkage (Mehta and Monteiro 2014). Best practice is to cure concrete for at least 7 days after placement, which allows the microstructure to densify and delays the onset of drying shrinkage. So when curing is seized, the effects of drying shrinkage will be additive to the stresses caused by thermal effects.

Autogenous shrinkage is defined as the "change in volume due to chemical process of hydration of cement exclusive of effects of applied load and change in either thermal condition or moisture content" (ACI CT 2016). When the water-to-cementitious materials ratio (*w/cm*) is above 0.42, the concrete has enough water for hydration, and the stresses related to autogenous shrinkage are neglegible (Mindness et al. 2002). Since all the CIP culverts surveyed in this study had a (*w/cm*) of 0.44, the effect of autogenous shrinkage was neglected in the remained of this work.

10.8.1 Drying Shrinkage Model

Since the B3 Model is used for creep prediction purposes, the shrinkage model from Bažant and Baweja (2000) shown in Equation 10-4 to Equation 10-15 is used in this study.

Mean shrinkage strain in the cross section:

$$\epsilon_{sh}(t, t_0) = -\epsilon_{sh\infty} k_h S(t) \quad \text{(in./in.} \times 10^{-6})$$

(Equation 10-4)

$$S(t) = \tanh \sqrt{\frac{t - t_0}{\tau_{sh}}}$$

(Equation 10-5)

Where,

$\epsilon_{sh}(t, t_0) =$ is the mean shrinkage in the cross section at time t related to curing time t_0,

$\epsilon_{sh\infty} =$ is the ultimate drying shrinkage,

$k_h =$ is a humidity dependent factor, and

$S(t) =$ is the time function defining the shape of the shrinkage curve.

Humidity dependence:

$$k_h = \begin{cases} 1 - h^3 & for \quad h \le 0.98 \\ -0.2 & for \ h = 1 \ (swelling \ in \ water) \\ linear \ interpolation & for \quad 0.98 \le h \le 1 \end{cases}$$

(Equation 10-6)

Size dependence:

$$\tau_{sh} = k_t(k_s D)^2 \quad (days)$$

(Equation 10-7)

$$D = 2v/s \ (in.)$$

(Equation 10-8)

$$k_s = \begin{cases} 1.00 & for \quad an \ infinite \ slab \\ 1.15 & for \ an \ infinite \ cylinder \\ 1.25 & for \ an \ infinite \ square \ prism \\ 1.30 & for \quad a \ sphere \\ 1.55 & for \ a \ cube \end{cases}$$

(Equation 10-9)

$$k_t = 190.8 t_0^{-0.08} \overline{f_c}^{-1/4} \ (days/in.^2)$$

(Equation 10-10)

Where,

$h =$ relative humidity,

$\tau_{sh} =$ size dependence factor,

k_s = the cross-section shape factor,

v/s = volume to surface ratio of the concrete member, and

$\overline{f_c}$ = cylinder compression strength.

Time–dependence of ultimate shrinkage:

$$E(t) = E(28)(\frac{t}{4 + 0.85t})^{1/2} \qquad \textbf{(Equation 10-11)}$$

$$\epsilon_{sh\infty} = \epsilon_{s\infty} \frac{E(607)}{E(t_0+\tau_{sh})} \quad \text{(in./in.}\times 10^{-6}) \qquad \textbf{(Equation 10-12)}$$

$$\epsilon_{s\infty} = -\alpha_1\alpha_2 \left[26\omega^{2.1}\overline{f_c}^{-0.28} + 270\right] \quad \text{(in./in.}\times 10^{-6}) \qquad \textbf{(Equation 10-13)}$$

$$\alpha_1 = \begin{cases} 1.0 & for \ Type \ \text{I} \ cement; \\ 0.85 & for \ Type \ \text{II} \ cement; \\ 1.1 & for \ Type \ \text{III} \ cement. \end{cases} \qquad \textbf{(Equation 10-14)}$$

$$\alpha_2 = \begin{cases} 0.75 & for \ steam-curing; \\ 1.2 & for \ sealed \ or \ normal \ curing \ in \ air \ with \ initial \\ & protection \ against \ drying; \\ 1.0 & for \ curing \ in \ water \ or \ at \ 100\% \ relative \ humidity. \end{cases}$$

$\qquad \textbf{(Equation 10-15)}$

Where,

$E(t)$ = factor for time-dependence of ultimate shrinkage,

$\epsilon_{s\infty}$ = a constant depend on water-cement ratio and compression strength,

ω = water-to-cement ratio,

124

α_1 = cement type dependence factor, and

α_2 = curing condition dependence factor.

10.9   CREEP EFFECTS

Creep is the time-dependent increase in strain when concrete is subjected to sustained stress. Often the time-dependent response of concrete is expressed in terms of compliance, that includes both elastic and time-dependent deformations (i.e. creep effects) (ACI 209 1992). The Modified B3 Model (Byard and Schindler 2015) discussed in Section 4.6.2 is used in this study to describe the creep effect on early-age concrete stress development. The work in Part I concluded that the Modified B3 Model is the most accurate model to predict early-age concrete stress development compare to other three models evaluated in Part I.

10.10   EFFECT OF REINFORCEMENT

The effect of reinforcement on hardening concrete structure is generally understood as follows: 1) in uncracked concrete at early ages subjected to thermal effects, the concrete and reinforcing bars experience similar deformations due to their similar coefficient of thermal expansion: 2) at this stage the concrete is not restrained by the reinforcing bars (Bjøntegaard 2011).

Sule and Breugel (2004) performed experiments to study the effect of reinforcement on early-age cracking due to autogenous shrinkage and thermal effects. Their results show that early-age concrete and reinforcement bars experienced similar deformations caused by the heat of hydration due to their similar coefficient of thermal expansion; and the effect of reinforcement on early-age concrete cracking is to avoid a big wide crack and to help redistribute the one big through crack into several smaller cracks (Sule and Breugel 2004). An example test result is presented in Figure 10-13, and it shows that the stress development of reinforced and the plain concrete is about the

same; therefore, the reinforcement does not influence the stress in concrete until after cracking occurs.

ACI 224 (1995) also stated that "Reinforcement in the culvert wall resist tensile stresses that develop in the wall. Cracking cannot be prevented by reinforcing the wall, but the widths of cracks that do form can be controlled".
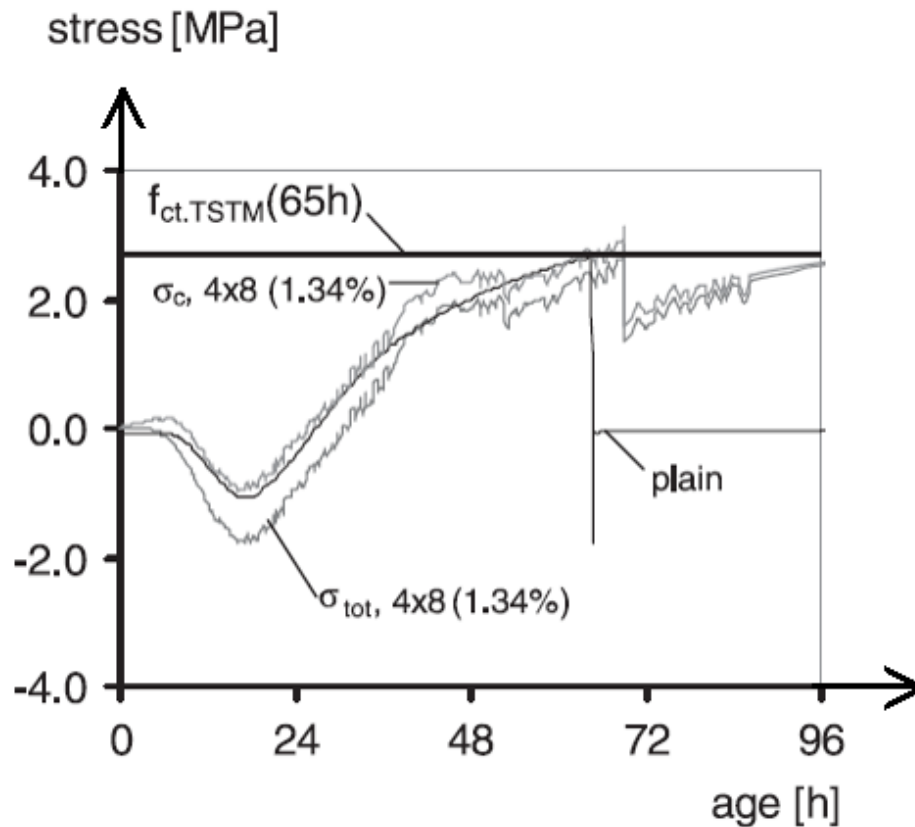

Figure 10-13 Stress development in NSC-specimens reinforced with four rebars compared to a plain specimen under semi-adiabatic curing condition (Sule and Breugel 2004)

This study is focused on determining when the first crack occurs, the location of the first crack, and the portions of concrete with the highest tensile stress and thus high cracking possibility, not to find the effect of reinforcement on limiting the crack width. Before cracking, the reinforcement

neither influences the tensile stress development in concrete nor affects the time of first cracking; however, post-cracking it does play a role to distribute cracks and control crack widths. Therefore, based on this behavior, neglecting the effect of reinforcement in this study is a reasonable assumption considering that this part of the dissertation's primary objective is to determine means to mitigate early-age cracking in CIP culverts. FEM with reinforcement is future work that could be done to determine the effect of reinforcement to control crack widths.

10.11 EXTERNAL RESTRAINT

Common examples of continuous external restraint are concrete slabs cast on rock/soil and walls cast on hardened slab/foundation. Figure 10-14 shows the degree of restraint at middle of the concrete member depending on the height above the base and the slenderness ratio L/H. The degree of restraint varies with the length-height ratio (L/H) and the distance to the bottom of the member. By locating the L/H and the approximate location of the wall, the restraint ratio can be found. The lower part of the walls are highly restrained while the degree of restraint is decreasing going upward and outward. The figure also shows that the restraint is generally high for a long wall (high L/H ratio), while for the shorter wall (low L/H ratio) the high restraint is only around the lower mid part of the wall.

For a concrete member with continuous external restraint, cracking will initiate at the base or restrained edge where the restraint ratio is the highest, and progress upward or outward until a location where the stress is insufficient to for the crack to continue (ACI 207.2R 2007). This type of crack is a through crack that cuts through the thickness of the wall, instead of a surface crack. Some of these cracks can extend through the entire height of the wall and may be wide (ACI 207.2R 2007).

Based on several 3D-analyses stated in Kanstad et al. (2001), the ratios for the degree of restraint were provided for typical restraint conditions: 1) Slab to slab: R = 0.05-0.52; 2) Wall on slab: R = 0.37-0.70; 3) Top slab on wall: R = 0.12-0.52.
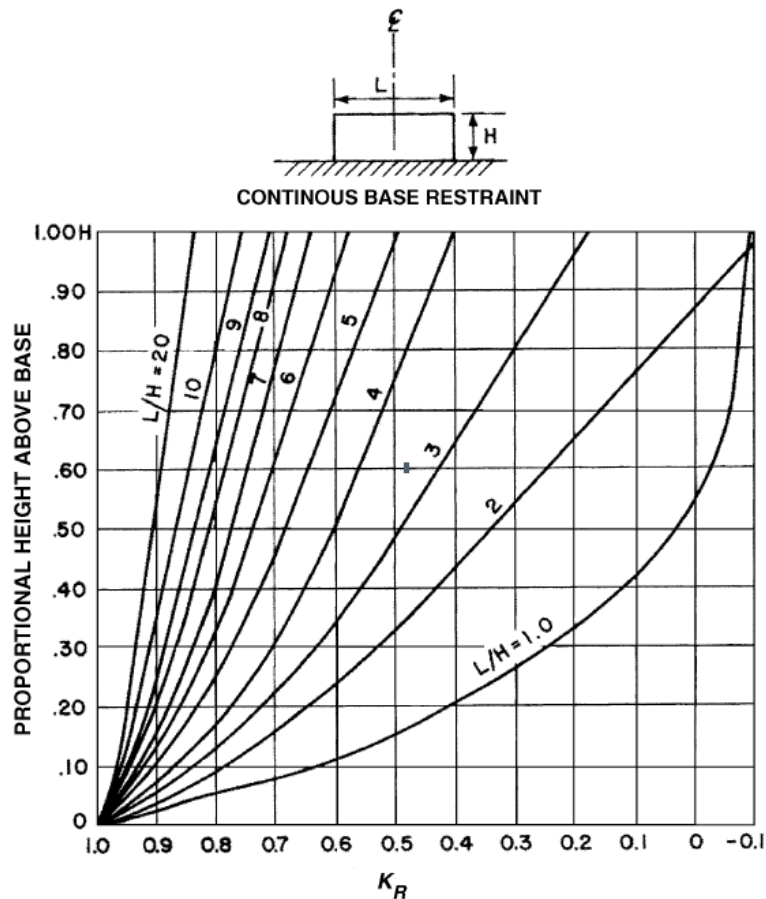

Figure 10-14 Degree of tensile restraint at center section (ACI 207.2 R 2007)

The influencing factors for the degree of external restraint in a hardening concrete wall are as follows (Bjøntegaard 2011):

1. Stiffness (Modulus of elasticity an cross-section area) of the restraining structure;

2. The geometry of the structure (length to height ratio L/H) effects the stress; distribution over the length and height of the member;

3. Joint-end slip failure decreases the degree of restraint, which is relatively difficult to simulate; and

4. The flexibility and stiffness of the ground (soil, rock, etc.) which restrains the wall.

10.12 ASSESSMENT OF CRACKING RISK

The cracking failure criterion for the model was based on the tensile stress-to-strength ratio (Equation 10-16) as presented by Riding et al. (2014). The cracking risk classification is based on a probability density function, which was obtained from the distribution of the tensile stress-to-strength at cracking from experimental data. Figure 10-15 shows one example of classification system of cracking probability, which classify a low, medium, high and very high cracking probability based on the cracking probability ranges of 0~25%, 25%~50%, 50%~75% and 75%~100%. When the tensile stress-to-strength ratio is above 0.67, the cracking probability was 75 percent, and at this ratio the cracking risk was defined as being at a "high" level (Riding et al. 2014).

$$\eta^{max} = \left[\frac{\sigma_t(t)}{f_{ct}^*(t)}\right]^{max}$$ **(Equation 10-16)**

Where,

η^{max} = the maximum cracking potential in the concrete member during the whole analysis time,

$\sigma_t(t)$ = the tensile stress (psi) in the concrete member at time t, and

$f_{ct}^*(t)$ = the tensile strength of the member at time t.

Kanstad et al. (2002) also used FEM and found that when the tensile stress-to-strength ratio was

in the range of 0.75 to 0.88, all walls of the 1115 ft long Maridal culvert in Norway showed 1 to 4
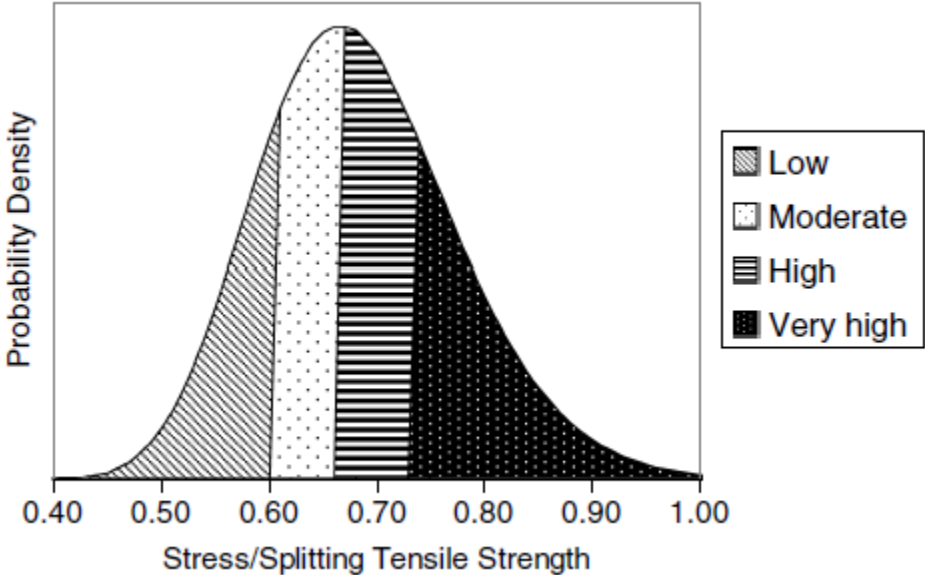
cracks in each 50 ft long section.

Figure 10-15 Cracking probability categories for stress to estimated splitting tensile

strength ratios (Riding et al. 2014)

CHAPTER 11 PART II: FINITE-ELEMENT MODELING OF CULVERTS

To simulate the early-age stress development of concrete of a cast-in-place culvert structure, the finite-element method is adopted here to account for the temperature development, changing mechanical properties of concrete, creep effects, drying shrinkage, and restraint of the culvert structure. The temperature history of the concrete from placement is simulated in a program called ConcreteWorks, and the results are used as inputs for the subsequent stress calculation in another finite-element program (ABAQUS). Creep and shrinkage effects are incorporated in the finite-element program based on the mathematical models covered in Chapter 10. The construction sequence and restraint conditions of the culvert structure are simulated based on as-built conditions

11.1 CONCRETE TEMPERATURE PROFILE

The concrete temperature profile used for the stress calculation in the FEM was obtained from ConcreteWorks, which is an early-age concrete temperature development and thermal stress analysis software (Riding 2007). The software is capable of analyzing environmental, construction, and concrete mixture proportions parameters in various types of concrete elements (Riding 2007).

11.1.1 ConcreteWorks Software

The concrete temperature profile used for the stress calculation in the FEM was obtained from ConcreteWorks, which was developed at UT Austin and is utilized by TXDOT and some other states (Poole et al. 2006). It is an early-age concrete temperature development and thermal stress analysis software which is capable of modeling the temperature history of concrete elements considering the geometry of the elements, concrete mixture proportioning, type of aggregates used, chemical composition of cementitious materials, environmental temperatures, weather conditions (including humidity, solar radiations, and wind speeds), and type of formwork used (Riding 2007).

It is a user-friendly software package for the design, analysis, and performace prediction of structural concrete, such as mass concrete, bridge decks, concrete pavements, and precast concrete members. ConcreteWorks can be downloaded freely from TxDOT website and the latest ConcreteWorks operator's manual is provided in (Riding et al. 2017).

The ConcreteWorks inputs are divided in nine main categories as listed in Table 11-1. When some inputs are not available, default values in the program can be used (Concrete Durability Center 2005). After entering all inputs and performing the analysis, the program will output predicted short-term temperature development profiles for many locations throughout the entire concrete element.

Table 11-1 ConcreteWorks Input Categories (Concrete Durability Center 2005)

Input Category	Specific Inputs
General	Time, date, and location of placement Duration of analysis (1-14 days)
Shape	Type and shape of element
Dimensions	Member dimensions specific to element shape
Mixture Proportions	Batch weights and properties of all materials
Material Properties	Chemical composition, hydration properties of element Type of aggregates used and corresponding CTEs
Mechanical Properties	Maturity function, equivalent age, and early-age creep inputs
Construction	Placement temperature, formwork type, method and duration of curing
Environment	Ambient weather data like temperature, wind and humidity
Corrosion	Details about reinforcing steel used

11.1.2 Temperature Results from ConcreteWorks

The concrete temperature profiles for summer, fall, and winter placement conditions were determined for Montgomery, Alabama, on construction dates of July 30th, October 15th, and

December 15th, respectively. Figure 11-1 to Figure 11-3 show the temperature profiles for normalweight concrete placed in summer, fall and winter seasons. Figure 11-4 and Figure 11-5 show the temperature profiles for SLW and ALW concrete placed in summer condition, respectively. The maximum temperature in concrete for the summer, winter and fall placement could reach 147 °F, 118 °F, and 86 °F, respectively. The ambient temperature approximately ranges from 68-86 °F, 50-77 °F, and 41-54 °F for the summer, winter, and fall placement.

To compare the temperatures in different concretes all placed in the summer, the maximum temperature in normalweight concrete, SLW concrete, ALW concrete is 147 °F, 154 °F, 163 °F. From these temperature results, it is shown that under the same ambient temperature, the maximum in-place concrete temperatures increased from normalweight concrete to lightweight concrete. Tankasala and Schindler (2017) also had the same conclusion that the maximum in-place concrete temperature increased as more lightweight aggregates were used in the concrete. Although LWAs in concrete increase the maximum concrete temperature, they could still improve the concrete's resistance to early-age cracking. This is because LWA concrete has a lower modulus of elasticity, coefficient of thermal expansion, and these properties contribute to improve the concrete's resistance to early-age cracking (Tankasala and Schindler 2017). These results will be verified in the following sections when the effects of different concrete types on concrete cracking will be studied.
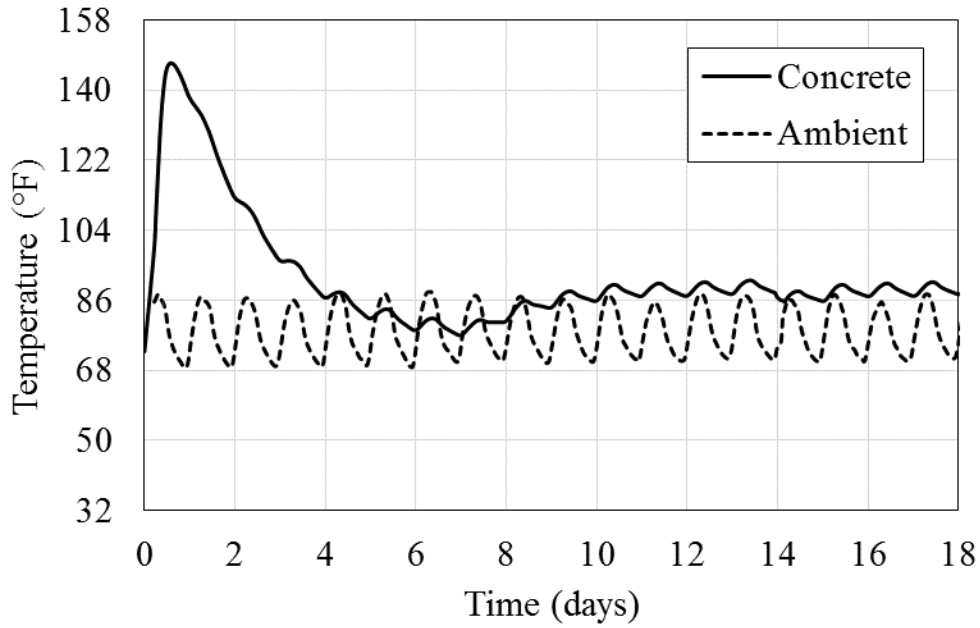
Figure 11-1 Summer placement temperatures (Normalweight concrete used in Culvert J)
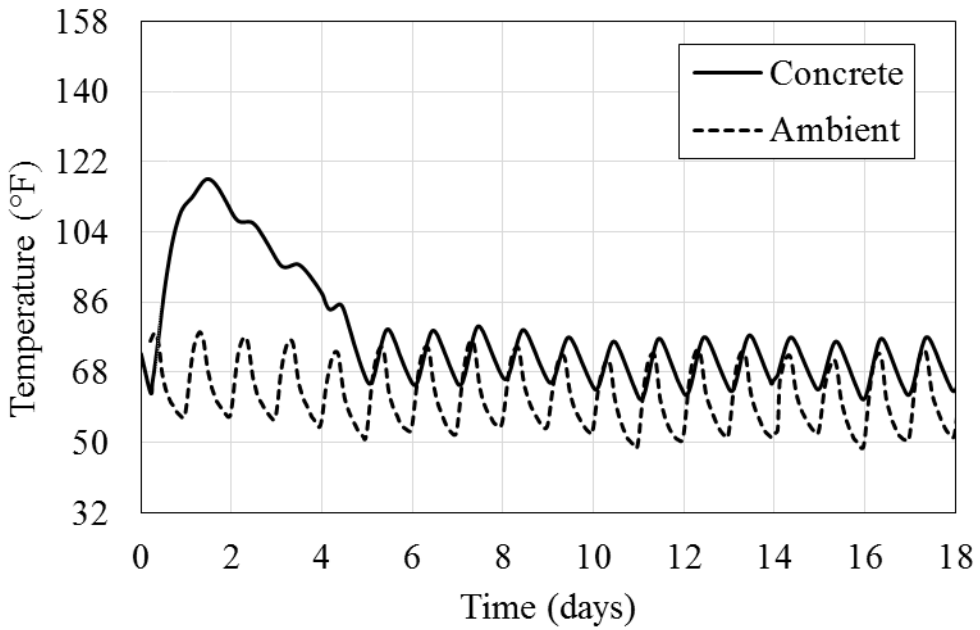

Figure 11-2 Fall placement temperatures (Normalweight concrete used in Culvert J)
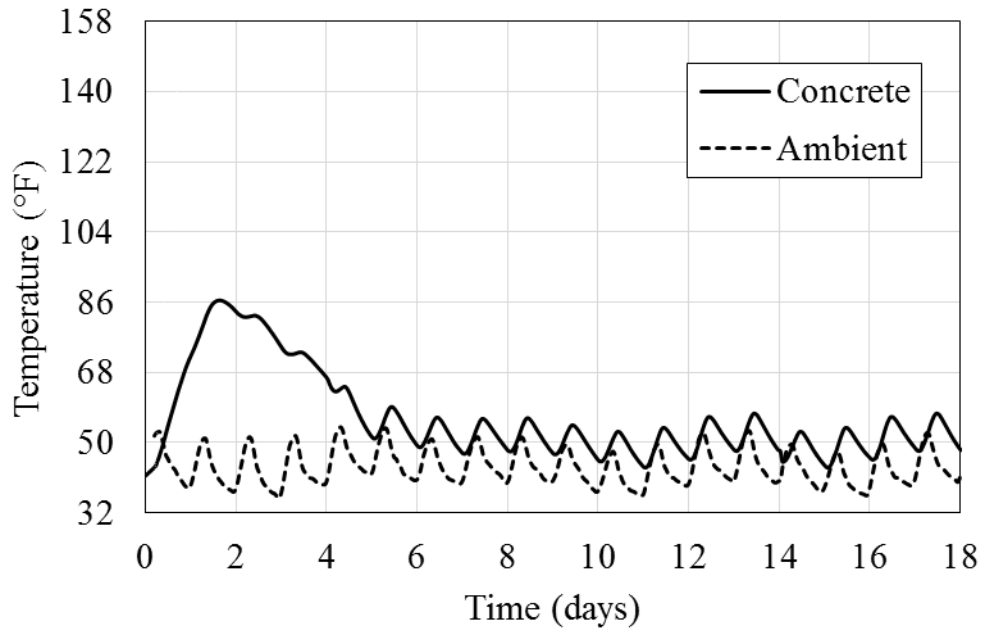
Figure 11-3 Winter placement temperatures (Normalweight concrete used in Culvert J)
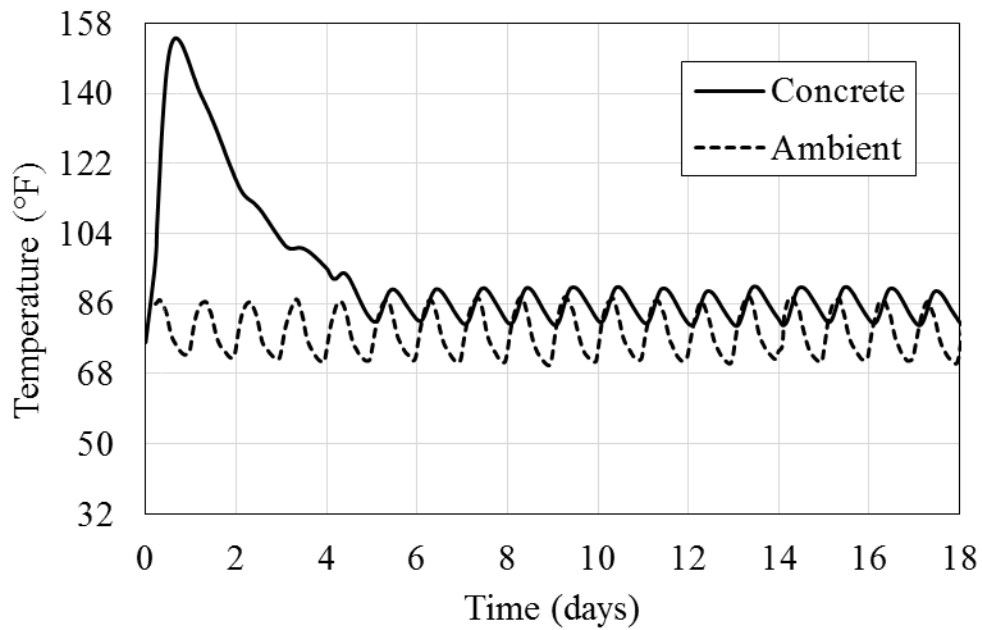

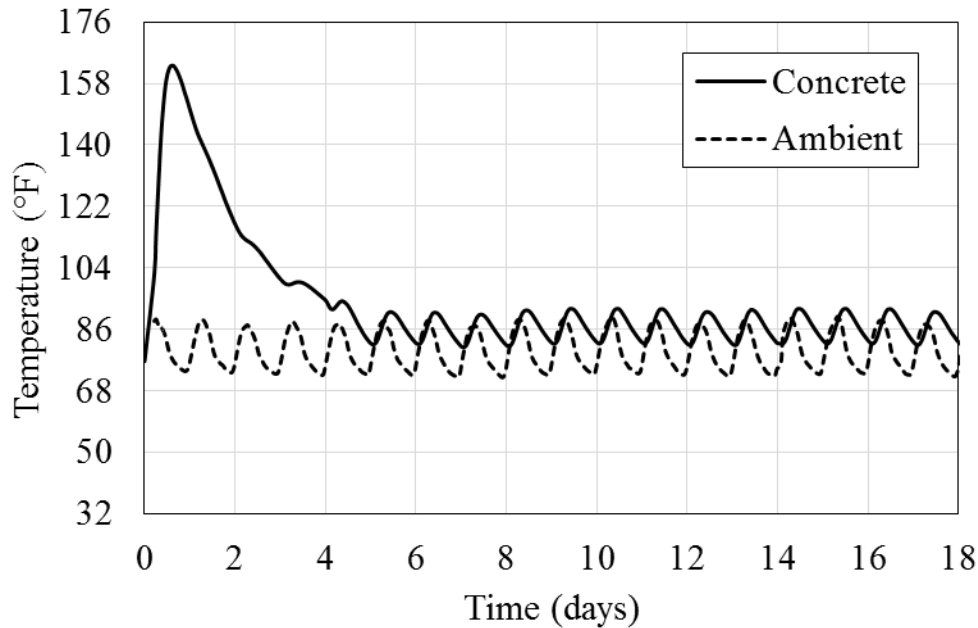**Figure 11-4 SLW concrete temperatures when placed under summer conditions**

Figure 11-5 ALW concrete temperatures when placed under summer conditions

11.2   INCORPORATING CREEP EFFECTS IN THE FEM

The Modified B3 Model was verified to accurately predict the early-age concrete stress development in Part I of this dissertation. Details of incorporating the creep model into the finite-element program has been discussed in Section 6.1.

11.3   INCORPORATING THERMAL AND DRYING SHRINKAGE EFFECTS IN THE FEM

The user-subroutine UEXPAN in ABAQUS was used to calculate incremental thermal strains as function of concrete temperature (Dassault Systèmes Simulia Corp. 2012). This subroutine can be used to define incremental thermal strains as functions of temperature, predefined field variables, and state variables.

The concrete coefficient of thermal expansion was used to calculate the thermal strain for each time step based on the concrete temperature change that occurred during the time step. The drying shrinkage model discussed in Section 10.8.1 was also coded into this subroutine by using the concrete properties. The total strain change due to thermal and shrinkage effects was then obtained and used to determine the stress increment at each time step.

11.3.1 Shrinkage Model Verification in FEM

A given concrete example was used to check the drying shrinkage code in ABAQUS. A prismatic concrete member with dimension of $3 \times 4 \times 12$ in. was simulated in the FEM. The properties of this given concrete are: 1) Type 1 cement concrete; 2) age when drying begins, t_0 =28 days; 3) relative humidity, h = 90%; 4) cylinder compressive strength, $\bar{f_c}$ = 4000 psi; 5) volume to surface ratio, v/s = 0.75 in.; 6) water content of concrete, w =8.23 lb/ft^3; 7) water-cement ratio, w/c =0.6; 8) k_s = 1, (for infinite slab); 9) α_1 = 1.0 (for Type I cement); 10) α_2 = 1.2 (for normal curing in air with initial protection against drying); and 11) calculating the drying shrinkage of concrete at age t =112 days.

The analytical calculations of drying shrinkage based on the shrinkage model in Section 10.8.1 are as follows:

$$D = \frac{2v}{s} = 2(0.75) = 1.5 \qquad \text{(Equation 11-1)}$$

$$k_t = 190.8 t_0^{-0.08} \bar{f_c}^{-1/4} = 190.8(28)^{-0.08}(4000)^{-1/4} = 18.377 \qquad \text{(Equation 11-2)}$$

$$\tau_{sh} = k_t(k_s D)^2 = 18.377(1 \times 1.5)^2 = 41.35 \qquad \text{(Equation 11-3)}$$

$$\epsilon_{s\infty} = -\alpha_1\alpha_2 \left[26\omega^{2.1}\overline{f_c}^{-0.28} + 270 \right] \quad \text{(Equation 11-4)}$$
$$= -1.0 \times 1.2[26 \times 8.23^{2.1}4000^{-0.28} + 270]$$
$$= -579.8 \ (\times 10^{-6}in./in.)$$

$$E(t) = E(28)(\frac{t}{4 + 0.85t})^{1/2} \quad \text{(Equation 11-5)}$$

$$\epsilon_{sh\infty} = \epsilon_{s\infty}\frac{E(607)}{E(t_0 + \tau_{sh})} = -579.8\frac{1.0804}{1.0496} = 596.8 \ (\times 10^{-6}in./in.) \quad \text{(Equation 11-6)}$$

$$S(t) = \tanh\sqrt{\frac{t - t_0}{\tau_{sh}}} = \tanh\sqrt{\frac{112 - 28}{41.35}} = 0.8907 \quad \text{(Equation 11-7)}$$

$$k_h = 1 - h^3 = 0.271 \quad \text{(Equation 11-8)}$$

$$\epsilon_{sh}(t, t_0) = -\epsilon_{sh\infty}k_hS(t) = -(-596.8) \times 0.271 \times 0.8907 \quad \text{(Equation 11-9)}$$
$$= 144 \ (\times 10^{-6}in./in.)$$

Therefore, the drying shrinkage for this concrete at the age of 112 days is 144×10^{-6} in./in.. These calculations were also done in Excel, with the concrete age from 28 days to 112 days, and the calculated drying shrinkage with time is plot in Figure 11-6. A concrete model was simulated in FEM with the parameters of the above example concrete, and the drying shrinkage development with time is also plot in in Figure 11-6. The drying shrinkage strain at 112 days from FEM is 144×10^{-6} in./in.. By comparing these two results, it is confirmed that the code in ABAQUS for drying shrinkage is ready to be used.
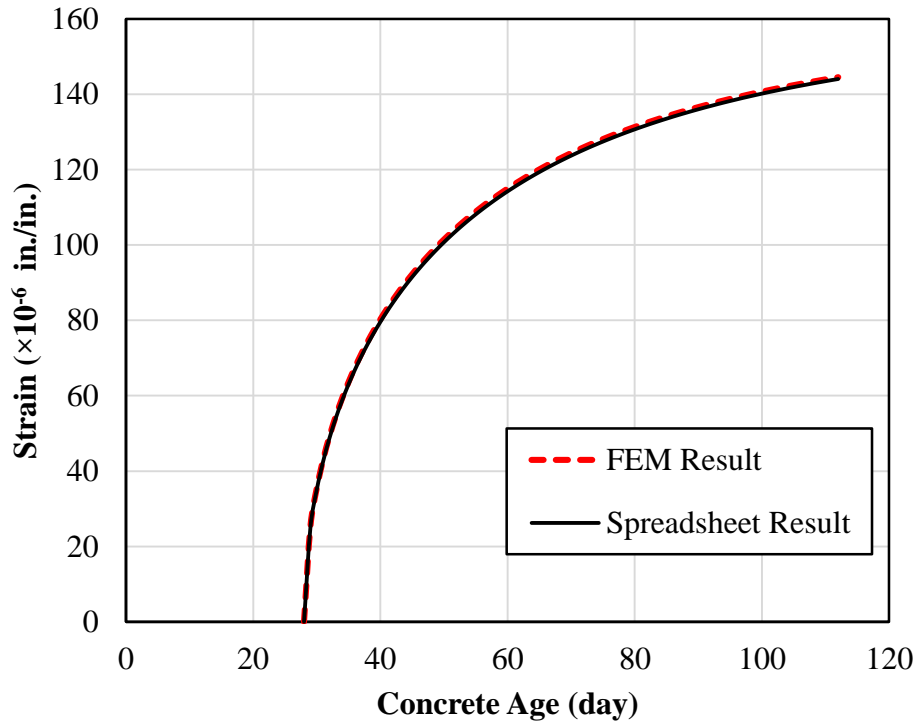
Figure 11-6 Drying Shrinkage Result

The concrete properties for the culverts were used to calculate the parameters for the drying shrinkage model in the FEM subroutine UEXPAN. Culvert base and wall have different dimensions, thus different volume-to-surface ratios (V/S). The smaller ratio was calculated to result in greater drying shrinkage. The volume-to-surface ratios of the base and wall for Culvert J based on its dimension shown in Figure 10-12, were calculated to be 8.33 and 6.37, respectively. The drying shrinkage resulted from these two ratios for the same age differ within 10%. Therefore, a constant volume-to-surface ratio of 6.37 was applied to all the culvert components for simplicity.

11.4   CULVERT MODEL MATERIAL PROPERTIES

The mixture proportions and other parameters of the concrete used for Culvert J are presented in Table 11-2. The effect of using different types of concrete will be studied in the following section.

Table 11-3 and Table 11-4 provide the properties of all-lightweight concrete (ALW) and sand-lightweight concrete (SLW) selected from Byard (2011). An average environmental humidity of 70% and start of exposure to drying at an age of 7 days was used for the drying shrinkage model.

Table 11-2 Concrete Properties of Culvert J (Minton 2012)

Parameter	Value	Parameter	Value
Water (lb/yd^3)	275	*w/cm*	0.44
Type I/II Portland Cement (lb/yd^3)	465	28-day Compressive Strength (psi)	4,000
Class C Fly Ash (lb/yd^3)	155	28-day Modulus of Elasticity (ksi)	3,600
No.67 Limestone (lb/yd^3)	1,857	Activation Energy (J/mol)	40 k
Fine Aggregate (lb/yd^3)	1,283	Coefficient of Thermal Expansion (/°F)	5.5×10^{-6}
Total Air Content	4 to 6%	Initial Set (hours)	5.0

Table 11-3 Properties of concrete for SLW (Shale 0.42 SLW Fall) [Byard 2011]

Parameter	Value	Parameter	Value
Water (lb/yd^3)	276	*w/cm*	0.42
Type I portland cement (lb/yd^3)	658	28-day Compressive strength (psi)	5,040
SD Shale Lightweight Coarse Aggregate (lb/yd^3)	933	28-day Modulus of elasticity (ksi)	3,190
SSD Normalweight Fine Aggregate (lb/yd^3)	1354	Activation Energy (J/mol)	41,520
Total air content	5.50%	Coefficient of Thermal Expansion (/°F)	5.2×10^{-6}
		Initial set (hours)	5.28

Table 11-4 Properties of concrete for ALW (Shale 0.42 ALW Fall) [Byard 2011]

Parameter	Value	Parameters	Value
Water (lb/yd^3)	276	*w/cm*	0.42
Type I Portland cement (lb/yd^3)	658	28-day Compressive Strength	4780
SD Shale Lightweight Coarse Aggregate (lb/yd^3)	948	28-day Modulus of elasticity (ksi)	2370
SD Shale Lightweight Fine Aggregate (lb/yd^3)	908	Activation Energy (J/mol)	41,520
Total air content	5.50%	Coefficient of Thermal Expansion (/°F)	4.0×10^{-6}
		Initial set (hours)	5.52

11.5   STAGED CONSTRUCTION OF CULVERT COMPONENTS

Since the culvert base is cast first and the wall and roof are cast later, and more culvert sections are also later constructed, the parts of the culvert concrete have different ages and thus different mechanical properties, creep, shrinkage, and temperature effects. ABAQUS has the ability to carry out multiple analysis steps over time, and the items such as loads, boundary conditions, and active elements can be changed at each step. The whole model was divided into several analysis steps to account for each construction stage. The sequential stages used to simulate the construction of a culvert were modeled by initially creating all elements of the FEM in the model definition, deactivating the parts not needed in the initial step, and then progressively reactivating them in desired steps. Therefore, their ages are corrected as needed to simulate when they are cast. The ABAQUS keyword that enables this feature is *Model Change, Remove/Add* (Dassault Systèmes Simulia Corp. 2012a).

11.6   MODELING OF GROUND RESTRAINT

A tie constraint connects two separate surfaces together so that there is no relative motion between them, and this restraint can fuse two regions even though the meshes created on the surfaces of the regions may be dissimilar (Dassault Systèmes Simulia Corp. 2012a). With this constraint, the master surface and slave surface are defined, the translational degrees of freedom of the slave surface are eliminated (the elimination of the rotational degrees of freedom is optional), and each node on the slave surface will experience the same motion as its closest node on the master surface. Therefore, it was used to connect previously cast concrete surfaces to newly cast concrete surfaces, such as the top surface of culvert base and the bottom surface of culvert walls, and the first base section and the second base section, except where a contraction joint was used to separate the movements between sections.

Three-dimensional modeling of culvert involves characterizing of the bond between the structure and the ground, and realistic modeling of the ground requires many parameters that should be obtained by laboratory tests or situ tests. Therefore, a simplified model where the ground is regarded as elastic material was used here. The elastic deformation of the ground can be modeled by elastic springs or interface elements.

Culverts in Alabama are typically constructed on a crushed stone subbase, and spring elements were used to model the behavior at this interface. Several studies on the frictional behavior of concrete pavement and various subbases show the relationship is nonlinear with an elastic stiffness followed by a plastic response. Wesevich et al. (1987) report an elastic stiffness value of 220 psi/in. for concrete on ¾ in. (19 mm) crushed stone. Jeong et al. (2014) performed push-off field test of a concrete slab with dimension of 30×39×8 in. cast on various subbase types and reported an elastic stiffness of frictional resistance of approximately 507 psi/in. for crushed-stone subbase, and this value was used in this FEM.

11.6.1 Spring Element

Spring elements can couple a force with a relative displacement, and they can be linear or nonlinear. The springs can be specified to connect two nodes, acting in a fixed direction, or connect a node and the assumed ground. The linear spring behavior can be specified with a constant stiffness (force per relative displacement), and the nonlinear spring can only be defined in ABAQUS INPUT file (not supported in ABAQUS/CAE) with several points to define the nonlinear spring force-relative relationship curve.

In the present work, the interface between the concrete base and the ground was modeled by spring elements. The vertical spring is capable of supporting only compression in the contact normal

direction, and zero spring stiffness was assigned (no tension resisted) when the culvert base lifts

up from the subbase. The horizontal or tangential stiffness was realized by linear springs with a

constant stiffness of 507 psi/in.. The effective stiffness value of each element was calculated and

input based on the total number of springs assigned and the total area of bottom of the culvert base.

11.6.2 Friction Stiffness Effect on Stress in Culvert Base and Wall

The culvert may be cast on different subbase conditions, such as soil, crushed stone, clay, and so

on. The friction resistance of concrete on various subbases would be different. The tests results of

the friction resistance of various subbases are shown in Figure 11-7 and Figure 11-8. The curve

with 3/4" Gravel in Figure 11-7 and the curve with Aggregate in Figure 11-8 both represent a

concrete slab on a crushed stone subbase. Therefore, the effect of the friction stiffness on the stress

in culverts is studied in this section.
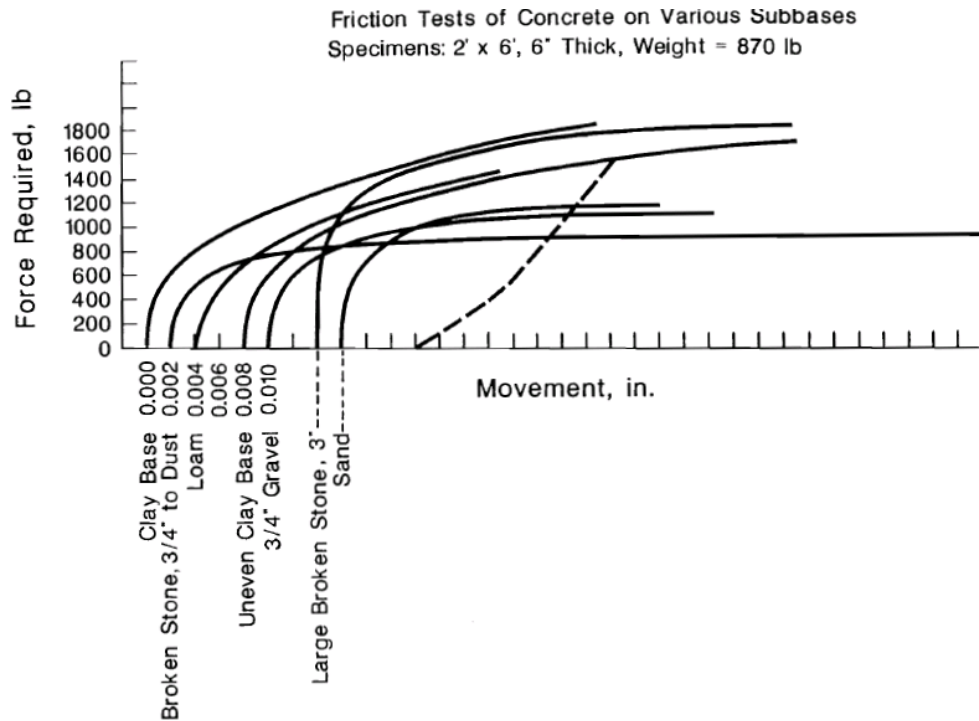
Figure 11-7 Curves showing movement versus force of test slabs on different subbases

(Goldbeck 1924)

144
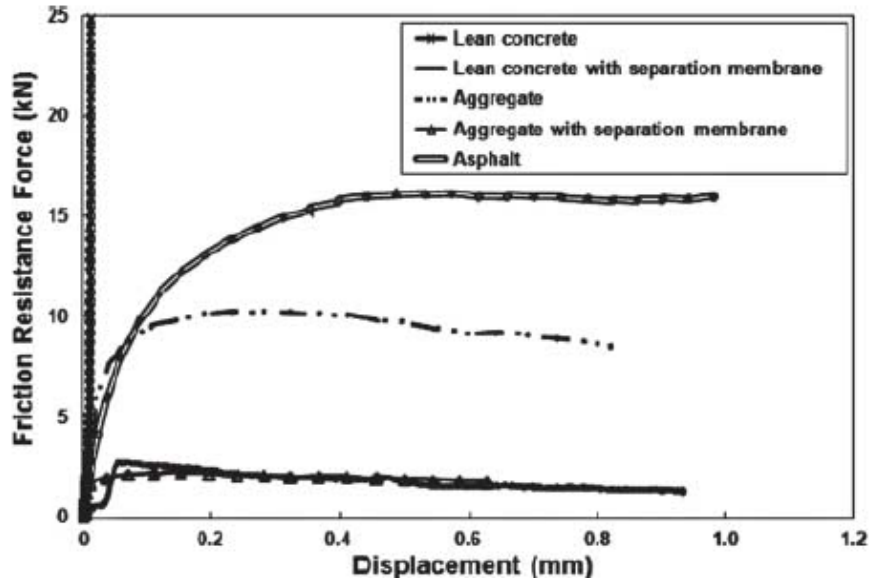
Figure 11-8 Displacement versus force of test concrete slabs on different subbases (Jeong et al. 2014)

For concrete structures resting on the ground, horizontal friction resistance occurs on the contact area and are usually represented by nonlinear behavior. The nonlinear relationship of friction resistance with displacement is usually approximated by a bilinear curve shown in Figure 11-9. Jeong et al. (2014) used this bilinear friction resistance force-displacement relationship in the finite element model of a concrete slab on different subbases, and compared the FEM results with the push-off field tests. Bosnjak (2000) also used this bilinear function for three different friction stiffnesses in a finite element model of a culvert wall on ground, and studied the influence of the friction on the restrained stress in culvert walls. Kim et al. (2000) also used the bilinear function for the bond behavior of reinforced concrete pavement and the ground in the FEM to study early-age cracking due to changes in temperature and drying shrinkage.

Force

Displacement
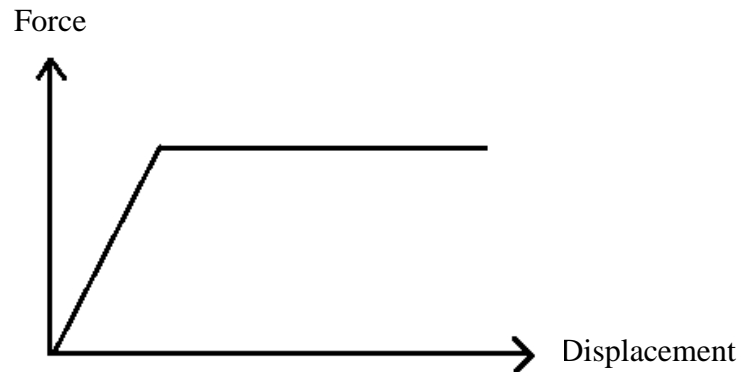
Figure 11-9 Bilinear friction stiffness

Figure 11-10 shows the test result of concrete slabs on various ground materials, the curve with 3*SW (which means the pushing force is three times slab self-weight) shows that there are unloading and reloading parts. When the load is unloading, the path is approximately parallel to the initial elastic stage. Since the temperature change leads the concrete to expand when concrete temperatures increase, and shrink when the temperatures decrease, there is a stage similar to having stress in a reverse direction or like unloading. Therefore, the bilinear curve to describe the friction behavior for concrete experience expansion and shrinkage is not accurate, and a hysteretic behavior should be developed to accurately simulate the nonlinear friction while accommodating unloading.
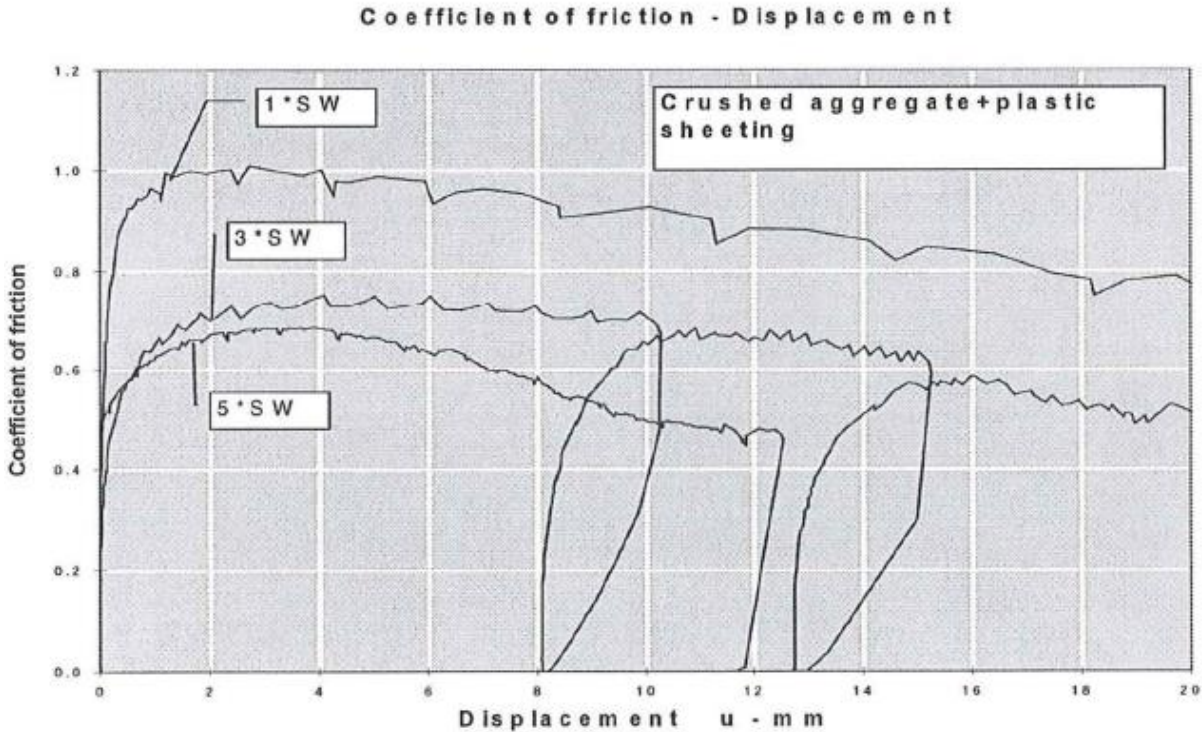
Figure 11-10 Frietian curve for test specimens on crushed aggregate covered with plastic sheeting (Kader 1999)

If a bilinear function is defined for the spring element in ABAQUS and unloading happens, it will follow the curve backward directly without the hysteretic behavior. Because of the complexity of nonlinear hysteresis behavior between the base and subgrade, a linear spring was used for the *horizontal* connection to simulate the frictional resistance, which leads to conservative estimates of concrete stresses. For the *vertical* connection between concrete base and subgrade, a constant spring stiffness of 1520 psi/in. was used when the spring elements experience compression, and zero spring stiffness was assigned (no tension resisted) when the culvert base lifts up from the subbase.

CHAPTER 12 PART II: FEM RESULTS

Culvert J is one of the culverts that exhibited extensive cracking on the AEB Project and was used as baseline model for the FEM. It has a total length of 892 ft with tied-construction joints (with continuous longitudinal reinforcement) every 50 ft (Minton 2012). Eight-node linear hexahedral (brick) elements with three translational degrees of freedom at each node (C3D8) were used. The three-dimensional FEM of one 50 ft section of Culvert J is shown in Figure 12-1. The finite element size used for this model is approximately 8 in.. At the start of this project, a 1 in. mesh size model was analyzed and these stress results were within 1% when compared to those of the 8 in. model. The effects of gravity of all culvert components were included in the model, as this affects the interaction with its supporting subbase. In this chapter, the FEM was used to perform parametric studies to determine the influence of changing the contraction joint spacing, two concrete CTE values, three placement seasons, two joint types, three construction sequences, and three concrete types on early-age cracking risk.
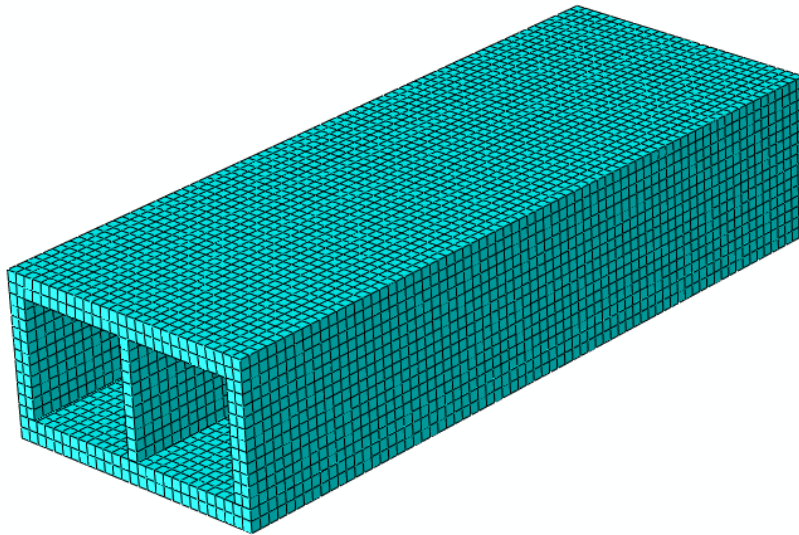
Figure 12-1 Finite-element model of one 50 ft section of Culvert J

12.1 CULVERT J STRESS RESULT

Figure 12-2 shows the temperature history of the culvert concrete and the ambient temperature used for the FEM for Culvert J under summer placement conditions. After concrete was cast, the temperature starts to rise because of the co-occurrence of heat of hydration and solar radiation peak effects. After reaching the peak temperature, the concrete gradually cools down until it is primarily influenced by solar and ambient temperature cycles.
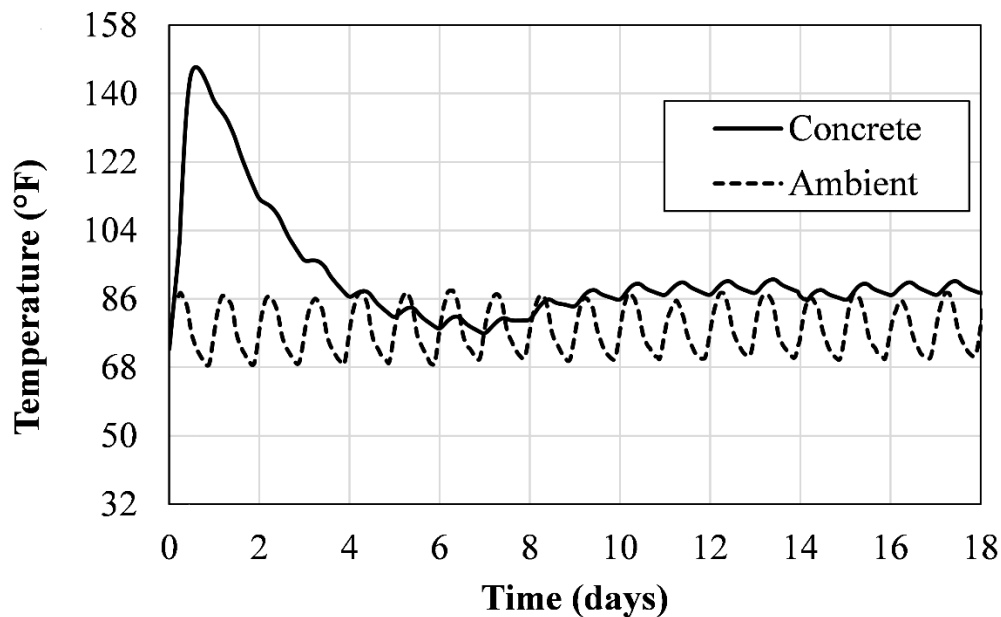
Figure 12-2 Temperature history of Culvert J under summer placement condition

The longitudinal stress development in the culvert base, wall, and roof compared with the tensile strength development with time is shown in Figure 12-3. Negative values represent compressive stresses and positive represent tensile stresses. The wall and roof are cast 7 days later than the base. All FEM stress results are from mid-length of the 50 ft section, which is where the restraint is the highest. For the culvert wall, results revealed that the maximum stress occurs near its interface

with the base, which is where wall stresses are plotted in Figure 12-3. Immediately following final

set, compressive stresses start to develop due to the rise in concrete temperature. When the concrete

begins to cool, tensile stresses develop because of the restraint of concrete contraction. Tensile

stresses in the roof are much less than in the base or wall, because the restraint to movement

provided by the base is much lower at the level of the roof.
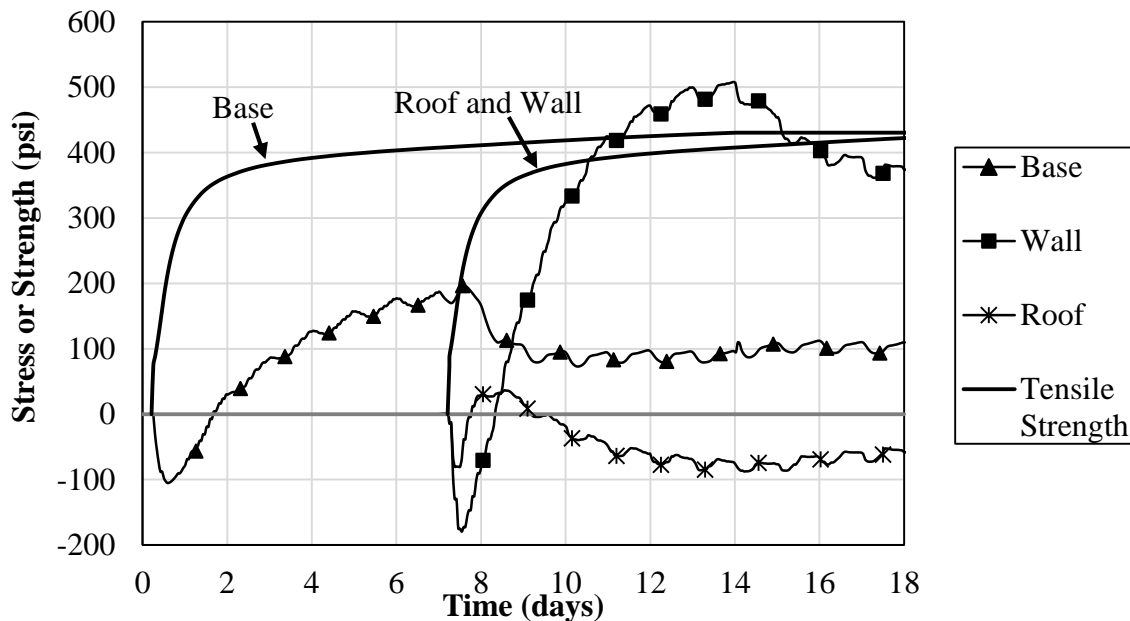
Figure 12-3 Stress and strength development for one section of Culvert J under summer

placement condition

Based on the stress and strength development shown in Figure 12-3, the tensile stress-to-strength

ratio over time was determined and is graphed for the base, wall, and roof in Figure 12-4. From

this figure, the cracking risk can be assessed, and a dashed line at 0.67 above which the cracking

risk is considered "high" (Riding et al. 2017) is shown as reference. It is clear from Figure 12-4

that the cracking risk in the wall quickly develops above the high threshold and remains high for

many days, whereas the cracking risk in the base is elevated but remains below the high cracking

risk threshold, and the cracking risk in the roof is very low. This finding explains why many of the surveyed culverts had wide cracks primarily in the walls and bases.
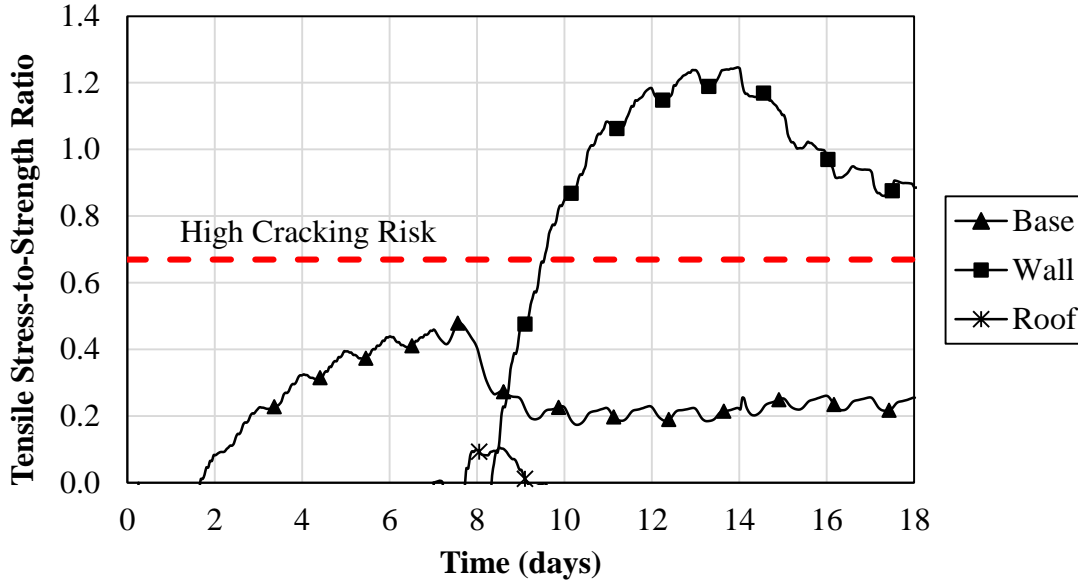
Figure 12-4 Tensile stress-to-strength ratio result for one section of Culvert J under summer placement

12.2 EFFECT OF DRYING SHRINKAGE

The drying shrinkage starts 7 days after concrete placement. Figure 12-5 shows the early-age stress development results for Culvert J with and without drying shrinkage effect. For culvert bases, the maximum stress is not influenced by the drying shrinkage because the maximum stress occurs at approximately between 7 to 8 days. The maximum stress in the base with shrinkage is 259 psi while the maximum stress in the wall without shrinkage is 250 psi. For culvert base after 9 days, the compressive stress is less in the base with shrinkage than the compressive stress of the base without shrinkage. The effect of drying shrinkage on the culvert walls is more obvious. Figure 12-5 shows that the tensile stress in the wall with shrinkage is more than that of the wall without shrinkage in a wide time range. The maximum stress of the wall with shrinkage is 502 psi while

the maximum stress in the wall without shrinkage is 481 psi, which leads to 21 psi difference. Therefore, drying shrinkage would lead to additional stresses in the culvert wall, and thus an increased tensile stress-to-strength ratio.
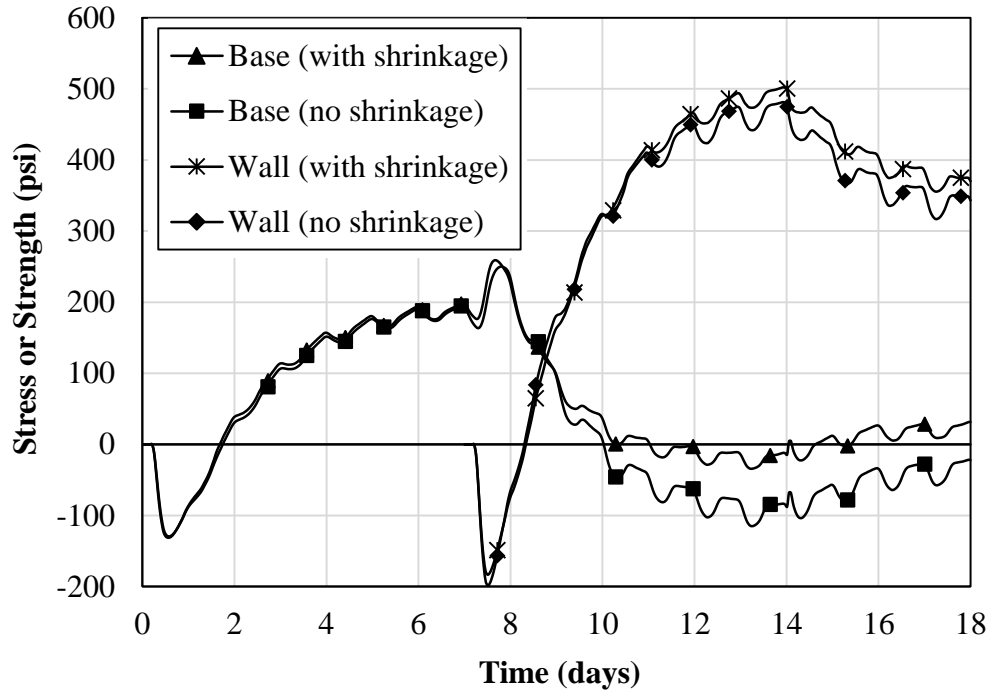
Figure 12-5 Stress development of Culvert J with and without drying shrinkage

12.3   EFFECT OF CONTRACTION JOINT SPACING

The effect of contraction joint spacing, assuming each length of culvert section is free to expand or contract from each other, on the cracking risk of culvert is evaluated herein. The following six contraction joint spacings were evaluated: 18 ft, 24 ft, 30 ft, 36 ft, 42 ft, and 50 ft. In this analysis, the base was cast first and wall and roof were added 7 days later. The maximum tensile stress-to-strength ratio envelope for the six contraction joint spacing is presented in Figure 12-6. From 0 to 8 days, the cracking risk of the base significantly decreases with decrease in contraction joint spacing. However, from 8 days and later it can been seen that the cracking risk in the culvert wall

152

changes little (less than 10 percent) with decrease in contraction joint spacing. As will be shown in the rest of this section, this is because the wall is highly restrained against movement by the base on which it is cast, so a change in contraction joint spacing does not significantly impact the wall stresses. This finding is similar to that of Bosnjak (2000) that concluded short and long culvert wall sections have similar maximum stresses.
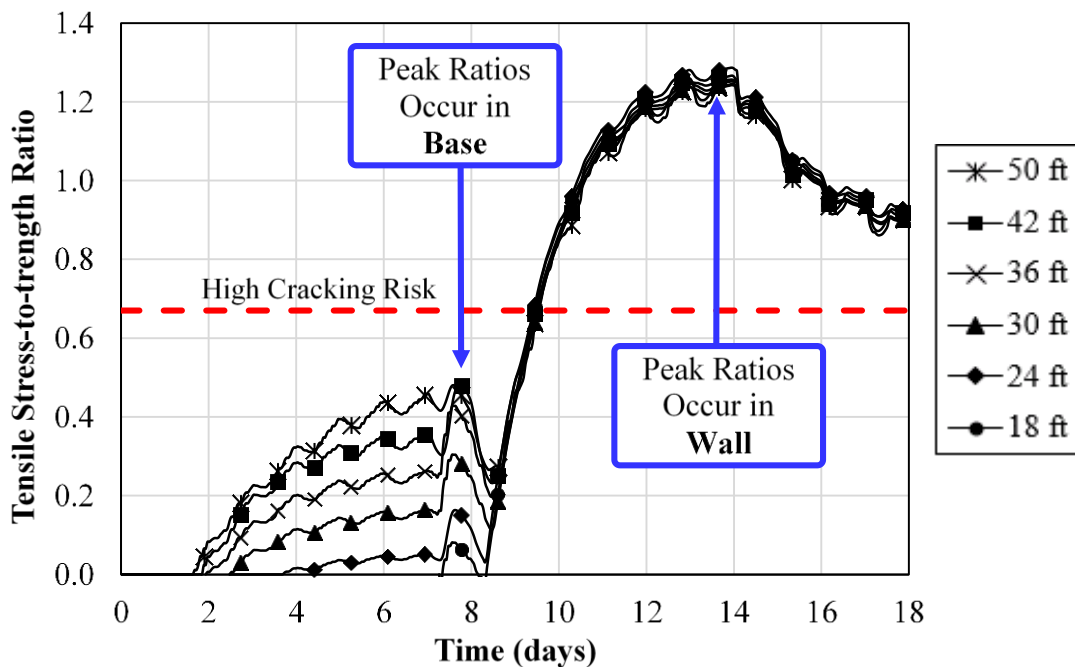
Figure 12-6 Effect of culvert contraction joint spacing on culvert cracking risk

Longitudinal stress contour plots of the culvert wall for short and long contraction joint spacings of 18 ft and 42 ft are shown in Figure 12-7. The maximum tensile stress of approximately 500 psi occurs near the bottom of the wall for both small and large contraction joint spacings. The stress decreases from bottom to top of the wall, and from mid-length to the end of the wall because this matches the change in restraint to movement provided. Based on the stress contour plot and location of maximum stresses, possible cracks in the short and long culvert wall are shown in Figure 12-8.
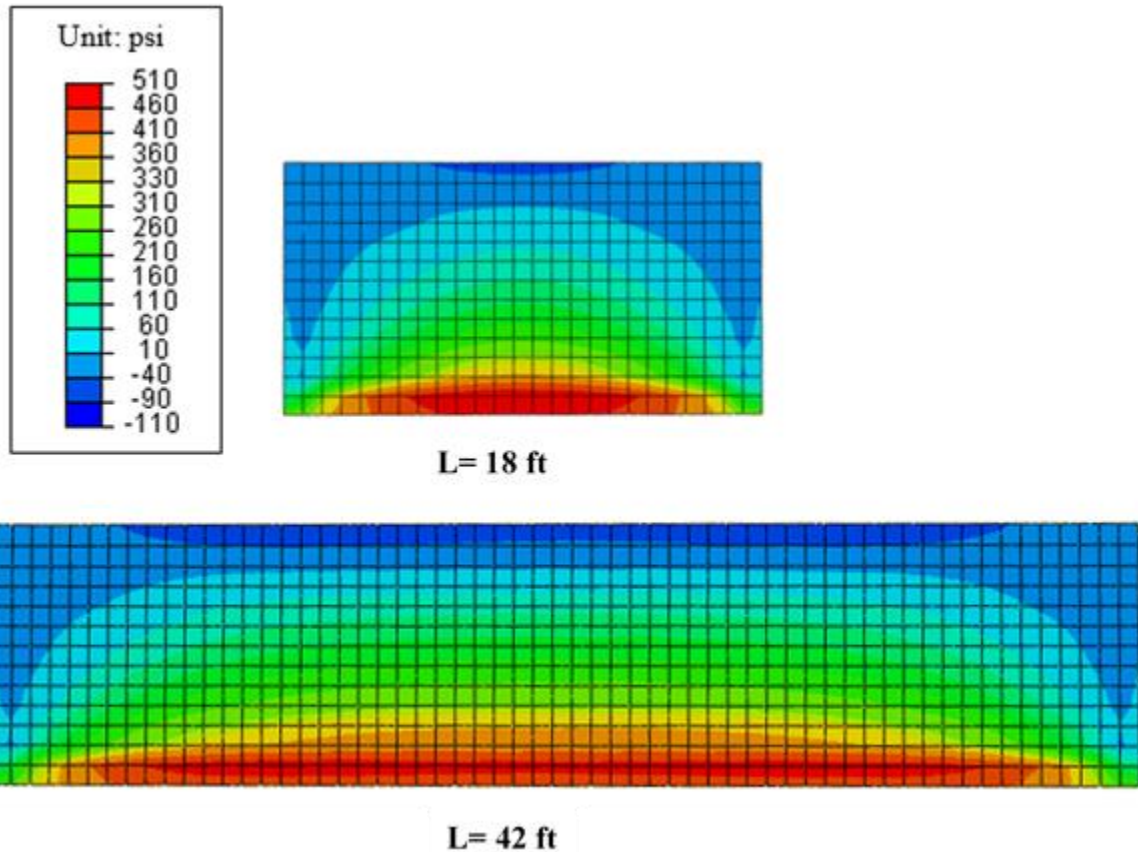
Figure 12-7 Impact of contraction joint spacing on wall stresses: longitudinal stress contours for short and long contraction joint spacings

Figure 12-8 Impact of contraction joint spacing on wall stresses: possible cracks for short and long walls (adapted from Rostásy et al. 1998)

12.4 EFFECT OF JOINT TYPE

An elevation view of Construction Sequence A is shown in Figure 12-9, which is similar to the actual construction sequence used to construct Culvert J. It includes three 50 ft culvert sections, consisting of three walls and roofs cast on three bases. The ages in Figure 12-9 represent the days when the culvert component is constructed relative to the start of construction of the first base. With this construction sequence, the delay between casting adjacent base sections is 2 days, the delay between adjacent wall sections is 2 days, and the delay between starting the first base and wall sections is 7 days.
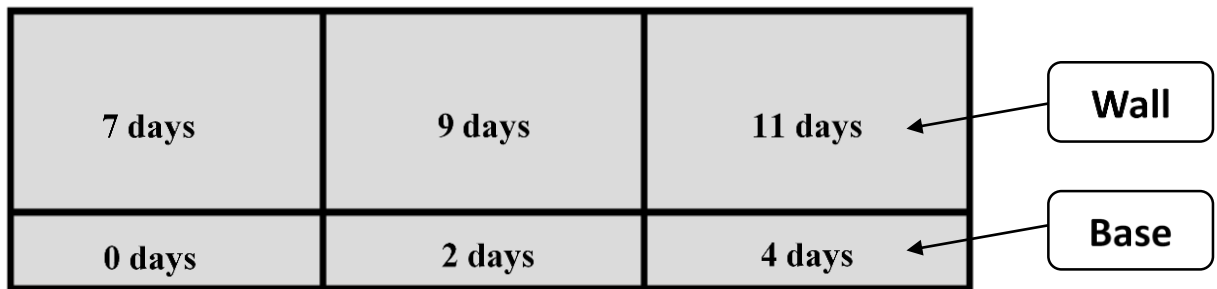
Figure 12-9 Elevation view Construction Sequence A

The effect of joint type when using Construction Sequence A on the stress-to-strength ratio in the culvert base and wall is shown in Figure 12-10. From this figure, it can be concluded that the joint type significantly influences the cracking risk of the base; however, the joint type does not have a significant impact on the cracking risk of the wall. The maximum cracking risk in the base with a tied-construction joint decreases from 1.23 to 0.72 when a contraction joint is used. Since the wall is highly restrained against movement by the base on which it is cast, a change in joint type has a small impact on the wall stresses.

155
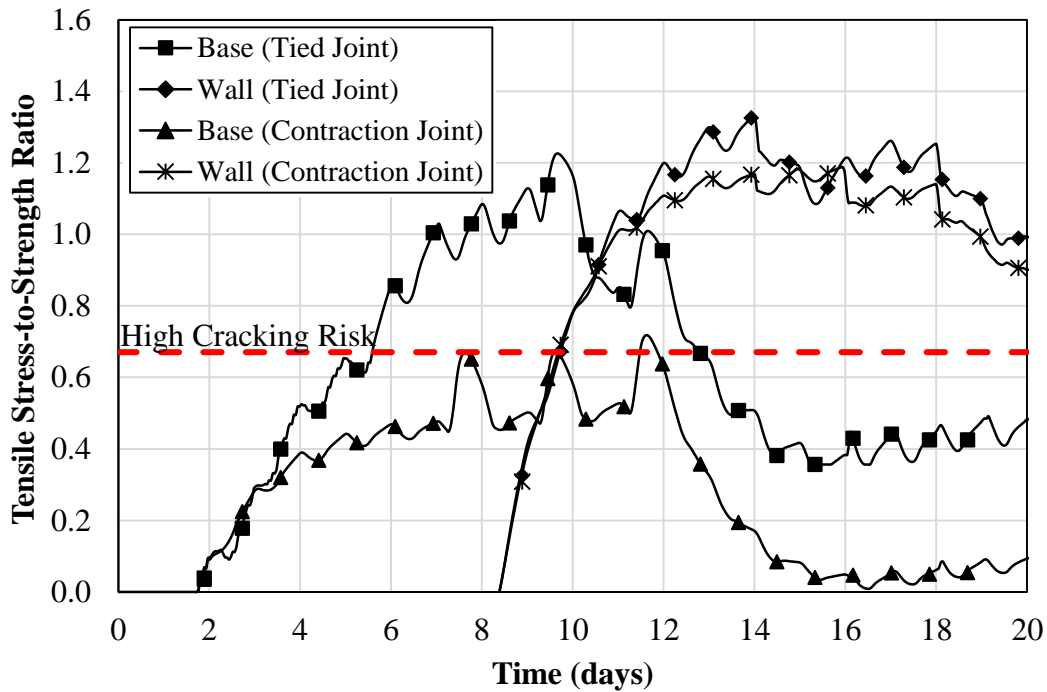
Figure 12-10   Effect of joint type on culvert cracking risk based on Construction Sequence A

12.5   EFFECT OF CONSTRUCTION SEQUENCE

Two additional construction sequences (B and C) were evaluated to determine if a change in construction sequence will reduce the occurrence of cracking. The elevation views of Construction Sequence B and C are shown in Figure 12-11 and Figure 12-12. In Construction Sequence B, the time delay between base sections is 2 days, the delay between wall sections is 6 days, and the delay between starting the first base and wall sections is 4 days. In Construction Sequence C, the time delay between base sections 4 days, the delay between wall sections is 4 days, and the delay between starting the first base and wall sections is 2 days. For Construction Sequences A, B and C, the delay between casting the wall and base is 7 days, 4 days, and 2 days, respectively.
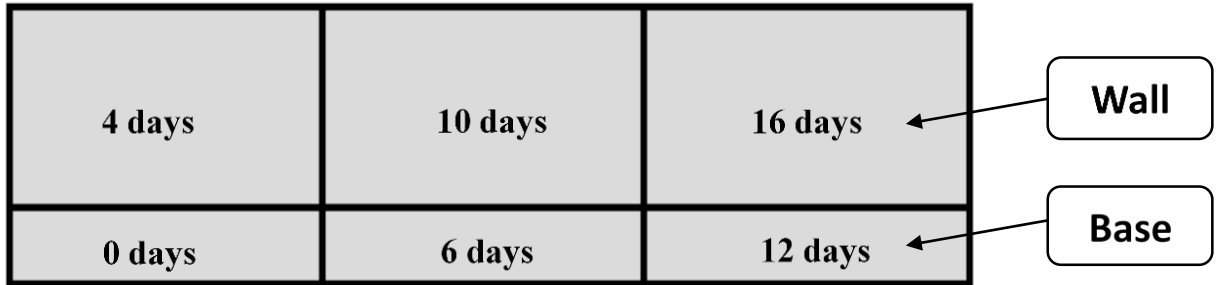
Figure 12-11 Elevation view construction sequence B
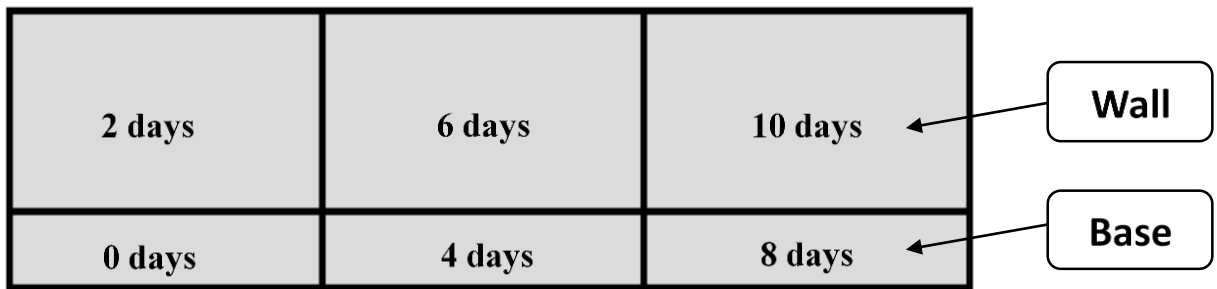
Figure 12-12 Elevation view construction Sequence C

Results for culverts with Construction Sequence C are discussed herein. Figure 12-13 to Figure 12-16 show the stress and strength development results of bases and walls of culvert under Construction Sequence C with contraction joints and tied joints, respectively. Comparing Figure 12-13 and Figure 12-14, the culverts both follow Construction Sequence C, and the three base sections using contraction joints in Figure 12-13 have smaller maximum stresses than the three base sections using tied joints in Figure 12-14. Comparing Figure 12-15 and Figure 12-16, the maximum stresses are closer to the strength curve for the three wall sections using contraction joints in Figure 12-16, than the stresses in the three wall sections using contraction joints in Figure 12-15. Therefore, it is concluded that the contraction joint helps to decrease the maximum stresses both in culvert bases and walls sections.
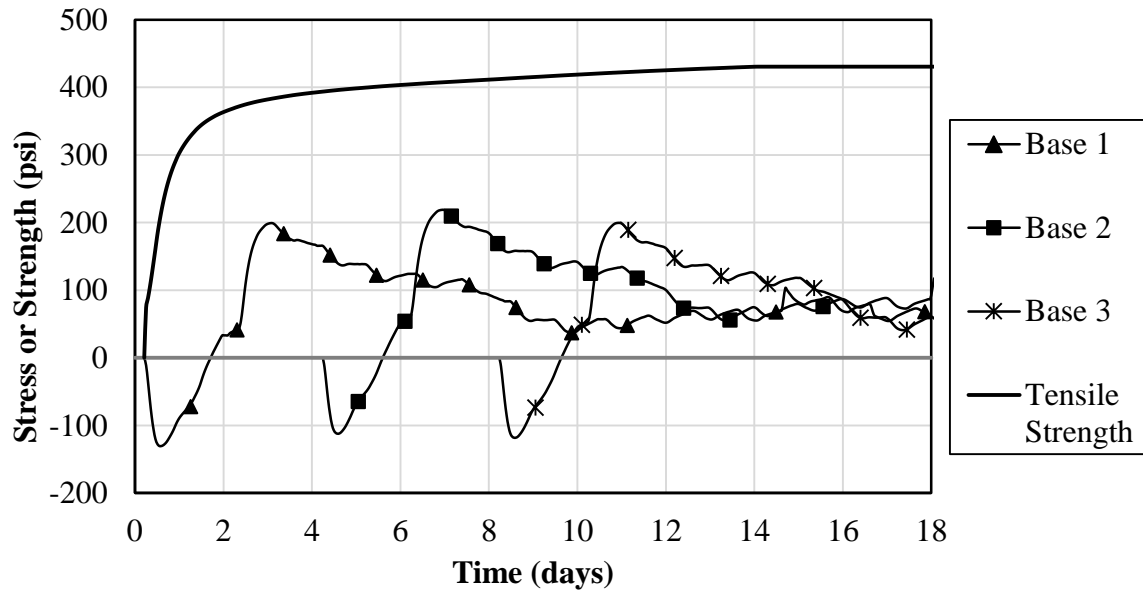
Figure 12-13 Stress and strength development of base sections in construction sequence C

with contraction joint
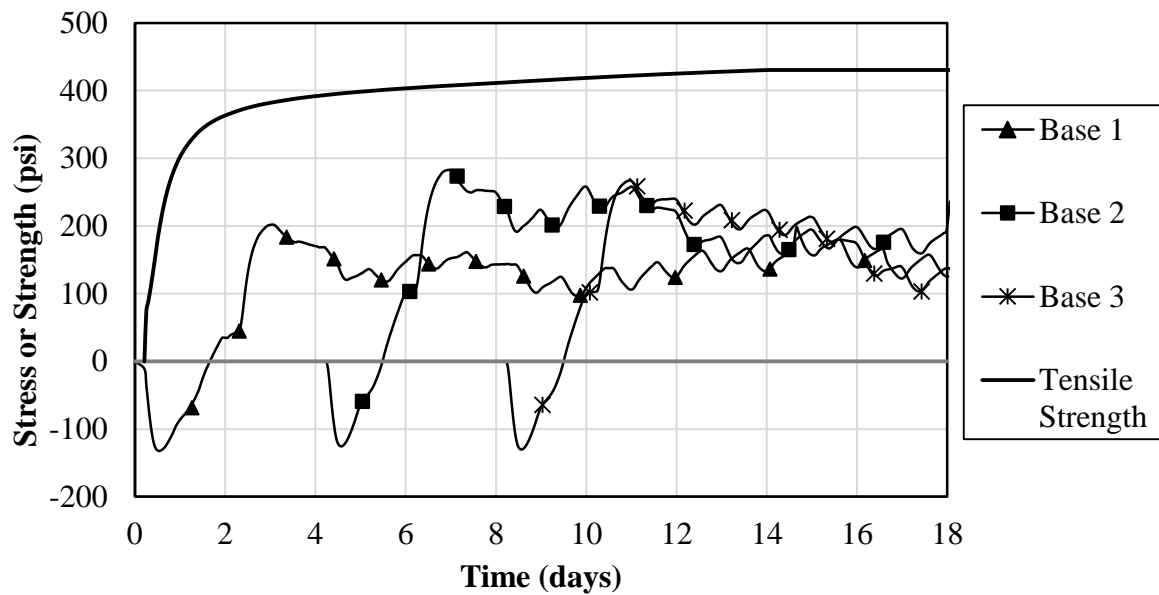
Figure 12-14 Stress and strength development of base sections in construction sequence C
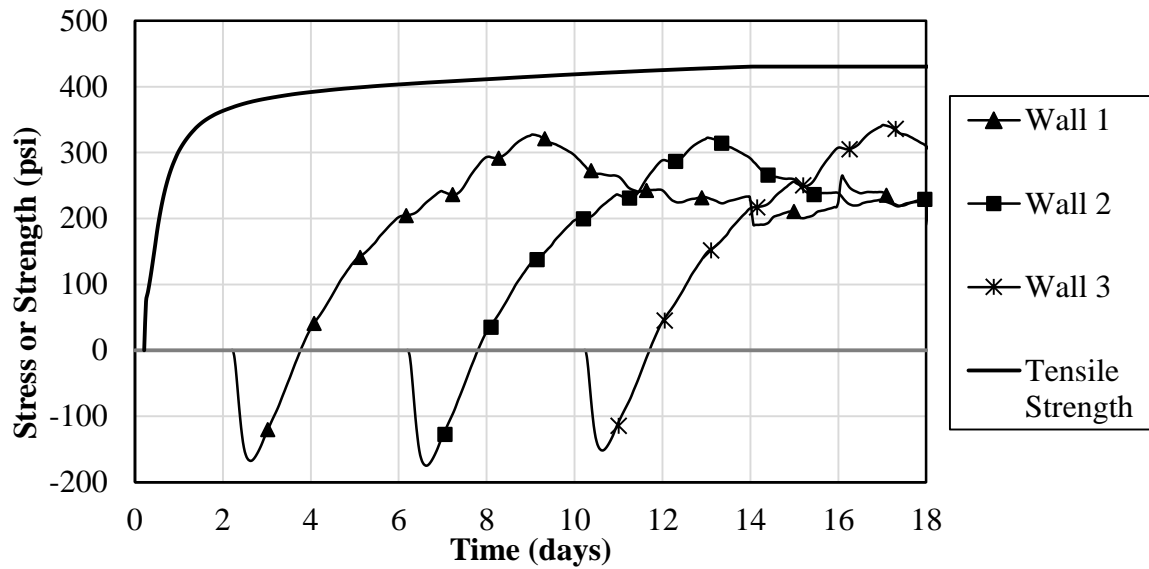
with tied joint

Figure 12-15 Stress and strength development of wall sections in construction sequence C

with contraction joint
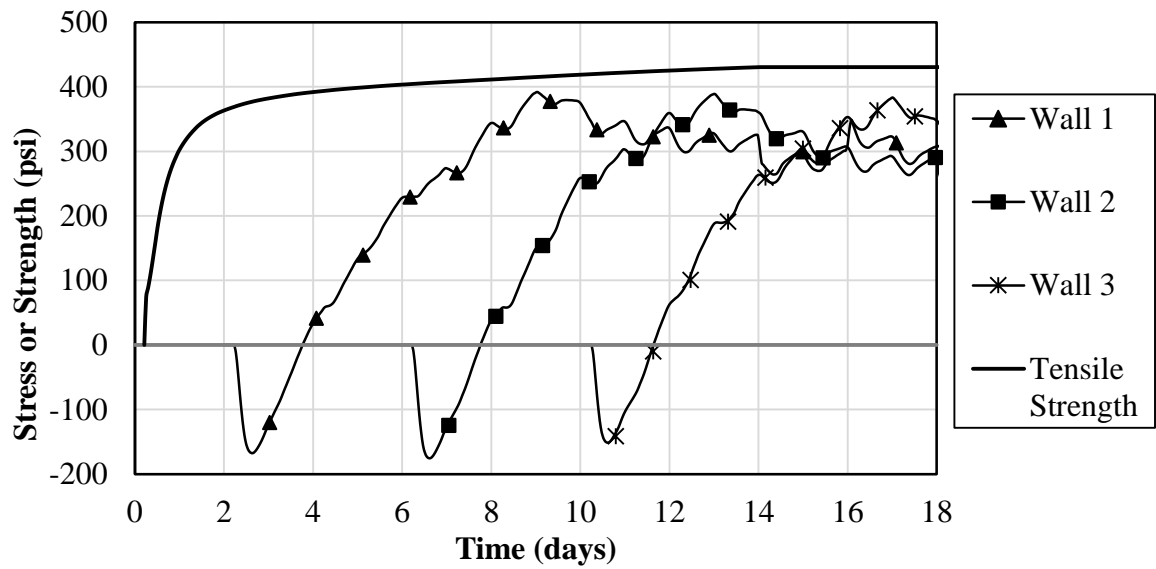
Figure 12-16 Stress and strength development of wall sections in construction sequence C

with tied joint

159

The maximum tensile stress-to-strength ratio in the base and wall for the three construction sequences modeled are summarized in Figure 12-17. In this figure, the first six columns for the culvert base show a decreasing trend of maximum cracking risk for both tied joints (gray columns) and contraction joints (white columns). Similarly, the cracking risk in the culvert wall also decreases systematically when changing from Construction Sequence A to B to C. From these results, it can be concluded that the younger the base when the wall is cast, the lower the stresses that develop in the wall. This is because the younger the base when the wall is cast on it, the lower the stiffness of the base, which reduces the restraint that the base provides for the wall.
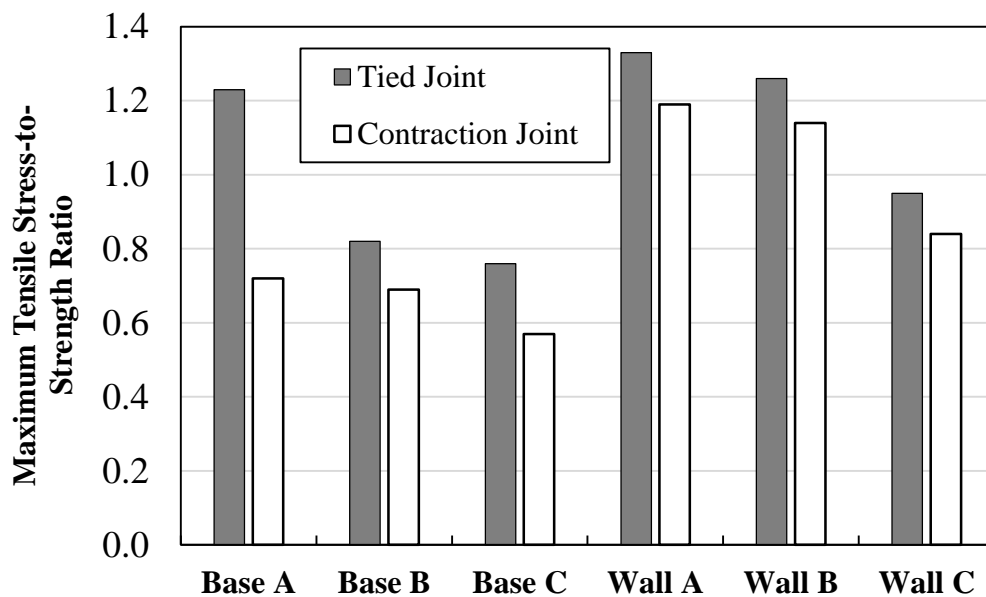
Figure 12-17 Effect of construction sequences on culvert cracking risk

12.6   EFFECT OF PLACEMENT SEASON

The effect of constructing culverts during different seasons on the cracking risk is evaluated in this section. The temperature history of summer, fall and winter placement conditions were generated with Concreteworks for Culvert J. Summer placement stress results are shown for Culvert J in

160

Figure 12-3. The stress results for Culvert J under fall and winter placement are shown in Figure 12-18 and Figure 12-19, respectively. The maximum stress-to-strength envelope for culverts constructed under summer, fall, and winter placement conditions are summarized in Figure 12-20. Summer placement leads to a much higher cracking risk, while winter placement leads to a much lower cracking risk, with fall placement in between these two extremes. This means that extensive culvert cracking is much more likely when construction occurs during hot weather conditions.
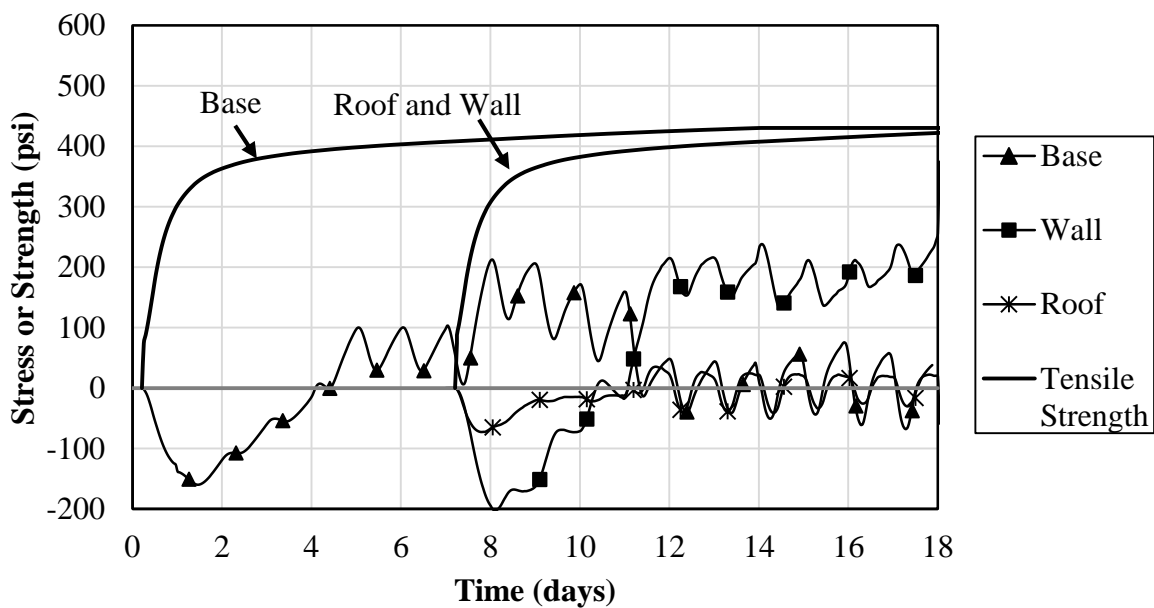
Figure 12-18 Culvert J stress result under fall placement
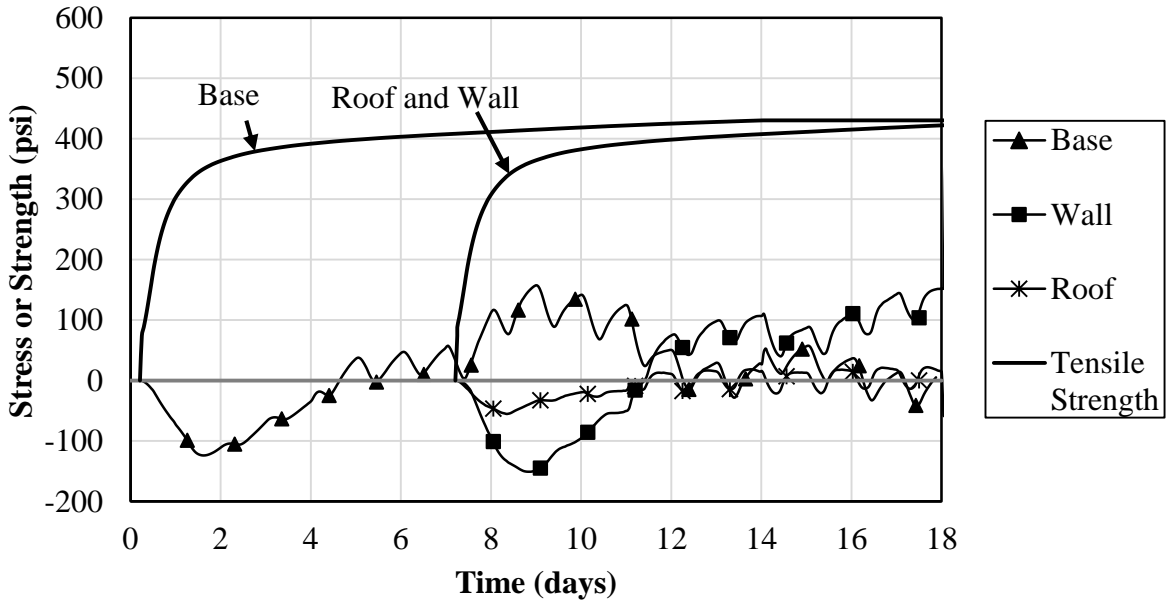
Figure 12-19 Culvert J stress result under winter placement
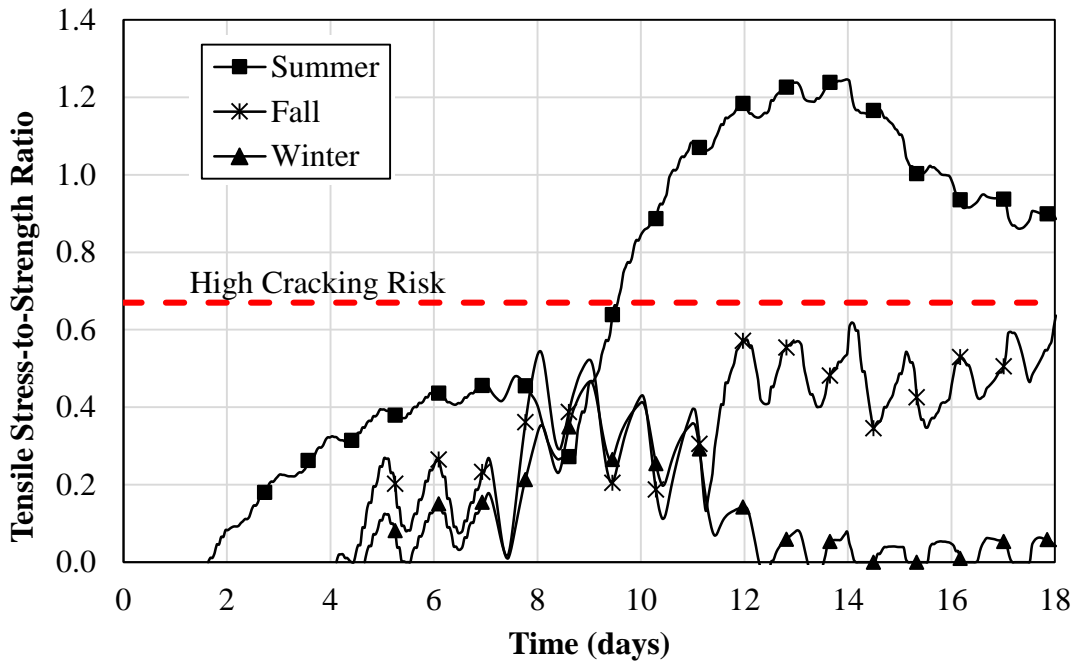
Figure 12-20 Effect of placement season on cracking risk

162

12.7   EFFECT OF COEFFICIENT OF THERMAL EXPANSION

The coarse aggregate type significantly affects the concrete's coefficient of thermal expansion (CTE) (Schindler et al. 2010). The stresses in culverts made with river gravel concrete with CTE of $6.95 \times 10\text{-}6/°F$ and limestone concrete with CTE of $5.52 \times 10^{-6}/°F$ were evaluated. Concrete with limestone coarse aggregate stress results are shown for Culvert J in

Figure 12-3. The stress results for concrete with river gravel are shown in Figure 12-21. Figure 12-22 summarizes the maximum stress-to-strength envelope for culverts using concrete with river gravel and limestone. The results in Figure 12-22 indicate that the use of a lower CTE concrete will decrease the cracking risk in the base and wall; however, due to the high restraint, the stresses in the wall remain above the high cracking risk threshold.
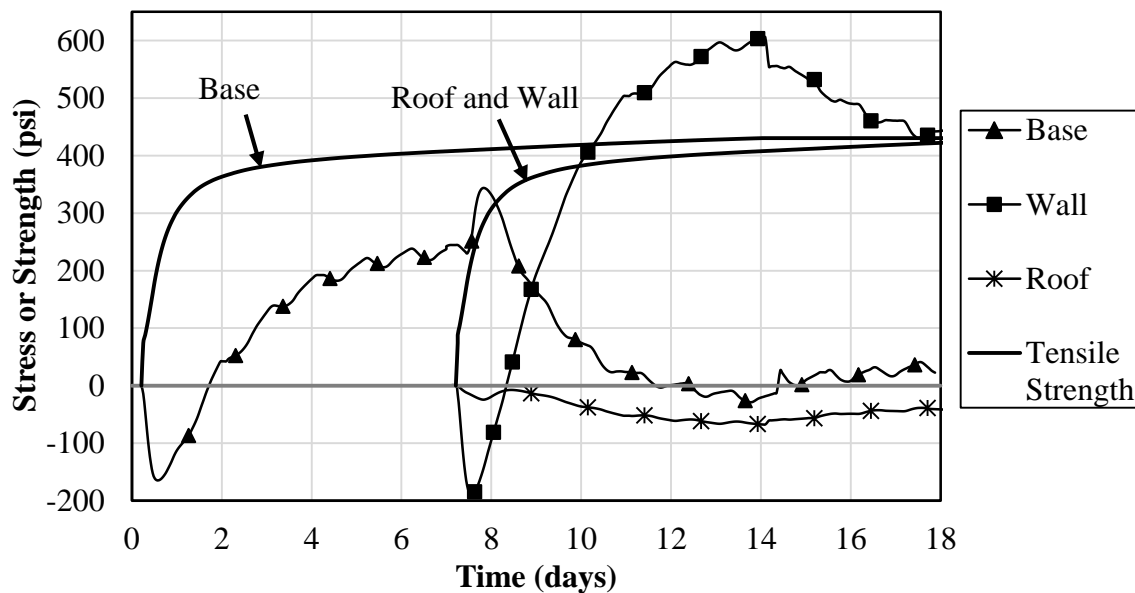
Figure 12-21 Stress result for culvert concrete with river gravel

163
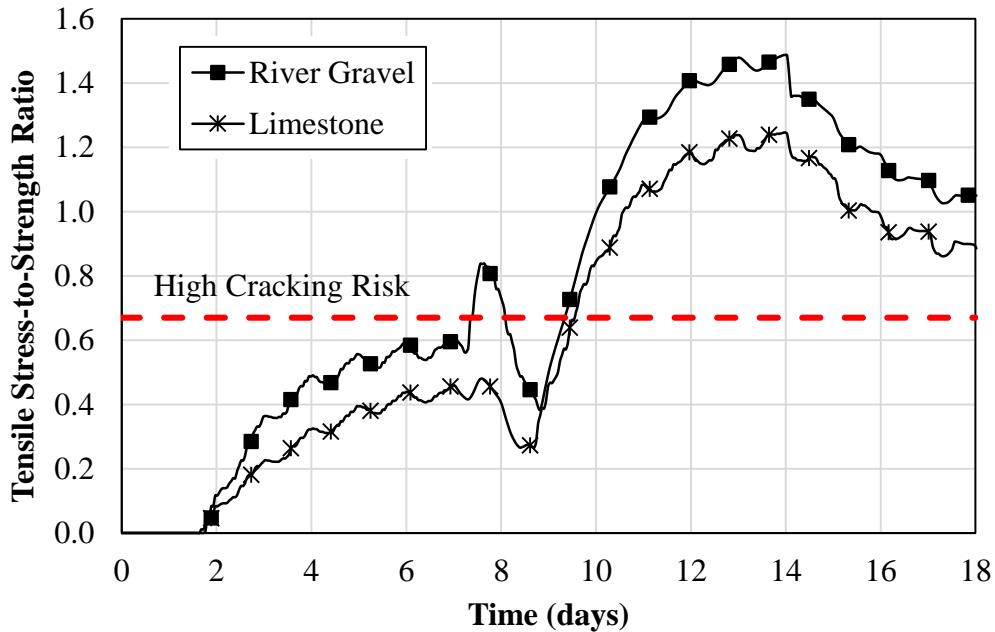
Figure 12-22 Effect of concrete CTE on cracking risk

12.8 USE OF LIGHTWEIGHT AGGREGATE CONCRETE

During the construction sequence analysis it was shown that the lower the stiffness of the base, the lower the stresses that develop in the wall. Based on this finding, the effect of adding lightweight aggregate to the concrete to reduce its modulus of elasticity was analyzed. Sand-lightweight (SLW) concrete and all-lightweight (ALW) concrete were used to evaluate the cracking risk compared to using normalweight (NW) concrete. The properties of SLW and ALW concrete were obtained from Byard (2011), who tested the stress development of various concretes made with lightweight aggregates. The SLW and ALW concretes have a *w/c* of 0.42 and their temperature profiles were obtained from ConcreteWorks using their mixture properties.

Culvert J results using normalweight concrete is shown in
Figure 12-3. The stress results for culverts with sand-lightweight concrete and all-lightweight concrete are shown in Figure 12-23 and Figure 12-24, respectively. The 28-day tensile strength of

164

normalweight concrete, sand-lightweight concrete, and all-lightweight concrete are 430 psi, 507
psi, and 492 psi, respectively. It is not reliable to compare the maximum stress for different
concrete types, because of the fact that the tensile strength development changes with the concrete
type. Therefore, the tensile stress-to strength ratios were estimated and shown in Figure 12-25 to
compare the cracking risk of each concrete type.
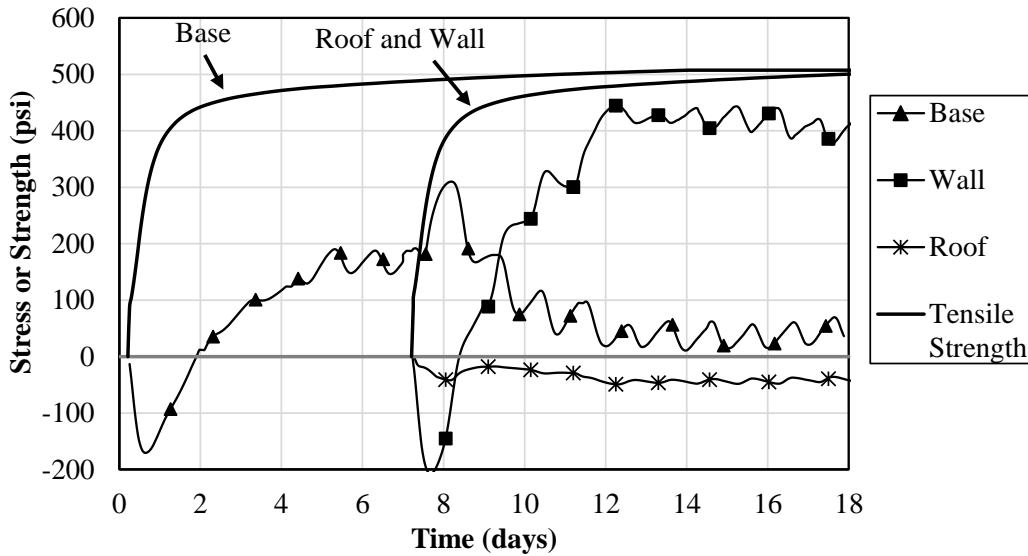
Figure 12-23 Stress result for culvert SLW concrete
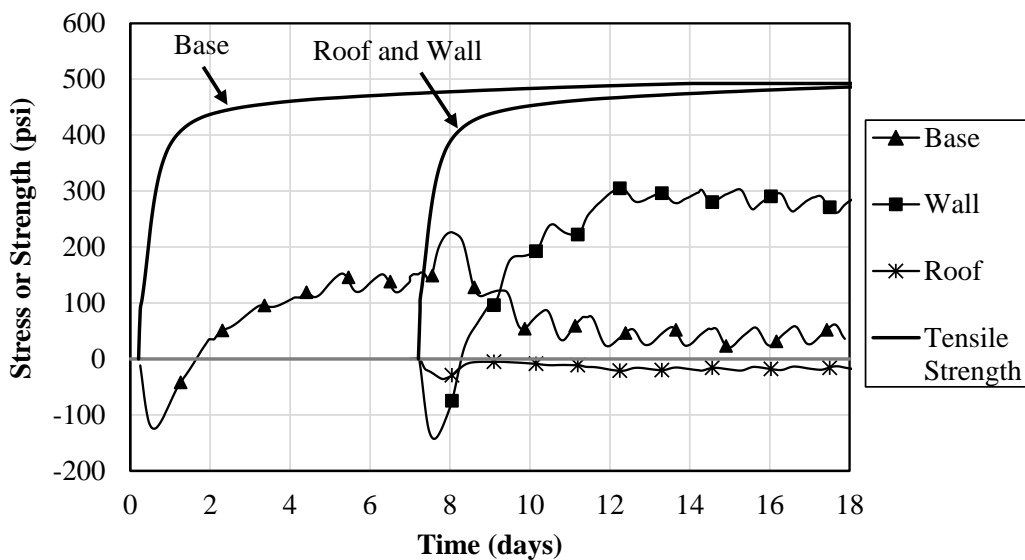
Figure 12-24 Stress result for culvert with ALW concrete
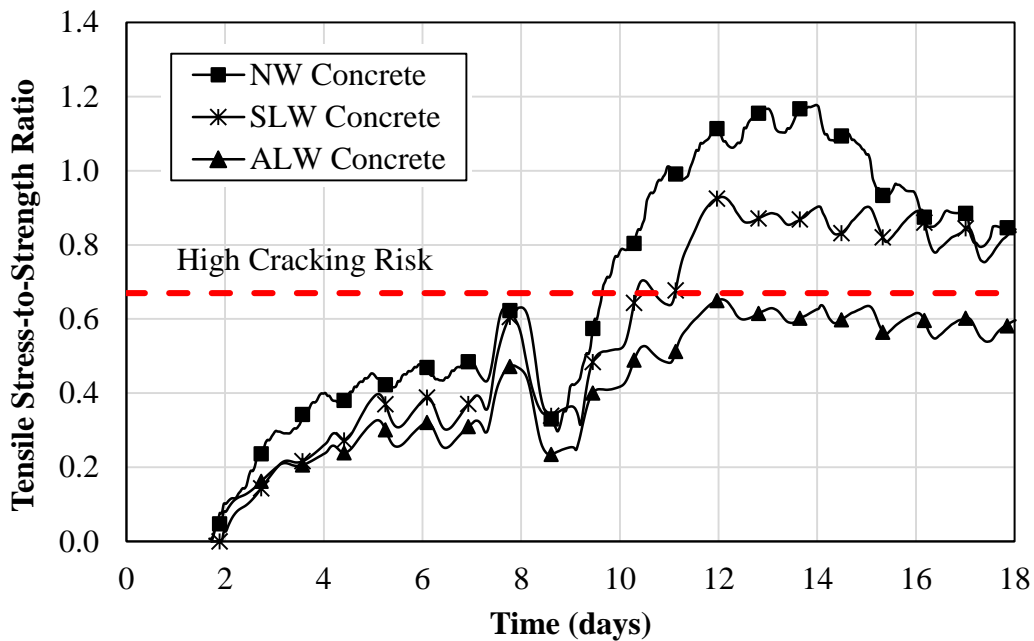
Figure 12-25 Effect of concrete types on cracking risk

Figure 12-25 reveals that use of ALW or SLW concrete significantly decreases the cracking risk in the culvert compared to using NW concrete. The ALW has the lowest cracking risk among the three concrete types, and this in attributed to the 34 percent reduction in modulus of elasticity when using ALW concrete as compared to NW concrete. This finding is similar to work of Byard (2011) that concluded that ALW and SLW concrete can decrease early-age cracking of bridge deck concrete.

CHAPTER 13 PART II: CONCLUSIONS

A three-dimensional, finite-element model (FEM) of cast-in-place concrete culverts was developed. The FEM of early-age stress development of concrete considering temperature effects, creep, and drying shrinkage was verified by experimental results in Part I. The calibrated FEM was used to determine the influence of changing the contraction joint spacing, two concrete coefficient of thermal expansion values, three placement seasons, two joint types, three construction sequences, and three concrete types on the early-age cracking risk. Results from this study support the following conclusions:

1. The cracking risk of the culvert wall, base, and roof was found to be high, moderate, and low, respectively, which explains why many surveyed culverts had wide cracks primarily in the walls and bases.

2. The practical contraction joint spacing evaluated in this study only significantly influences the cracking risk in the culvert base, but has little effect on the cracking risk of the wall. This is because the base provides a very high degree of restraint to the wall.

3. Use of contraction joints can help significantly decrease the cracking risk in the culvert base compared to use of tied-construction joints, but they do not have a significant effect on the maximum cracking risk in the culvert wall.

4. Wall cracking risk increases with the age (maturity) of the base concrete at the time when the wall is constructed. Use of a construction sequence that attains the youngest (lowest stiffness) base when the wall is cast, reduces the cracking risk in the wall.

5. Hot weather construction leads to the highest cracking risk, while cold weather placement results in a much smaller cracking risk, with fall placement conditions in between these two extremes.

6. Use of a lower coefficient of thermal expansion concrete decreases the cracking risk in the base and wall.

7. Use of sand-lightweight concrete or all-lightweight concrete significantly decreases the cracking risk in the culvert compared to using normalweight concrete. The all-lightweight concrete most decreases the cracking risk among the three concrete types evaluated.

PART III:
FINITE-ELEMENT MODELING OF EARLY-AGE CONCRETE STRESS BEHAVIOR
UNDER HIGH-LEVEL OF TENSILE STRESS

CHAPTER 14 PART III: INTRODUCTION

14.1   BACKGROUND

Cracks in bridge decks, foundations, culvert walls, tunnel linings and other structural concrete elements caused by restraint of volume change during hydration have been an well-known problem. When tensile stress in concrete exceeds its tensile strength, cracking occurs. Therefore, stress assessment and cracking risk of early-age concrete have attracted considerable interest (ACI 231 2010), because early-age cracking can influence aesthetics, cause leakage, and decrease long-term durability. Reliable material models and structural analysis methods are needed to estimate the risk of cracking and to evaluate potential options to mitigate early-age cracking in concrete.

Early-age stress development in concrete is influenced by temperature change, modulus of elasticity, creep or relaxation, shrinkage, thermal coefficient of expansion, and the restraint conditions. In the absence of cracking or strain softening, the models to describe the constitutive stress-strain relationships are for linear visco-elastic aging creep, augmented by the shrinkage and thermal expansion (Emborg 1998). However, as tensile stresses increase, stress levels become higher and higher, and knowledge of nonlinear creep behavior at high stresses is essential to determine the risk of cracking in concrete structures, and both micro cracking and at later age cracks, have a dominating effect on nonlinear tensile creep (Emborg 1998).

In the absence of creep, the stress-strain constitutive relation is an algebraic stress-strain relation mostly with an ascending part until the peak stress and a descending part that describes the tensile strain softening (Bažant and Chern 1985). The use of a creep model coupled with high-stress nonlinearity would be more accurate to describe early-age concrete behavior as it approaches failure (Gutsch and Rostasy 1995). Bernander (1982) found that the only way to simulate test results (thermal stresses at restrained deformations) was to modify a creep function used for

170

nonlinear behavior at high tensile stress levels. Modeling of the non-linear stress-strain behavior at high tensile stress levels seems to give an accurate description of the stress development when micro cracks start to develop and the concrete finally reaches failure (Emborg 1998). Stress predictions with linear models give a rather good description of the compressive stress development but implies far too high tensile stresses, thus overestimating the cracking risk (Emborg 1998).

The Modified B3 Model (Byard and Schindler 2015) that was shown in Part I to accurately predict the early-age concrete stress development is adapted Part III. However, the authors of the Modified B3 Model limited the calibration of this model to a stress to strength ratio of 70%, because the principle of superposition that they used was deemed invalid above a high stress level (Bažant and Wittmann 1982). Therefore, adjustments were made to the Modified B3 Model to consider high-stress nonlinearity (microcracking and strain-softening) effects on the development of early-age tensile stresses. The experimental results of 22 concrete mixtures subjected to restraint to volume change tests were used to verify the accuracy of the proposed finite-element model from initial setting to the age of cracking.

14.2   RESEARCH APPROACH

As a starting point, the finite-element method developed in Part I is used; however, it is modified herein to predict early-age stress development is developed to consider temperature effects, modulus of elasticity, creep or stress relaxation, shrinkage, and coefficient of thermal expansion. Nonlinear behavior at high tensile stresses is present in concrete and should be considered to obtain an accurate thermal stress analysis. Therefore, the high-stress nonlinearity was considered in this study by adjusting the model with a reduced effective modulus when the tensile stress is above 70% of its tensile strength. The experimental results of 22 concrete mixtures subjected to restraint

to volume change tests were used to verify the accuracy of the proposed finite-element model from initial setting to the age of cracking.

14.3 RESEARCH OBEJECTIVES

Part III focuses on finite-element modeling of early-age concrete behavior under high level of tensile stress. The research described in this part has the following objectives:

- Use the most accurate creep model obtained from Part I to model early-age concrete stress development from initial setting to cracking.

- Correct the model with a reduced effective modulus and a damage factor to account for high-stress nonlinearity when the tensile stress is above 70% of its tensile strength.

- Compare the stress results from the FEM to the measured stress results from experiments to verify the accuracy of the proposed model that accounts for creep and high-stress nonlinearity.

14.4 RESEARCH OUTLINE

This part of the dissertation comprises of five chapters. A literature review covering concrete nonlinear tensile stress-strain behavior with and without creep effects, rate-type creep law, and experimental work to verify the proposed models are summarized in Chapter 15. The process of modeling early-age concrete behavior using the finite-element method (FEM), which includes incorporating material properties, creep effects, and nonlinear behavior at high-stress level are presented in Chapter 16. The modeling results of early-age concrete stress development from setting to the age of cracking and comparisons with experimental work are covered in Chapter 17. Conclusions for this part are presented in Chapter 18.

CHAPTER 15 PART III LITERATURE REIVIEW

15.1 CONCRETE NONLINEAR TENSILE STRESS-STRAIN BEHAVIOR IN THE ABSENCE OF CREEP

Nonlinear behavior in tension of concrete can be considered before and after the tensile stress exceeds the tensile strength, which is called pre-peak and post-peak behavior. Jonasson (1994) modeled the pre-peak behavior in tension by using a nonlinear stress-strain relationship. Huaggaard (1997) performed tensile stress tests, and the results showed that the limit of linearity is approximately in the range of 60% to 80% of the tensile strength. Jonasson (1994) and Heldlund (2000) proposed analytical expressions for the nonlinear stress-strain behavior at high tensile stresses (pre-peak behavior) for loading in tension, and the unloading was modeled by use of the initial elastic modulus at the origin (see Figure 15-1). In many instances, researchers neglect pre-peak nonlinear behavior when predicting the early-age tensile stress (Bosnjak 2000; Bažant and Oh 1983), and concrete is modeled as elastic prior to cracking, which is a conservative assumption that over-estimates early-age concrete tensile stresses (Emborg 1998).

Modeling post-peak behavior, where the major principle tensile stress exceeds its tensile strength, can be accomplished by using fracture mechanics can be used to characterize the behavior including the effect of cracking. The parameters that describe post-peak behavior of concrete after cracking, fracture energy, and ultimate strain are age dependent for young concrete (Emborg 1998). Since restrained to volume change tests with rigid cracking frames (RCF) were used in this study, the concrete is subjected to fixed restraint provided by Invar bars; therefore, when the maximum tensile stress is reached in the RCF, failure occurs, and the post-peak behavior of the concrete is not captured. Therefore, the post-peak behavior is not considered herein.
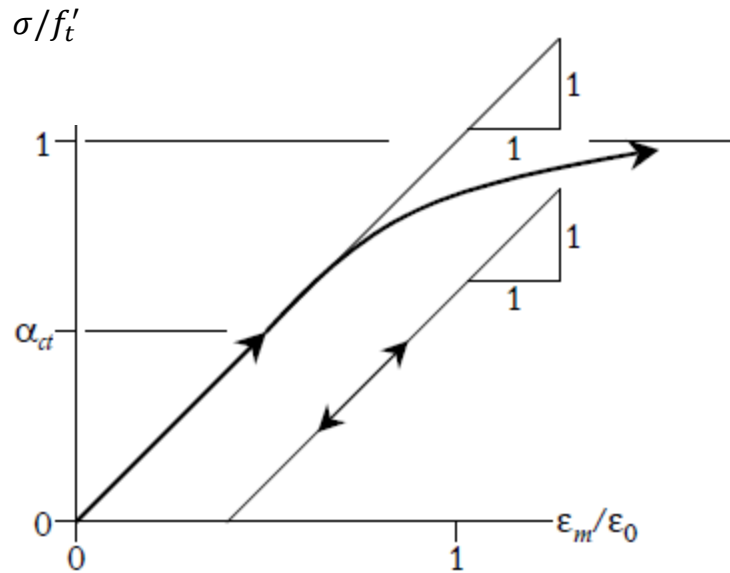
Figure 15-1 Nonlinear stress –strain behavior at tension according to Jonasson (1994)

[α_{ct} =stress level above which nonlinear behavior is present, $\varepsilon_m/\varepsilon_0$ = material strain to

strain at tensile strength]

15.2   RATE-TYPE CREEP LAW

Creep is the time-dependent increase in strain when concrete is subjected to sustained stress. Often the time-dependent response of concrete is expressed in terms of compliance, that includes both elastic and time-dependent deformations (i.e. creep effects) (ACI 209 1992). The Modified B3 Model (Byard and Schindler 2015) discussed in Section 4.6.2 is used in this study to describe the creep effect on early-age concrete stress development. The work in Part I concluded that the Modified B3 Model is the most accurate model to predict early-age concrete stress development compare to other three models evaluated in Part I. In this study, three-dimensional, finite-element modeling (FEM) by commercial program ABAQUS will be used with the rate-type creep law to predict the development of early-age concrete stresses from initial setting to the age of cracking.

The rate-type creep law in the FEM uses a step-by-step analysis, and in each time step, the integration points of each finite element is considered within the UMAT subroutine. The inelastic creep problem for the structure is reduced to a sequence of elasticity problems by converting the incremental stress-strain relation for each time step, Δt, to a quasi-elastic stress-strain relation as shown in Equation 15-1 (Yu et al. 2012).

$$\Delta\sigma = E''(\Delta\varepsilon - \Delta\varepsilon'') \qquad \textbf{(Equation 15-1)}$$

Where, in the three-dimensional FEM, $\Delta\boldsymbol{\sigma}$ is a 6×1 column matrix of stress increments during each time step (psi), $\boldsymbol{E''}$ is a 6×6 matrix of incremental effective modulus (psi) for an isotropic material using a constant concrete Poisson ratio, $\Delta\boldsymbol{\varepsilon''}$ is a 6×1 column matrix of inelastic strain increments due to creep (in./in.), and $\Delta\boldsymbol{\varepsilon}$ is a 6×1 column matrix of strain increments due to shrinkage and thermal dilation (in./in.). This quasi-elastic stress-strain relation makes it possible to calculate the strain response for any stress history (creep), as well as the stress response for any given strain history (relaxation) (Bažant and Prasannan 1989a,b). More details of the rate-type creep law can be found in Section 4.4. Based on the code programed in the ABAQUS subroutine for the Modified B3 Model, modifications were made to account for effect of high-stress nonlinearity in the FEM.

15.3   NONLINEAR CONCRETE BEHAVIOR AT HIGH-STRESS LEVEL COUPLED WITH CREEP

A smeared crack relationship that describes the tensile-strain softening with or without simultaneous creep (and shrinkage) has been proposed by Bažant and Chern (1985). Strain softening is considered as additive to the strain due to creep, shrinkage, thermal, and elastic deformations. To consider the effect of cracking (high stress level) on concrete stress analysis, a realistic model would be the cohesive crack model with rate-dependent softening, which is

175

reported by Bažant and Li (1997). This model uses a boundary integral formulation of the cohesive crack model in terms of compliance functions for loads applied anywhere on the crack surfaces. However, it is virtually impossible to implement the these complicated models with FEM programs (Bažant et al. 2012).

Bažant and Prasannan (1989a) propose theory that is simple to apply with finite-element analysis and accounts for the nonlinearity of creep with respect to stress. The nonlinear dependence of creep on stress was approximted by the approach shown in Equation 15-2 (Bažant and Prasannan 1989a).

$$F[\sigma(t)] = \frac{1 + s^2}{1 - \Omega} \qquad \textbf{(Equation 15-2)}$$

$$s = \frac{\sigma(t)}{f'_c} \qquad \textbf{(Equation 15-3)}$$

$$\Omega = s^{10} \qquad \textbf{(Equation 15-4)}$$

Where,

Ω represents the damage of concrete at high stress, and

s is the ratio of stress to the strength of concrete at time t.

If $< 0.7, \Omega \cong 0$. This means that if the stress is lower than 70% of the strength, the factor Ω is close to 0, and can be neglected. For the compliance function of the B3 Model, considering the nonlinear dependence on stress that has a constant stress applied at age t', the expression is shown in Equation 15-5 (Bažant and Prasannan 1989a). In this equation, the functions multiplying q_2,

q_3, and q_4 represent the nondimensionalized forms of the aging viscoelstic compliance, the nonaging viscoelastic compliance, and the flow compliance, respectively.

$$J(t, t', \sigma) = q_1 + q_2 F(\sigma) Q(t, t') + q_3 F(\sigma) \ln[1 + (t - t')^n] \qquad \textbf{(Equation 15-5)}$$

$$+ q_4 F(\sigma)(\frac{t}{t'})$$

$$J(t, t', \sigma) = \varepsilon(t)/\sigma \qquad \textbf{(Equation 15-6)}$$

For the stress-strain relation in Equation 15-6, in addition to the creep part with nonlinear stress effect, $F(\sigma)$, the influence of high-stress nonlinearity on the constant modulus of elasticity can be added to the parameter q_1. Thus, the effect of nonlinearity on the elastic behavior and creep are all corrected by the introduction of $F(\sigma)$ in the stress-strain relation. A damage factor is defined as D as shown in Equation 15-7. When the stress is less than 70% of strength, $F(\sigma) = 1$. When the stress-to-strength ratio, s, equals 0.7, 0.8, and 0.9, the corresponding value of D equals 0.65, 0.54, and 0.36, respectively.

$$D = {^1/_{F(\sigma)}} \qquad \textbf{(Equation 15-7)}$$

Bažant et al. (2012) uses this method for the time-dependent structural analysis by the FEM to calculate the deflections of prestressed box girders. These authors replace the effective modulus by a further reduced modulus when the tensile stress exceeds $0.7 f'_t$ to account for the effect of cracking (Bažant et al. 2012). Bažant et al. (2012) reduces the effective incremental modulus, E'', for the current time step to $E''/4$ when the concrete tensile stress exceeds 70% of its strength $(0.7 f'_t)$ (as shown in Figure 15-2), and this effective modulus includes the effect of creep. With this approach, this means that the damage factor, D, equals 1/4 when the tensile stress in concrete

exceeds $0.7f'_t$. The tensile stress resultant from the model with $E''/4$ happens to be about the same as that obtained with a more realistic model consisting of a bilinear softening stress-strain relationship with an unreduced tensile strength limit and the softening modulus of about $-E''/3$ (Bažant et al. 2012) that is also shown in Figure 15-2. In the algorithm for the finite-element program ABAQUS, modeling of tensile softening behavior (i.e. negative $-E''/3$) was intractable, because it interfered with the programming of the exponential algorithm for creep, and this is why a positive modulus $E''/4$ had to be adopted instead of a negative $-E''/3$ (Bažant et al. 2012).
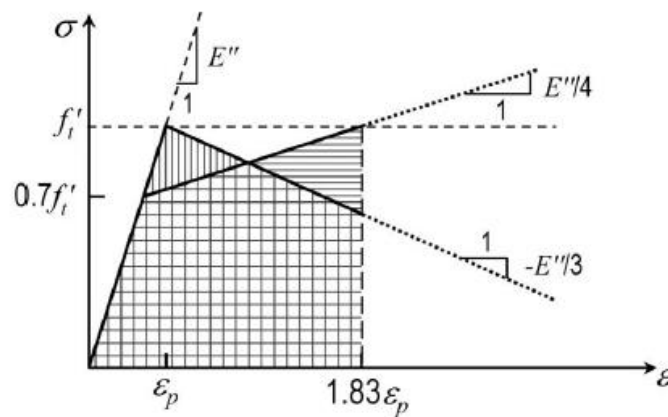
Figure 15-2 Strain-stress relation if tensile strength is exceeded (Bažant et al. 2012)

15.4   EXPERIMENTAL WORK TO VERIFY THE MODEL

15.4.1 Restrained Stress Measurement

Restrained to volume change tests with rigid cracking frames (RCF) were used to measure the early-age stress development in various concretes. The rigid cracking frame consists of dog-bone shaped formwork with dimensions of 6×6×49 in., two mild steel crossheads, and two Invar sidebars. The formwork is lined with plastic and then sealed after concrete placement; therefore, no drying shrinkage is allowed to develop. The concrete curing temperature in the setup is

controlled to simulate typical concrete elements such as bridge decks, mass concrete, etc. More details of the RCF testing used for this study can be found in Byard (2011).

After the concrete starts to hydrate and volume change starts to occur due to temperature and autogenous shrinkage effects, the concrete deformations are restrained which causes stress to develop. The concrete stress developed in the RCF is influenced by the temperature change, coefficient of thermal expansion, modulus of elasticity, creep (relaxation), and autogenous shrinkage. For the RCF, the deformation of concrete is restrained by the Invar bars; however, the stiffness of the Invar bars is such that some small deformation is allowed to occur. Therefore, the degree of restraint that the Invar bars provide for the maturing concrete needs to be considered when predicting the concrete stress development in this test.

15.4.2 Early-Age Concrete Stress Development Database

Experimental results from Byard (2011) were used here to calibrate the model proposed herein. Twenty-two concrete mixtures with different aggregate type and curing conditions were tested. Concretes tested contained coarse normalweight aggregate that included river gravel (RG) and limestone (LS). In addition, lightweight aggregates (LWA) that consisted of expanded clay, shale, and slate were used to produce internal curing (IC), and sand-lightweight (SLW), and all-lightweight (ALW) concretes. The SLW concrete contains coarse LWA and fine normalweight aggregate. The ALW concrete's coarse and fine aggregates are both LWA. The IC concrete contained coarse normalweight aggregate and a small portion of fine normalweight aggregate was replaced with prewetted fine LWA. The 22 concretes with a water-to-cement ratio (*w/c*) of 0.42 were tested under both fall (Fall) and summer (Sum) simulated temperature conditions. Simulation of summer-time placement started with a concrete temperature of 95 °F and fall season started with a concrete temperature of 73 °F. All concretes used Type I cement without any supplementary

cementing materials. The mixture proportions of four example concretes with four different coarse aggregate types are presented in Table 15-1. The measured and predicted stress development for these four concretes will be shown as examples herein.

Table 15-1 Sample mixture proportions

Item	0.42 Clay SLW (Sum)	0.42 Shale SLW (Sum)	0.42 LS (Sum)
Water Content (lb/yd^3)	276	276	260
Type 1 Cement Content (lb/yd^3)	658	658	620
Water-Reducing Admixture (oz/yd^3)	52.6 (High-Range)	39.5 (High-Range)	31
Coarse Aggregate (lb/yd^3)	1029 (SD Lightweight Clay)	933 (SD Lightweight Shale)	1760 (SSD Limestone)
Fine Aggregate (lb/yd^3)	1316 (SSD River Sand)	1354 (SSD River Sand)	1211 (SSD River Sand)
Total Air Content (%)	5.5	5.5	5.5
Water-to-cement Ratio (*w/c*)	0.42	0.42	0.42

Note: SD = pre-wetted surface dry; SSD = saturated surface dry

These concretes are designed for use in bridge deck applications, with a changing temperature caused by differences in the concrete mixture proportions, thermal conductivity of the aggregate, placement temperature, ambient temperatures, solar radiation, weed speed, and so on. The simulated bridge deck temperatures in the RCF for summer and fall placements were determined for Montgomery, Alabama on construction dates of August 15 and October 15, respectively by

using heat transfer software that accounts for the concrete's heat of hydration (Byard 2011). Figure 15-3 shows the temperature history of two example concrete mixtures with summer and fall season placement conditions, respectively. After concrete placement, the temperature starts to rise because of the heat of hydration of the cement. After reaching the peak temperature, the concrete gradually cools down to the ambient temperature. By using simulated concrete temperature profiles for bridge deck applications, there are small up and down fluctuations in temperature caused by changes in solar radiation and ambient temperature effects, which lead to the thermal induced loading and unloading effects in the concrete specimens.
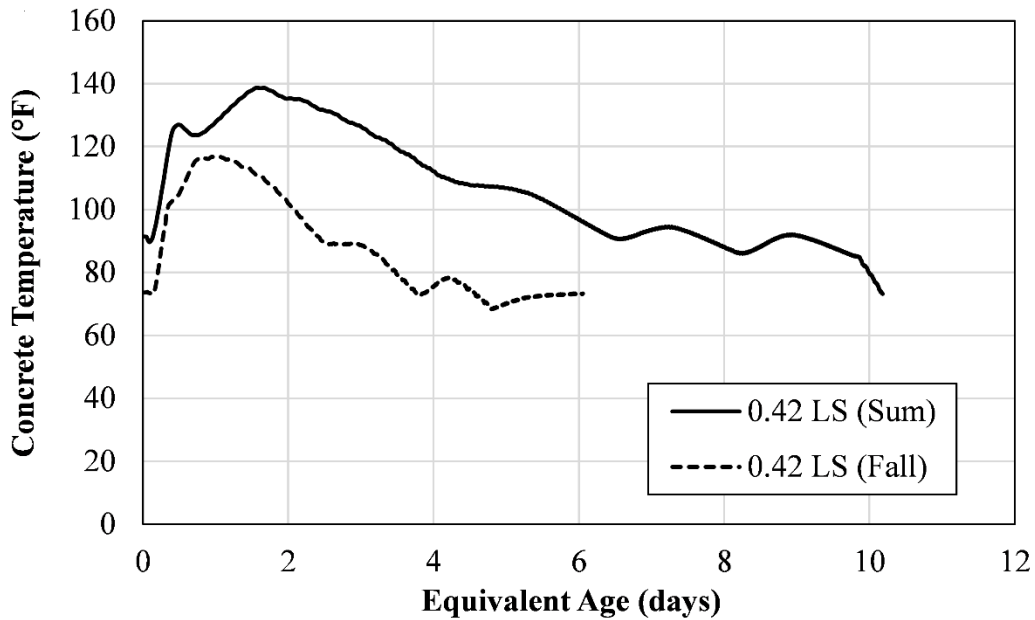
Figure 15-3 Concrete temperature histories of two example concrete mixtures

CHAPTER 16 PART III: FINITE-ELEMENT MODEL

Eight-node, linear hexahedral (brick) elements with three translational degrees of freedom at each node (C3D8) were used for the FEM. For the rigid cracking frame (RCF), the deformation of concrete is restrained by the Invar bars, and at the same time there is always some deformation in the Invar bars. These strains were captured by modeling the two Invar bars in the FEM of the RCF. The FEM mesh for the RCF with concrete is shown in Figure 16-1. The Invar side bars were assigned a modulus of elasticity of 21,500 ksi to match that of Invar. The crossheads at the two ends were assigned a very high modulus of elasticity to function as a rigid body to restrain both the concrete and Invar bars.
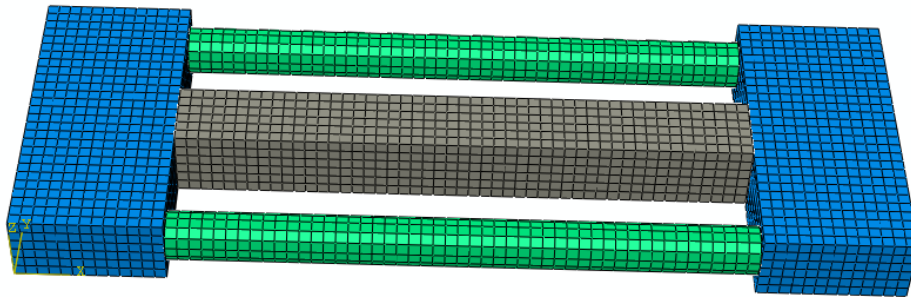
Figure 16-1 Mesh of finite-element model of rigid cracking frame

The concrete temperature profiles and CTE values of each concrete mixture were input into the FEM. Next, the thermal strain was calculated based on the CTE, and the small deformations of the Invar bars were calculated by the FEM itself and considered with the thermal strain to get the final strain to calculate the concrete stresses. Next, based on the strain increment in each time step and the compliance subroutine, the stress with time was calculated and output from the FEM. The effect of varying concrete temperatures on all concrete properties was considered by using the

equivalent-age maturity method (Carino 2004). Therefore, all ages mentioned in this study, unless stated differently, are presented in equivalent age. Since the concrete in the RCF was sealed, no moisture loss occurred; therefore, drying creep and drying shrinkage were neglected.

16.1   MODELING CREEP IN THE FEM

The Modified B3 Model was shown to accurately predict early-age concrete stress development in Part I of this dissertation. The details of the Modified B3 Model is presented in Section 4.6.2. Details of incorporating the creep model into the finite-element program has been discussed in Section 6.1.

16.2   MODEL FOR COMBINING HIGH-STRESS NONLINEARITY AND CREEP

The stress development predicted by using FEM and the Modified B3 Model without considering high-stress nonlinearity and the measured stress development for the 0.42 LS (Sum) mixture are shown in Figure 16-2. Since the concrete tensile strength development is different in the RCF specimen than the splitting tensile specimen, the tensile strength development in the RCF was obtained from testing splitting tensile strength specimens (Byard and Schindler 2015). This was done by determining a scaling factor, which equals the ratio of measured stress at cracking in the RCF to the cylinder splitting tensile strength at the same equivalent age (Byard and Schindler 2015). In Figure 16-2, a curve is shown to define the 70% of the scaled strength development to distinguish the stress part below $70\% f'_t$ for linear-elastic analysis and the part above $70\% f'_t$ includes the effect of high-stress nonlinearity. From this figure, it can be seen that the Modified B3 Model with linear-elastic feature overestimates the tensile stress at high-stress levels.

183
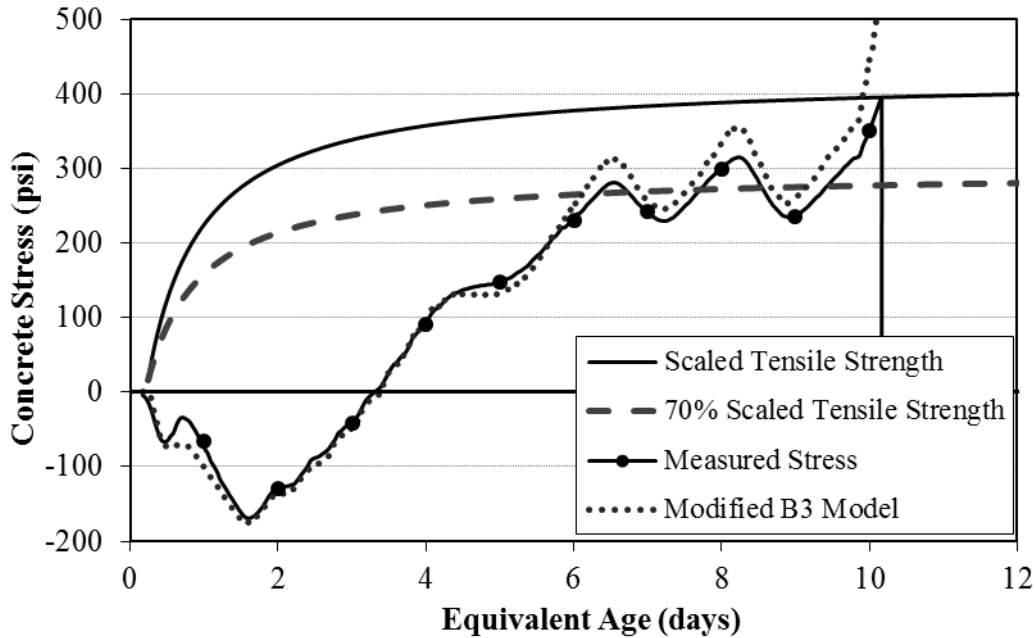
Figure 16-2 Measured and Modified B3 Modeled stress development with scaled strength development for mixture 0.42 LS (Sum)

The predicted versus measured concrete stress residuals versus concrete age relative to cracking age in equivalent age expressed as a percent is shown in Figure 16-3. These residuals are only shown for the data above $70\% f'_t$. Also presented in Figure 16-3, are the various percentages of the data points that fall within the following four residual stress ($\sigma_{Residual}$) ranges: $\sigma_{Residual} <$ -50 psi, -50 psi $\leq \sigma_{Residual} < 0$ psi, 0 psi $\leq \sigma_{Residual} < 50$ psi, and 50 psi $\leq \sigma_{Residual}$. From Figure 16-3, it can be seen that the Modified B3 Model without considering high-stress nonlinearity, tends to overestimate the measured stress, as 83% of data points are above the zero stress residual and 32% of the data points are overestimated by 50 psi or more. Therefore, the Modified B3 Model as proposed by Byard and Schindler (2015) needs to be corrected to account for the effects of high-stress nonlinearity.
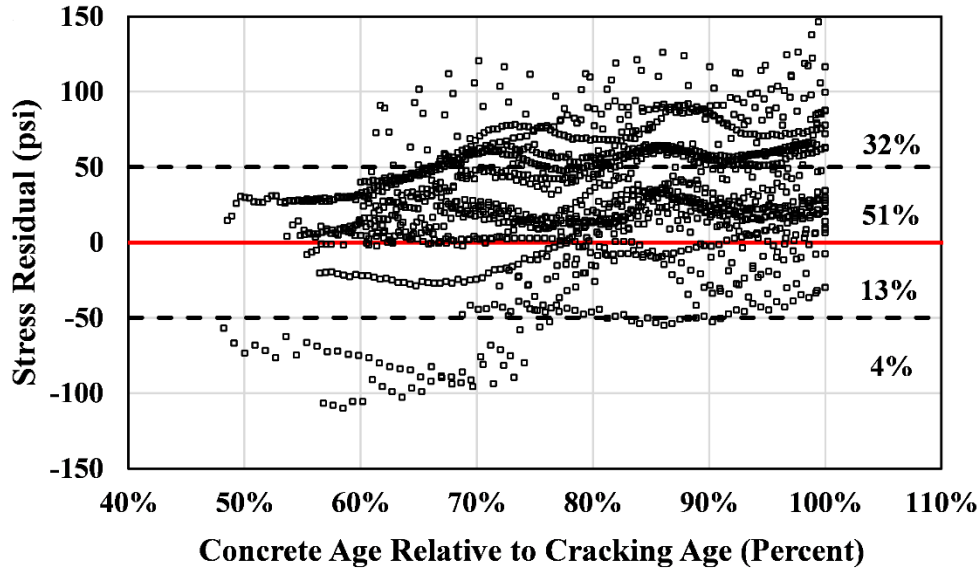
Figure 16-3 Residual result for stress above 70%f'_t by Modified B3 Model without considering high-stress nonlinearity

The approach with the nonlinear stress effect, $F(\sigma)$, as proposed by Bažant and Prasannan (1989a) is used herein. The effective incremental modulus is replaced by a reduced modulus when the concrete tensile stress exceeds 70%f'_t to account for the effect of high-stress nonlinearity. Bažant et al. (2012) reduced the effective incremental modulus, E'', for the current time step to $E''/4$ when the concrete tensile stress exceeds 70% of its strength. Similarly, the effective incremental modulus, E'', for the current time step is modified to $D \times E''$ when the tensile stress in concrete exceeds 70%f'_t, and herein D values of 1.0, 1/4, 1/2, and 2/3 will be evaluated to assess the accuracy of this approach. In order to assess the response of the original Modified B3 Model, a D value of 1.0 is used, and for the Bažant et al. (2012) approach, a D value of 1/4 was used.

Due to temperature fluctuations, thermal unloading and reloading occurs in the specimen as can be seen in Figure 16-2. Jonasson (1994) and Heldlund (2000) proposed a model with the unloading path follows an elastic modulus, and experimental results from Chen et al. (2016) also showed an

185

elastic unloading curve. Therefore, for unloading, the stress always corresponds to a path-independent elastic modulus. Reloading proceeds along the same path as unloading until again reaching $70\% f'_t$, after which it will again start to follow inelastic behavior due to high-stress nonlinearity. When unloading occurs, the concrete will respond with an unreduced incremental modulus E'', regardless the stress is below or above $70\% f'_t$. Therefore, when the stress is in reloading stage the following cases could occur: 1) if the stress is less than 70% f'_t, it will behave with an unreduced modulus E'', and 2) if the stress exceeds $70\% f'_t$, it will behave with a reduced modulus $D \times E''$. An example of unloading and reloading stress states is shown in Figure 16-4. When $\sigma(t) \leq 70\% f'_t$ the following stages apply: 1) stage I (all ages before the stress first exceeds $70\% f'_t$) where the incremental modulus $= E''$, 2) stage IV (a part of stress unloading) where the incremental modulus $= E''$, and 3) stage V (a part of stress reloading) where the incremental modulus $= E''$. When $(t) > 70\% f'_t$ the following stages apply: 1) stage II where the incremental modulus $= D \times E''$, 2) stage III (a part of stress unloading) where the incremental modulus $= E''$, and 3) stage VI (a part of stress reloading) where the incremental modulus $= D \times E''$.
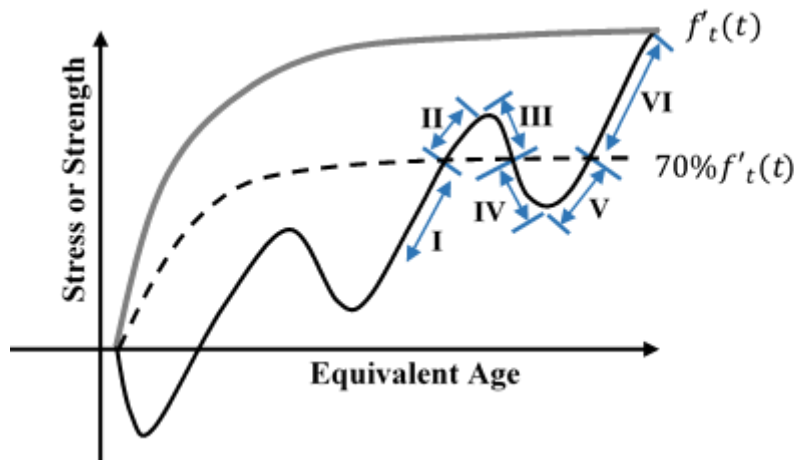
Figure 16-4 Stress with equivalent age diagram to illustrate various loading and unloading stages

CHAPTER 17 PART III: RESULTS AND DISCUSSIONS OF RESULTS

17.1   ASSESSMENT OF ACCURACY OF STRESS PREDICTIONS

17.1.1 Stress Residual Assessment

The stress residual analysis provided herein consists of calculating the difference between the measured stress and the predicted stress. Al-Manaseer and Lam (2005) also used the residual stress assessment method to assist with the visual evaluation of accuracy of various shrinkage and creep models. The stress residual value is calculated by Equation 17-1. A positive stress residual means the predicted stress is greater than the measured stress and means the stresses are overestimated, and vice versa.

$$\sigma_{Residual} = y_i - f_i \qquad \textbf{(Equation 17-1)}$$

Where,

$\sigma_{Residual}$ = stress residual (psi),

y_i = predicted stress (psi) from FEM, and

f_i = measured stress (psi).

17.1.2 Statistical Assessment

To evaluate how well a model predicts the measured stress, the coefficient of determination (r^2) and unbiased estimate of standard deviation (Sj) were determined to provide more information quantitative other than the residual stress analysis presented above. Equation 17-2 defines the calculation of the coefficient of determination and Equation 17-3 expresses the unbiased estimate of standard deviation of the absolute error (Montgomery et al. 2015).

$$r^2 = 1 - \frac{SS_{Res}}{SS_T}$$

$$S_j = \sqrt{\frac{1}{n-1}\sum_1^n(y_i - f_i)^2}$$

Where,

SS_{Res} = sum of squares of the error (psi^2) =$\sum(y_i - f_i)^2$,

SS_T = total sum of square of the error (psi^2) = $\sum(y_i - \bar{y}_i)^2 = \sum y_i^2 - n\bar{y}^2$,

$\bar{y}$ = mean measured data (psi),

S_j = unbiased estimate of the standard deviation of the absolute error (psi), and

n = number of data points (unitless).

The coefficient of determination (r^2) provides a measure of how well the predicted data represents measured data set. The closer the r^2 values to 1, the better the prediction model. The smaller the value of Sj, the less deviation of the predicted value to the measured data, the better the prediction model.

17.2 EXAMPLE OF RESULTS

The measured stress development and the stress development predicted with the FEM with reduced effective modulus are plotted versus equivalent age in Figure 17-1. Negative values represent compressive stress and positive values represent tensile stress. Immediately following final set, compressive stress develops due to the rise in concrete temperature and the restraint of concrete expansion. When the concrete begins to cool, tensile stresses develop because the concrete is

188

restrained against contraction. After the concrete goes to tension, the stress generally increases but fluctuates up and down because of the fluctuating temperature changes. From the results in Figure 17-1, it can be seen that the stress predicted from the FEM in the elastic range matches well with the experimental result; however, in the range above 70% f_t' (delineated as Region B in Figure 17-1) where tensile stress level is high, the Modified B3 Model without considering high-stress nonlinearity significantly overestimates the measured tensile stresses.

Also shown in Figure 17-1 are the predicted stress results for the three models with different reduced effective incremental modulus with $D=1/4$, 1/2, and 2/3, respectively. The smaller the value of D, the more stress is reduced in the high tensile stress level. It can be seen that the model with $D=1/4$ reduces the predicted stress too much at a high stress level, which leads to underestimation of the measured stress. Whereas, it can be seen that the two models with $D=1/2$ and $D=2/3$ more accurately predict the measured stress and effectly capture the effect of high-stress nonlinearity. There also does not appear to be too much difference in the stress predicted with the two models with $D=1/2$ and $D=2/3$. The goodness of fit attained by these two models will be future evaluated by the residual and regression analysis results that will be covered in the following sections.
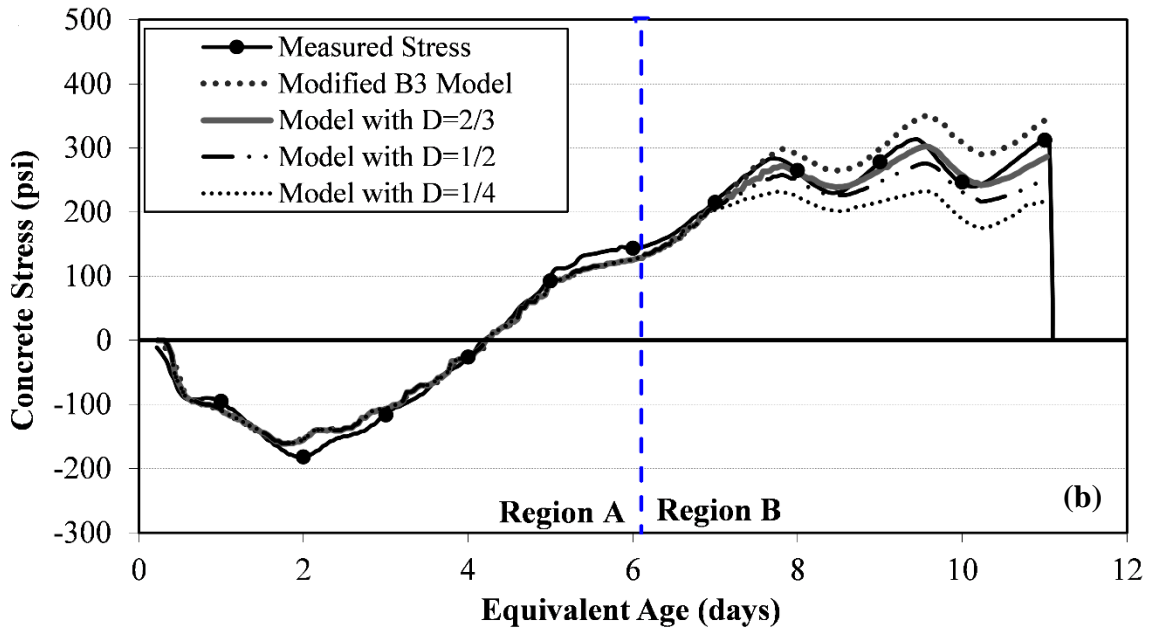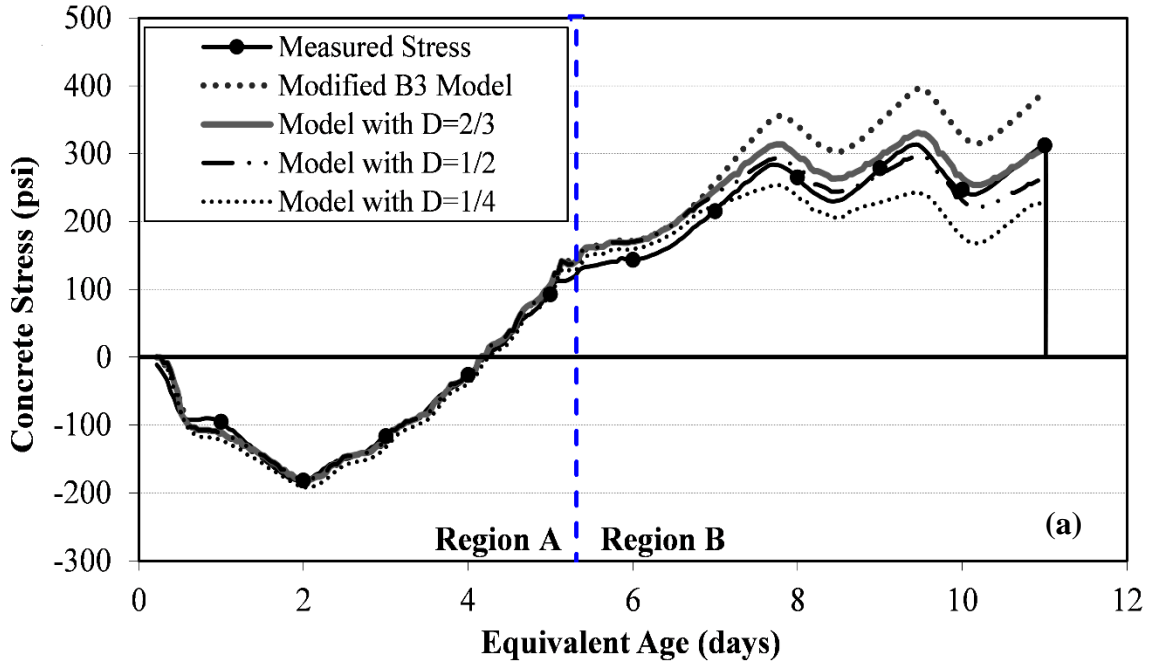
Figure 17-1 Stress development results for: (a) 0.42 Shale SLW (Sum), (b) 0.42 Clay SLW (Sum) [Region A: $\sigma(t) \leq 70\% f_t'(t)$, Region B: $\sigma(t) > 70\% f_t'(t)$]

17.3   RESIDUAL ANALYSIS RESULTS

The predicted versus measured concrete stress residuals versus concrete age relative to cracking age in equivalent age expressed as a percent for the three models with reduced effective modulus are shown in Figure 17-2 to Figure 17-4. The concrete age relative to cracking age is used here for two reasons: 1) when the concrete approaches cracking, the stress level is high and if the effect of high-stress nonlinearity is not considered, the stress residuals are higher values; and 2) different concrete mixtures have different final cracking ages. Additionally, the use of the concrete age relative to cracking age expressed as percent is used to equally evaluate the general trend for all the tested mixtures. The differences of the four proposed models lie in the inelastic range that is above 70% f_t', therefore only data points above 70% f_t' are used in Figure 17-2 to Figure 17-4 to verify the effect of high-stress nonlinearity. Also presented in Figure 17-2 to Figure 17-4, are the various percentages of the data points that fall within the following four residual stress ranges: $\sigma_{Residual} < $ -50 psi, -50 psi $\leq \sigma_{Residual} < 0$ psi, 0 psi $\leq \sigma_{Residual} < 50$ psi, and 50 psi $\leq \sigma_{Residual}$.

The stress residual analysis result for the original Modified B3 Model without considering high-stress nonlinearity tends was previously shown in Figure 16-3. It can be seen in Figure 16-3 and Figure 17-2 to Figure 17-4 that for the Modified B3 Model, the models with $D=1/4$, $D=1/2$, and $D=2/3$, the residuals that fall in the range of ±50 psi are 64%, 71%, 91% and 95%, respectively. This quantifies that the Modified B3 Model without considering high-stress nonlinearity tends has the least data points that fall in the ±50 psi residual range. It can also be observed from Figure 16-3 that the data points in the Modified B3 Model generally have an ascending trend, which clearly indicates an increasing trend to overestimate the stress as cracking is approached. The models with $D=1/2$ and $D= 2/3$ both have more than 91% of the data points that fall within the range of ±50 psi, which is a significant improvement in prediction accuracy when compared to the Modified B3

Model which only has 64% in that range. When considering stress residuals exceeding 50 psi and less than -50 psi for the Modified B3 Model in Figure 16-3, the data points are more spread out, whereas the stress residuals for the models with $D=1/2$ and $D=2/3$ in Figure 17-3 and Figure 17-4 fall in a much narrower band as cracking is approached.
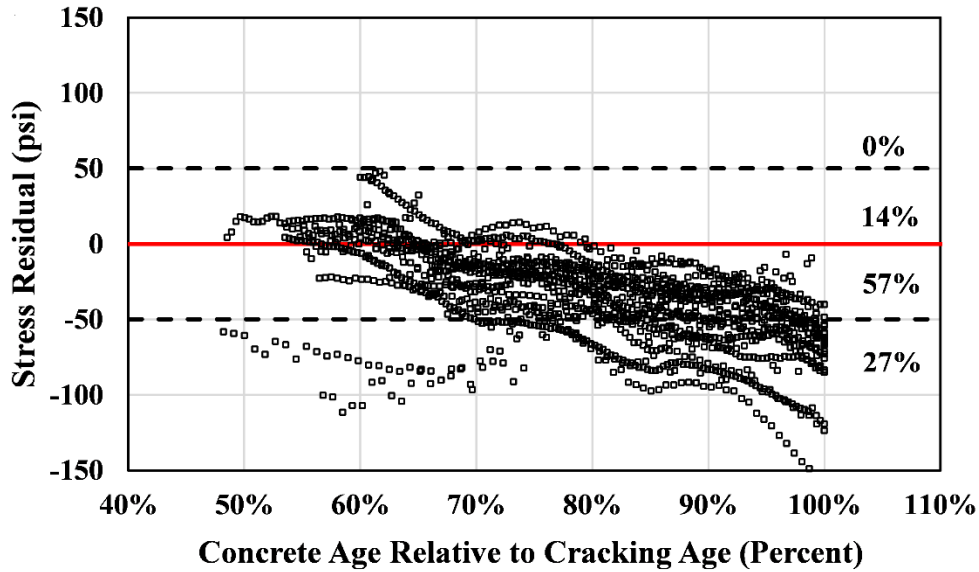
Figure 17-2 Residual results for stress above 70%f_t' by model with $D=1/4$
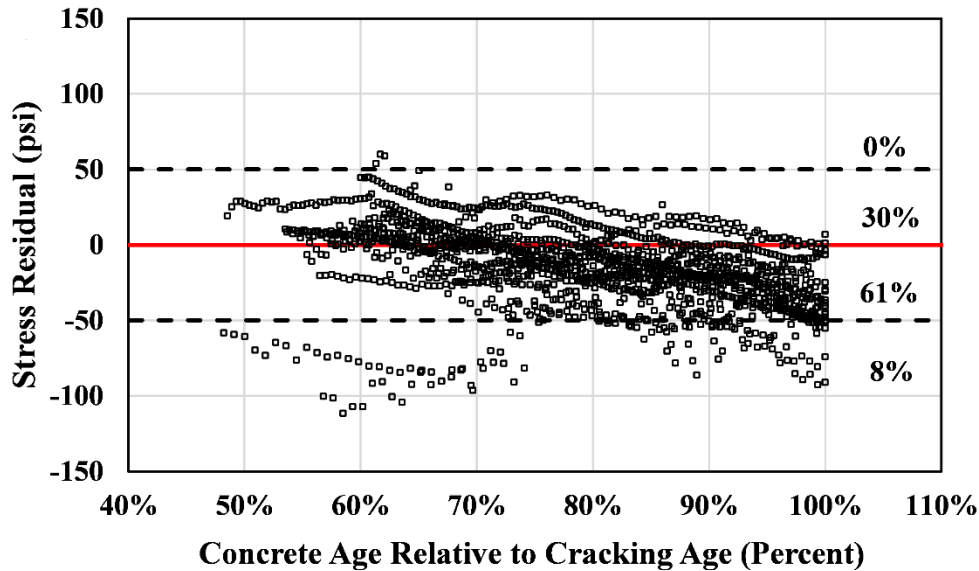
Figure 17-3 Residual results for stress above 70%f_t' by model with $D=1/2$
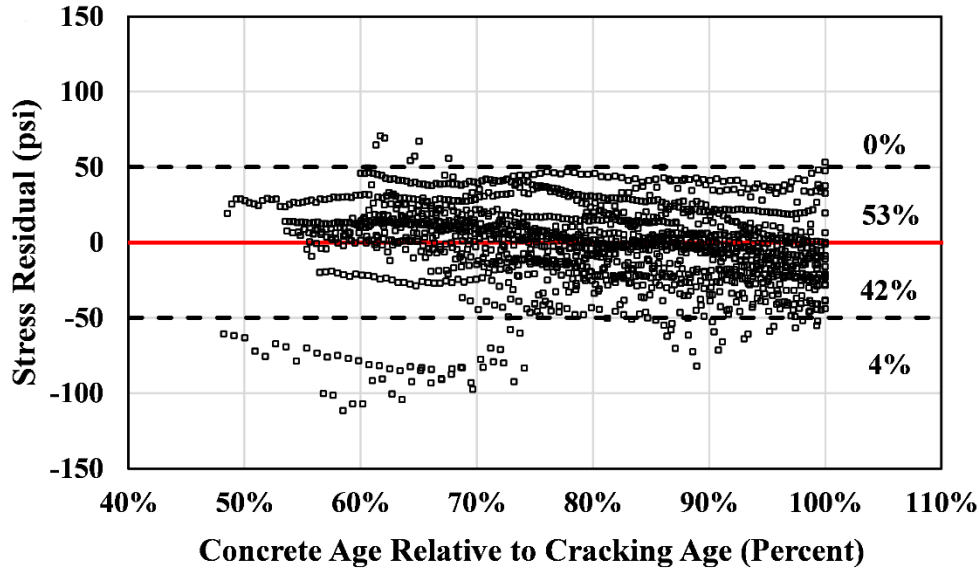
Figure 17-4 Residual results for stress above 70%f'_t by model with D=2/3

The model with D=1/4 shown in Figure 17-2 underestimates the majority of the measured stresses with a total of 84% data points below the zero stress residual. The model with D=1/2 shown in Figure 17-3 overestimates 30% of the measured stresses in the range from 0 to 50 psi, and underestimates 61% of the stresses in the range from 0 to -50 psi. The model with D=2/3 shown in Figure 17-4 overestimates 53% of the measured stress in the range from 0 to 50 psi, and underestimate 42% in the range from 0 to -50 psi. Therefore, the model with D=2/3 provides equally well balanced estimates in the positive and negative stress residual ranges compared to the other three models, which indicates that there is little to no bias to either underestimate or overestimate the measured stresses. Therefore, the proposed model with D =2/3 has two improvements, one is to balance the overestimation and underestimation error, and another advantage is to reduce the error between the predicted and measured stress from setting to cracking.

17.4   STATISTICAL ANALYSIS RESULTS

The r^2 and Sj values for the predicted versus measured stress by the proposed four models for the stress part beyond 70% of tensile strength with original Modified B3 Model (MB3), reduced incremental modulus of $E''/4, E''/2,$ and $2E''/3$ for each concrete are presented in Table 17-1. The overall r^2 and Sj values computed for all the data collected for all 22 concretes are also presented at the bottom of Table 17-1, and provide a measure of how well the four models predict the measured stress at the high tensile stress level.

From Table 17-1 can be seen that the overall r^2 of the original Modified B3 Model is 0.39 which is the lowest, and its Sj equals 49 psi which is the highest among the four models. The model with $D=2/3$ has the highest overall r^2 value of 0.81 and the smallest Sj value of 27 psi; therefore, this model performs the best compared to the other models considered. For the model with $D=2/3$, the overall r^2 value of 81% for all the data sets suggests that 81% of the error in data is explained by the model.

Also analyzed, is the overall accuracy of the models considering the stress development from initial setting to cracking stress. The overall models describe both the linear-elastic part and the high stress level part when stresses are above $70\% f_t'$. The r^2 values for the predicted versus measured stress with data points from initial setting to cracking for the original Modified B3 Model, and models with $D=1/4$, $D=1/2$, and $D=2/3$ are 0.931, 0.937, 0.962, and 0.965, respectively. The Sj values for original Modified B3 Model, models with $D=1/4$, $D=1/2$, and $D=2/3$ are 38 psi, 36 psi, 28 psi, and 27 psi, respectively. Therefore, it can be concluded from these results that the Modified B3 Model with $D=2/3$ provides the most accurate estimate of the measured stress from setting to cracking.

Table 17-1 Statistical results for data above 70%f'_t for the four models with different reduced effective modulus and summary data for all data collected

Mixture	r^2				Sj (psi)			
	$D=1$	$D=1/4$	$D=1/2$	$D=2/3$	$D=1$	$D=1/4$	$D=1/2$	$D=2/3$
0.42 Slate IC (Fall)	0.44	-0.73	-0.14	0.16	25	44	36	31
0.42 Slate IC (Sum)	-0.19	-0.28	-0.19	-0.15	46	47	46	45
0.42 Slate SLW (Fall)	0.68	-5.83	-1.31	0.38	18	85	49	26
0.42 Slate SLW (Sum)	0.90	0.59	0.88	0.98	19	38	20	8
0.42 Slate ALW (Fall)	-6.30	-4.09	0.42	0.46	54	45	15	15
0.42 Slate ALW (Sum)	-10.04	-2.40	-1.52	-1.33	81	45	39	37
0.42 Clay IC (Fall)	0.72	0.37	0.66	0.83	19	28	21	15
0.42 Clay IC (Sum)	0.98	0.73	0.84	0.88	7	29	22	19
0.42 Clay SLW (Fall)	0.47	-4.23	-1.21	0.52	21	67	44	20
0.42 Clay SLW (Sum)	-0.08	0.13	0.86	0.90	45	40	16	14
0.42 Clay ALW (Fall)	-10.43	0.18	0.34	-1.46	86	23	20	40
0.42 Clay ALW (Sum)	-1.18	-2.34	0.53	0.94	53	66	25	9
0.42 Shale IC (Fall)	0.66	-0.31	0.62	0.88	23	44	24	13
0.42 Shale IC (Sum)	0.87	0.52	0.81	0.91	22	43	27	18
0.42 Shale SLW (Fall)	0.51	0.04	0.74	0.94	22	31	16	8
0.42 Shale SLW (Sum)	-0.29	0.33	0.83	0.79	63	45	23	25
0.42 Shale ALW (Fall)	-16.32	-3.32	0.76	-1.75	66	33	8	26
0.42 Shale ALW (Sum)	-4.65	-0.15	0.27	-0.83	57	26	21	33
0.42 RG (Fall)	-0.62	-1.13	-0.78	-0.70	58	66	60	59
0.42 RG (Sum)	-1.40	-1.64	-1.37	-1.26	61	63	60	59
0.42 LS (Fall)	0.74	0.50	0.73	0.75	21	29	21	20
0.42 LS (Sum)	0.24	0.59	0.93	0.93	33	24	10	10
All Data Points	**0.39**	**0.46**	**0.78**	**0.81**	**49**	**46**	**30**	**27**

CHAPTER 18 PART III: CONCLUSIONS

A three-dimensional, finite-element model of concrete subjected to restraint to volume change tests was developed and its results were compared to experimental results. This FEM was used to simulate the early-age concrete stress development from setting to cracking considering temperature histories, changing mechanical properties, and creep effects. The high-stress nonlinearity coupled with creep effects were considered by reducing the incremental effective modulus E'' to $D \times E''$ when the concrete tensile stress is above 70% of its tensile strength. Four models with different damage factor (D) values of 1/4, 1/2, 2/3, and 1 were evaluated to assess their accuracy to predict early-age concrete stresses at stress levels above 70% of its tensile strength. The experimental results of 22 concretes subjected to restraint to volume change tests were used to verify the accuracy of the proposed FEM from initial setting to the age of cracking. The concretes tested had varying aggregate types and chemical admixtures, and they were tested under different temperature histories. The results presented in this part of this dissertation support the following conclusions:

- The finite-element model with D=2/3 provides accurate predictions of measured early-age concrete stresses from initial setting to the age of cracking.

- The residual analysis of the Modified B3 Model, and models with D=1/4, D=1/2, and D=2/3 show that the Modified B3 Model without considering high-stress nonlinearity overestimates the early-age concrete stresses that above $70\% f_t'$, while the model with D=1/4 significantly underestimates the measured stresses. The model with D=2/3 provides equally well balanced estimates in the positive and negative stress residual ranges.

- The statistical analysis of concrete stress based on the Modified B3 Model, and models with $D=1/4$, $D=1/2$, and $D=2/3$, resulted in r^2 of 0.39, 0.46, 0.78, and 0.81, and S_j of 49 psi, 46 psi, 30 psi, and 27 psi, respectively when all the stress data considering above a concrete tensile strength of 70%. These results show that the Modified B3 Model with $D=2/3$ provides the most accurate predictions of the early-age concrete stress development from initial setting to the age of cracking.

CHAPTER 19 OVERALL SUMMARY, CONCLUSIONS, AND RECOMMENDATIONS

19.1   SUMMARY

Early-age cracking of concrete may influence the long-term durability of a structure (Darwin and Browning 2008). Cracking occurs when the tensile stress in concrete exceeds its tensile strength. Early-age stress development in concrete is influenced by temperature changes, modulus of elasticity, creep or stress relaxation, shrinkage, coefficient of thermal expansion, and the degree of restraint. Three-dimensional, finite-element model (FEM) was used to simulate the early-age stress development of concrete. This study include three main parts: 1) finite-element modeling of early-age concrete stress development with four creep models, 2) finite-element modeling of and analysis of early-age cracking risk of cast-in-place concrete culverts, and 3) finite-element modeling of early-age concrete stress behavior under high-level of tensile stress.

For Part I, the FEM was used to simulate the early-age concrete stress development considering temperature histories, changing mechanical properties, and creep effects. Four creep compliance models including the B3 Model, Modified B3 Model, B3 Model with RT, and B4 Model were incorporated in the finite-element model. Experimental results from restraint to volume change tests with rigid cracking frames were used to assess the accuracy of the finite-element analysis with the four creep models. The experimental tests include 72 concrete mixtures, which contain varying cementitious materials, mixture proportions, temperature histories, aggregate types, water-to-cementitious materials ratios, and chemical admixtures.

For Part II, measures to mitigate early-age cracking in culverts by evaluating the cracking risk were analyzed, because extensive cracking was found in several cast-in-place concrete culverts in

Alabama that can decrease the long-term durability. Finite-element analysis was used to model the early-age stress by accounting for the following factors: construction sequencing, support restraint, concrete constituents, temperature effects, the time-dependent development of mechanical properties, creep/relaxation, and drying shrinkage. A parametric study was performed to quantify the effect of changing joint spacing, joint type, construction sequence, concrete coefficient of thermal expansion, placement season, and concrete type on the early-age cracking risk. The FEM results revealed the measures to reduce the risk of early-age cracking in cast-in-place concrete culverts.

For Part III, nonlinear behavior at high tensile stresses is considered in the FEM. Most models are for the elastic and time-dependent behavior at normal stress levels in which the effect of cracking or the level of tensile stress is not considered. However, high-stress nonlinearity coupled with creep is of paramount importance when determining the cracking risk of concrete. Nonlinear behavior at high tensile stresses is present in concrete and should be considered to obtain an accurate cracking risk analysis. The Modified B3 Model was proved to be the most accurate models for early-age concrete stress modeling compared to other evaluated models used in Part I. Therefore, the high-stress nonlinearity was considered in this study by correcting the Modified B3 Model with a reduced effective modulus when the tensile stress is above 70% of its tensile strength. The experimental results of 22 concrete mixtures subjected to restraint to volume change tests were used to verify the accuracy of the proposed FEM from initial setting to the age of cracking. The statistical assessment method and stress residual method were used to determine the accuracy of the proposed models compared to the original linear-elastic model.

19.2   CONCLUSIONS

The focus of Part I was to investigate the level of accuracy of four creep models including the B3 Model, Modified B3 Model, B3 Model with R_T, and B4 Model that were incorporated in the three-dimensional, FEM. Early-age stress development from restraint to volume change tests from 72 concretes were used to verify the accuracy of the four creep models. The stress residual method of comparing predicted stress to measured stress, and the statistical assessment method to determine the coefficient of determination r^2 and unbiased estimate of standard deviation Sj were used to analyze the stress data. The research presented in Part I support the following conclusions:

- The FEM provides accurate predictions of measured early-age concrete stresses.

- The residual analysis of the four creep models show that the B3 Model and B4 Model generally overestimate the early-age concrete stress, while the B3 Model with R_T underestimates the stresses. The B4 Model significantly overestimates the early-age compressive stress when its modifiers for concrete constituents are induced. The Modified B3 Model provides the best prediction of early-age concrete stresses.

- The statistical analysis of stress results based on the B3 Model, Modified B3 Model, B3 Model with RT, and B4 Model resulted in r^2 of 0.83, 0.88, 0.82, -0.15 and Sj of 66 psi, 56 psi, 69 psi and 172 psi, respectively for all the data in the database. These results show that the Modified B3 Model provides the most accurate predictions of the early-age concrete stress among the models considered.

The focus of Part II was to investigate measures to mitigate the early-age cracking risk of cast-in-place concrete culverts. A three-dimensional, FEM of cast-in-place concrete culverts was developed. The calibrated FEM was used to determine the influence of changing the contraction

joint spacing, two concrete coefficient of thermal expansion values, three placement seasons, two joint types, three construction sequences, and three concrete types on early-age cracking risk. The research presented in Part II support the following conclusions:

- The cracking risk of the culvert wall, base, and roof was found to be high, moderate, and low, respectively, which explains why many surveyed culverts had wide cracks primarily in walls and bases.

- The practical contraction joint spacing evaluated in this study only significantly influences the cracking risk in the culvert base, but has little effect on the cracking risk of the wall. This is because the base provides a very high degree of restraint to the wall.

- Use of contraction joints can help significantly decrease the cracking risk in culvert base compared to use of tied-construction joints, but they do not have a significant effect on the maximum cracking risk in the culvert wall.

- Wall cracking risk increases with the age (maturity) of the base concrete at the time when the wall is constructed. Use of a construction sequence that attains the youngest (lowest stiffness) base when the wall is cast, reduces the cracking risk in the wall.

- Hot weather construction leads to the highest cracking risk, while cold weather placement results in a much smaller cracking risk, with fall placement conditions in between these two extremes.

- Use of a lower coefficient of thermal expansion concrete decreases the cracking risk in the base and wall.

- Use of sand-lightweight concrete or all-lightweight concrete significantly decrease the cracking risk in the culvert compared to using normalweight concrete. The all-lightweight concrete most decreases the cracking risk among the three concrete types evaluated.

201

Part III is focused on the nonlinear behavior at high tensile stresses by using the FEM to predict stresses from setting to cracking. High-stress nonlinearity coupled with creep effects were considered by reducing the incremental effective modulus E'' to $D \times E''$ when the concrete tensile stress is above 70% of its tensile strength. Four models with different damage factor (D) values of 1/4, 1/2, 2/3, and 1 were evaluated to assess their accuracy to predict early-age concrete stresses at stress levels above 70% of its tensile strength. The experimental results of 22 concretes subjected to restraint to volume change tests were used to verify the accuracy of the proposed FEM from initial setting to the age of cracking. The concretes tested had varying aggregate types and chemical admixtures, and they were tested under different temperature histories. The results presented in this part support the following conclusions:

- The FEM with $D=2/3$ provides accurate predictions of measured early-age concrete stresses from initial setting to the age of cracking.

- The residual analysis of the Modified B3 Model, and models with $D=1/4$, $D=1/2$, and $D=2/3$ show that the Modified B3 Model without considering high-stress nonlinearity overestimates the early-age concrete stresses that above $70\%f_t'$, while the model with $D=1/4$ significantly underestimates the measured stresses. The model with $D=2/3$ provides equally well balanced estimates in the positive and negative stress residual ranges.

- The statistical analysis of concrete stress based on the Modified B3 Model, and models with $D=1/4$, $D=1/2$, and $D=2/3$, resulted in r^2 of 0.39, 0.46, 0.78, and 0.81, and Sj of 49 psi, 46 psi, 30 psi, and 27 psi, respectively when considering all the stress data above a concrete tensile strength of 70%. These results show that the

Modified B3 Model with $D = 2/3$ provides the most accurate predictions of the early-age concrete stress development from initial setting to the age of cracking.

19.3   RECOMMENDATIONS FOR FUTURE RESEARCH

In this section, some suggestions to improve future efforts to model early-age concrete stresses are given.

- Thermocouples and strain gauges should be embedded in full-scale concrete elements in order to obtain temperature history and strain data of in-place concrete. However, the strain data cannot be directly and easily used to calculate the thermal stress due to the complexities related to in-place restraint conditions. Therefore, the use of an instrument to measure in-place thermal stress in concrete at early-age, which is called stress meter, shall be considered.

- Stress data for full-scale concrete elements should be collected and a finite-element model of this structure should be developed. Comparisons of FEM stress results and stress meter results are needed to further validate the models proposed in this study and verify its applicability in structural elements.

REFERENCES

AASHTO 2016. *LRFD Bridge Design Specifications 7th Edition with 2016 interim revisions*. American Association of State Highway and Transportation Officials, Washington DC.

AASHTO T336. 2009. *Standard Method of Test for Coefficient of Thermal Expansion of Hydraulic Cement Concrete*. Washington D.C.: American Association of State Highway and Transportation Officials.

ACI 207 2007. *Report on Guide to Thermal and Volume Change Effects on Cracking of Mass Concrete*. American Concrete Institute (ACI 207.2R-07), Farmington Hills, MI.

ACI 209. 1971. *Report on Creep Shrinkage Temperature in Concrete Structures.* American Concrete Institute, Detroit, Michigan, 1971, sp. 27-13, pp. 258-269.

ACI 209. 1992. *Report on Prediction of Creep, Shrinkage, and Temperature Effects in Concrete Structures*. American Concrete Institute, Farmington Hills, MI.

ACI 209. 2008. *Guide for Modeling and Calculating Shrinkage and Creep in Hardened Concrete*. American Concrete Institute (ACI 209.2R-08), Farmington Hills, MI.

ACI 224. 1995. *Report on Joints in Concrete Construction*. American Concrete Institute (ACI 224.3R-95), Farmington Hills, MI.

ACI 224. 2001. *Report on Control of Cracking in Concrete Structures*. American Concrete Institute (ACI 224R-01), Farmington Hills, MI.

ACI 224. 2007. *Report on Causes, Evaluation, and Repair of Cracks in Concrete Structures*. American Concrete Institute, Farmington Hills, MI.

ACI 231. 2010. *Report on Early-Age Cracking: Causes, Measurement, and Mitigation*. American Concrete Institute, Farmington Hills, MI.

ACI 318. 2014. *Building Code Requirements for Structural Concrete and Commentary*. American Concrete Institute. Farmington Hills, MI.

ACI 350. 2001. *Code Requirements for Environmental Engineering Concrete Structures (ACI 350-01) and Commentary (ACI 350R-01)*. American Concrete Institute, Farmington Hills, MI.

ACI 360. 2006. *Report on Design of Slabs-on-Ground*. American Concrete Institute (ACI 360R-06), Farmington Hills, MI.

ACI CT-16. 2016. *Concrete Terminology-An ACI Standard*. American Concrete Institute, Farmington Hills, MI.

ALDOT. 2001. Proj. No. HPP-0192 (6) Anniston East Bypass Sta. 257+69 Calhoun County. Single 6'x6' Box Culv. (78' Fill Max). Alabama Department of Transportation (ALDOT).

ALDOT. 2010. General Notes and Miscellaneous Details. Standard Drawing CS-3-1. Alabama Department of Transportation (ALDOT).

ALDOT. 2012. *Standard Specifications for Highway Construction*. Alabama Department of Transportation (ALDOT).

Al-Manaseer, A., and J. Lam. 2002. *Statistical Evaluation of Shrinkage and Creep Models*. ACI Materials Journal, Vol. 102, No.3, pp. 170-176.

ASTM C 1074.2016. *Standard Practice for Estimating Concrete Strength by the Maturity Method*. ASTM International, West Conshohocken, PA.

ASTM C 403. 2016. *Standard Test Methods for Time of Setting of Concrete Mixtures by Penetration Resistance*. ASTM International, West Conshohocken, PA.

Bažant, Z.P., 1972. Numerical Determination of Long-Range Stress History from Strain History in Concrete. *Matériaux et Construction*, Vol. 5, No. 3, pp.135-141.

Bažant, Z. P. 1975. Theory of Creep and Shrinkage in Concrete Structures: A Precis of Recent Developments. *Mechanics Today*, 2, pp. 1-93.

Bažant, Z. P. 1982. Mathematical Models for Creep and Shrinkage of Concrete Structures. Creep and Shrinkage in Concrete Structures (ed. Bažant and Wittmann), John Wiley & Sons, New York, NY, pp. 163-256.

Bažant, Z. P., B. H. Oh. 1983. Crack band theory for fracture of concrete. *Matériaux et construction*, Vol. 16, No.3, pp. 155-177.

Bažant, Z.P., J. Chern. 1985. Strain softening with creep and exponential algorithm. Journal of Engineering Mechanics, Vol. 111, No. 3, pp. 391-415.

Bažant, Z. P., and S. Baweja. 2000. Creep and Shrinkage Prediction Model for Analysis and Design of Concrete Structures: Model B3. *ACI Special Publications*, 194, 1-84.

Bažant, Z. P., and S. Prasannan. 1989a. Solidification Theory for Concrete Creep. I: Formulation. *Journal of Engineering Mechanics*, Vol. 115, No. 8, pp. 1691-1703.

Bažant, Z. P., and S. Prasannan. 1989b. Solidification Theory for Concrete Creep. II: Verification and Application. *Journal of Engineering Mechanics*, Vol. 115, No. 8, pp. 1704-1725.

Bažant, Z. P., and S. S. Kim. 1979. Approximate Relaxation function for concrete. *ASCE Journal of Structural Division*, Vol. 105, No. 12, pp. 2695-2705.

Bažant, Z. P., and Y. Xi. 1995. Continuous Retardation Spectrum for Solidification Theory of Concrete Creep. *Journal of Engineering Mechanics*, Vol. 121, No. 2, pp. 281-288.

Bažant, Z. P., Y. Li. 1997. Cohesive crack with rate-dependent opening and viscoelasticity: I. Mathematical model and scaling. *International Journal of Fracture*, Vol. 86, No. 3, pp. 247–265.

Bažant, Z.P., M.H. Hubler, and M. Jirásek. 2013. Improved Estimation of Long-Term Relaxation Function from Compliance Function of Aging Concrete. *Journal of Engineering Mechanics*, Vol. 139, No. 2, pp. 146-152.

Bažant, Z. P., M. Hubler, and R. Wendner. 2014. Model B4 for Creep, Drying Shrinkage and Autogenous Shrinkage of Normal and High-Strength Concretes with Multi-Decade Applicability. TC-242-MDC multi–decade creep and shrinkage of concrete: material model and structural analysis. *RILEM Materials and Structures*, 48, pp. 753-770.

Bažant, Z. P., Q. Yu, and G. Li. 2012. Excessive Long-Time Deflections of Prestressed Box Girders. II: Numerical Analysis and Lessons Learned. *Journal of Structural Engineering*, Vol. 138, No.6, pp. 687-696.

Bentz, D.P., and W.J. Weiss. 2011. *Internal Curing: A 2010 State-of-the- Art Review*. Publication NISTIRR 7765. NIST, U.S. Department of Commerce.

Bentz, D.P., P. Lura, and J.W. Roberts. 2005. Mixture proportioning for internal curing. *Concrete International*, Vol. 27, No.2, pp. 35-40.

Bernander, S., S. Gustafsson. 1982. Temperature stresses in early age concrete due to hydration. *In Proceedings from International Conference on Concrete at Early Ages*, RILEM, Paris, France, Vol. 2, pp. 218-221.

Bosnjak, D. 2000. *Self-induced cracking problems in hardening concrete structures*. Doctoral Dissertation, The Norwegian University of Science and Technology, Trondheim, Norway

Byard, B. E. 2011. *Early-Age Behavior of Lightweight Aggregate Concrete. Doctoral Dissertation,* Auburn University, AL.

Byard, B. E., and A. K. Schindler, 2015. Modeling Early-Age Stress Development of Restrained Concrete. *Materials and Structures*, Vol. 48, No. 1-2, pp. 435-450.

Bjøntegaard, Ø. 2011. *Basis for and practical approaches to stress calculations and crack risk estimation in hardening concrete structures–State of the Art*. Norwegian Public Roads Administration.

Bosnjak, D. 2000. *Self-Induced Cracking Problems in Hardening Concrete Structures*. Doctoral Dissertation. The Norwegian University of Science and Technology, Trondheim, Norway.

Carino N. J. 2004. The Maturity Method. *Handbook on Nondestructive Testing of Concrete*, (Ed. by Malhotra V.M., and N.J. Carino), 2nd EDN. ASTM International, West Conshocken, pp. 5.1-5.47.

Castro, J., L. Keiser., M. Golias., and W. Weiss. 2011. Absorption and Desorption of Fine Lightweight Aggregate for Applications to Internally Cured Concrete Mixtures. *Cement and Concrete Composites*, Vol. 33, No. 10, pp. 1001-08.

Chen, X., J. Bu, L. Xu. 2016. Effect of strain rate on post-peak cyclic behavior of concrete in direct tension. *Construction and Building Materials*, Vol. 124, pp. 746-754.

Concrete Durability Center. 2005. Concrete Works Version 2.0 User's Manual. Sponsored by Texas Department of Transportation: Project 0-4563.

ConnDOT. 2000. Drainage Manual. Connecticut Department of Transportation (ConnDOT).

Darwin, D., and J. Browning. 2008. *Construction of Low Cracking High Performance Concrete (LC-HPC) Bridge Decks: Field Experience*. In Proceedings of Concrete Bridge Conference, National Concrete Bridge Council, Skokie, IL.

Dassault Systèmes Simulia Corp. 2012a. Abaqus Analysis User's Manual, Providence, RI, USA.

Dassault Systèmes Simulia Corp. 2012b. Abaqus User Subroutines Reference Manual, Providence, RI, USA.

Emborg. M. 1998. Development of Mechanical Behavior at Early Ages. In RILEM Report 15, *Prevention of Thermal Cracking in Concrete at Early Ages* (Ed. by R. Springenschmid), E&FN Spon, London, pp. 76–148.

Emborg, M. 1998. Models and Methods for Computation of Thermal Stresses. In RILEM Report 15, *Prevention of Thermal Cracking in Concrete at Early Ages* (Ed. by R. Springenschmid), E&FN Spon, London, pp. 178-222.

Expanded Shale Clay and Slate Institute. 2012. *ESCSI Guide Specifications for Internally Cured Concrete*, Information Sheet 4001.1, ESCSI.

FDOT. 2011. Plans Preparation Manual. Florida Department of Transportation (FDOT).

Gardner, N. J. 2004. Comparison of Prediction Provisions for Drying Shrinkage and Creep of Normal Strength Concretes, Canadian Journal for Civil Engineering, Vol. 31, No.5, pp. 767-775.

Gardner, N. J., and M. J. Lockman. 2001. Design Provisions for Drying Shrinkage and Creep of Normal Strength Concrete. *ACI Materials Journal*, Vol. 98, No. 5, pp. 159-167.

Goldbeck, A. T. 1924. Friction Tests of Concrete on Various Sub-Bases. *Public Roads*, Vol. 5, No. 5, pp. 19-20, 23.

Gopalaratnam, V.S., S. P. Shah. 1985. Softening response of plain concrete in direct tension. *In Journal Proceedings*, Vol. 82, No. 3, pp. 310-323.

Greene, G., and B.A. Graybeal. 2013. *Synthesis and Evaluation of Lightweight Concrete Research Relevant to the AASHTO LRFD Bridge Design Specifications: Potential Revisions for Definition and Mechanical Properties*. Publication FHWA –HRT-13-030. FHWA, U.S Department of Transportation.

Gutsch, A., and F. S. Rostasy. 1995. Young concrete under high tensile stresses-creep, relaxation and cracking. *In Thermal Cracking In Concrete at Early Age, Proceedings of the International RILEM Symposium* (Ed. by R. Springenschmid), E&FN Spon, London, pp.111-118.

Haugaard-Nielsen, A. B. 1997. *Mathematical modeling and experimental analysis of early age concrete*. Doctoral Dissertation, Technical University of Denmark

Hedlund, H. 2000. *Hardening concrete: measurments and evaluation of non-elastic deformation and associated restraint stresses*. Doctoral Dissertation, Lulea University of Technology

He, W., Y. Wu, K. M. Liew. 2008. A fracture energy based constitutive model for the analysis of reinforced concrete structures under cyclic loading. *Computer Methods in Applied Mechanics and Engineering*, Vol. 197, No. 51-52, pp. 4745-4762.

Holt, E. 2001. *Early Age Autogenous Shrinkage of Concrete*. Doctoral Thesis. The University of Washington in Seattle.

Huebner, K. H., D. L. Dewhirst, D. E. Smith, and T. G. Byrom. 2008. *The Finite Element Method for Engineers*. John Wiley & Sons, New York.

Jeong, J., J. Park, J. Lim, and S. Kim. 2014. Testing and Modeling of Friction Characteristics between Concrete Slab and Subbase Layers. *Road Materials and Pavement Design*, Vol. 15, No. 1, pp. 114-130.

Jensen, O.M., Ø. Bjøntegaard, T.A. Hammer, and E.J. Sellevold. 2007. Mechanisms of Internal Water Curing. In RILEM Report 41, *Internal Curing of Concrete* (Ed. by Kovler and Jensen), RILEM publications, Bagneux, France, pp.15-27.

Jonasson, J. 1994. *Modeling of temperature, moisture and stresses in young concrete*. Doctoral Dissertation, Lulea University of Technology.

Kader A. K. 1999. *Investigation on Friction between Concrete Slabs and Subgrades*. Report TVBK-5099, Lund Institute of Technology.

Kanstad T., D. Bosnjak, and J.A. Øverli. 2001. *3D Restraint Analyses of Typical Structures with Early-Age Cracking Problems*, IPACS report, TU Luleå, ISBN 91-8958-32-x.

Kanstad, T., P. F. Takács, and D. Bosnjak. 2002. Field Measurements versus Calculated Results for Norwegian High Performance Concrete Structures. *In Finite Elements in Civil Engineering Applications: Proceedings of the Third Diana World Conference*, Tokyo, Japan, 9-11, p. 107.

Kelly P. A. 2018. Solid Mechanics Lecture Notes - An Introduction to Solid Mechanics. The University of Auckland. Available from

http://homepages.engineering.auckland.ac.nz/~pkel015/SolidMechanicsBooks/index.html

Kim, S., M. C. Won, and B. F. McCullough. 2000. *Three-Dimensional Nonlinear Finite Element Analysis of Continuously Reinforced Concrete Pavements*. No. FHWA/TX-00/1831-1. Center for Transportation Research, Bureau of Engineering Research, the University of Texas at Austin.

Kosmatka, S.H., B. Kerkhoff, and W.C. Panarese. 2002. *Design and Control of Concrete Mixtures*, 14th ed. Portland Cement Association.

Krauss, P. D., and E. A. Rogalla. 1996. *Transverse Cracking in Newly Constructed Bridge Decks*. NCHRP Report 380, National Research Council, Washington, DC.

Liu, Y., and G. Glass. 2013. Effects of Mesh Density on Finite Element Analysis. No. 2013-01-1375. SAE Technical Paper.

Malhotra, V. M., and N. J. Carino. 2003. *Handbook on Nondestructive Testing of Concrete*, Second Edition. CRC press.

Mangold, M. 1998. Methods for Experimental Determination of Thermal Stresses and Crack Sensitivity in The Laboratory. In RILEM Report 15, *Prevention of Thermal Cracking in Concrete at Early Ages* (Ed. by R. Springenschmid), E&FN Spon, London, pp. 26–39.

Meadows, J. 2007. Early-age cracking of mass concrete structures. Doctoral Dissertation, Auburn University, AL.

Mehta, P. K., Monteiro, P.J.M. (2014). *Concrete: Microstructure, Properties, and Materials*. 4th Ed. McGraw-Hill, New York.

McCullough, B.F., and T. Dossey. 1999. *Controlling Early-Age Cracking in Continuously Reinforced Concrete Pavement: Observations from 12 Years of Monitoring Experimental Test Sections in Houston*, Texas. Transportation Research Record 1684, pp. 35-43.

McMillan, F. R. 1916. *Method of Designing Reinforced Concrete Slabs—Discussion of A.C. Janni's paper*. Transactions of the ASCE, 80, p. 1738.

Minton, L. W. 2012. *Mitigation of Cracking in Cast-In-Place Reinforced Concrete Box Culverts in Alabama*. Master Thesis. Auburn University, Auburn, Alabama.

Mindness, S., J. Young, and D. Darwin. 2002. *Concrete*, 2nd ed. Prentice Hall. Upper Saddle River, N.J.

Montgomery, D. C., E. A. Peck, and G. G. Vining. 2015. *Introduction to Linear Regression Analysis*, John Wiley & Sons, New York.

Neville, A.M. 2011. *Properties of Concrete*, 5th ed. Pearson Education Limited. NJ.

Neville, A. M., W. H. Dilger, and J. J. Brooks. 1983. *Creep of Plain and Structural Concrete*. Construction Press.

Neville, A. M., and J. J. Brooks. 1991. Superplasticizers. *Concrete Technology,* Longman, New York, pp. 156.

Østergaard, L., D. A. Lange, S. A. Altoubat, and H. Stang. 2001. Tensile Basic Creep of Early-Age Concrete under Constant Load. *Cement and Concrete Research*, Vol. 31, No. 12, pp. 1895-1899.

Pinto, R. C. A., and K. C. Hover. 1999. Application of Maturity Approach to Setting Times. ACI Materials Journal, Vol. 96, No. 6, pp. 686-691.

Poole, J. L, K. A. Riding, R. A. Browne, and A. K. Schindler. 2006. Temperature Management of Mass Concrete Structures. *Concrete Construction World of Concrete*, Vol. 51, No. 11, pp. 47–53.

Rostásy, F. S., T. Tanabe, and M. Laube. 1998. Assessment of External Restraint. In RILEM Report 15, *Prevention of Thermal Cracking in Concrete at Early Ages* (Ed. by R. Springenschmid), E&FN Spon, London, pp. 150–177.

Riding, K.A. 2007. *Early Age Concrete Thermal Stress Measurement and Modeling. Doctoral Dissertation*. University of Texas, Austin, Texas.

Riding, K. A., J.L. Poole, A.K. Schindler, M.C.G. Juenger, K.J. Folliard. 2009. Effects of construction time and coarse aggregate on bridge deck cracking. *ACI Materials Journal*, Vol. 106, No. 5, pp. 448-454.

Riding, K. A., J. L. Poole, A. K. Schindler, M. C. G. Juenger., and K. J. Folliard. 2014. Statistical Determination of Cracking Probability for Mass Concrete. *ASCE Journal of Materials in Civil Engineering*, Vol. 26, No. 9.

Riding, K., A.K. Schindler, P. Pesek, T. Drimalas, and K.J. Folliard 2017. Concreteworks V3 Training/User Manual. Centre for Transportation Research. Austin, TX.

Jensen, O.M., Bjøntegaard, Ø., Hammer, T.A. and Sellevold, E.J., 2007. Mechanisms of Internal Water Curing. In RILEM Report 41, *Internal Curing of Concrete* (Ed. by Kovler and Jensen), RILEM publications, Bagneux, France, pp.15-27.

Schindler, A. K. 2004. Effect of temperature on hydration of cementitious materials. *Materials Journal*, Vol. 101, No. 1, pp. 72-81.

Schindler, A. K., and B. F. McCullough. 2002. The Importance of Concrete Temperature Control during Concrete Pavement Construction in Hot Weather Conditions. *Journal of the Transportation Research Board*, No. 1813, pp. 3-10.

Schindler, A. K., M. L. Hughes, R. W. Barnes, and B. E. Byard. 2010. *Evaluation of Cracking of the US 331 Bridge Deck*. Publication FHWA/ALDOT 930-645. FHWA, U.S. Department of Transportation.

Springenschmidt, R., R. Breitenbucher., and M. Mangold. 1994. Development of the Cracking Frame and Temperature-Stress Testing Machine. In RILEM Proceedings 25, *Thermal Cracking in Concrete at Early Ages*, (ed. R. Springenschmidt), London, E & FN Spon, pp. 137-45.

Shalon R., and D. Ravina. 1960. *Studies in Concreting in Hot Countries*. Proceedings of the International Rilem Symposium on Concrete and Reinforced Concrete in Hot Countries, BRS, Haifa, Israel, Vol. I.

Sule, M., and K. V. Breugel. 2004. The Effect of Reinforcement on Early-Age Cracking due to Autogenous Shrinkage and Thermal Effects. *Cement and Concrete Composites*, Vol. 26, No.5, pp. 581-587.

Tankasala, A. 2017. *Early-age Cracking of Lightweight Mass Concrete*. Doctoral Dissertation, Auburn University, AL.

Tankasala, A., A.K. Schindler, K.A. Riding. 2017. Risk of Thermal Cracking from Use of Lightweight Aggregate in Mass Concrete. *Journal of the Transportation Research Board*, TRR No. 2629, pp. 42-50.

Tazawa, E. 1998. Autogenous Shrinkage and Its mechanism. *Autogenous Shrinkage of Concrete* (ed. E. Tazawa), E&FN Spon, London.

Transportation Research Board. 1979. Durability of concrete bridge decks. *NCHRP Synthesis of highway Practice*, No.57, Transportation Research Board, Washington, DC, May, 61 pp.

Truman, K.Z., D.J. Petruska, and C.D. Norman. 1991. Creep, shrinkage, and thermal effects on mass concrete structure. *Journal of engineering mechanics*, Vol. 117, No. 6, pp.1274-1288.

Turner-Fairbank Highway research Center. 1998. Hydraulic Design of Highway Culverts, Report #FHWA-IP-85-15 U.S. Department of Transportation, Federal Highway Administration, McLean, Virginia.

Umehara, H., T. Uehara, T. Iisaka, and A. Sugiyama. 1995. Effect of Creep in Concrete at Early Ages On Thermal Stress. In RILEM Proceedings 25, *Thermal Cracking in Concrete at Early Ages*, (Ed. by R. Springenschmidt), London, E & FN Spon, pp. 79-86.

Wesevich, J. W., B. F. McCullough, and N. H. Burns. 1987. Stabilized Subbase Friction Study for Concrete Pavements. Publication FHWA/TX-87+459-1. FHWA, U.S. Department of Transportation.

WisDOT. 2011. Bridge Manual. Wisconsin Department of Transportation (WisDOT).

Witasse, R., and M., Hendriks. 2002. Finite element modeling of early age concrete behavior using DIANA. In *Finite Elements in Civil Engineering Applications: Proceedings of the 3rd International DIANA World Conference on Finite Elements in Civil Engineering,* Tokyo, pp. 9-11.

Wu, S., D. Huang, F.B. Lin, H. Zhao, and P. Wang. 2011. Estimation of cracking risk of concrete at early age based on thermal stress analysis. *Journal of Thermal Analysis and Calorimetry*, Vol.105, No.1, pp.171-186.

Yu, Q., Z. P. Bažant, and R. Wendner. 2012. Improved Algorithm for Efficient and Realistic Creep Analysis of Large Creep-Sensitive Concrete Structures. *ACI Structural Journal*, Vol.109, No. 5, pp. 665-675.

APPENDIX A: MEASURED AND PREDICTED STRESS DEVELOPMENT FROM

PROJECT A
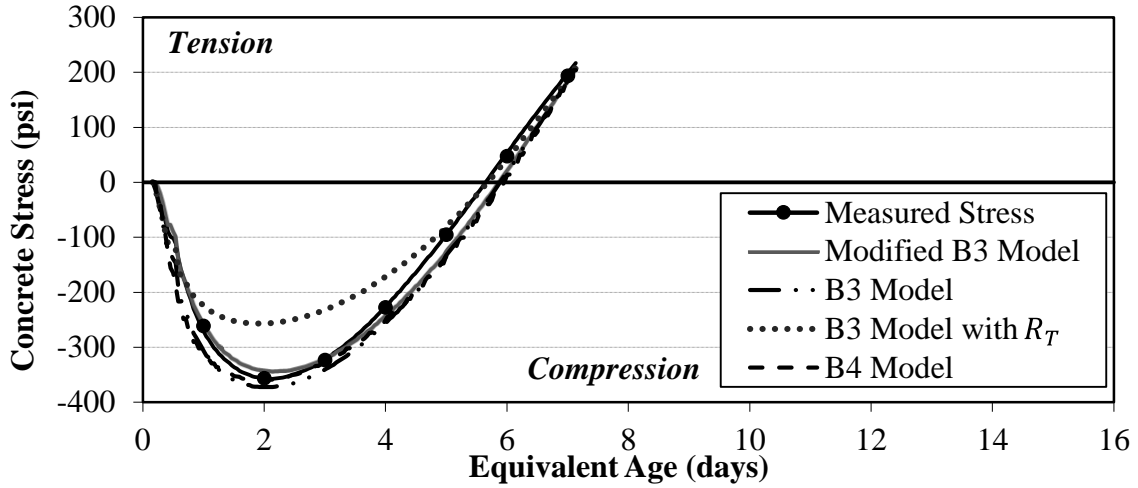
Figure A-1 Stress development results for 12A (Control 73 ºF)
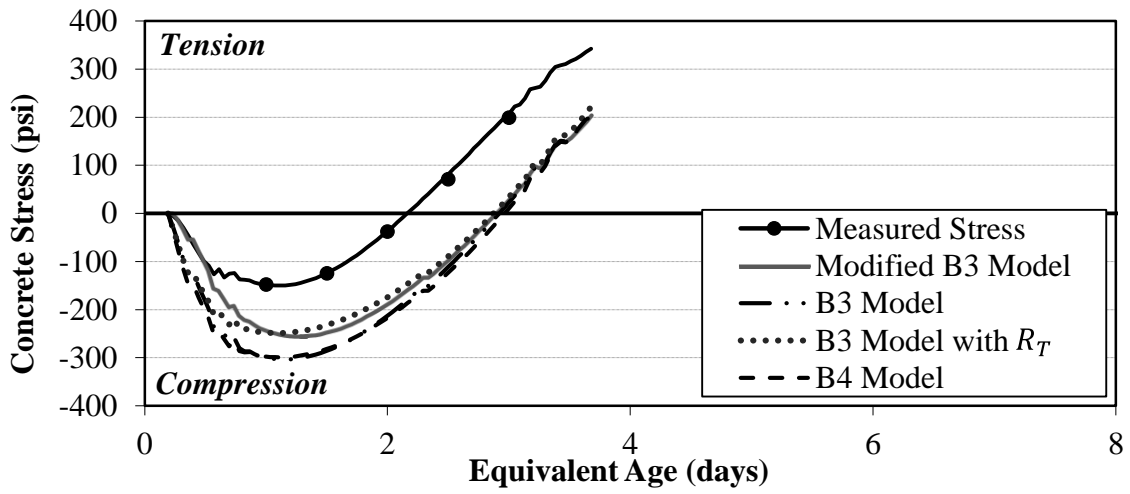
Figure A-2 Stress development results for 12B (Control 50ºF)
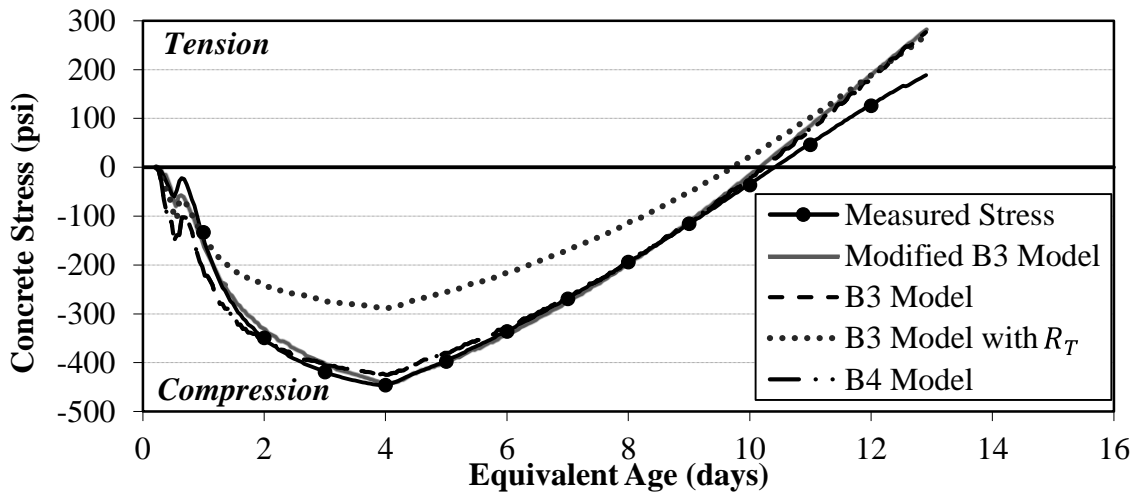
Figure A-3 Stress development results for 12C (Control 95ºF)

218
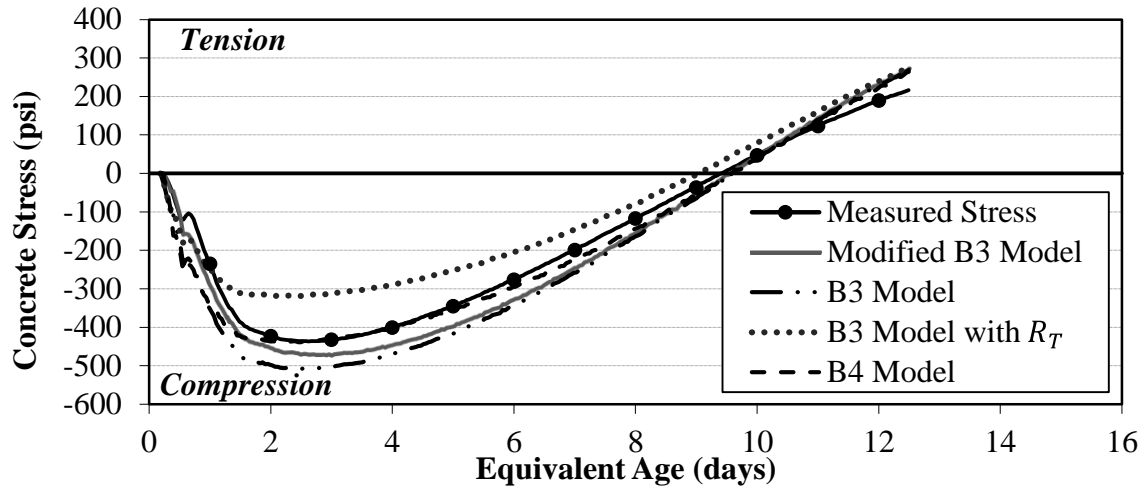
Figure A-4 Stress development results for 12D (Control 73ºF)
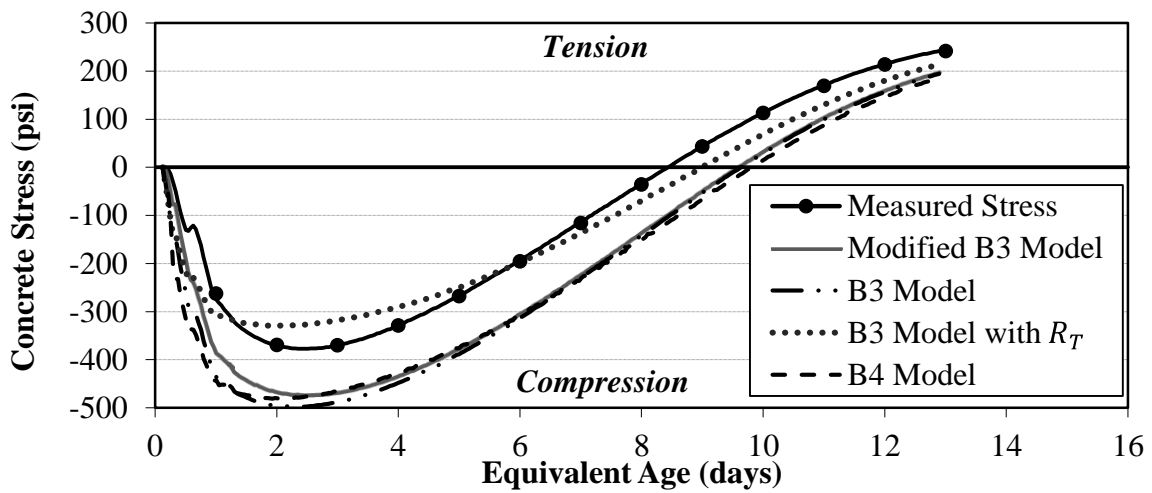
Figure A-5 Stress development results for 12E (Control 5 ºF)
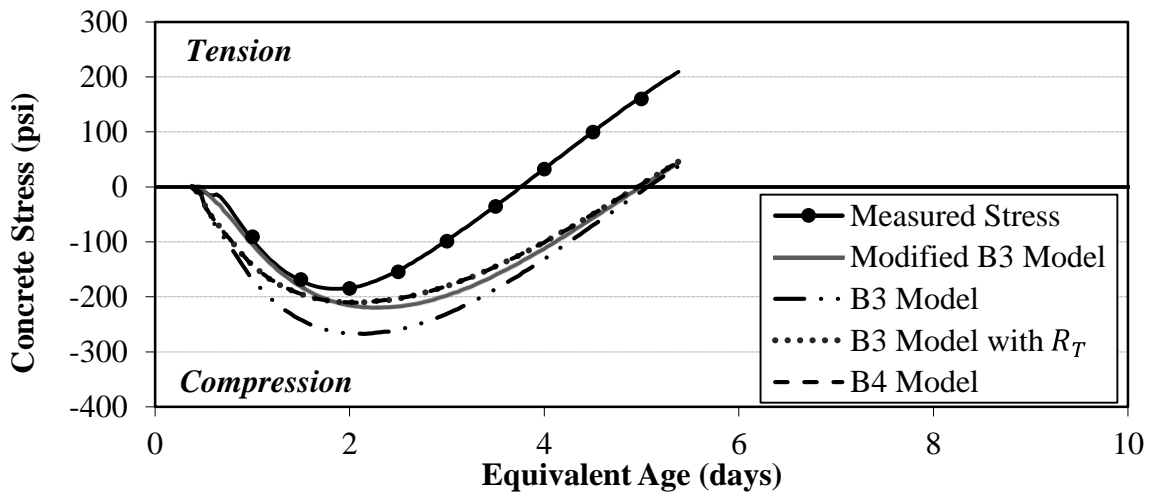
Figure A-6 Stress development results for 21 (30%Class C)
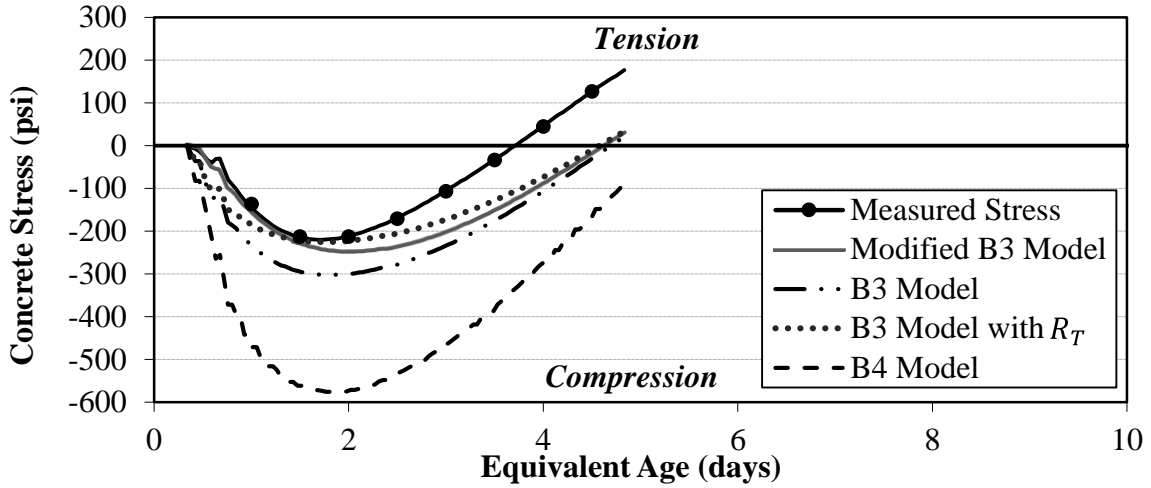
Figure A-7 Stress development results for 22 (20%Class C)
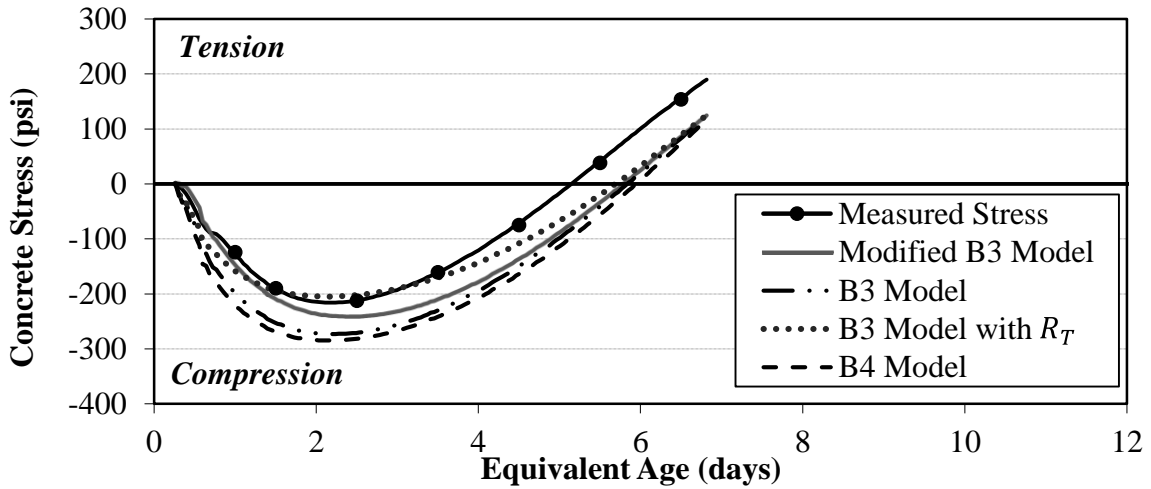
Figure A-8 Stress development results for 23A (30%Slag 73ºF)
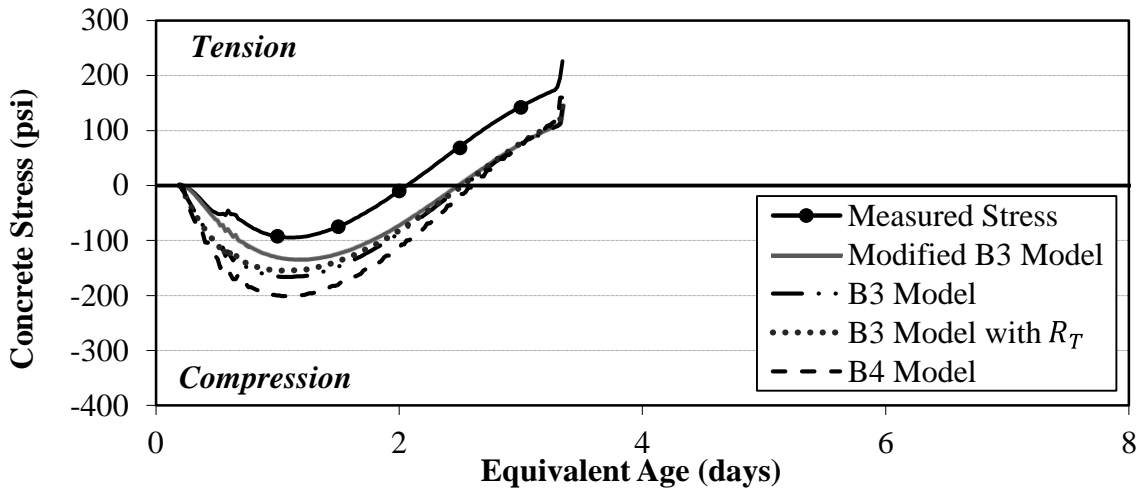
Figure A-9 Stress development results for 23B (30%Slag 50ºF)
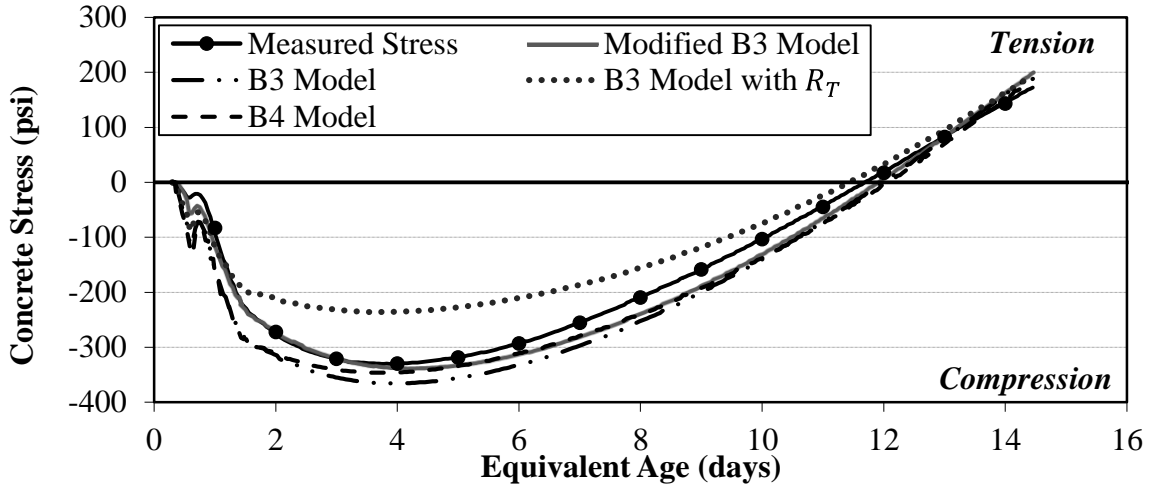
Figure A-10 Stress development results for 23C (30%Slag 95ºF)
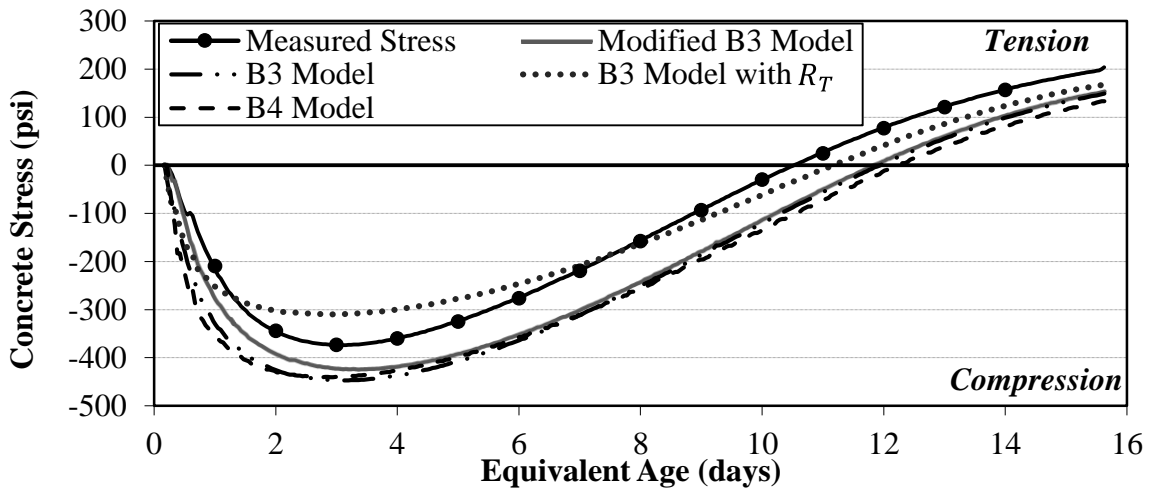
Figure A-11 Stress development results for 23E (30%Slag 50ºF)
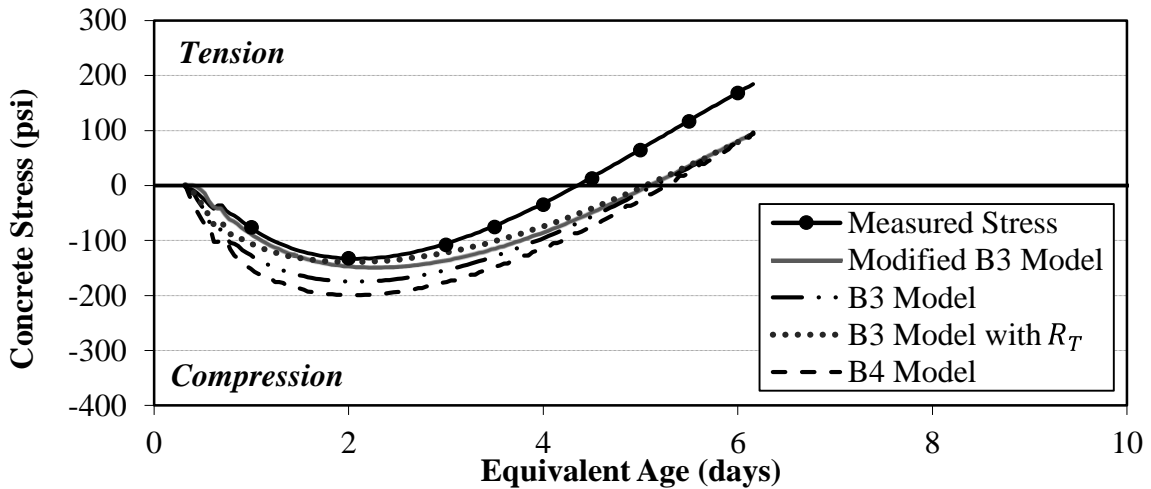
Figure A-12 Stress development results for 24A (50%Slag 73ºF)

221
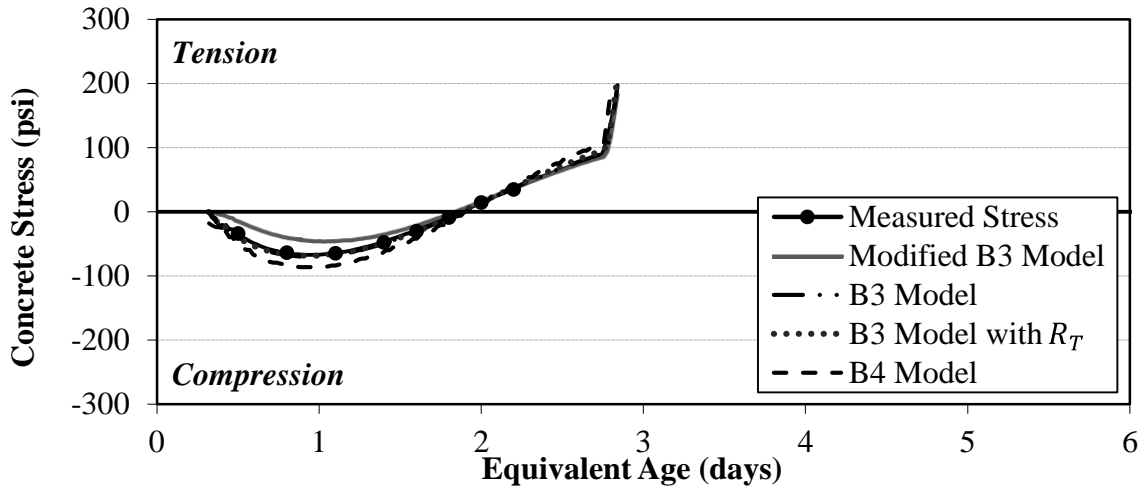
Figure A-13 Stress development results for 24B (50%Slag 50ºF)
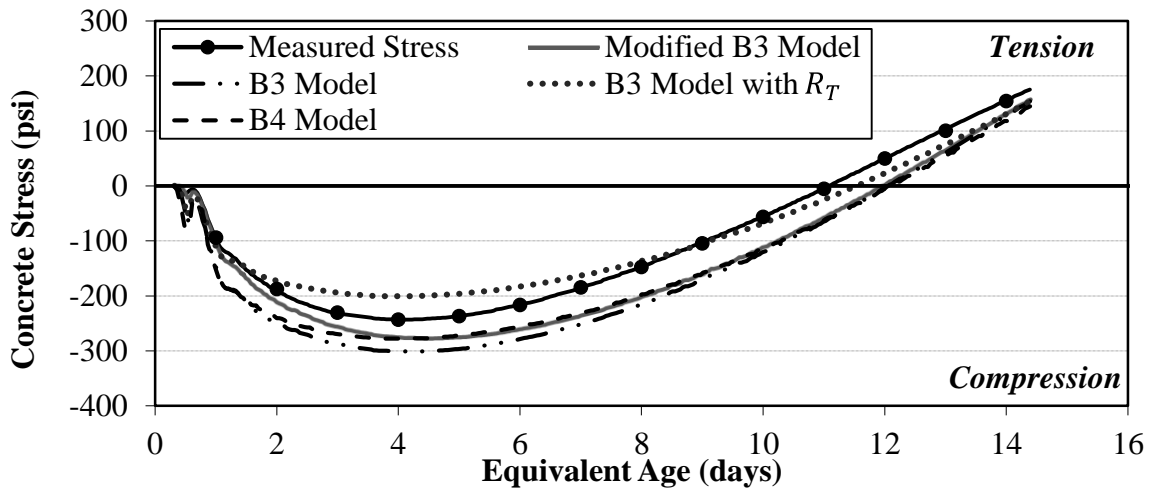
Figure A-14 Stress development results for 24C (50%Slag 95ºF)
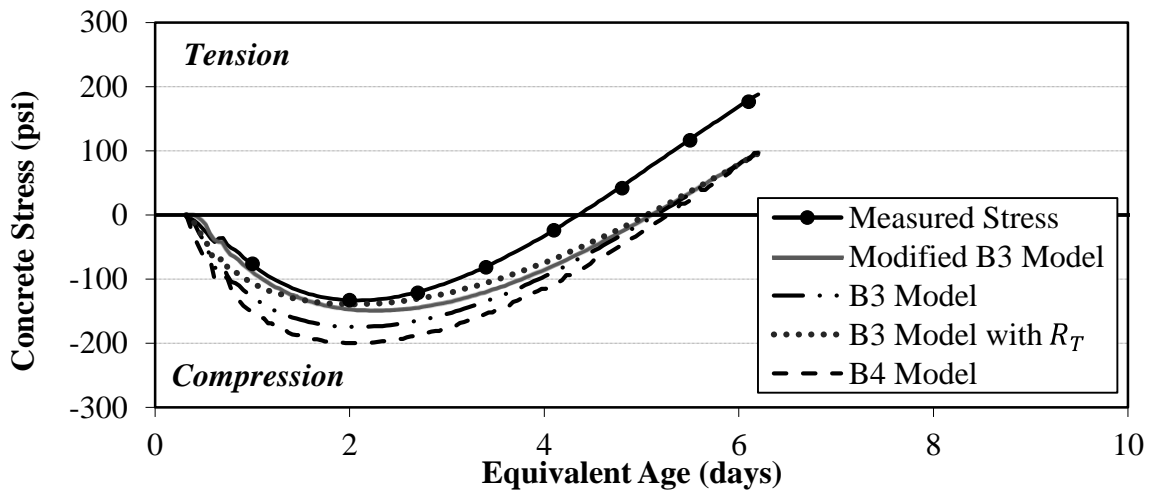
Figure A-15 Stress development results for 24D (50%Slag 73ºF)

222
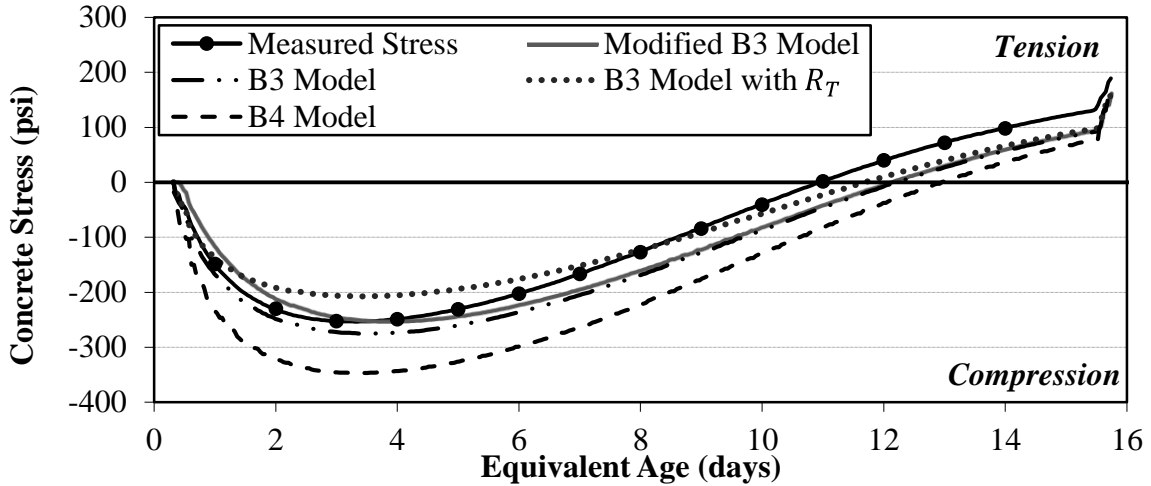
Figure A-16 Stress development results for 24E (50%Slag 50ºF)
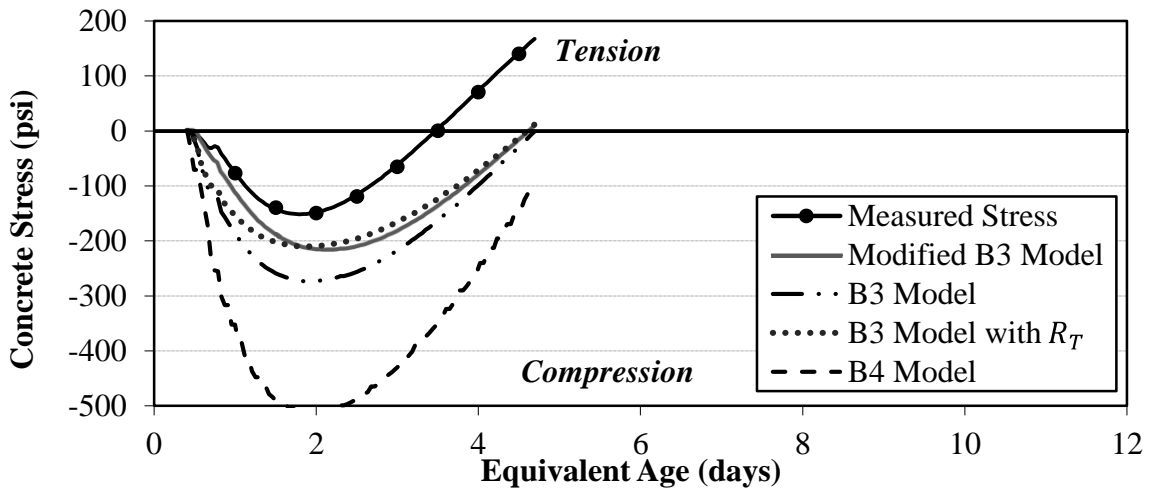
Figure A-17 Stress development results for 25 (25%ClassC 6%Slag)
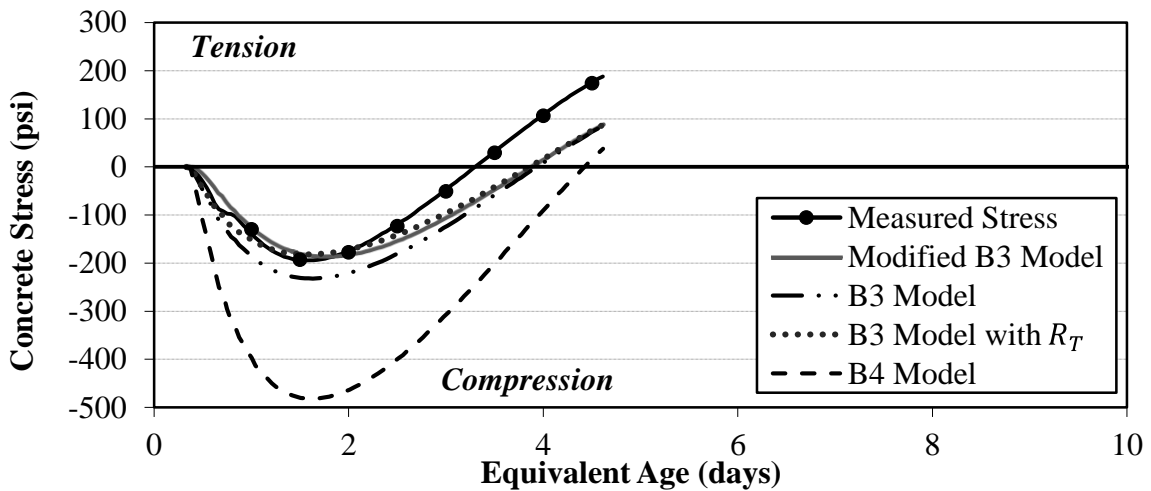
Figure A-18 Stress development results for 26 (25%ClassF 6%Slag)

223
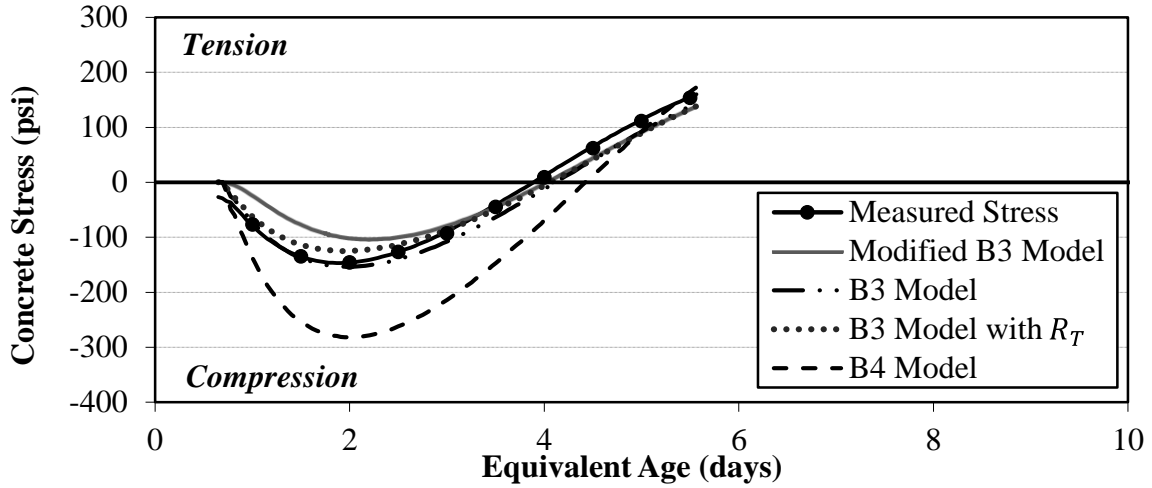
Figure A-19 Stress development results for 27 (20%ClassF 30%Slag)
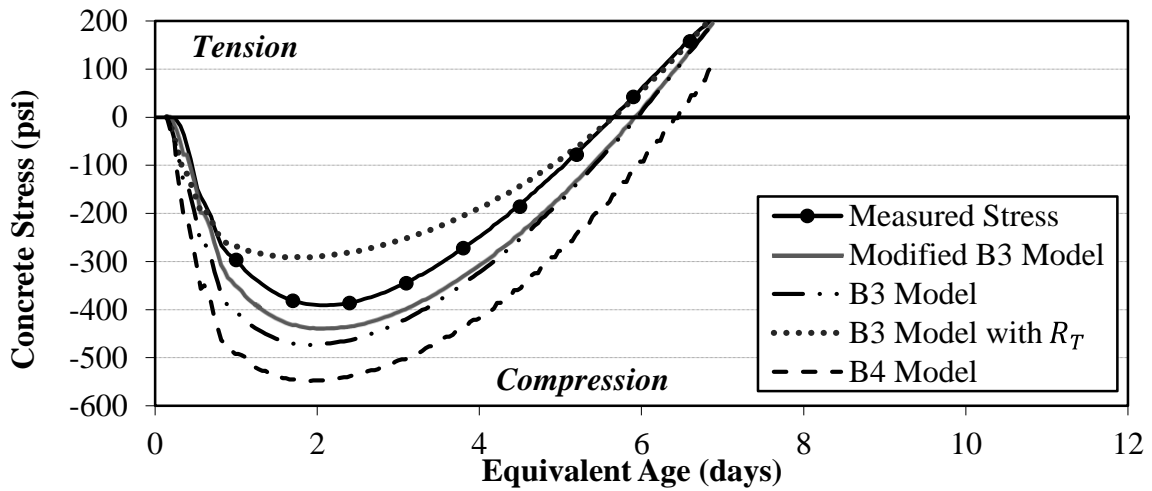
Figure A-20 Stress development results for 28 (W/C=0.32)
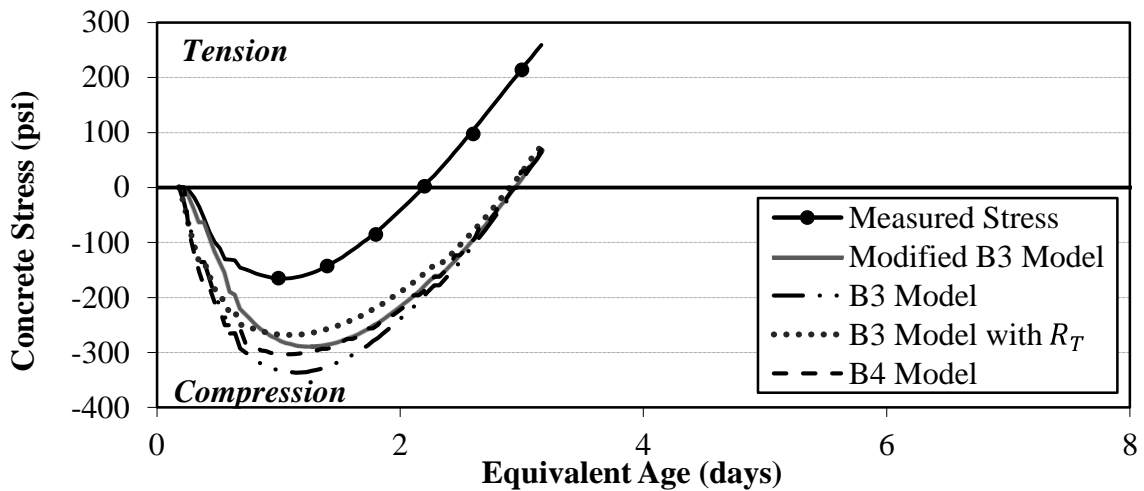
Figure A-21 Stress development results for 30B (W/C=0.38 50ºF)
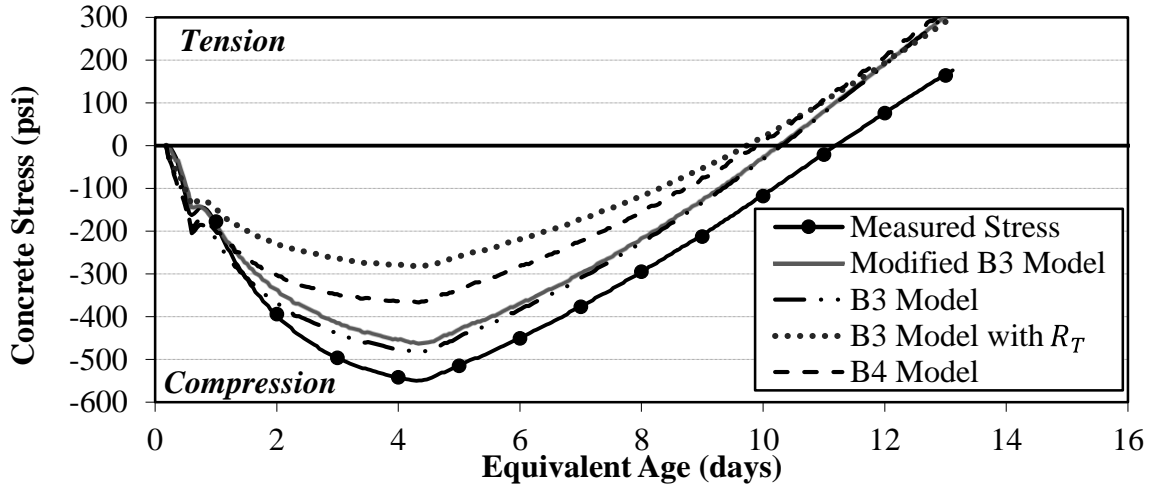
Figure A-22 Stress development results for 30C (W/C=0.38 95ºF)
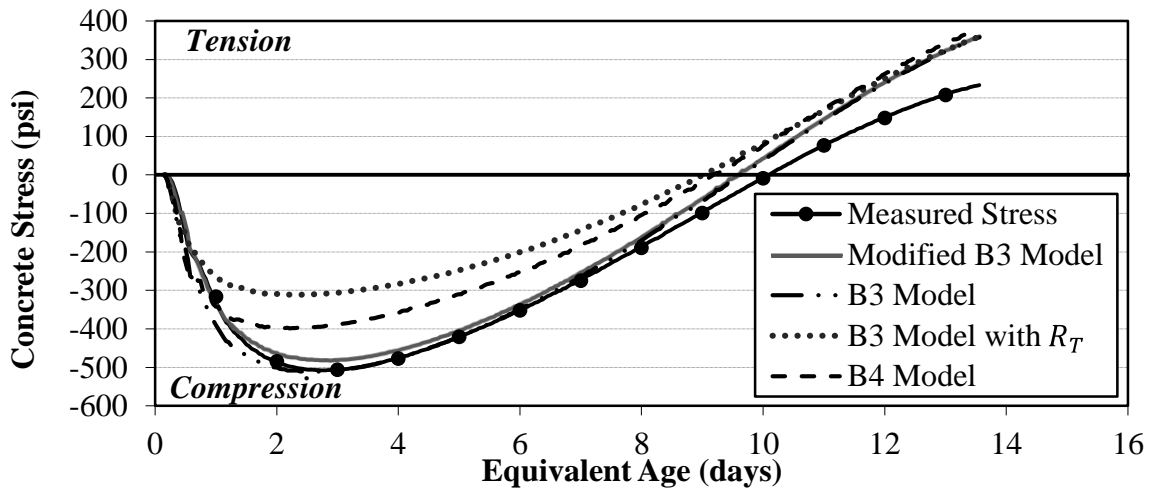
Figure A-23 Stress development results for 30D (W/C=0.38 73ºF)
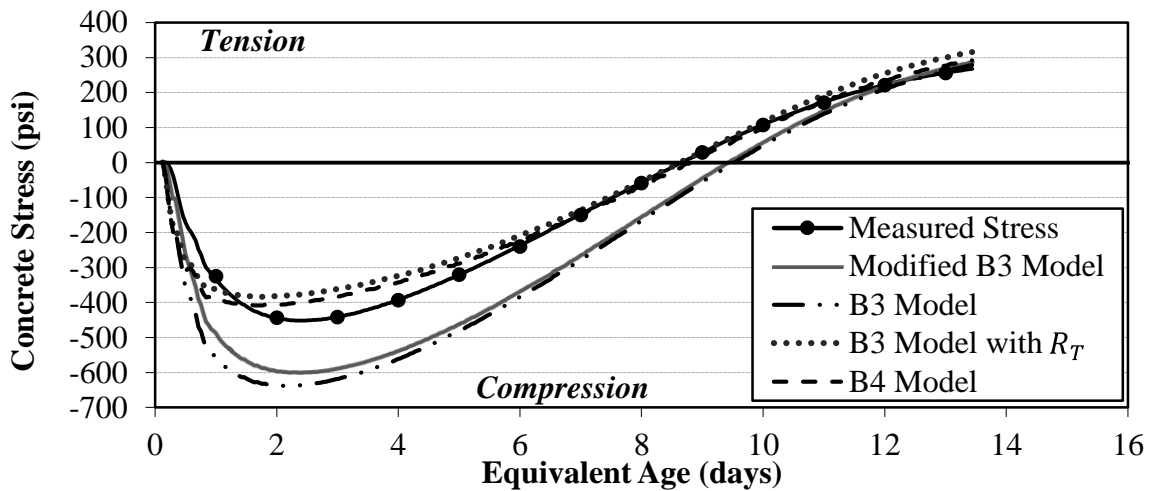
Figure A-24 Stress development results for 30E (W/C=0.38 50ºF)

225
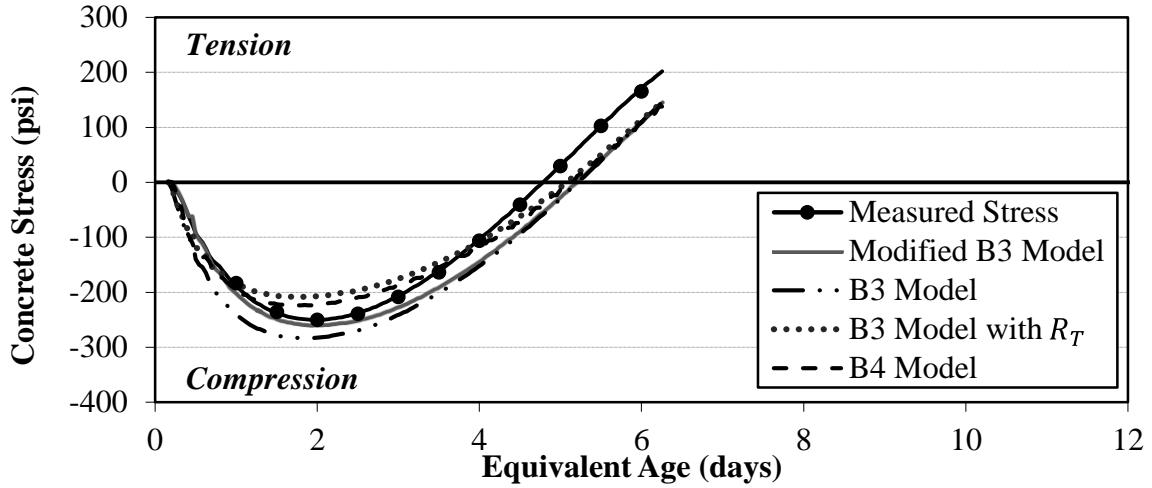
Figure A-25 Stress development results for 31 (W/C=0.48)
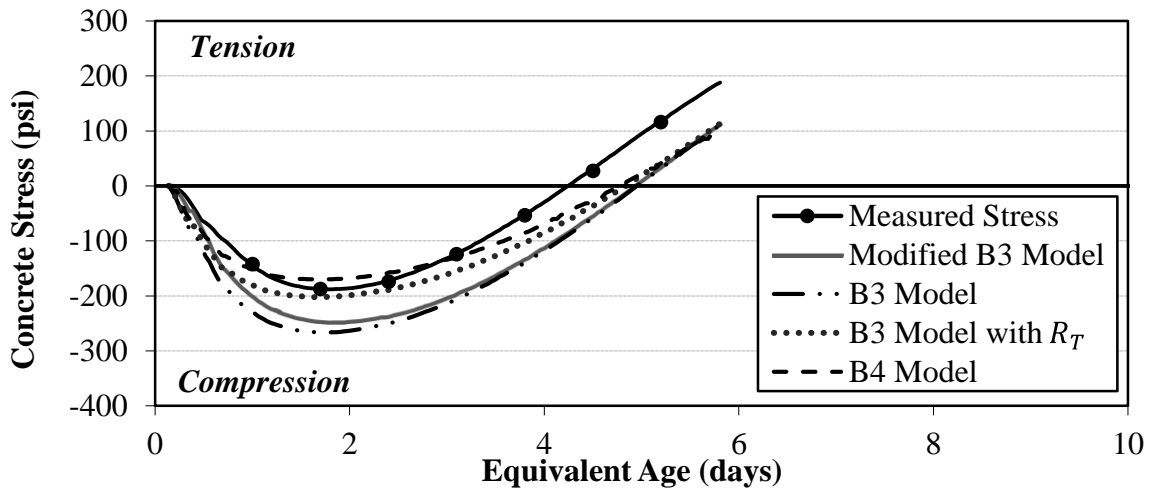
Figure A-26 Stress development results for 32 (W/C=0.53)
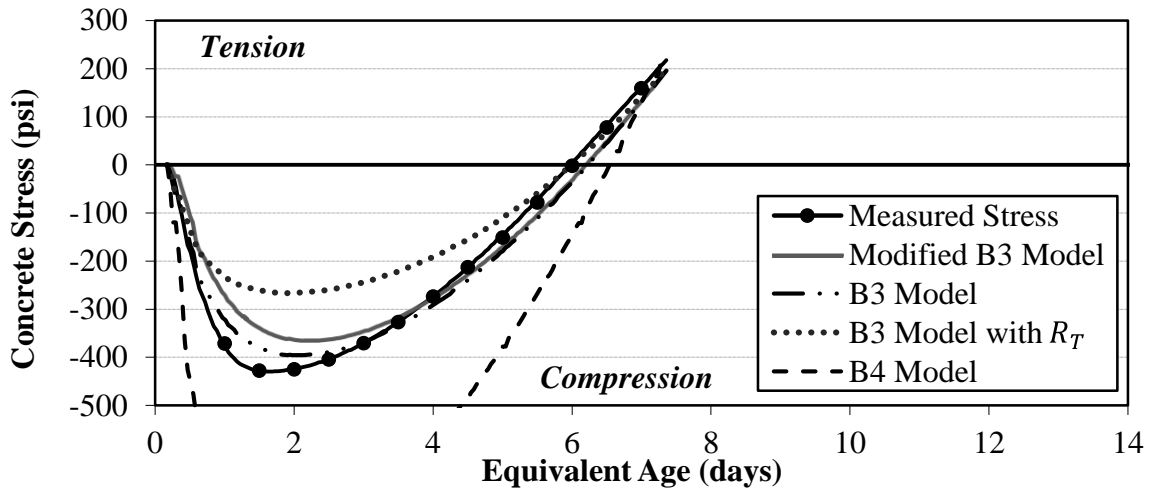
Figure A-27 Stress development results for 33A (Type III 73ºF)

226
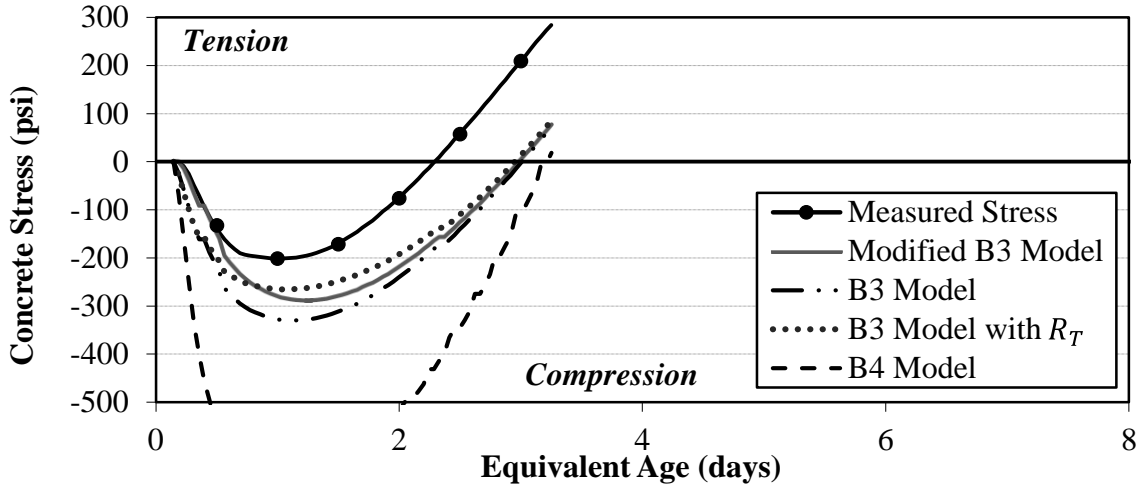
Figure A-28 Stress development results for 33B (Type III 50ºF)
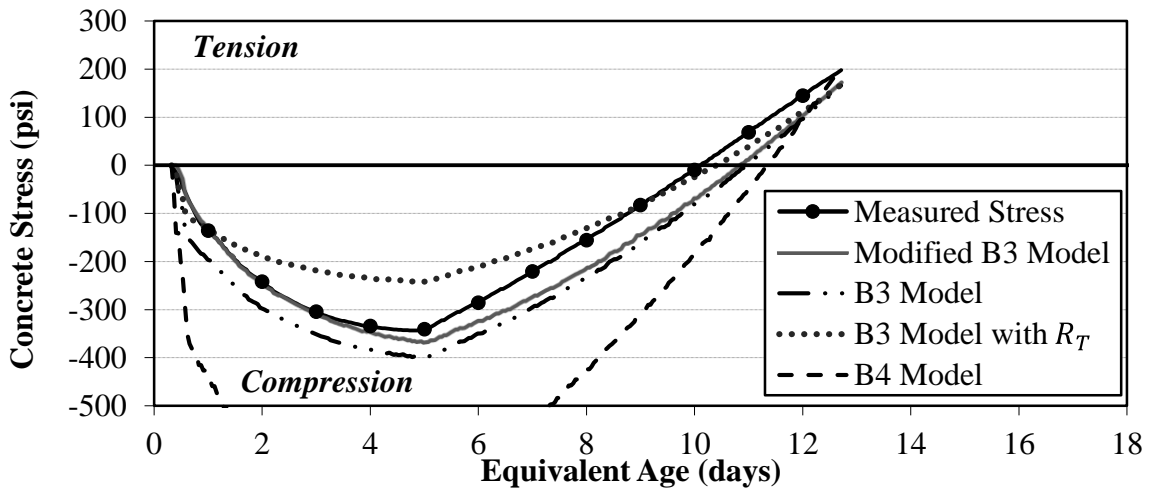
Figure A-29 Stress development results for 33C (Type III 95ºF)
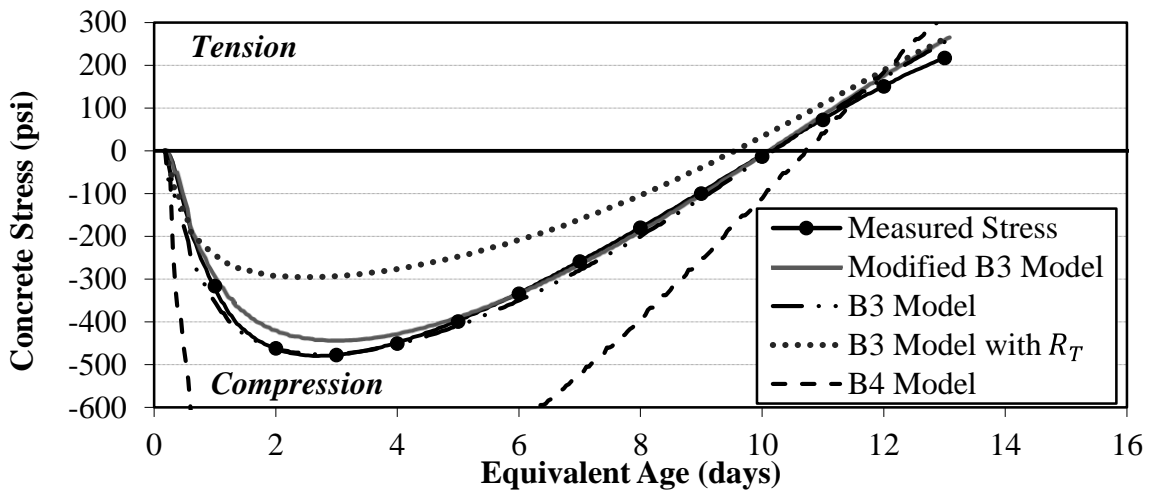
Figure A-30 Stress development results for 33D (Type III 73ºF)

227
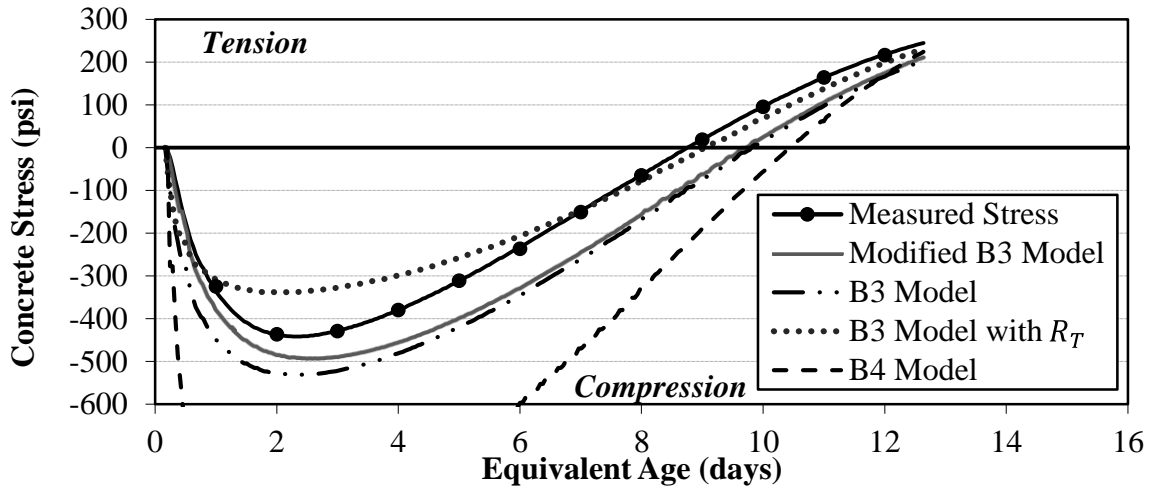
Figure A-31 Stress development results for 33E (Type III 50ºF)
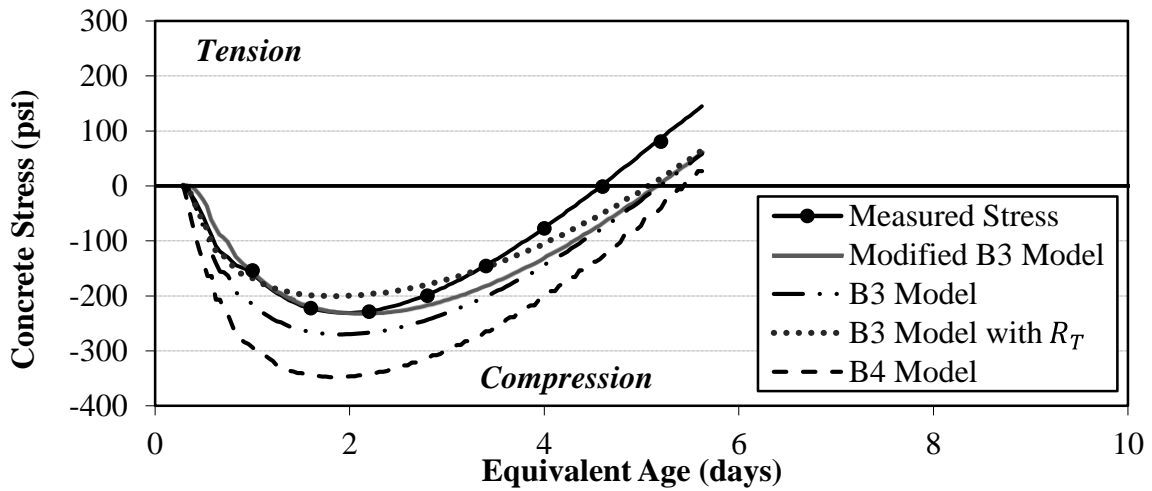
Figure A-32 Stress development results for 34 (AEA)

APPENDIX B: MEASURED AND PREDICTED STRESS DEVELOPMENT FROM

PROJECT B
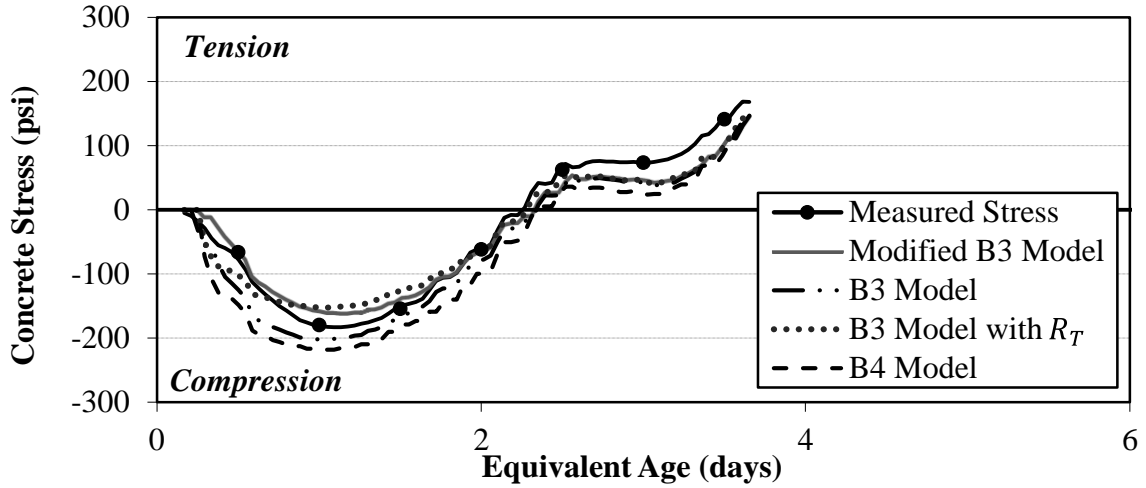
Figure B-1 Stress development results for 0.42 Slate IC (Fall)
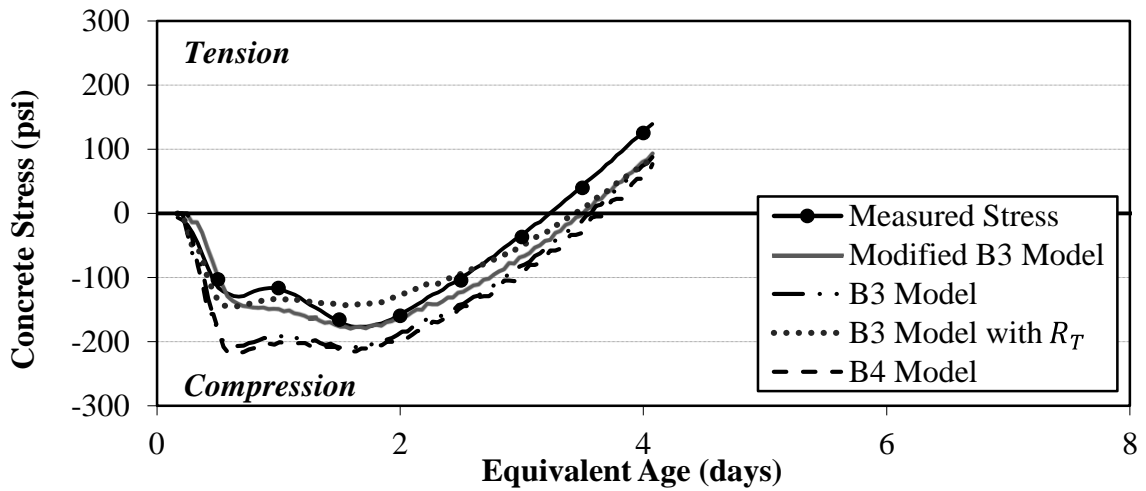
Figure B-2 Stress development results for 0.42 Slate IC (Sum)
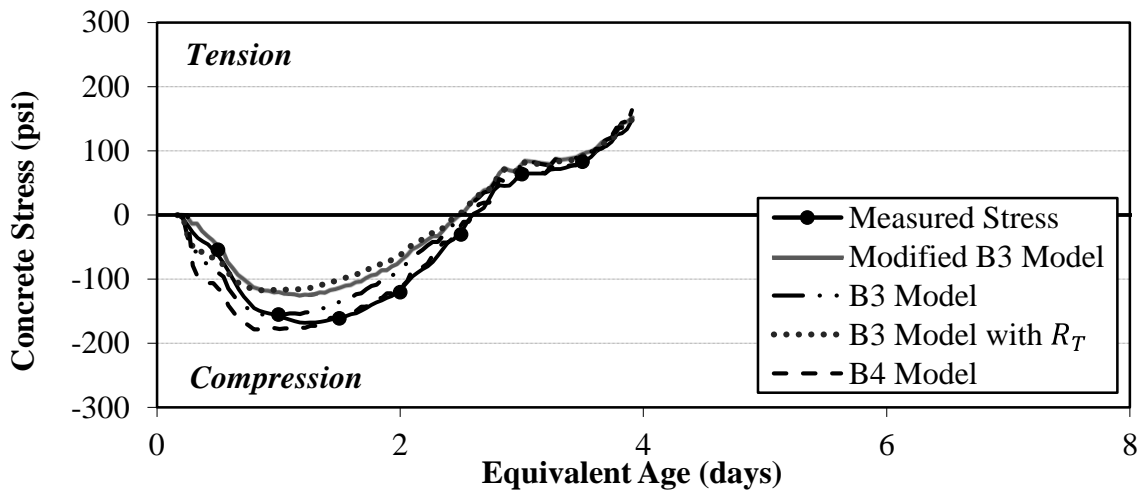
Figure B-3 Stress development results for 0.42 Slate SLW (Fall)
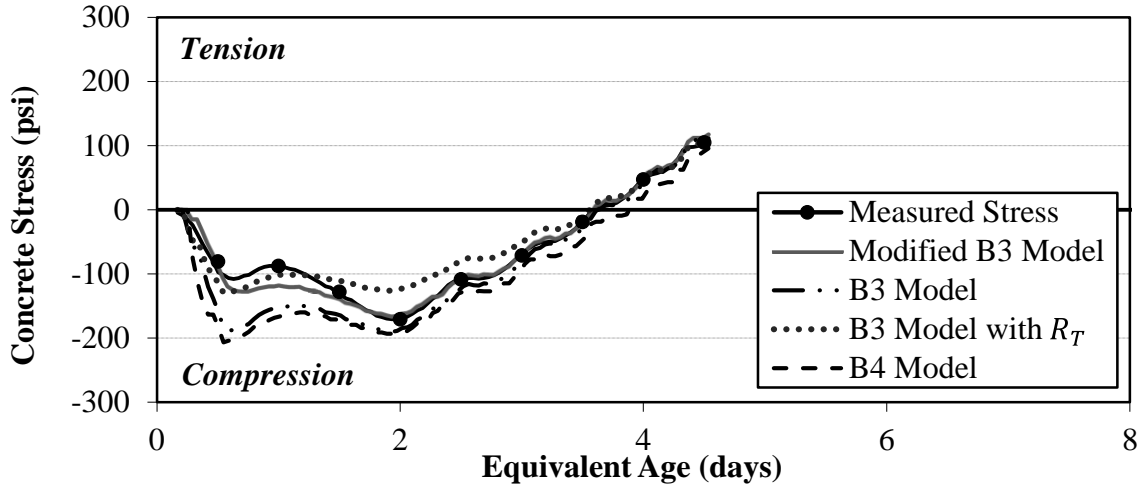
Figure B-4 Stress development results for 0.42 Slate SLW (Sum)
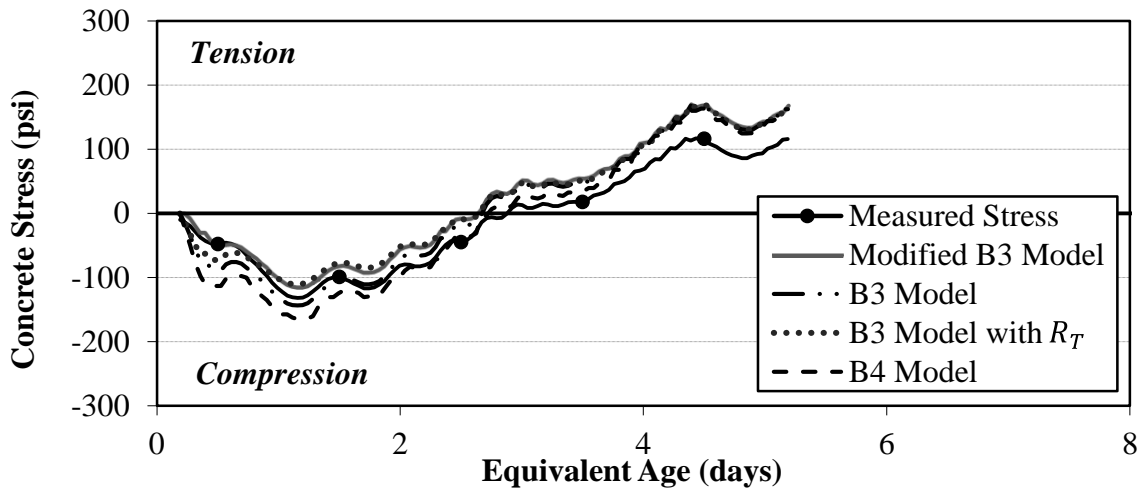
Figure B-5 Stress development results for 0.42 Slate ALW (Fall)
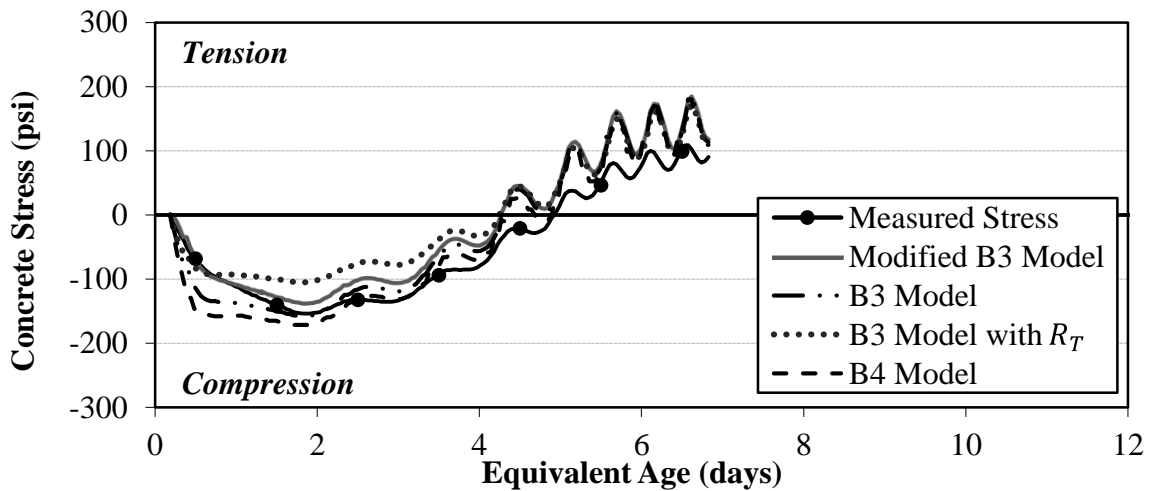
Figure B-6 Stress development results for 0.42 Slate ALW (Sum)

231
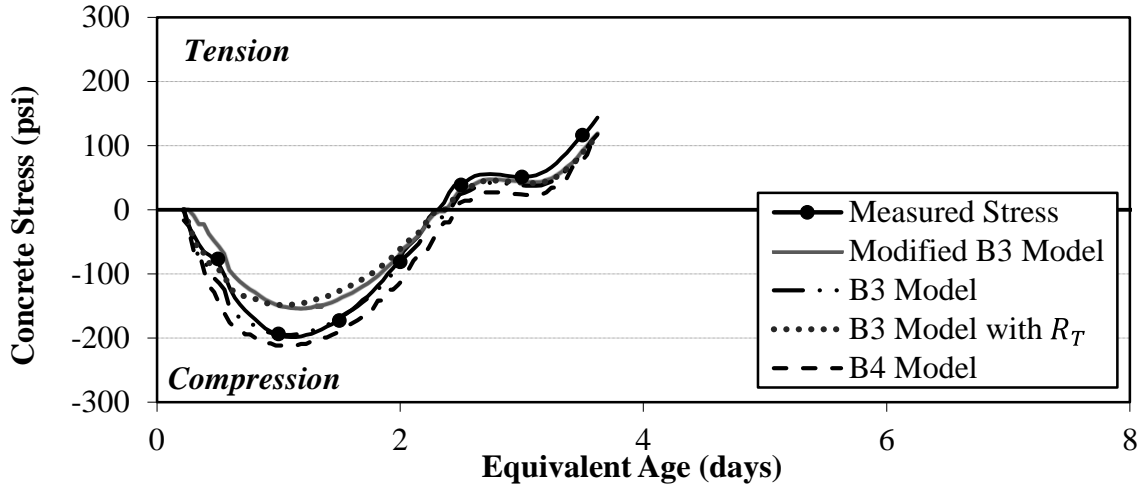
Figure B-7 Stress development results for 0.42 Clay IC (Fall)
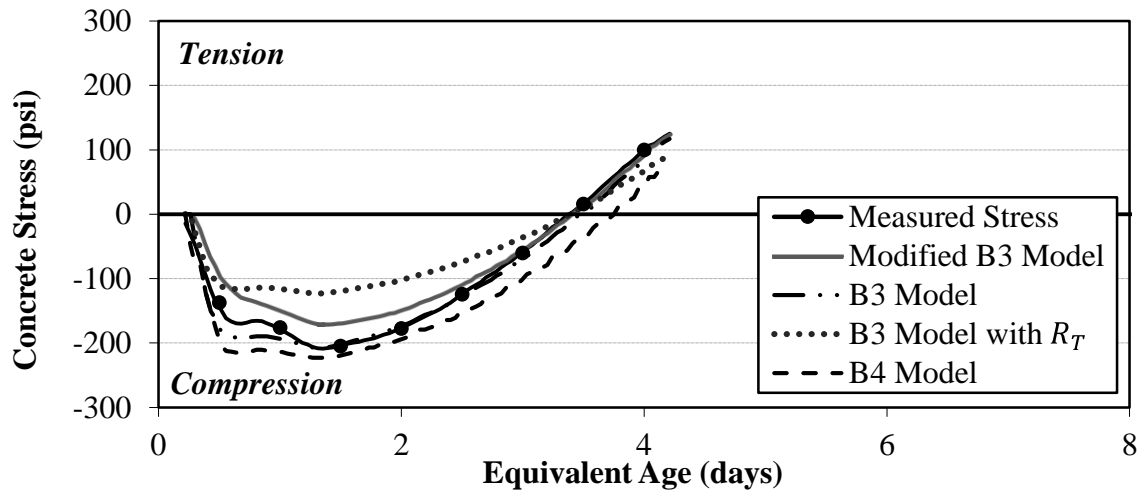
Figure B-8 Stress development results for 0.42 Clay IC (Sum)
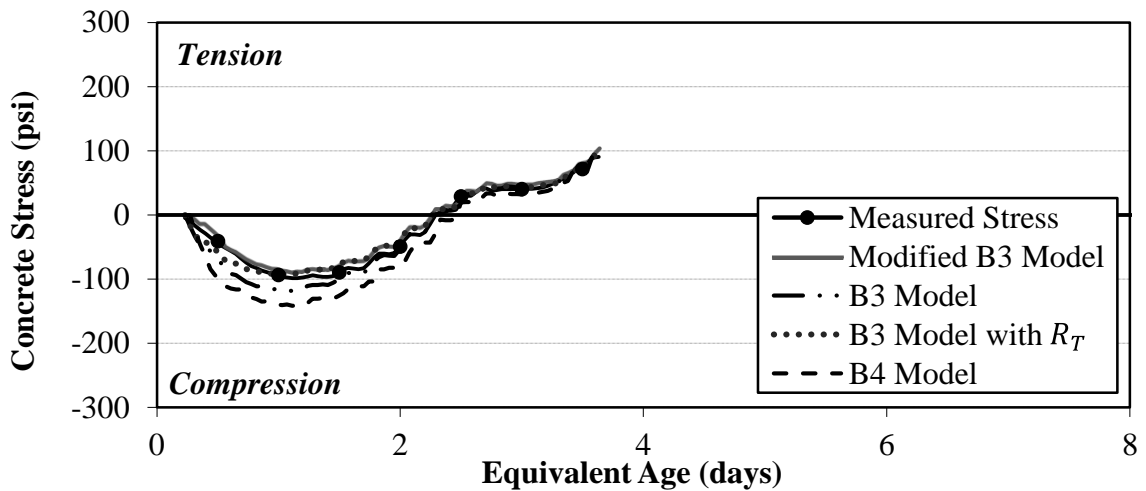
Figure B-9 Stress development results for 0.42 Clay SLW (Fall)

232
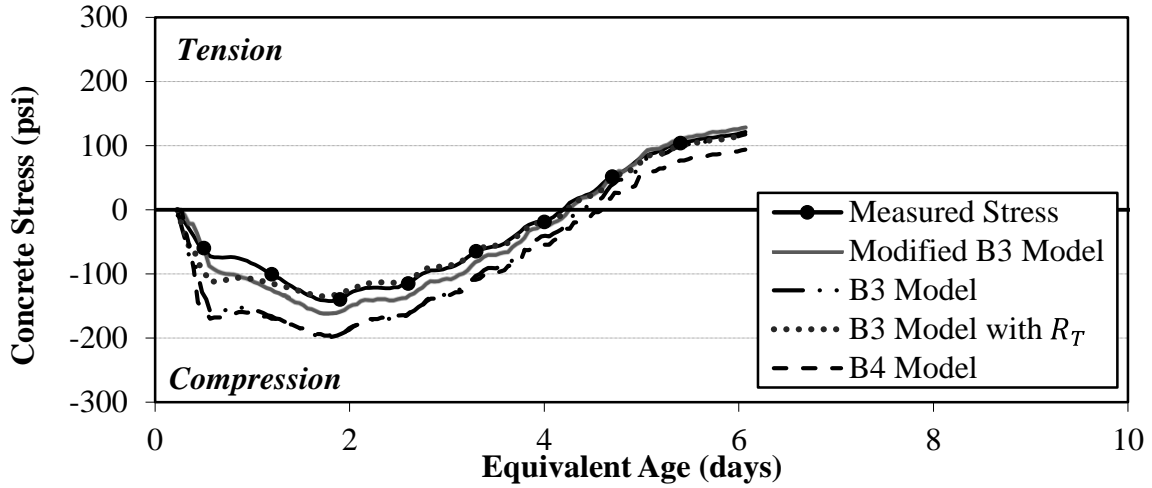
Figure B-10 Stress development results for 0.42 Clay SLW (Sum)
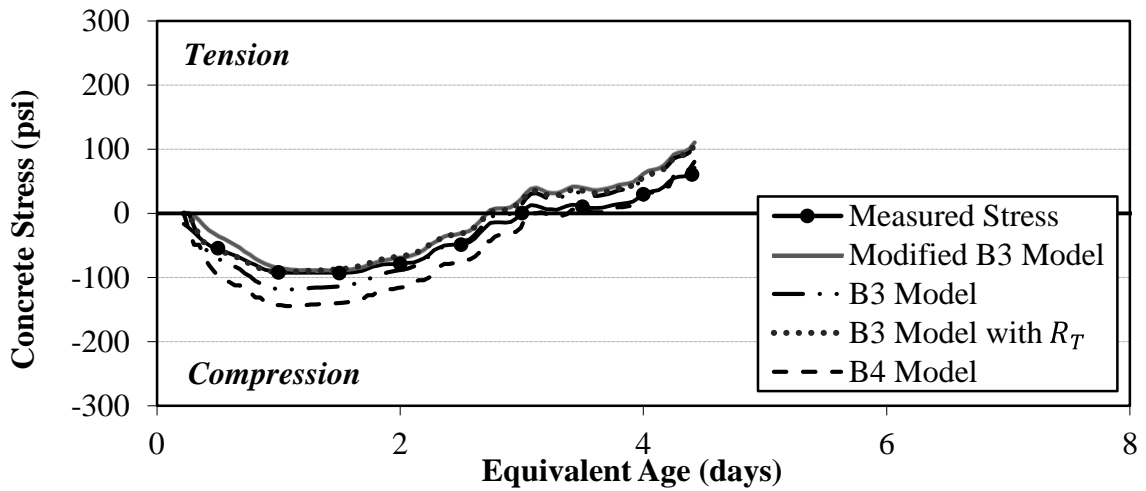
Figure B-11 Stress development results for 0.42 Clay ALW (Fall)
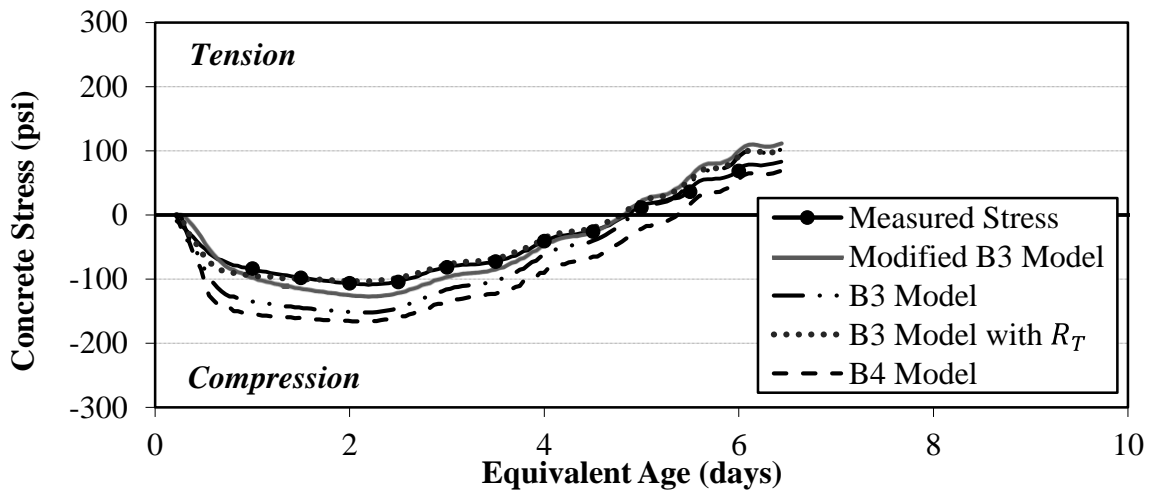
Figure B-12 Stress development results for 0.42 Clay ALW (Sum)

233
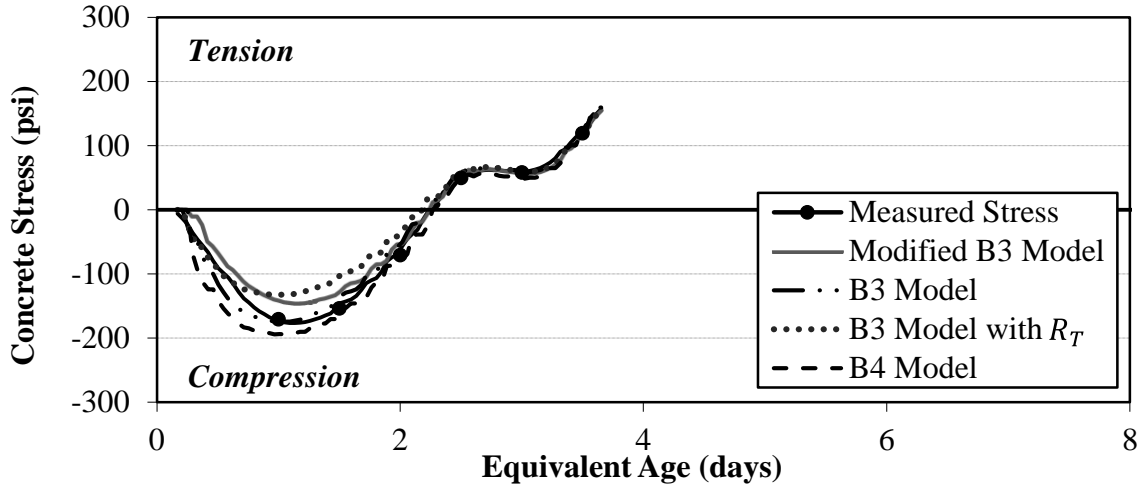
Figure B-13 Stress development results for 0.42 Shale IC (Fall)
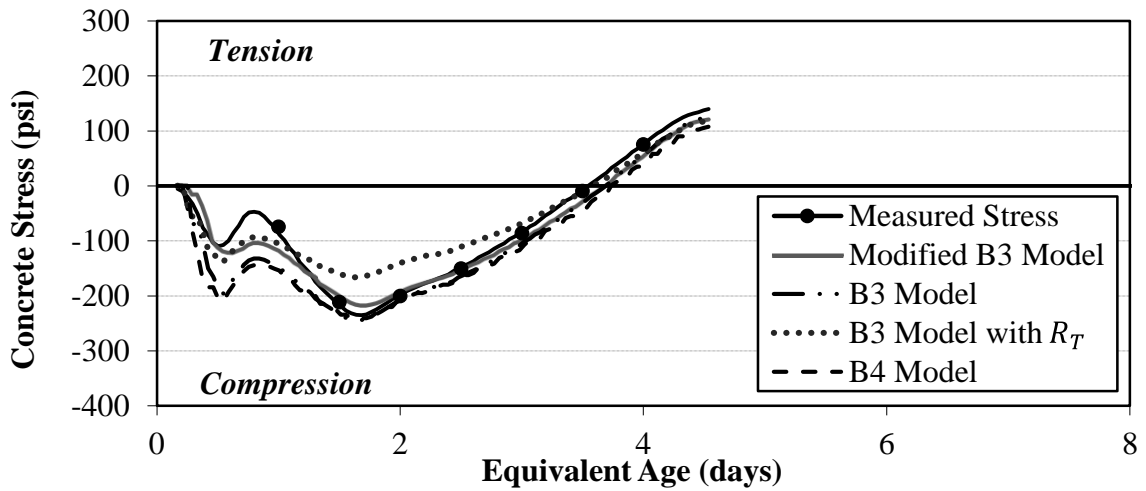
Figure B-14 Stress development results for 0.42 Shale IC (Sum)
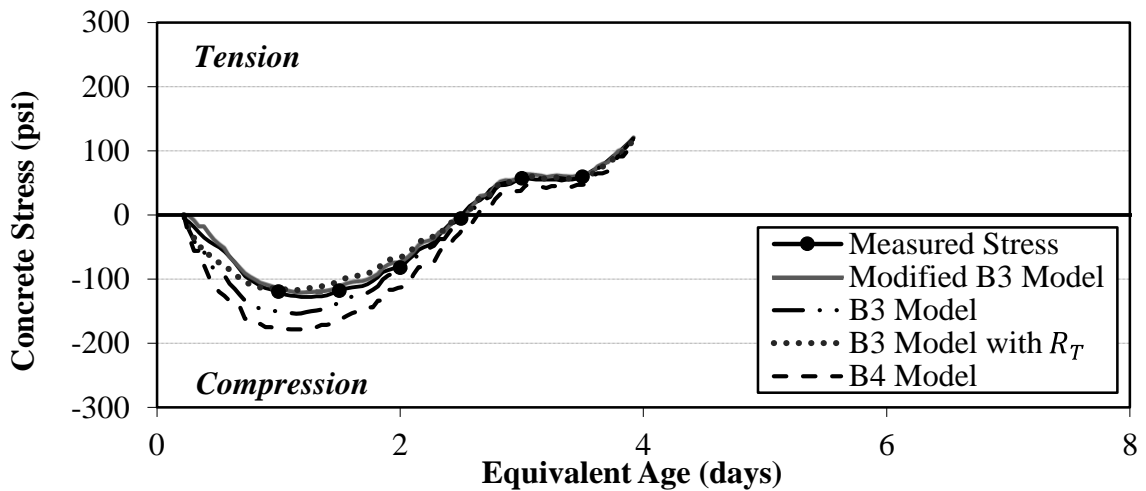
Figure B-15 Stress development results for 0.42 Shale SLW (Fall)

234
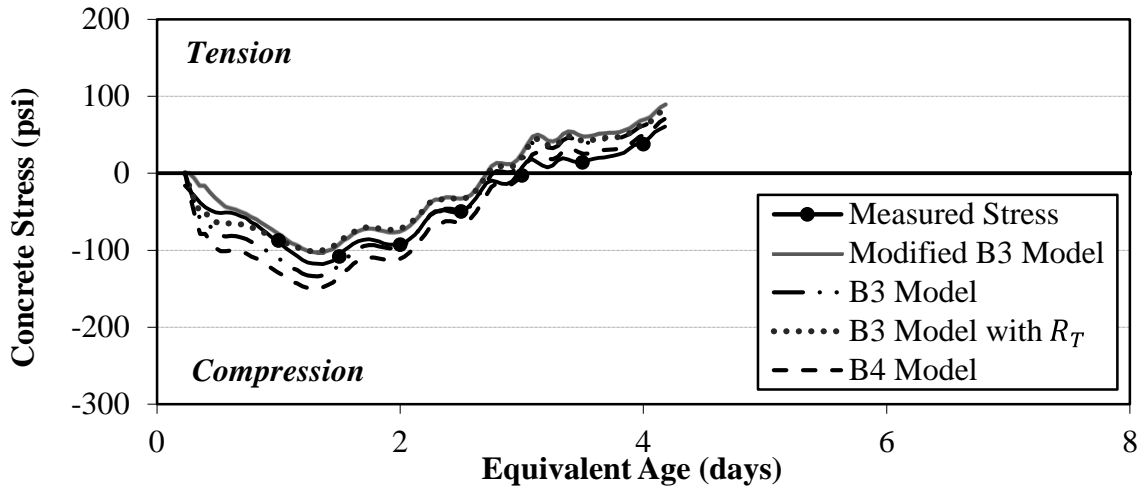
Figure B-16 Stress development results for 0.42 Shale ALW (Fall)
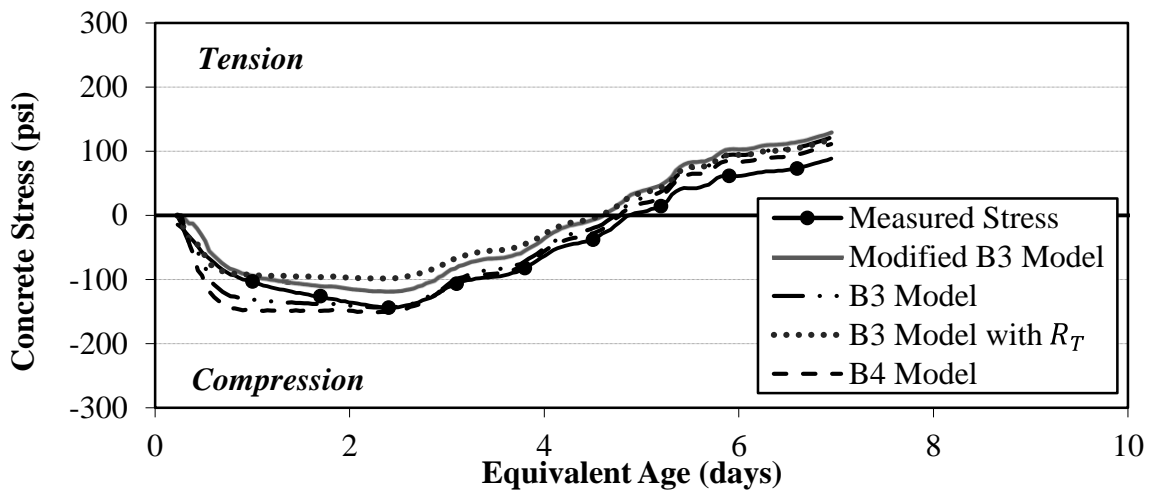
Figure B-17 Stress development results for 0.42 Shale ALW (Sum)
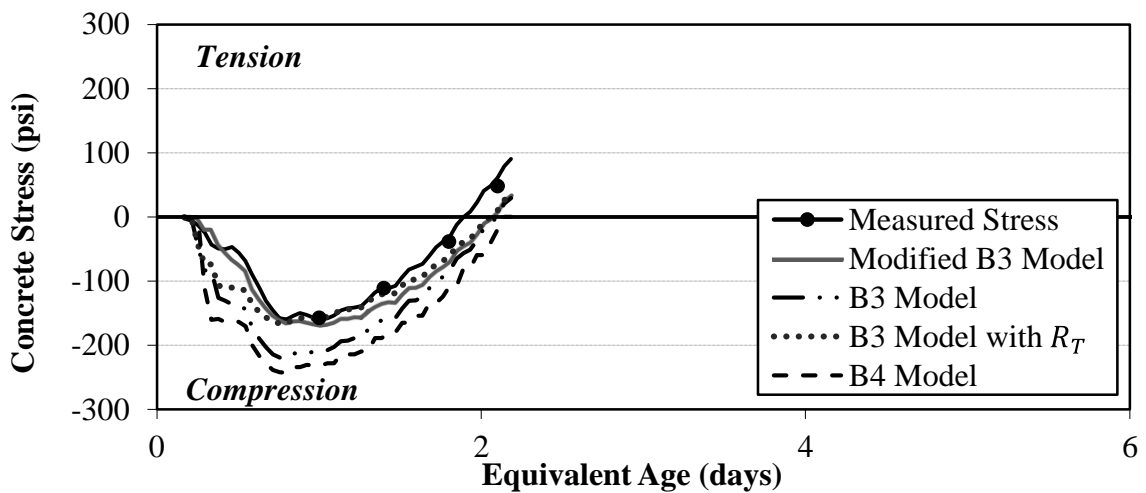
Figure B-18 Stress development results for 0.42 RG (Fall)

235
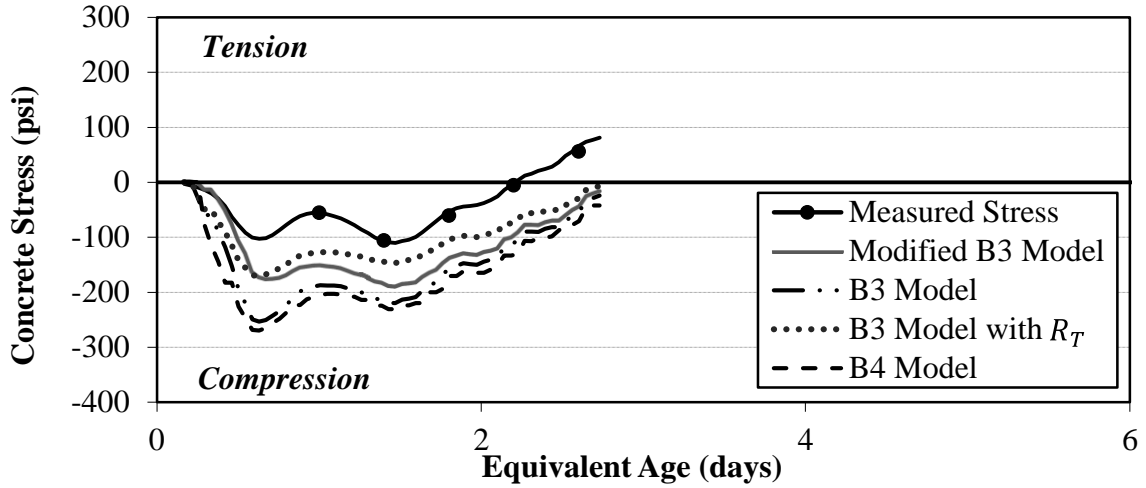
Figure B-19 Stress development results for 0.42 RG (Sum)
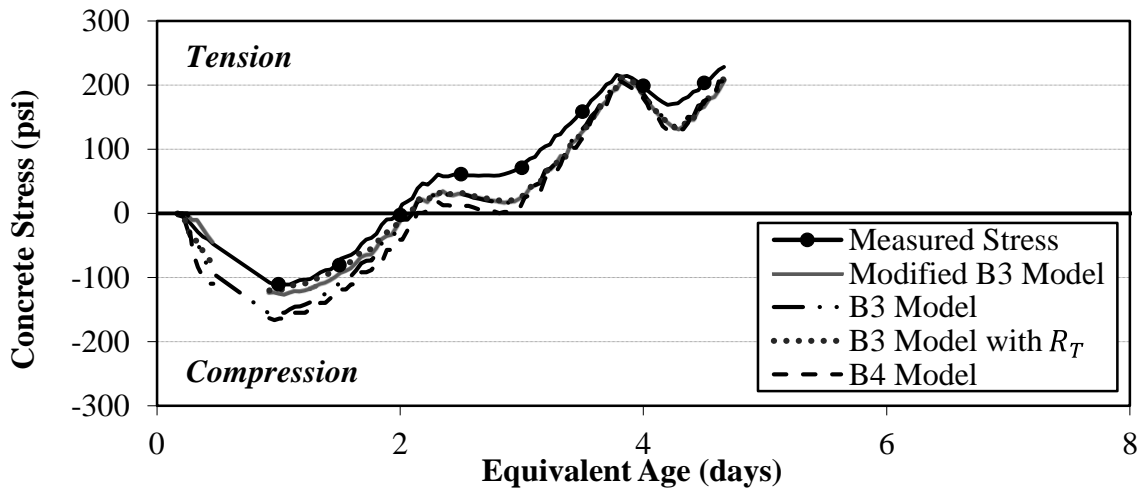
Figure B-20 Stress development results for 0.42 LS (Fall)
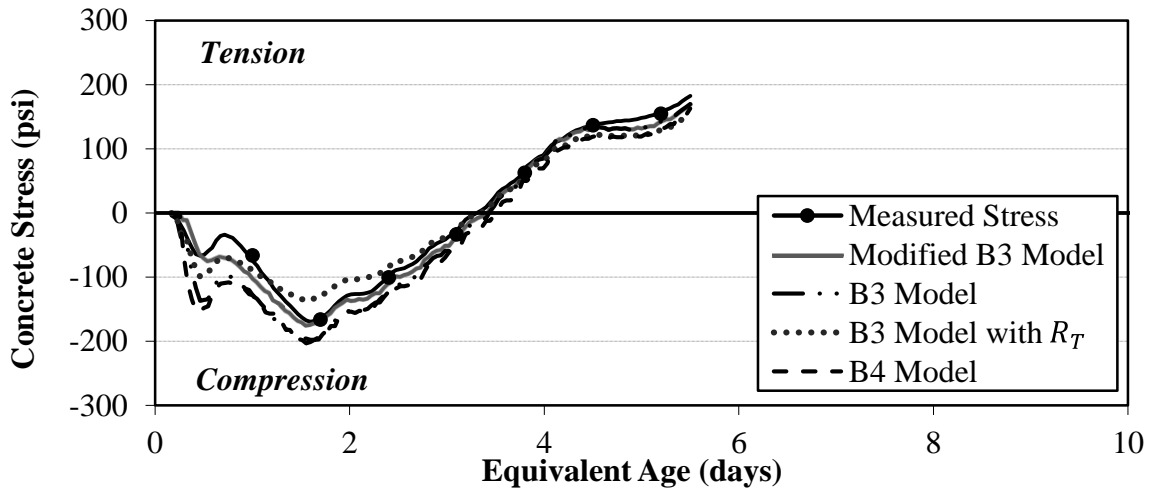
Figure B-21 Stress development results for 0.42 LS (Sum)

236
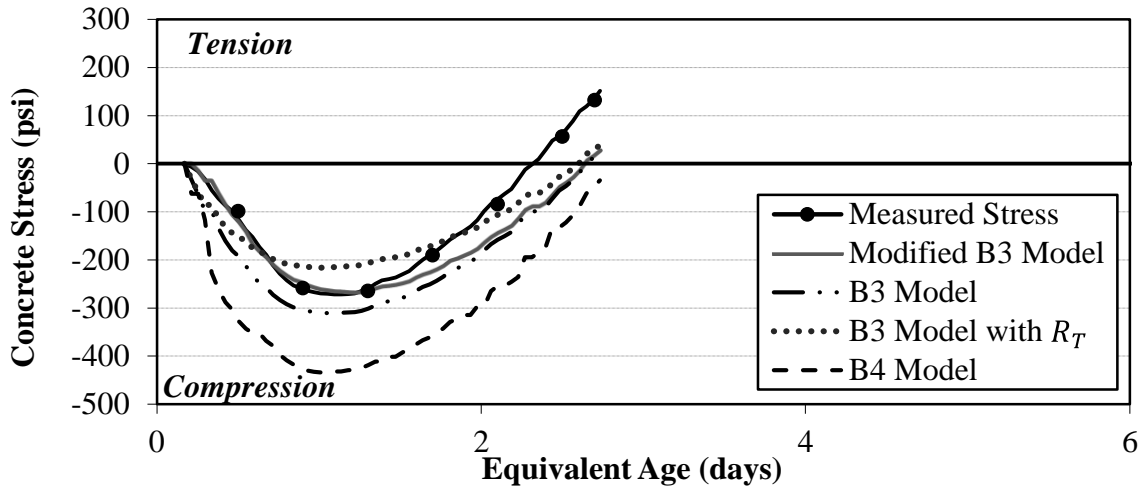
Figure B-22 Stress development results for 0.36 RG (Fall)
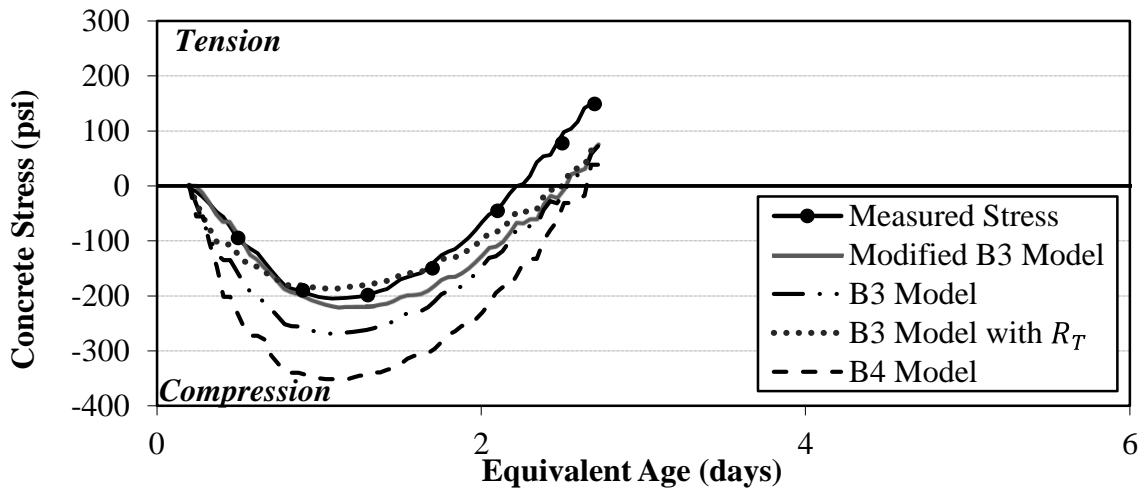
Figure B-23 Stress development results for 0.36 ICM (Fall)
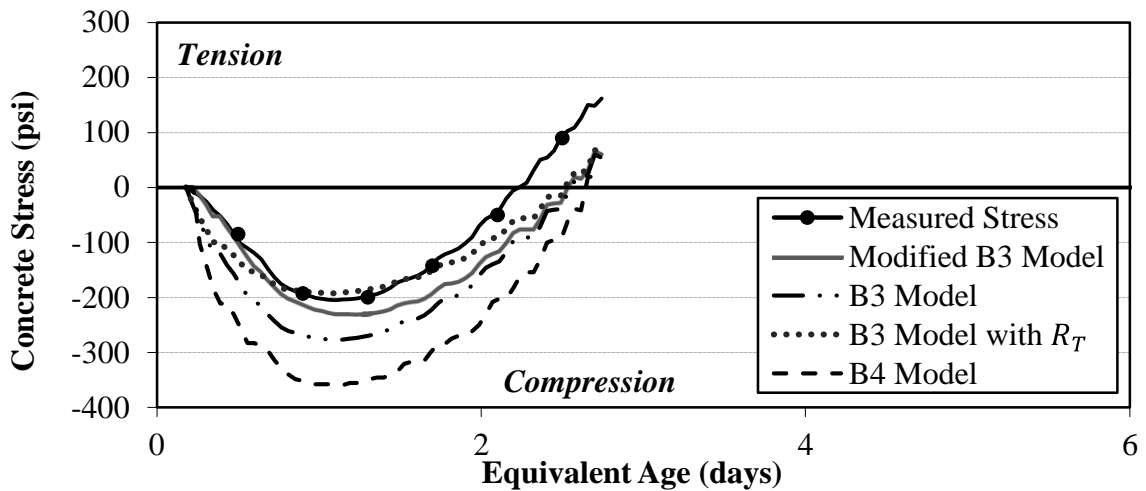
Figure B-24 Stress development results for 0.36 ICH (Fall)

237
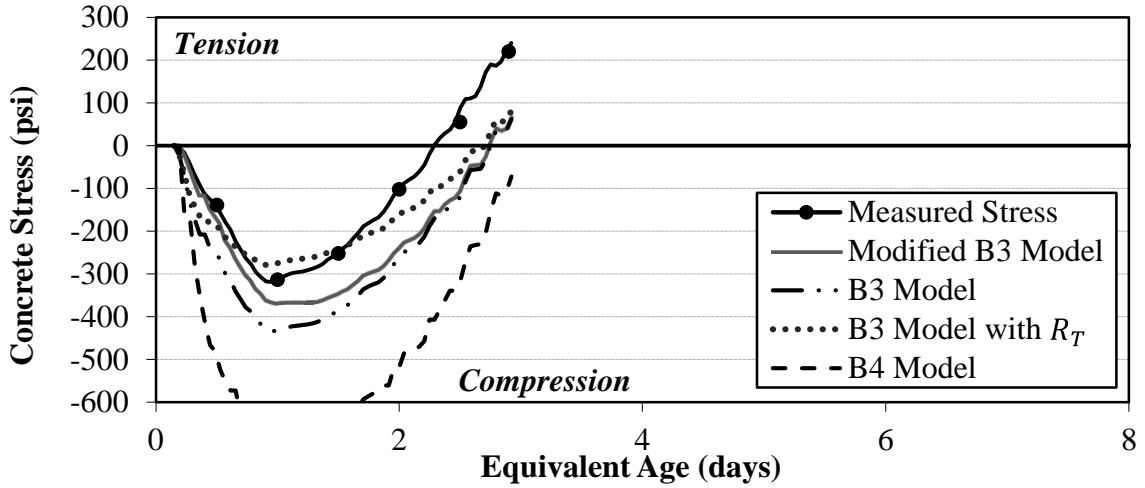
Figure B-25 Stress development results for 0.30 RG (Fall)
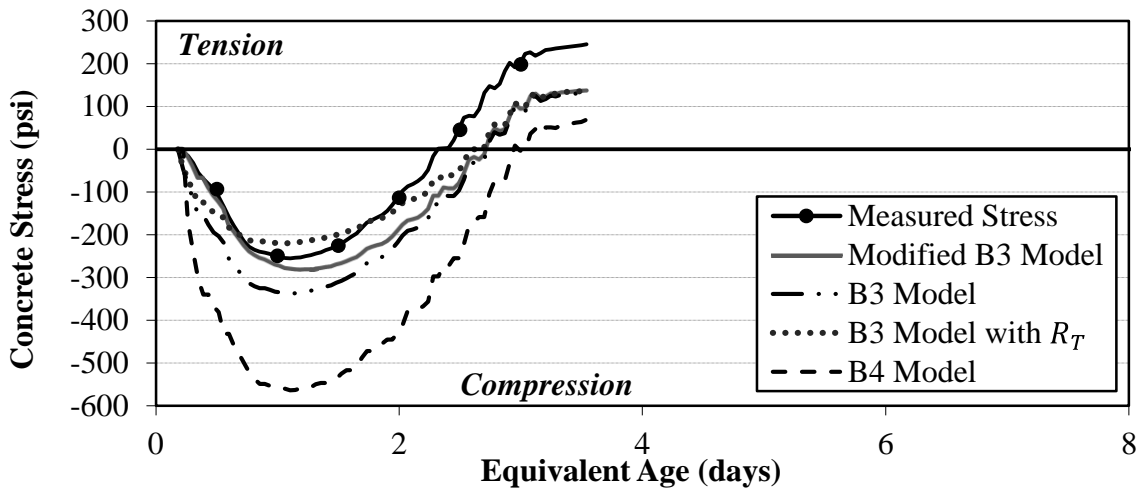
Figure B-26 Stress development results for 0.30 ICM (Fall)
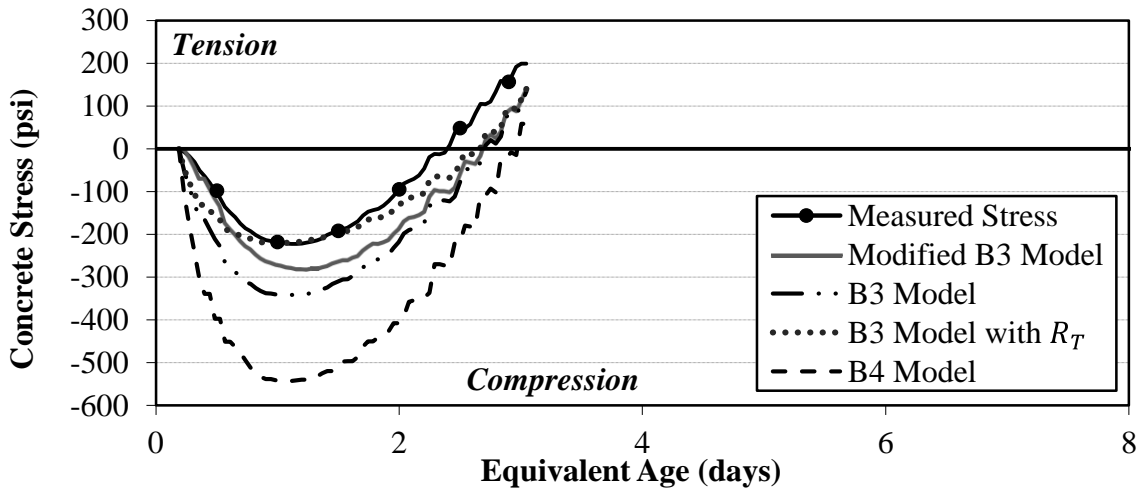
Figure B-27 Stress development results for 0.30 ICH (Fall)

238

APPENDIX C: MEASURED AND PREDICTED STRESS DEVELOPMENT FROM

PROJECT C
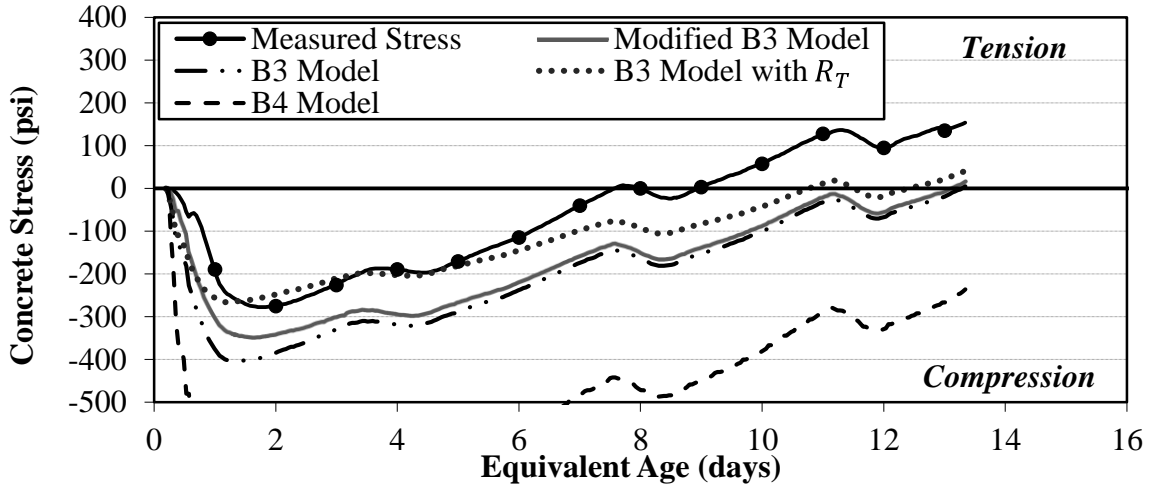
Figure C-1 Stress development results for REF 0.38
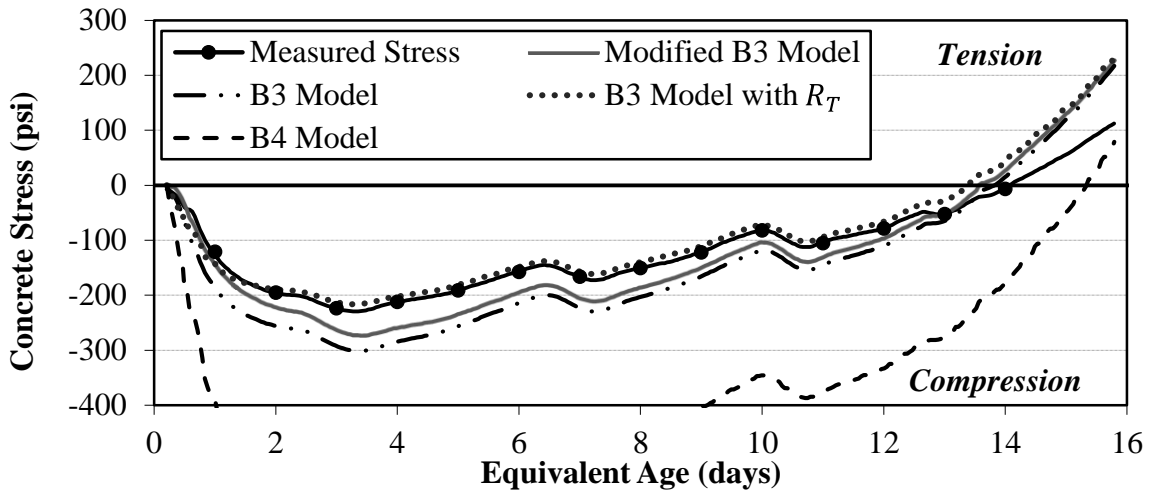
Figure C-2 Stress development results for ISLWC 0.38
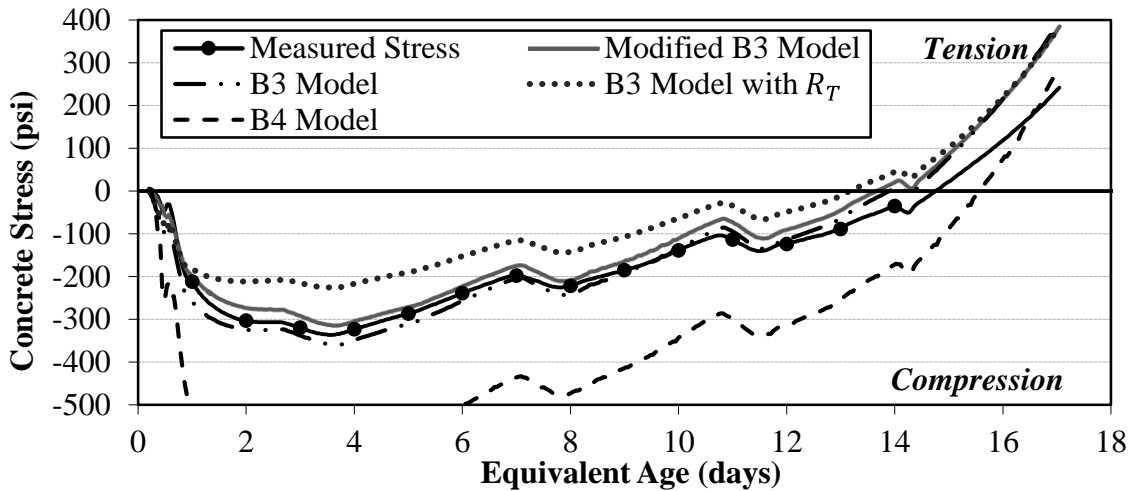
Figure C-3 Stress development results for SLWC 0.38

240
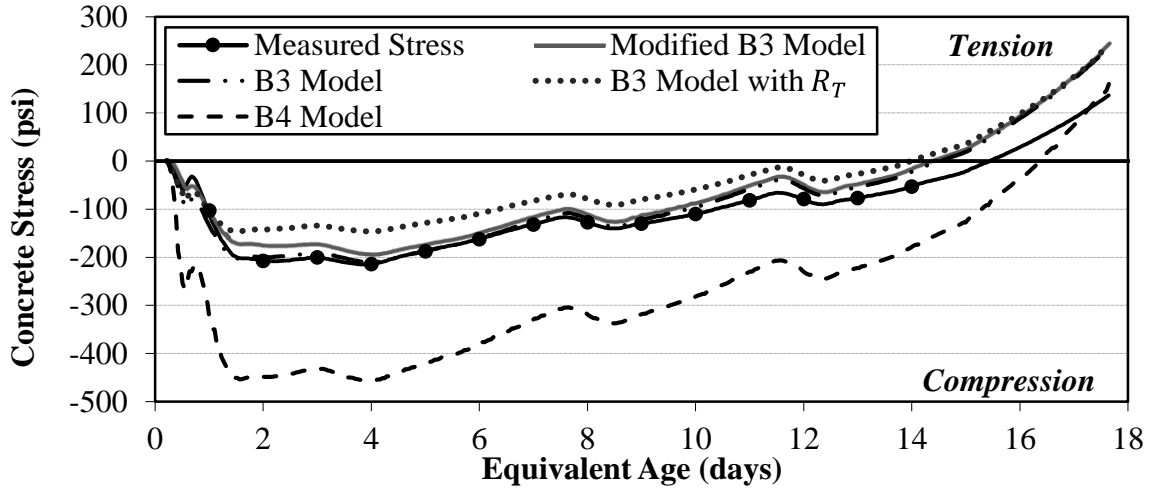
Figure C-4 Stress development results for ALWC 0.38
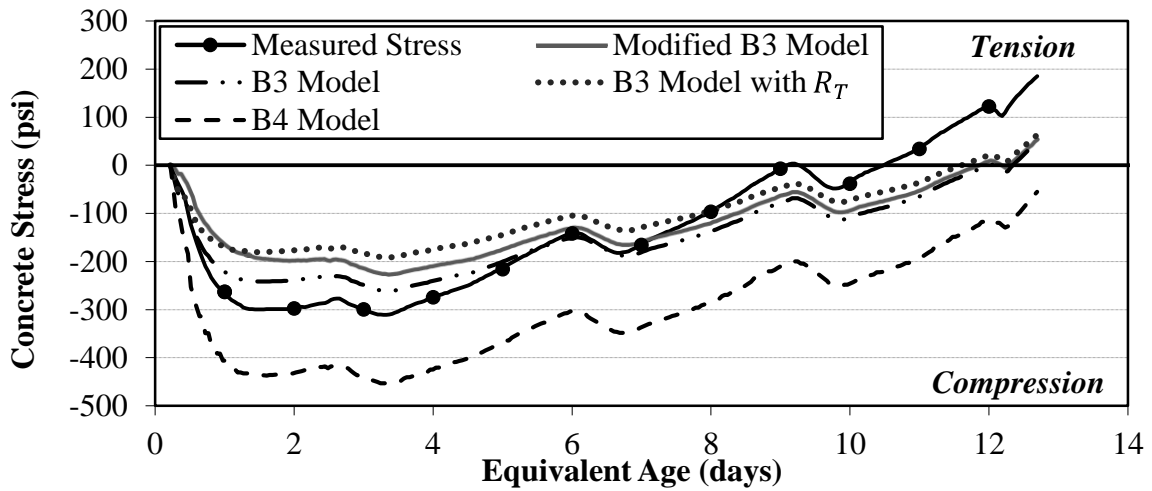
Figure C-5 Stress development results for REF 0.45
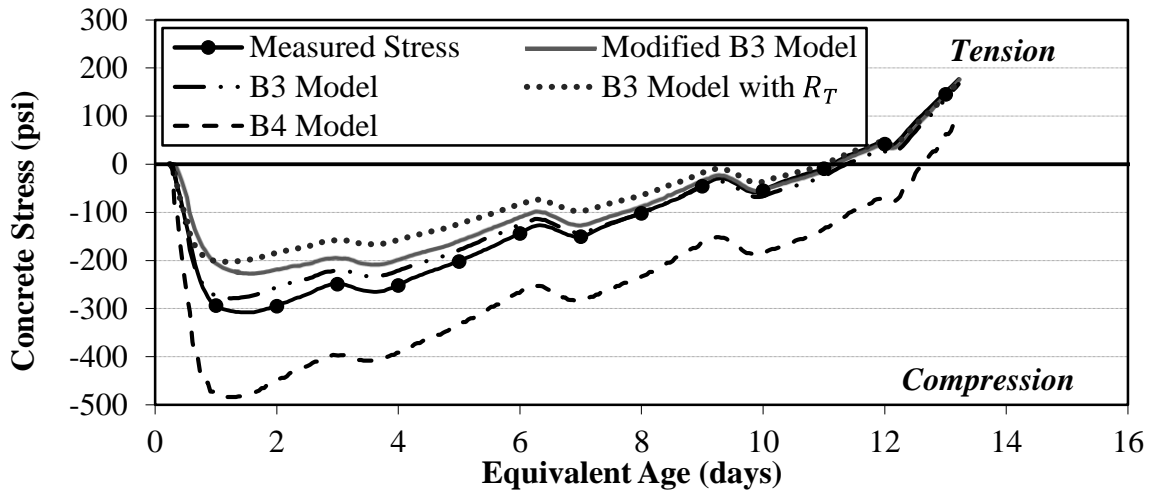
Figure C-6 Stress development results for ICC 0.45
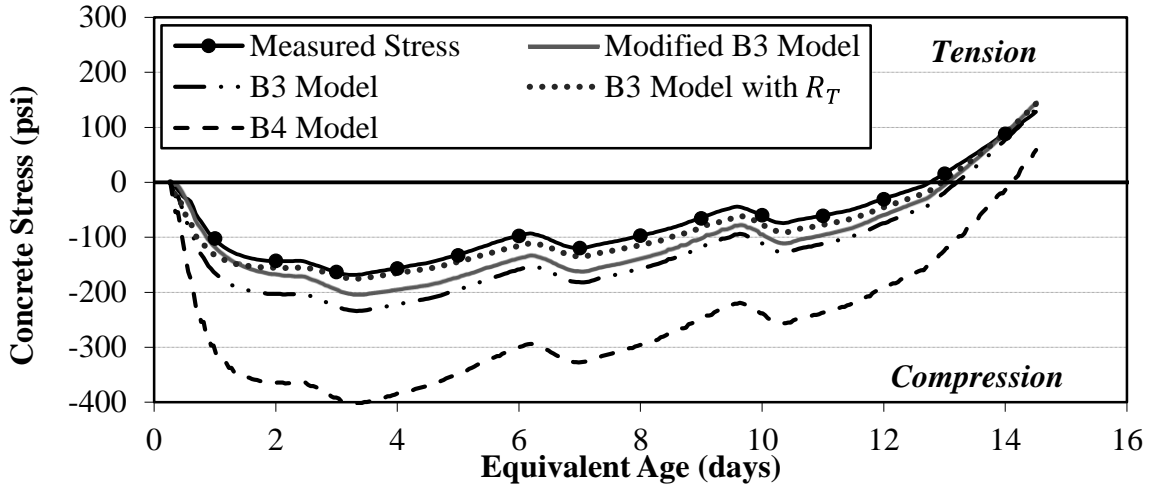
Figure C-7 Stress development results for ISLWC 0.45
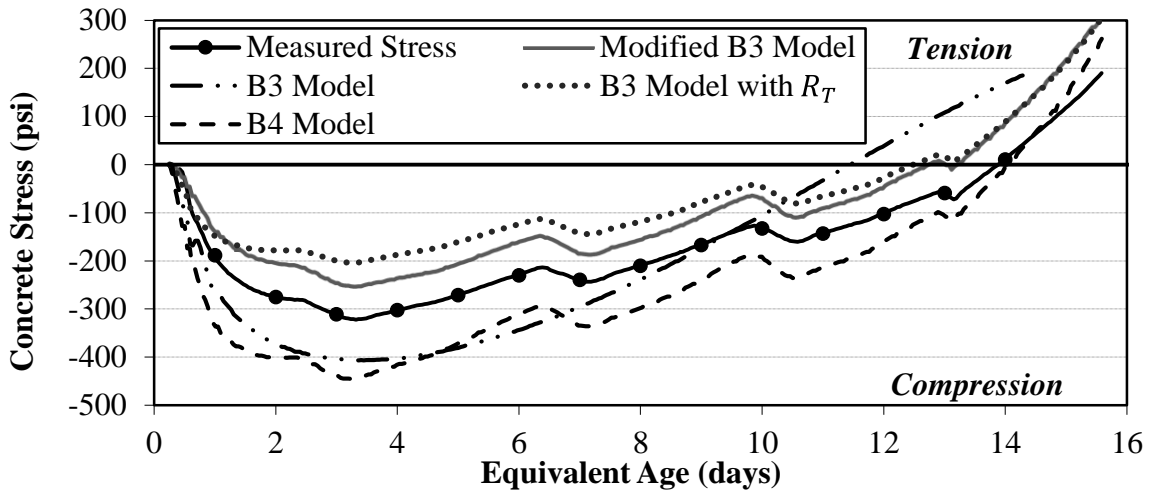
Figure C-8 Stress development results for SLWC 0.45
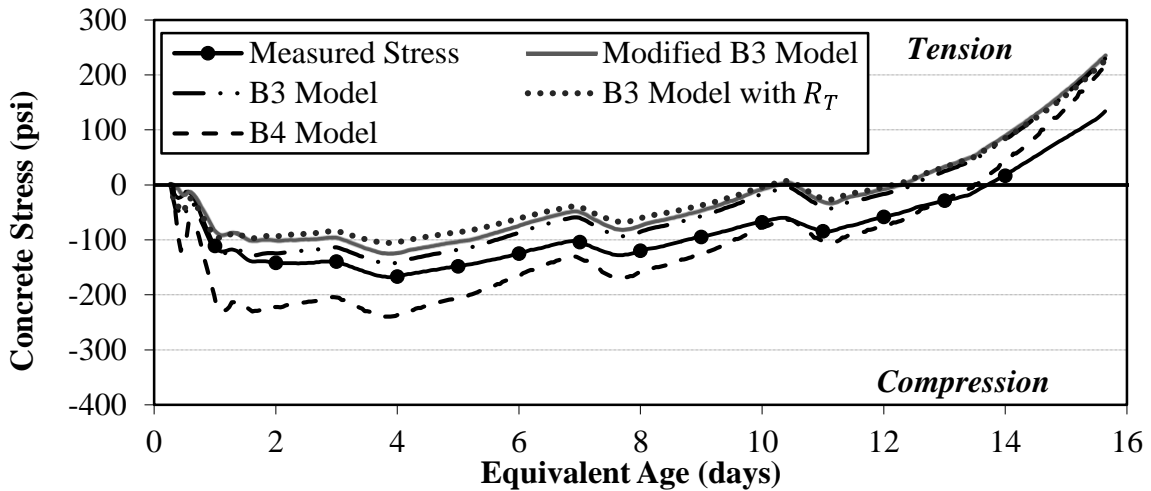
Figure C-9 Stress development results for ALWC 0.45

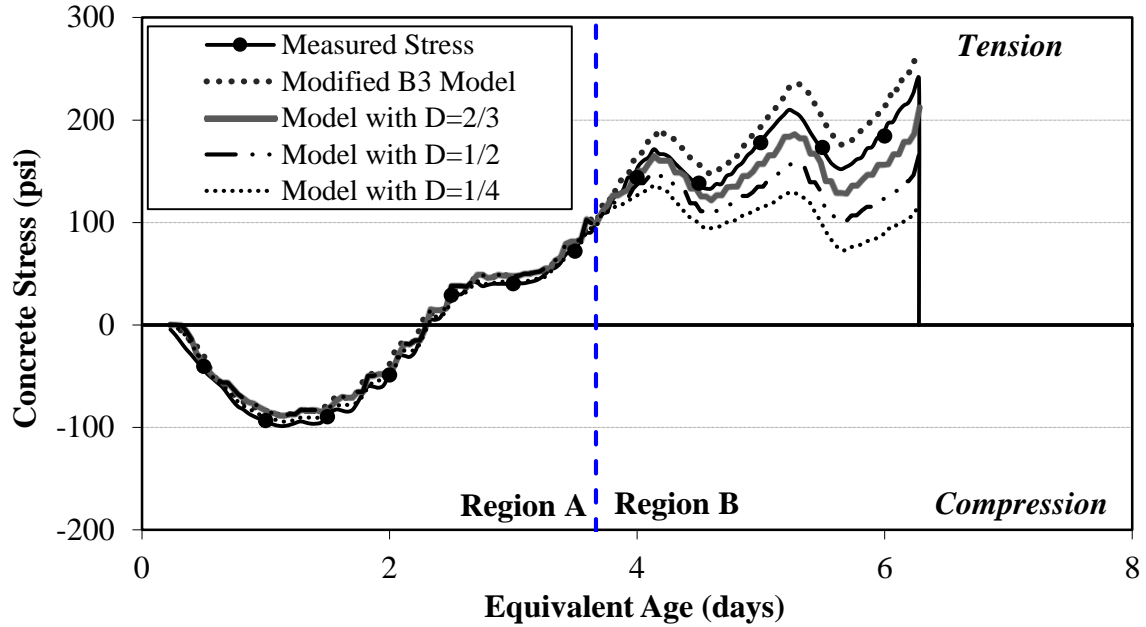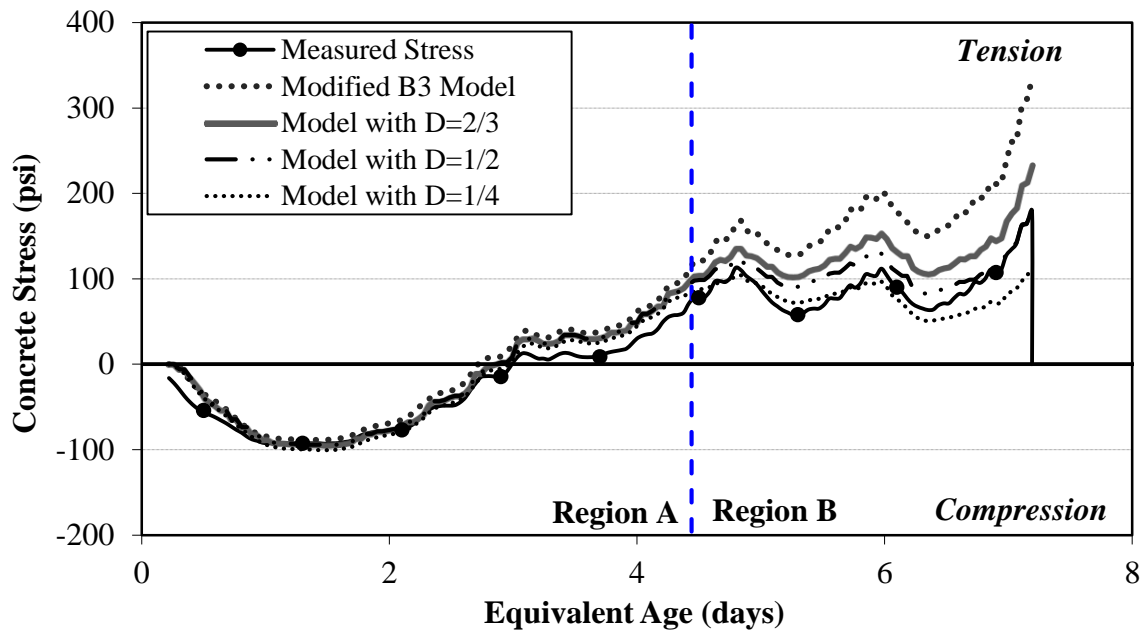**APPENDIX D: STRESS DEVELOPMENT RESULTS FROM SETTING TO CRACKING**
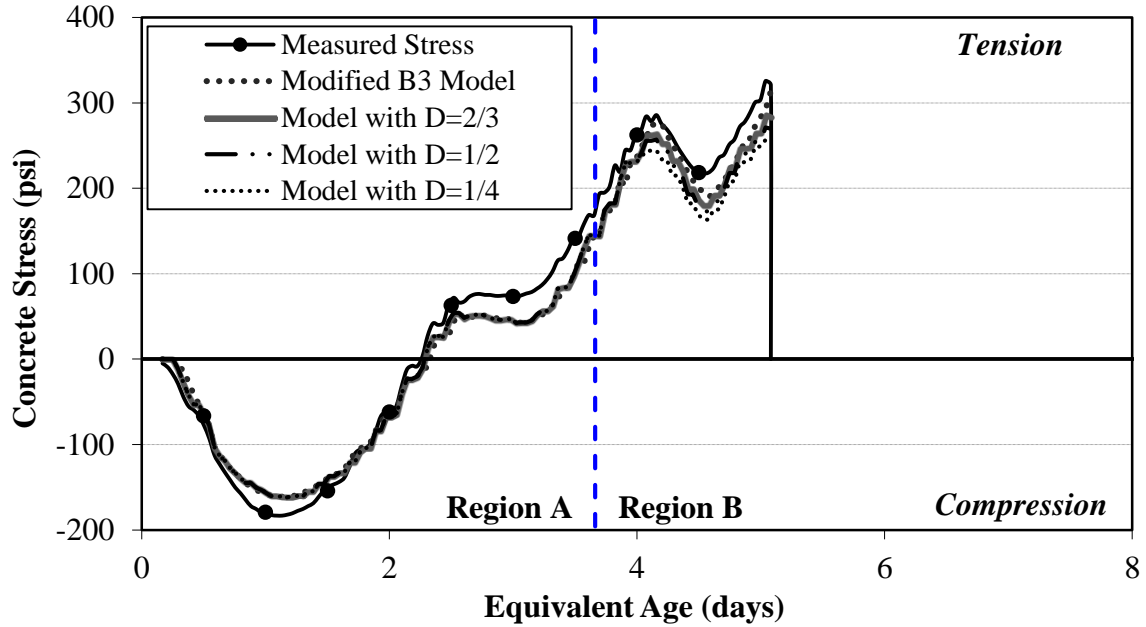
Figure D-1 Stress development results for 0.42 Slate IC (Fall) [Region A: $\sigma(t) \leq 70\% f'_t(t)$, Region B: $\sigma(t) > 70\% f'_t(t)$]
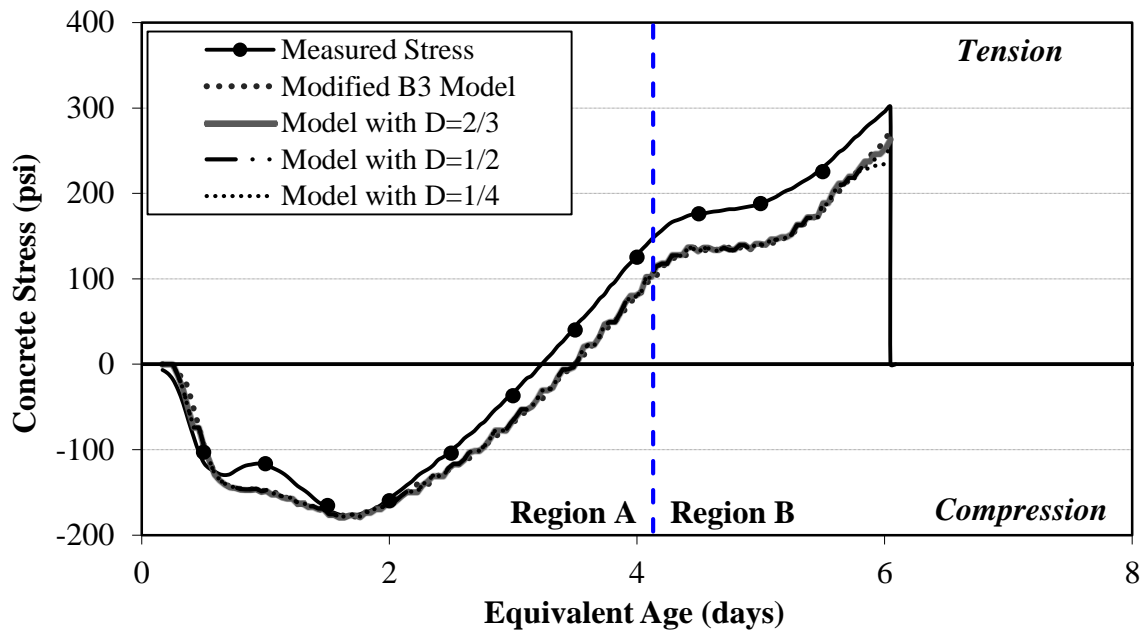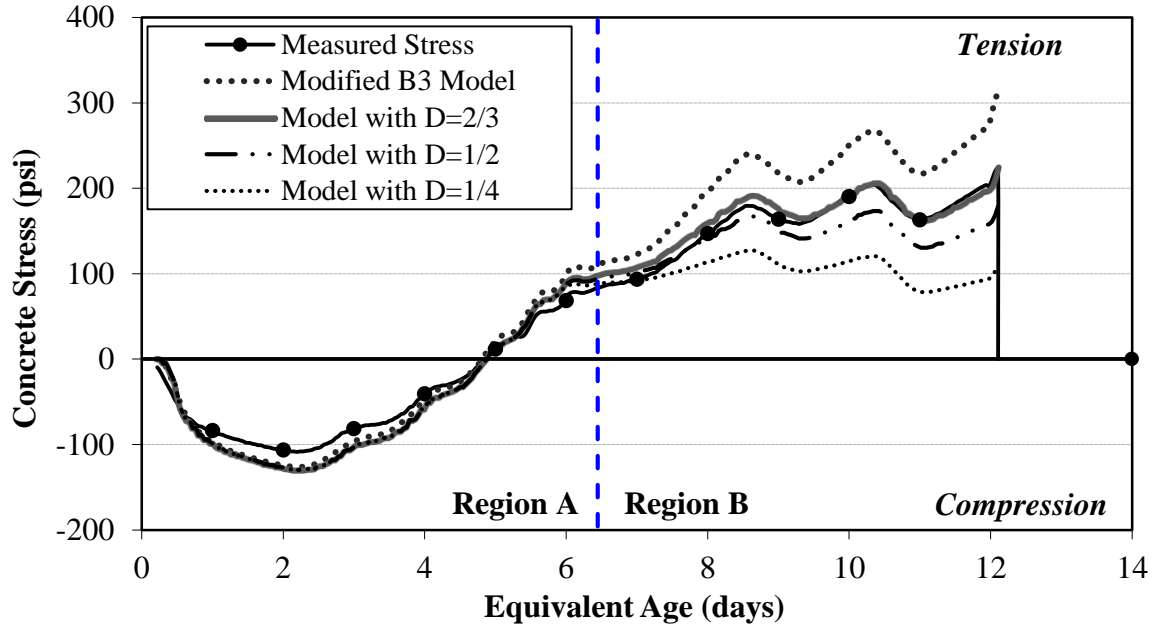

Figure D-2 Stress development results for 0.42 Slate IC (Sum) [Region A: $\sigma(t) \leq 70\% f'_t(t)$, Region B: $\sigma(t) > 70\% f'_t(t)$]
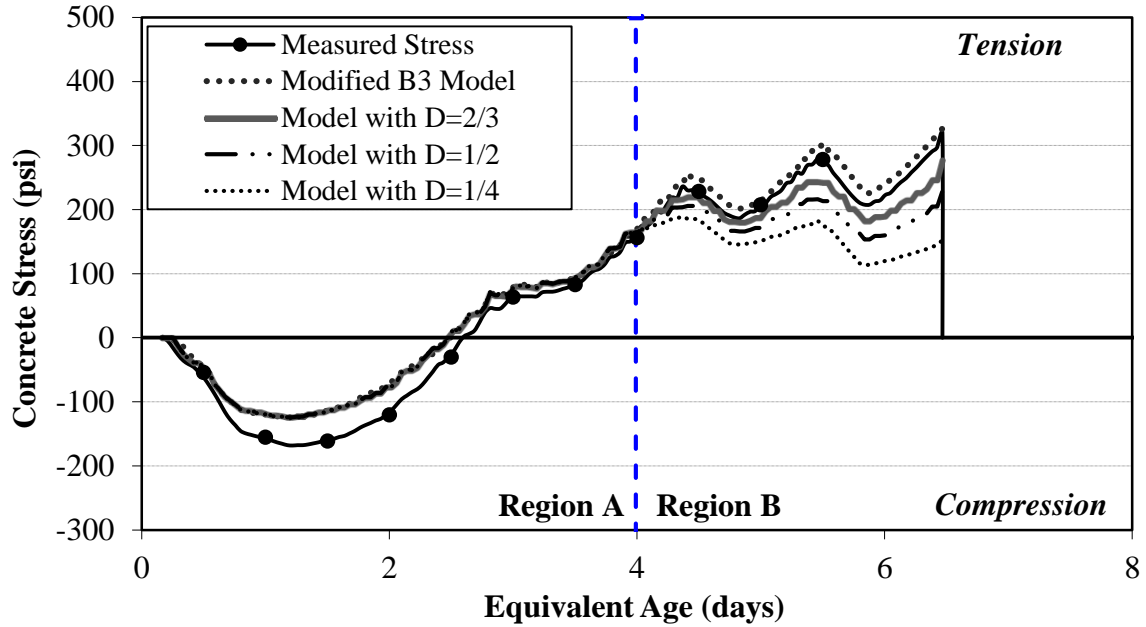
Figure D-3 Stress development results for 0.42 Slate SLW (Fall) [Region A: $\sigma(t) \leq 70\% f_t'(t)$, Region B: $\sigma(t) > 70\% f_t'(t)$]
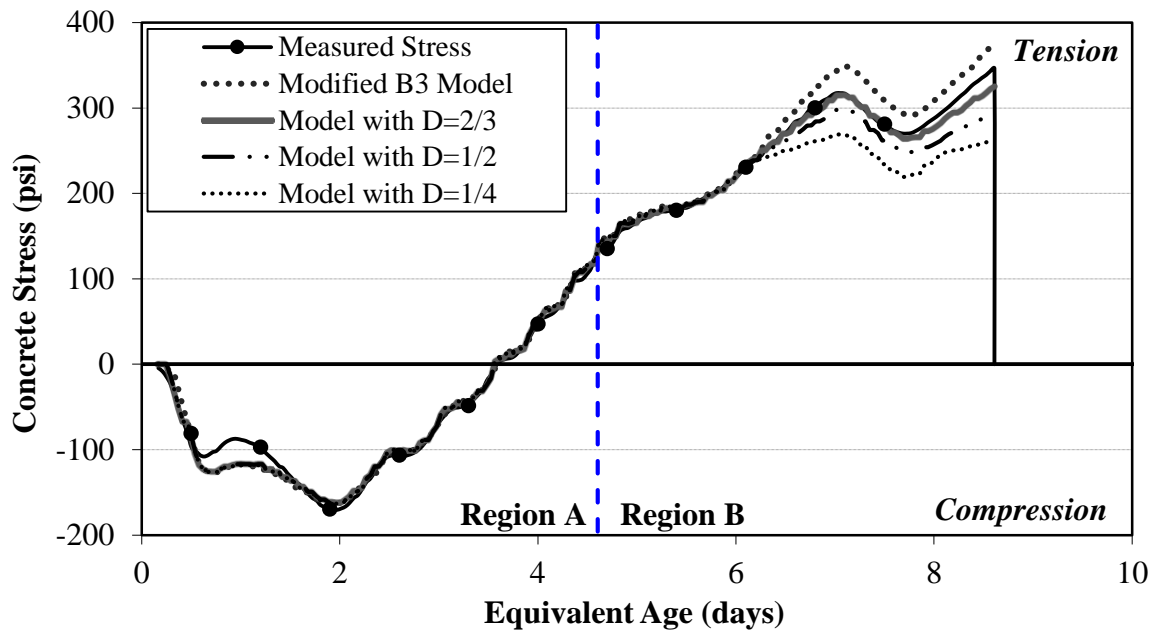
Figure D-4 Stress development results for 0.42 Slate SLW (Sum) [Region A: $\sigma(t) \leq 70\% f_t'(t)$, Region B: $\sigma(t) > 70\% f_t'(t)$]
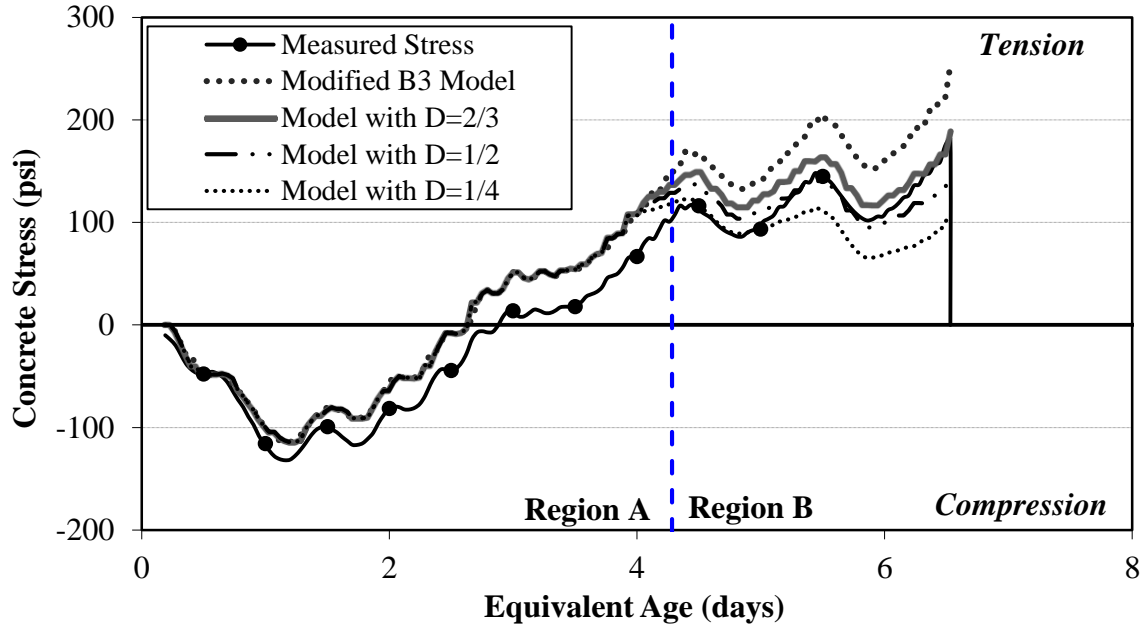
Figure D-5 Stress development results for 0.42 Slate ALW (Fall) [Region A: $\sigma(t) \leq 70\%f'_t(t)$, Region B: $\sigma(t) > 70\%f'_t(t)$]
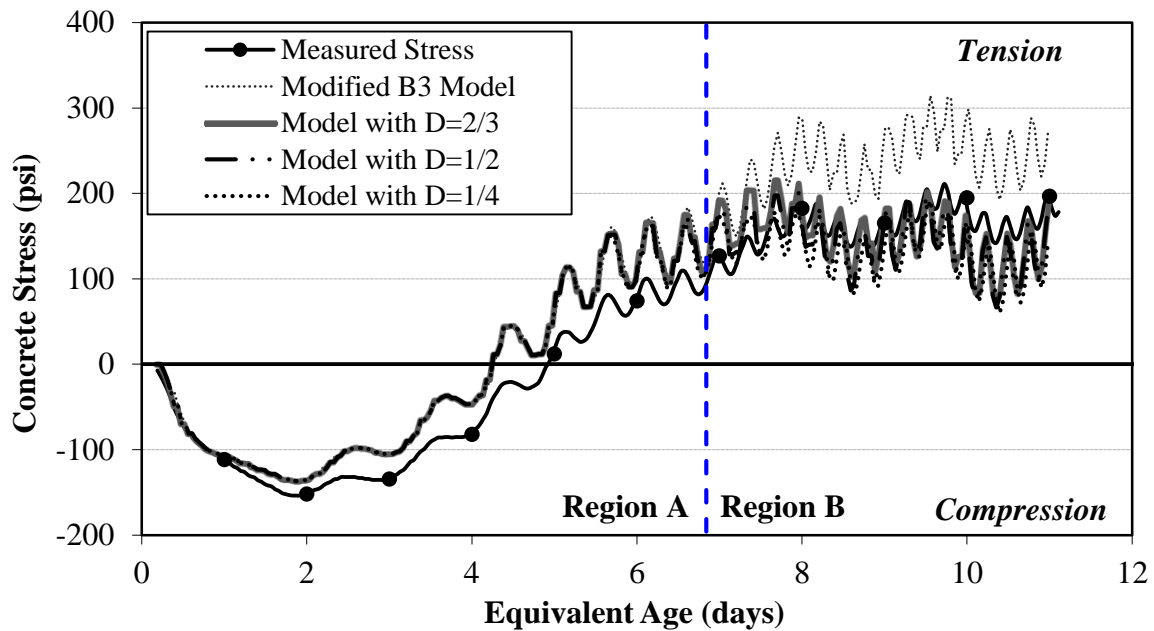
Figure D-6 Stress development results for 0.42 Slate ALW (Sum) [Region A: $\sigma(t) \leq 70\%f'_t(t)$, Region B: $\sigma(t) > 70\%f'_t(t)$]
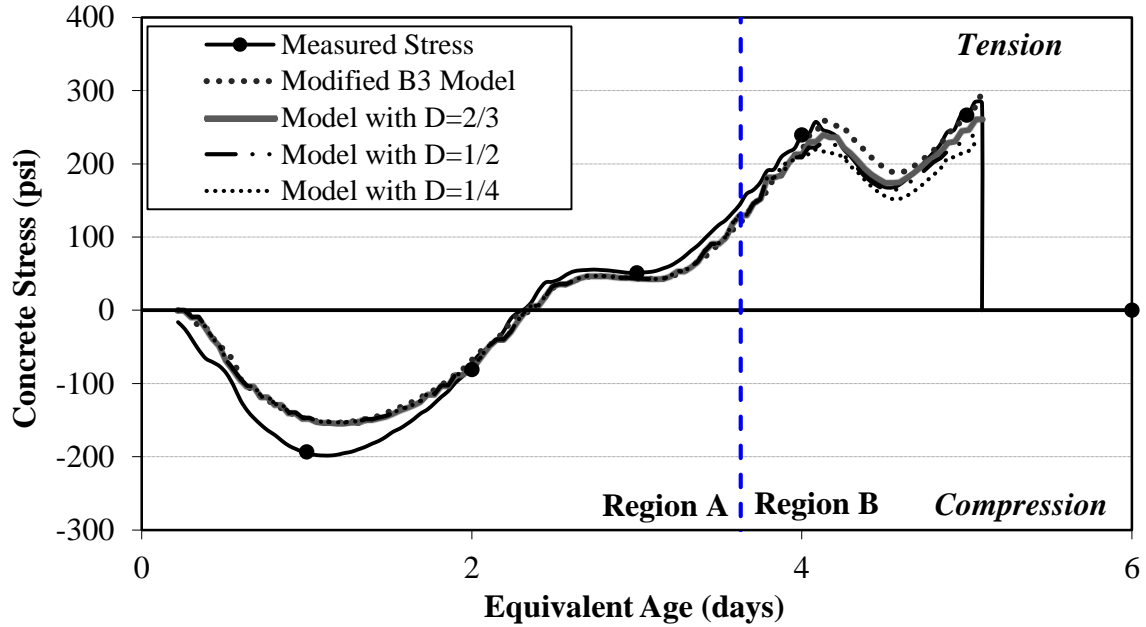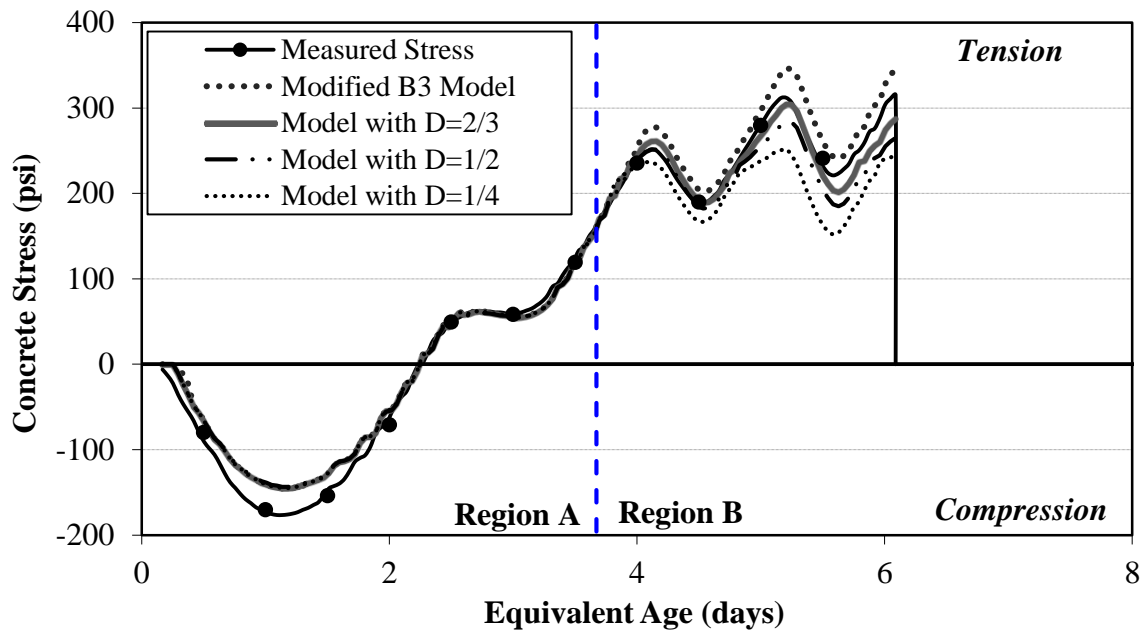
Figure D-7 Stress development results for 0.42 Clay IC (Fall) [Region A: $\sigma(t) \leq 70\%f'_t(t)$, Region B: $\sigma(t) > 70\%f'_t(t)$]
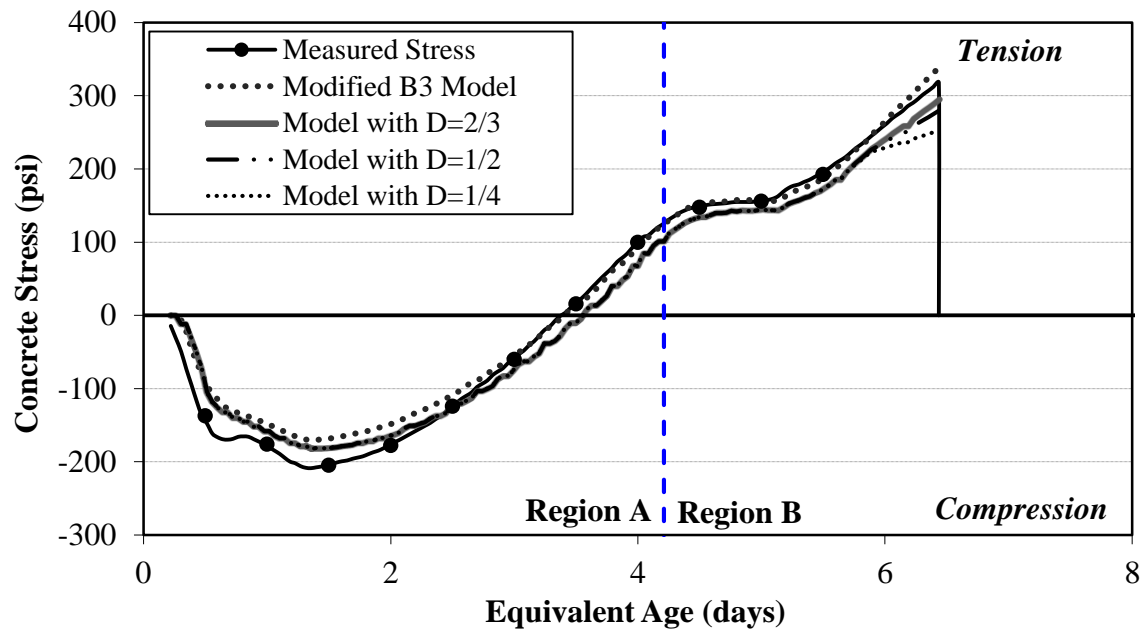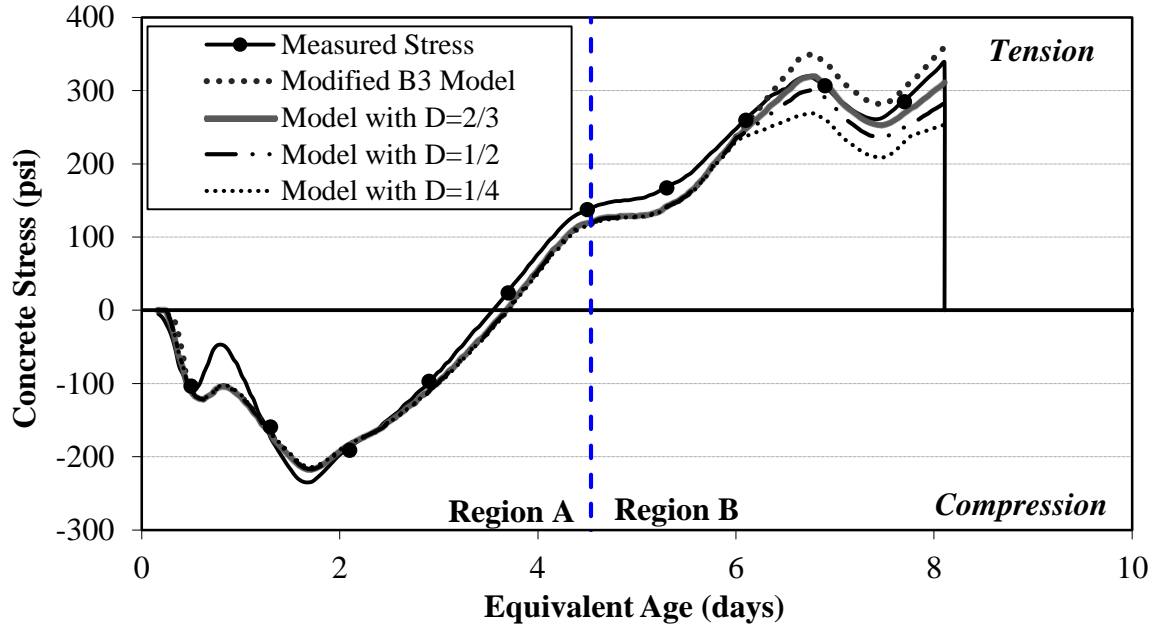

Figure D-8 Stress development results for 0.42 Clay IC (Sum) [Region A: $\sigma(t) \leq 70\%f'_t(t)$, Region B: $\sigma(t) > 70\%f'_t(t)$]
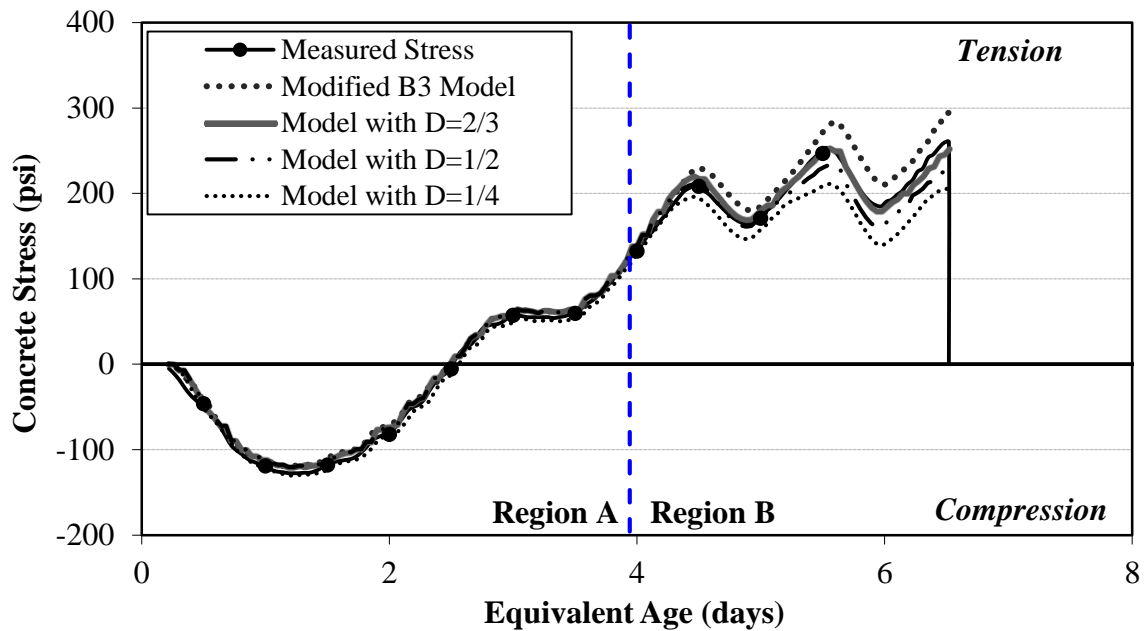
Figure D-9 Stress development results for 0.42 Clay SLW (Fall) [Region A: $\sigma(t) \leq 70\%f'_t(t)$, Region B: $\sigma(t) > 70\%f'_t(t)$]
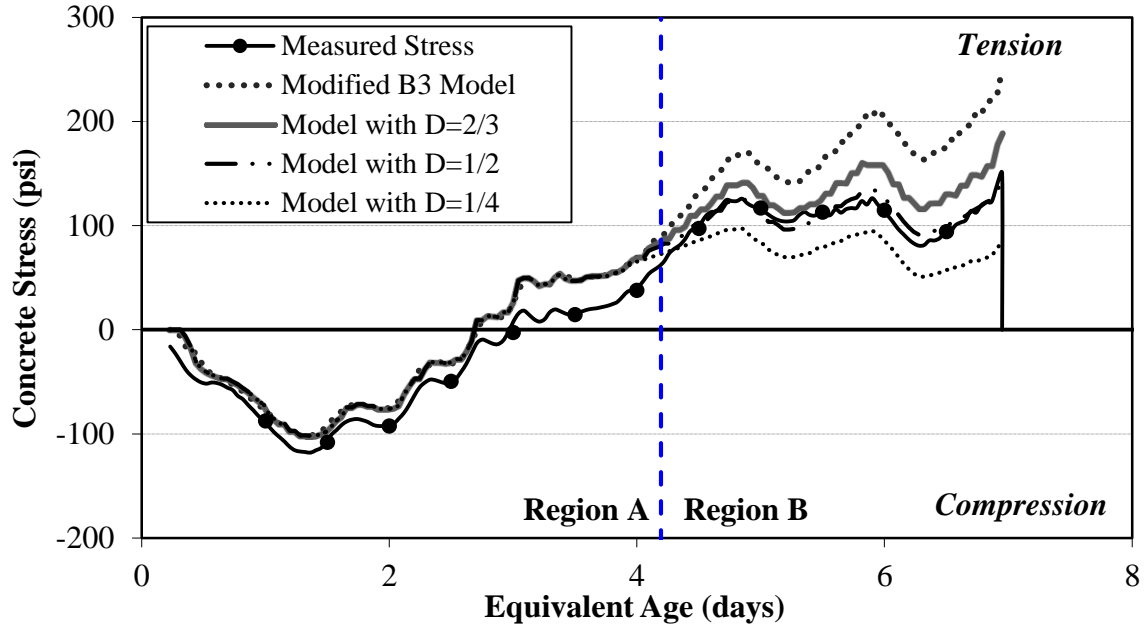

Figure D-10 Stress development results for 0.42 Clay ALW (Fall) [Region A: $\sigma(t) \leq 70\%f'_t(t)$, Region B: $\sigma(t) > 70\%f'_t(t)$]

Figure D-11 Stress development results for 0.42 Clay ALW (Sum) [Region A: $\sigma(t) \leq 70\% f'_t(t)$, Region B: $\sigma(t) > 70\% f'_t(t)$]

Figure D-12 Stress development results for 0.42 Shale IC (Fall) [Region A: $\sigma(t) \leq 70\% f'_t(t)$, Region B: $\sigma(t) > 70\% f'_t(t)$]
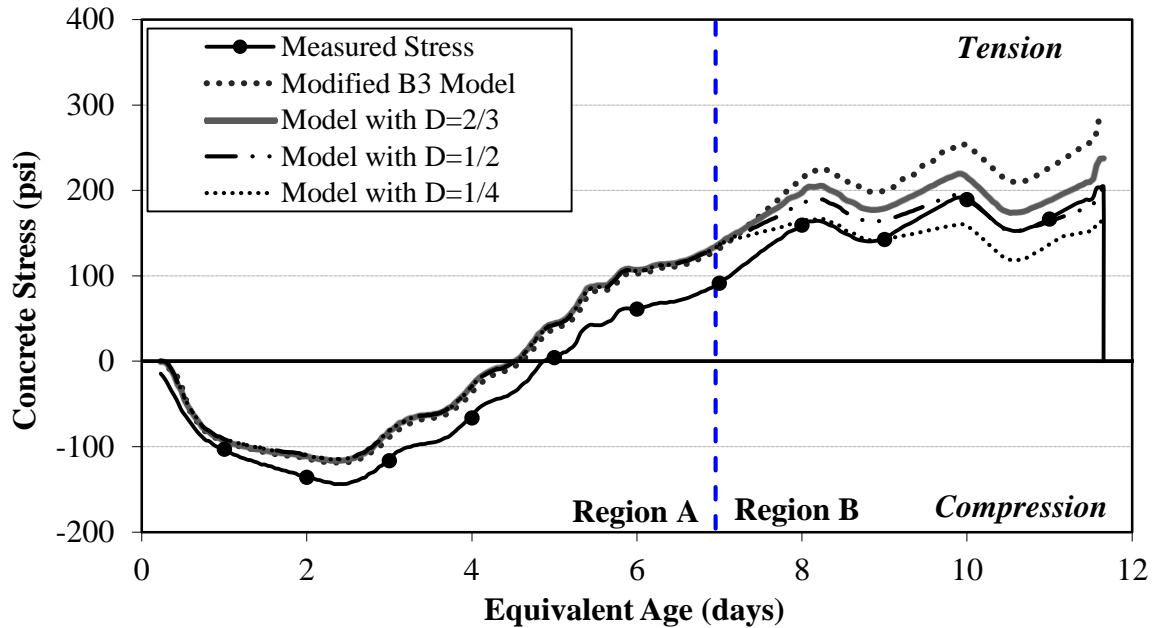
Figure D-13 Stress development results for 0.42 Shale IC (Sum) [Region A: $\sigma(t) \leq 70\%f_t'(t)$, Region B: $\sigma(t) > 70\%f_t'(t)$]
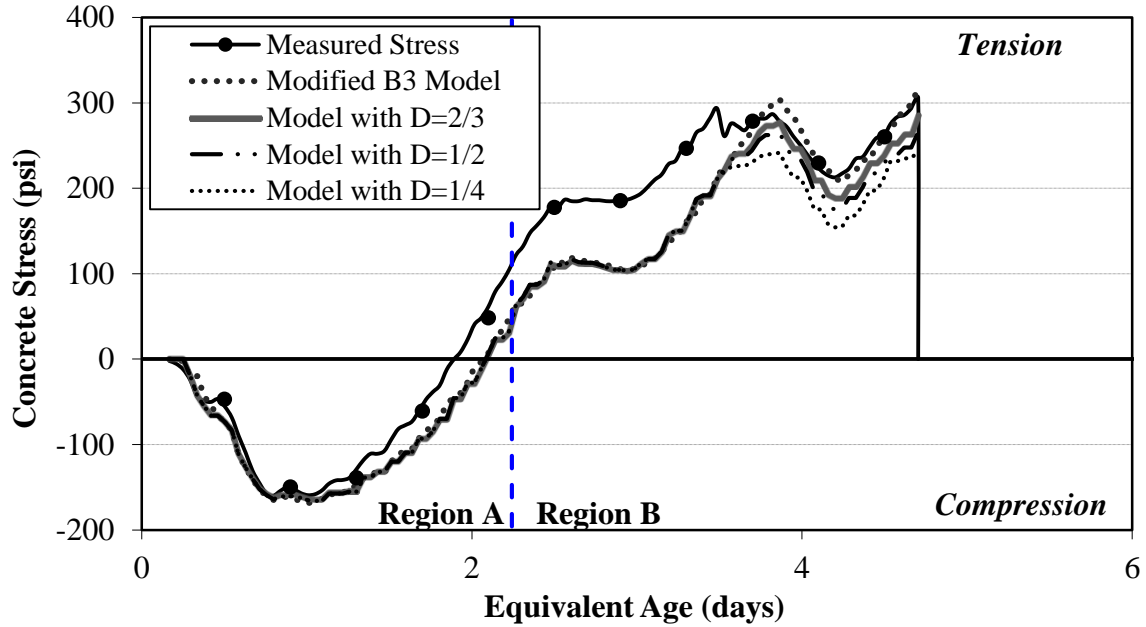

Figure D-14 Stress development results for 0.42 Shale SLW (Fall) [Region A: $\sigma(t) \leq 70\%f_t'(t)$, Region B: $\sigma(t) > 70\%f_t'(t)$]

Figure D-15 Stress development results for 0.42 Shale ALW (Fall) [Region A: $\sigma(t) \leq 70\%f'_t(t)$, Region B: $\sigma(t) > 70\%f'_t(t)$]

Figure D-16 Stress development results for 0.42 Shale ALW (Sum) [Region A: $\sigma(t) \leq 70\%f'_t(t)$, Region B: $\sigma(t) > 70\%f'_t(t)$]

251

Figure D-17 Stress development results for 0.42 RG (Fall) [Region A: $\sigma(t) \leq 70\% f'_t(t)$, Region B: $\sigma(t) > 70\% f'_t(t)$]
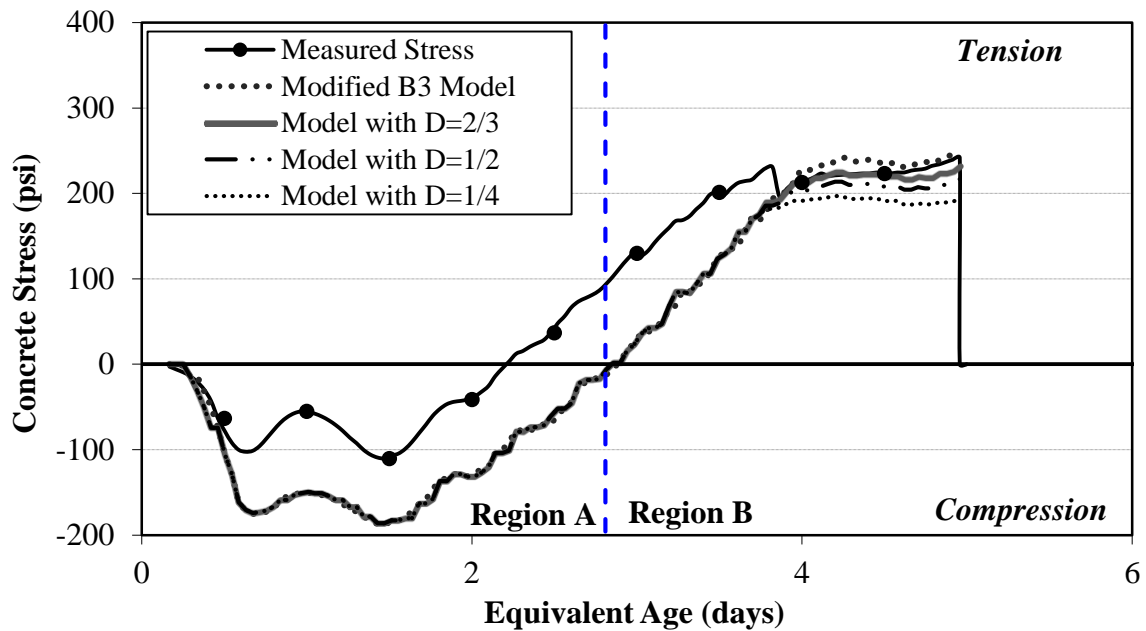

Figure D-18 Stress development results for 0.42 RG (Sum) [Region A: $\sigma(t) \leq 70\% f'_t(t)$, Region B: $\sigma(t) > 70\% f'_t(t)$]
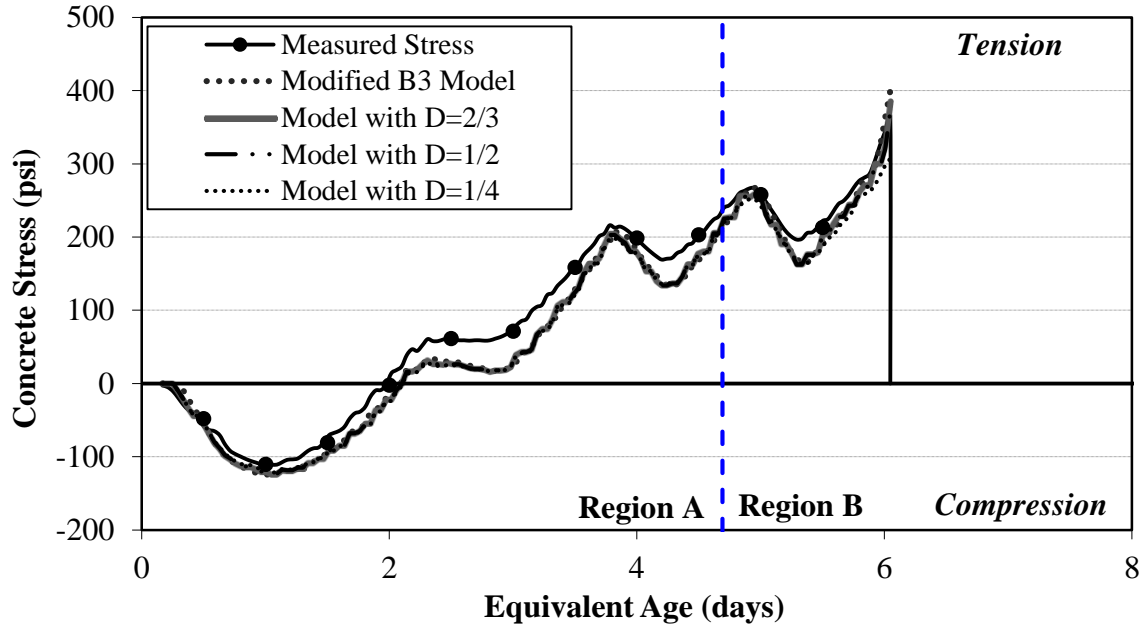
Figure D-19 Stress development results for 0.42 LS (Fall) [Region A: $\sigma(t) \leq 70\%f'_t(t)$, Region B: $\sigma(t) > 70\%f'_t(t)$]
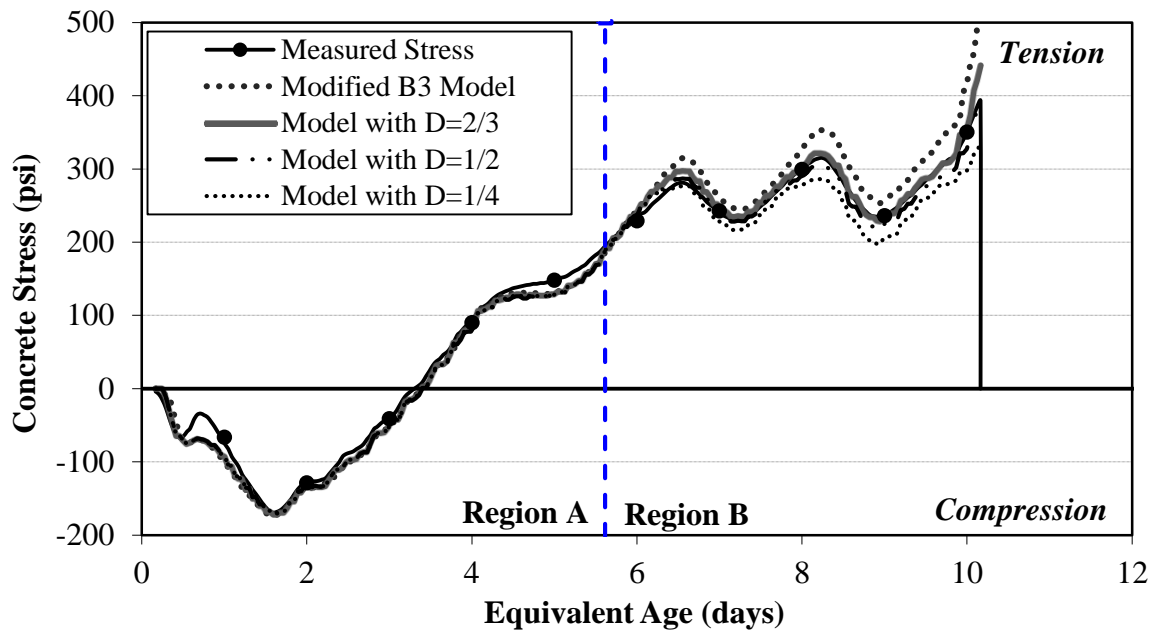

Figure D-20 Stress development results for 0.42 LS (Sum) [Region A: $\sigma(t) \leq 70\%f'_t(t)$, Region B: $\sigma(t) > 70\%f'_t(t)$